Ron Fleming

ANL/RERTR/TM-17

THE FORD NUCLEAR REACTOR DEMONSTRATION PROJECT FOR THE EVALUATION AND ANALYSIS OF LOW ENRICHMENT FUEL

Final Report

by

William Kerr, John S. King, John C. Lee,
William R. Martin, and David K. Wehe

ARGONNE NATIONAL LABORATORY, ARGONNE, ILLINOIS

Operated by THE UNIVERSITY OF CHICAGO
for the U. S. DEPARTMENT OF ENERGY
under Contract W-31-109-Eng-38

Reproduced from the best available copy.

Available to DOE and DOE contractors from the
Office of Scientific and Technical Information
P.O. Box 62
Oak Ridge, TN 37831
Prices available from (615) 576-8401, FTS 626-8401

Available to the public from the
National Technical Information Service
U.S. Department of Commerce
5285 Port Royal Road
Springfield, VA 22161

Distribution Category:
General Reactor Technology (UC-520)

ANL/RERTR/TM-17

THE FORD NUCLEAR REACTOR DEMONSTRATION PROJECT FOR THE EVALUATION AND ANALYSIS OF LOW ENRICHMENT FUEL

Final Report

by

William Kerr, John S. King, John C. Lee,
William R. Martin, and David K. Wehe

Prepared by
The University of Michigan
Department of Nuclear Engineering
and the
Michigan-Memorial Phoenix Project
Ann Arbor, MI 48109
Under Subcontract Number 31-109-38-4973

Prepared for
ARGONNE NATIONAL LABORATORY
9700 South Cass Avenue
Argonne, Illinois 60439

Received July 1988
Printed July 1991

Project Participants

William Kerr
John S. King
John C. Lee
William R. Martin
David K. Wehe

Reed R. Burn
Gary Cook

Joo Hyun Baik
Felippe Beaklini
Forrest B. Brown
Clifton Drumm
Keith Flint
Brent Heuser
Daewon Kim
Baard Johansen
David C. Losey
Joao Moreira
Gerald Munyan
Horacio Nakata
James Rathkopf
James Sheridan
Gayle J. Stankiewicz
Jasmina Vujic
Tzu-Chiang Wan
Roger Wigent

Table of Contents

LIST OF TABLES

LIST OF FIGURES

THE FORD NUCLEAR REACTOR DEMONSTRATION PROJECT FOR THE EVALUATION AND ANALYSIS OF LOW ENRICHMENT FUEL

Final Report

by

William Kerr, John S. King, John C. Lee,
William R. Martin, and David K. Wehe

ABSTRACT

The whole-core LEU fuel demonstration project at the University of Michigan was begun in 1979 as part of the Reduced Enrichment Research and Test Reactor (RERTR) Program at Argonne National Laboratory. An LEU fuel design was selected which would produce minimum perturbations in the neutronic, operations, and safety characteristics of the 2-MW Ford Nuclear Reactor (FNR). Initial criticality with a full LEU core on December 8, 1981, was followed by low- and full-power testing of the fresh LEU core, transitional operation with mixed HEU-LEU configurations, and establishment of full LEU equilibrium core operation. The transition from the HEU to the LEU configurations was achieved with negligible impact on experimental utilization and safe operation of the reactor.

Experimental efforts in the demonstration centered around measurement of spatial and spectral neutron flux distributions. The spatial measurements utilized iron wire activations and SPNDs. Multiple foil activations were performed in both the HEU and LEU cores to determine detailed neutron flux spectra. The sensitivity of the unfolded flux to the flux spectrum input to the unfolding codes was studied, as were inconsistencies or deficiencies in activation cross section data for the foil materials.

Other reactor parameters measured during the demonstration included shim rod reactivity worth, temperature and void coefficients of reactivity, and power defect of reactivity. Measurements of the leakage flux at various beam ports were also made to monitor the progress of the transition from HEU to LEU configurations.

An extensive reactor analysis effort complemented the experimental measurements. Various neutronic codes were adapted, modified, or developed to perform the necessary reactor physics calculations.

This report provides a detailed summary of the development of calculational techniques and models for the FNR, measurement techniques and results, and comparison of measured and calculated quantities.

I. INTRODUCTION

The University of Michigan Department of Nuclear Engineering and the Michigan-Memorial Phoenix Project have been engaged in a cooperative effort with Argonne National Laboratory to test and analyze low enrichment fuel in the Ford Nuclear Reactor (FNR). The effort was begun in 1979 as part of the Reduced Enrichment Research and Test Reactor (RERTR) Program to demonstrate, on a whole core basis, the feasibility of enrichment reduction from 93% to below 20% in MTR-type fuel designs.

The key technical basis of the low enrichment uranium (LEU) fuel is to reduce the ^{235}U enrichment to below 20% while increasing, at the same time, the uranium loading of each fuel element to compensate for the reactivity loss due to the larger ^{238}U content. The required uranium loading can be achieved by increasing the uranium density in the fuel meat and by increasing the fuel volume fraction. At the same time, it is necessary to insure that fuel elements operate within their thermal-hydraulic limits.

The first phase in our investigation performed in preparation for the LEU fuel testing in the FNR core included: (a) initiation of the development of experimental and analytical techniques applicable for neutronic evaluation of the MTR-type fuel elements, (b) determination of a LEU

design for the FNR, (c) preparation of a preliminary FNR license amendment and (d) a thermal-hydraulic testing program for the MTR-type fuel elements. The 1979 Summary Report [Ker80] includes a discussion of the initial phase of the FNR LEU project.

Subsequent effort during 1980 was devoted to improving and validating the experimental techniques and analytical methods to be used in characterizing the high enrichment uranium (HEU) and LEU cores for the FNR. The experimental effort focused on the measurement of in-core and ex-core spatial flux distributions and the measurement of ex-core spectra. In the analytical area, emphasis was placed on improving and verifying the computer codes and calculational models used to predict the neutronic behavior of the FNR. In addition, a series of thermal/hydraulic tests were performed for the MTR-type fuel elements and an amendment to the FNR Safety Analysis Report was submitted as part of the required License Amendment to the U.S. Nuclear Regulatory Commission to permit use of the LEU fuel in the FNR. Approval was granted in February, 1981. The 1980 Summary Report [Ker81] presents the details of this phase of the LEU project.

The continuation of the project into 1981 culminated with the loading of the LEU core into the FNR and the achievement of criticality on December 8, 1981. The critical loading followed one-for-one replacements of HEU fuel elements with

LEU fuel elements in the center and periphery of the FNR core. Following the critical loading, approximately six weeks of low power testing of the LEU core was performed, including measurement of control rod worths, full core flux maps and spectral measurements, both in-core and ex-core. This was then followed by two months of high power testing (2MW) during which similar measurements were taken. The experimental and analytical work performed during this phase of the LEU demonstration testing has been summarized in the 1982 Summary Report [Ker83].

Testing of the LEU fuel at the FNR continued during 1983 and 1984. This included comparison of LEU core configurations with mixed HEU-LEU configurations. Unfolding of the neutron flux spectra using multiple foil activation analysis was a major undertaking during this phase of the project. Considerable effort was also expended during this period on the comparison of subcadmium flux ratios measured with rhodium self-powered neutron detectors (SPNDs) and with wire activations. Simulation and analysis of these flux data were performed to explain the spatial-spectral dependence of the SPND sensitivity factor. Measurements and analysis of reactivity parameters for LEU core configurations were also undertaken. The 1983/1984 Summary Report [Ker84], which covers the period January 1, 1983 through June 30, 1984, presents a detailed description of the analytical and

experimental effort conducted during this phase of the LEU project.

During the last phase of the project, through the end of 1985, the principal focus was to resolve the various outstanding technical items and prepare this Final Report. The major issues during this period were the resolution of discrepancies between measured and predicted in-core and ex-core thermal fluxes, the measurement of subcadmium flux levels and the determination of detector sensitivities, the verification of 3-D analysis capability with the UM3DB code (formerly identified as UMDIF), and the determination of eigenvalue bias factors to help explain differences between measured and predicted core multiplication factors and control rod worths. Other items included a detailed analysis of the IAEA LEU/HEU benchmark problem, the analysis of partially-inserted control rods with UM3DB and the updating of transverse bucklings. In addition, an error in the LEOPARD library was corrected and a final ENDF/B-IV LEOPARD library, including an ENDF/B-IV fission product correlation, was released.

This report describes the overall effort in some detail. Since it is the Final Report of the project, it is a comprehensive review and discussion of effort on the project since its inception in January, 1979. Thus, the report of work during the last phase of the project has been integrated

with the overall report and not specifically identified. To the extent possible, this Final Report is a comprehensive review and summary of the entire FNR demonstration project and readers should not need to refer to previous summary reports, which can be obtained from the authors if necessary.

The Final Report is organized as follows:

- Section I -- this introduction
- Section II -- neutronic methods development and verification
- Section III -- demonstration experiments
- Section IV -- design and optimization of the LEU fuel for the FNR and the Safety Analysis Report
- Section V -- simulation and analysis of the FNR core (HEU and LEU)
- Section VI -- summary and conclusions
- Appendix A -- new ENDF/B-IV LEOPARD library
- Appendix B -- selected data base for the FNR

II. NEUTRONIC METHODS DEVELOPMENT AND VERIFICATION

A. Introduction

The development of an analysis capability for the FNR is an essential aspect of the overall LEU fuel demonstration project. The design and analysis of the LEU fuel and the simulation and analyses of the HEU and LEU cores necessitates the capability to perform detailed calculations of the HEU and LEU cores. In addition to static diffusion theory calculations, these analyses have to include the effects of fuel element depletion as well as placement in the reactor, since the fuel cycle of the FNR, as for all research reactors, is complicated by frequent shutdowns, power level changes, and fuel shuffles and reloads. Calculations are needed to compare with experimental measurements of in-core spectra and flux levels as well as overall criticality. In addition, there is a need to predict the flux distributions and spectra in the H_2O and D_2O reflectors as well as in the core in order to compare with experimental measurements at the beam tubes. Both HEU and LEU cores need to be evaluated because one of the objectives of the project was to assess the impact of the LEU fuel on the FNR performance and operation, including the effect on the experimental facilities which use the FNR as a source of neutrons. Since the FNR is a very complicated neutronic configuration with its relatively compact geometry (hence high leakage and steep

flux gradients), strong control rods, and complicated ex-core configuration with the D_2O tank on the north face, the task of developing an analysis capability is not a simple one. Although the commercial light water reactor (LWR) industry has a highly-developed neutronic analysis capability, for the most part these methods cannot be used directly with the FNR because of the fuel plate geometry (versus fuel pins), steep flux gradients, and the relatively heterogeneous nature of the FNR core compared with an LWR core. Also, commercial LWR fuel is slightly enriched (2-3%) and one needs to be careful in applying these methods to the analysis of LEU fuel (<20%), not to mention HEU fuel (93%).

Therefore, a substantial effort was made to develop an analysis capability for the FNR core which might also be of use to other MTR-type research reactors and perhaps other research reactors as well. This analysis capability can be divided into the following major categories:

- Spectrum calculations
- Multigroup diffusion (MGD) calculations
- Transport theory calculations
- Fuel cycle calculations
- Special calculations (reflectors, control rods, etc.)
- Overall code verification - IAEA Benchmark

Each of these areas is described in some detail in the following sections.

Our approach has been to make use of well-accepted methods wherever possible, since many of the available neutronic methods can be adapted to analyze the FNR core with minor modifications. In addition, the use of standard "commercial" neutronic codes has the advantage that many reactor analysts will be familiar with them and will have more confidence in the methods. Also, we have made use of computer codes in the public domain to the extent possible to facilitate the export of our computer package to other installations, including overseas locations. Table II-1 summarizes the computer codes that we have implemented on our computer system for the analysis of the FNR, along with references and short descriptions and notes to indicate the extent to which changes were made to accommodate the specific MTR-type fuel utilized in the FNR. In some cases, the changes were so extensive that the code was renamed, such as the UM2DB code, which is an extensively modified version of the well-known 2DB code [Lit69].

The calculations that have been performed to verify the adequacy of the various computer codes for MTR-type configurations were done over the duration of the LEU project. During this time, many revisions and modifications were made to the various codes, in particular UMLEO and

Table II-1. List of Neutronics Computer Codes

Code Name	Project Use	Comments	Changes
LEOPARD (UMLEO)	•generate few group constants •depletion	•0-D Unit Cell •54 fast groups (MUFT) •172 thermal groups (SOFOCATE) •B-1 leakage correction •ENDF/B-IV library	Substantial
EPRI-HAMMER	•generate few group constants •verify LEOPARD •control rod calculations	•1-D integral transport •54 fast groups •30 thermal groups •THERMOS scheme •B-1 leakage correction •ENDF/B-IV library	None
2DB (UM2DB)	•compute flux, power, burnup distributions and k_{eff}	•2-D diffusion theory •depletion capability	Substantial
ANSIN XSDRN	•ex-core flux	•1-D discrete ordinates •transport theory	None
TWOTRAN	•control rod calculations	•2-D discrete ordinates •transport theory	None
VENTURE	•benchmark 3-D calculations •determine transverse buckling for 2DB	•3-D diffusion theory	None
PDQ-7	•benchmark 3-D calculations	•3-D diffusion theory	None
1DX	•leakage flux calculations	•1-D diffusion theory	None
3DB	•compute flux/power distribution and k_{eff} as a function of depletion	•3-D diffusion theory	None
UM3DB	•same as 3DB	•3-D diffusion theory •same capabilities as UM2DB	New Code
CINDER	•generate lumped fission product correlation	•point depletion •linear chains	Some
LINX	•construct burnup dependent cross section library for UM2DB and UMD3DB from UMLEO runs	•no physics	New Code

UM2DB. In all cases the changes were verified at the time with direct comparisons of actual FNR configurations. However, many of the original verification calculations reported in Section II have not been updated to reflect the latest versions of the codes. In general, the calculations as referenced in Sections IV and V do utilize the latest versions but many of the benchmark calculations cited in Section II reflect older versions of the codes. These calculations were taken from earlier Summary Reports and no attempt was made to update them. At some point it would be useful to reproduce the benchmark calculations with the latest versions of the computer codes but since the new versions were verified against actual FNR configurations, we are confident that the comparisons reported in Section II are still valid.

B. Spectrum Calculations

This section describes the computer codes used to generate multigroup diffusion (MGD) constants for the 2-D and 3-D diffusion theory codes which are used for the overall analysis of the FNR. The UMLEO code is a revised version of LEOPARD [Bar63,Str65] and was renamed due to the extensive modifications. It is the principal spectrum code that is used for the generation of the bulk of the MGD constants. The EPRI-HAMMER code [Bar78] is the other spectrum code, and is used to generate cross sections for the control rods and

associated fuel elements ("special" fuel elements). The following sections describe these codes briefly along with a discussion of the modifications made to the codes and a brief description of any special considerations that should be kept in mind when these codes are used to analyze the FNR fuel (or any MTR-type fuel).

1. UMLEO

The UMLEO code is a spectrum code used to generate multigroup diffusion constants for light water reactor pin cell lattices. The UMLEO code combines the spectrum codes MUFT [Boh57] and SOFOCATE [Ams57]. The MUFT code performs a fast spectrum calculation for a LWR lattice by solving the Fourier-transformed slowing down equations with 54 energy groups. SOFOCATE utilizes the Wigner-Wilkins [Wig44] model to generate the thermal spectrum using 172 energy groups. The UMLEO code combines the two spectrum calculations with a critical buckling search and an "omega-search" for the ^{238}U resonance absorption to yield a total ^{238}U resonance integral consistent with experimental data [Str65]. In addition, the thermal spectrum calculation includes the Amouyal-Benoist-Horowitz (ABH) method [Amo57] to generate disadvantage factors for the fuel and clad in order to account for thermal flux depression in these regions. Thus the basic MUFT and SOFOCATE infinite medium calculations are supplemented with the ABH method to handle thermal

heterogeneities and the "omega-search" to account for resonance heterogeneities (i.e., ^{238}U).

Modifications to UMLEO

Many modifications have been made to the UMLEO code to make it suitable for MTR-type plate lattices. The principal modifications are described briefly below, and Table II-2 includes a complete list of changes that have been made.

•Slab Geometry Option

The original LEOPARD code was developed and verified for LWR pin cell lattices [Str65]. Since these lattices utilize slightly-enriched fuel pins, substantial changes were necessary to allow the analysis of HEU and LEU plate lattices. Changes were made to include slab geometry versions of the ABH method and the Dancoff factor calculation, as well as minor changes to account for volume fractions, mean chord lengths, etc. These changes supplement the original LEOPARD model and the pin cell geometry option is still operational.

•Lattice/Non-Lattice Edits

UMLEO performs the infinite medium spectrum calculations on a homogeneous "total cell" consisting of the usual "lattice cell" of fuel, clad, and moderator and the "non-lattice cell" of extra core material, such as side plates and water hole for special fuel elements. Modifications have been made to edit macroscopic cross

Table II-2. Modifications to LEOPARD (UMLEO)

Modification	Purpose	Method
slab geometry option	•analysis of plate-type fuels	•ABH method for thermal disadvantage factors for slabs •volume fractions, mean chord length, Dancoff factor redefined for slabs •minor input changes
lattice/non-lattice edits	•allow separate few-group constants for lattice and non-lattice	•neutron conservation, with separate disadvantage factors for lattice region
xenon cross section edits	•allows space-dependent xenon calculation in UM2DB	•transmit σ_a^{Xe} and Σ_a^{Xe} to UM2DB (via LINX)
output few-group constant tablesets as functions of depletion	•automate data transfer to UM2DB •allow interpolation in UM2DB based on depletion	•create output file compatible with modified UM2DB (via LINX)
ENDF/B-IV Library	•replace original cross section data base with latest evaluated cross sections	•modify LEOPARD cross section processing code (SPOTS) to generate new LEOPARD library
restart capability	•allow parametric calculations at any depletion step	•save all parameters needed to re-initialize code
added thermal expansion coefficent for Al	•allow thermal expansion of fuel and clad	•minor addition to input routine
correlations for lumped fission product cross sections	•burnup >> commercial reactor, correlations in code must be modified	•develop new correlations based on EPRI-CINDER runs
option for burnup dependent NLPF input	•incorporate spectral effects of flux peaking variations due to burnup	•minor input changes

sections for the lattice and non-lattice regions as well as the usual total cell cross sections. This allows a diffusion theory calculation of a "heterogeneous" core consisting of separate lattice and non-lattice cells, as well as the conventional homogeneous core calculation which would utilize the total cell cross sections.

•ENDF/B-IV UMLEO Library

A new library for the UMLEO code containing ENDF/B-IV data has been developed as reported in [Rat81]. The new library is necessary to remedy differences observed between pin cell data generated by the EPRI-HAMMER and UMLEO codes. This disagreement was attributed mainly to differences in their respective cross section data bases. The HAMMER code uses ENDF/B-IV data while the original UMLEO code used an early industrial cross section library. Inspection of microscopic cross sections generated by the two codes shows serious disagreement for several important isotopes including oxygen, aluminum, and ^{235}U. In order to correct this discrepancy a library for UMLEO was assembled from MUFT and SOFOCATE compatible libraries obtained from the Westinghouse Electric Corporation [Hen80]. Implementation of the new library required modification of the UMLEO code to accommodate the additional data contained in the ENDFB-IV library and to update some of the physical constants "hardwired" into the code. The new library and the modified version of the UMLEO

code have been verified extensively by the simulation of 55 critical experiments, comparison with established benchmark codes such as the HAMMER code, and modeling of the depletion of fissile fuel in pressurized water reactor (PWR) fuel.

On the average, the multiplication constants obtained for the 55 cold, clean lattices with the new library were closer to 1.0 than were the results with the old library. It should be noted that the artificial biases in the original UMLEO library have been removed. Since these biases were included to make the predicted eigenvalues agree with the critical experiments, the result would seem to confirm the adequacy of the new library for thermal reactor experiments. Better, but not perfect, agreement between the EPRI-HAMMER and UMLEO codes has also been achieved with the new library. The comparisons between the measured concentrations of actinides in PWR fuel and those calculated with the two UMLEO libraries indicate that their differences are slight and that both libraries model the burnup and depletion of the actinides to similar accuracy.

Table II-3 contains some important microscopic cross sections obtained by the UMLEO code with its two libraries and the HAMMER code. The disagreement between HAMMER and UMLEO results with the old library is essentially eliminated for the ENDF/B-IV library. This is expected because, as mentioned earlier, the HAMMER code also uses ENDF/B-IV as its

Table II-3. Comparison of Selected HAMMER and LEOPARD Microscopic Cross Sections for MTR-Type Fuel

			LEOPARD			
			Old Library		ENDF/B-IV	
Element	Cross Section	HAMMER	value	% diff.	value	% diff.
^{16}O	σ_{a1}	1.16×10^{-2}	34.4×10^{-2}	3124	1.14×10^{-2}	-1.72
^{27}Al	σ_{a3}	1.08×10^{-2}	2.80×10^{-2}	159	0.997×10^{-2}	-7.69
^{27}Al	σ_{a1}	6.80×10^{-3}	9.74×10^{-3}	47.24	6.36×10^{-3}	-6.18
^{27}Al	σ_{a2}	3.06×10^{-3}	3.50×10^{-3}	14.38	3.02×10^{-3}	-1.31
^{235}U	$\nu\sigma_{f1}$	3.07	3.12	1.63	3.39	10.42
^{235}U	σ_{a3}	39.3	37.0	-5.85	39.7	1.02
^{235}U	σ_{f3}	63.9	59.3	-7.20	63.6	-0.47

data base. The disagreement on the macroscopic level between HAMMER and UMLEO results has not been completely eliminated, as seen in Table II-4. In fact, for some parameters the old library yields results which are closer to those of HAMMER than with the new library. The serious discrepancies, such as the fast fission cross section for ^{235}U, have been reduced by the use of the UMLEO ENDF/B-IV library. Although the ENDF/B-IV UMLEO library does not provide perfect agreement with benchmark codes, it can be used with more confidence than the old data set. Differences between LEOPARD-

Table II-4. Comparison of HAMMER and LEOPARD Two-Group Macroscopic Constants for MTR-Type Fuel

		LEOPARD			
		Old Library		ENDF/B-IV	
Parameter	HAMMER	value	% diff.	value	% diff.
HEU FUEL					
k_∞	1.76447	1.76302	-0.08	1.76610	0.09
ϕ_1/ϕ_2	3.6736	3.8063	3.61	3.8311	4.20
Σ_{a1}	3.8131×10^{-3}	3.8860×10^{-3}	1.91	3.7620×10^{-3}	-1.34
Σ_{f1}	2.1050×10^{-3}	2.0138×10^{-3}	-4.33	2.1608×10^{-3}	-2.65
Σ_{a2}	0.10832	0.11312	4.43	0.11370	5.13
Σ_{f2}	8.1130×10^{-2}	8.4828×10^{-2}	4.56	8.5249×10^{-2}	5.08
LEU FUEL					
$k\infty$	1.65980	1.66196	0.13	1.66368	0.23
ϕ_1/ϕ_2	4.6196	4.7911	3.71	4.8317	4.59
Σ_{a1}	6.9685×10^{-3}	6.9712×10^{-3}	0.04	6.8765×10^{-3}	-1.32
Σ_{f1}	2.7718×10^{-3}	2.5600×10^{-3}	-7.64	2.7390×10^{-3}	-1.18
Σ_{a2}	0.12643	0.13252	4.82	0.13327	5.41
Σ_{f2}	0.0958	0.10063	5.04	0.10111	5.54

calculated results and predictions of benchmark codes or experimental data can be attributed primarily to the UMLEO methodology rather than its data base.

Additional details regarding the implementation of the ENDF/B-IV library into UMLEO may be found in [Ker81], [Ker83] and [Rat81]. For convenience, a summary of this effort, which was reported in [Ker83] has been reproduced in Appendix A.

•Burnup Library for UM2DB/UM3DB

The UMLEO code has been modified to write macroscopic cross sections and selected microscopic cross sections as a function of burnup. These cross sections are processed by the LINX code to construct a burnup-dependent cross section library for the 2-D and 3-D diffusion theory codes UM2DB and UM3DB, which are described in a later section. The burnup library allows an efficient and convenient fuel cycle analysis with UM2DB and UM3DB.

•Miscellaneous Changes

Other changes to UMLEO have involved primarily improvements or corrections to previous capabilities. The restart capability has been generalized to permit the generation of derivative cross-sections for feedback calculations. The thermal expansion effects on uranium number density were changed to allow for expansion of input isotopic uranium densities. Previously, UMLEO corrected

uranium densities only when present in UO_2. Efforts were also made to update a number of physical constants used in the UMLEO code. New correlations for lumped fission product cross sections were developed through the EPRI-CINDER code as discussed in Section 2.E.3. To allow for the effects of depletion-dependent flux peaking factors on the spectrum, an additional input option has been added to provide for a burnup-dependent non-lattice peaking factor (NLPF). The binary few-group cross-section burnup library passed to LINX was improved by including more complete identifying parameters.

Verification of UMLEO

This section discusses the analyses that have been performed to verify the modifications made to the UMLEO code. In some cases these calculations duplicate results presented in Appendix A for the ENDF/B-IV library verification; however, they are included below for convenience.

•TRX Critical Lattices

A comparison of measured and calculated parameters for two UO_2 critical lattices [Har70b] shown in Table II-5 illustrates the typical accuracy of the UMLEO code for lattices of 1.3% enriched fuel rods. A similar comparison is given in Table II-6 for a very severe test -- the TRX natural uranium slab criticals [Har70b]. These experiments consisted of 11 one-inch thick natural uranium slabs driven

Table II-5. TRX Rodded UO_2 Critical Lattice Results

	W/F = 2.35			W/F = 4.02		
Parameter†	Experiment††	UMLEO	% Diff	Experiment	UMLEO	% Diff
ρ^{28}	1.311	1.2763	-2.6	0.83	0.7792	- 6.1
δ^{25}	0.0981	0.0999	1.8	0.0608	0.0608	0.0
δ^{28}	0.0914	0.0893	-2.3	0.0667	0.0596	-10.6
CR*	0.792	0.7703	-2.7	0.644	0.6218	- 3.4
B^2	0.0057	0.00557	-2.3	0.005469	0.00526	- 3.8
k†††	1.0	0.9965	0.35	1.0	0.9944	0.56

Notes: † $\rho^{28} = \frac{\text{U-238 epithermal capture}}{\text{U-238 thermal capture}}$

$\delta^{25} = \frac{\text{U-235 epithermal fission}}{\text{U-235 thermal fission}}$

$\delta^{28} = \frac{\text{U-238 fissions}}{\text{U-235 fissions}}$

$CR^* = \frac{\text{U-238 captures}}{\text{U-235 fissions}}$

B^2 = critical buckling

†† WAPD-TM-931 (1970)

††† Measured value assumed to be 1.0; calculated value is based on UMLEO run with measured critical buckling input

Table II-6. TRX Natual Uranium Slab Criticals

W/F = .5				W/F = 1.09		
Parameter†	Experiment††	UMLEO	% Diff	Experiment	UMLEO	% Diff
ρ 28	2.63	2.591	-1.5	1.21	1.106	-8.6
δ 25	0.267	0.326	22.0	0.124	0.147	18.6
δ 28	0.264	0.268	1.5	0.190	0.176	-7.4
CR*	2.056	1.910	-7.1	1.387	1.283	-7.5
B^2	-0.0037	-0.0029	22.0	-0.0013	-0.00091	30.0
k†††	1.0	1.028	2.8	1.0	1.011	1.1

Notes: † ρ 28 = $\frac{\text{U-238 epithermal capture}}{\text{U-238 thermal capture}}$

δ 25 = $\frac{\text{U-235 epithermal fission}}{\text{U-235 thermal fission}}$

δ 28 = $\frac{\text{U-238 fissions}}{\text{U-235 fissions}}$

CR* = $\frac{\text{U-238 captures}}{\text{U-238 fissions}}$

B^2 = critical buckling

†† WAPD-TM-931 (1970)

††† Measured value assumed to be 1.0; calculated value is based on UMLEO run with measured critical buckling input.

to criticality by the leakage from a highly enriched driver lattice. We believe the calculated results compare reasonably well with the experiments, especially considering that the very large fuel plate thickness invalidates some assumptions of the UMLEO code.

•Comparison with HAMMER

A more reasonable test of the modified UMLEO code is given in Table II-7 where UMLEO is compared with the more accurate HAMMER code for typical LEU and HEU MTR-type fuels. This comparison demonstrates that the modified version of UMLEO yields results which are in good agreement with the more accurate and expensive integral transport calculation contained in HAMMER. For both the HEU and LEU plate-type fuel shown in Table II-7 and for numerous other cases we have examined, UMLEO accurately predicts integral parameters (k_∞, material buckling, etc.) and shows reasonable agreement for few-group constants.

Based on these comparisons, the UMLEO code and its data base appear adequate for our analysis. Due to the short computing time and low cost of the UMLEO code, coupled with its reasonable accuracy and depletion capability, it has been used to generate few-group constants for all routine core physics analyses for the FNR.

Table II-7. Comparison of UMLEO and HAMMER Results for MTR-Type Fuel

Parameter	93% Alloy		19.5% UAl_x	
	UMLEO	HAMMER	UMLEO	HAMMER
k_∞	1.5477	1.5500	1.5150	1.5116
ϕ_1/ϕ_2	2.41	2.40	2.76	2.75
Age	51.5	49.9	49.1	47.5
D_1	1.434	1.372	1.424	1.360
Σ_{a1}	0.00204	0.00182	0.00358	0.00344
Σ_{r1}	0.0258	0.0257	0.0254	0.0253
$\nu\Sigma_{f1}$	0.00206	0.00223	0.00256	0.00274
D_2	0.284	0.272	0.280	0.269
Σ_{a2}	0.0597	0.0594	0.0676	0.0668
$\nu\Sigma_{f2}$	0.0948	0.0935	0.110	0.108

Special Considerations for the FNR

•Lattice and Non-lattice Regions

Particular care must be used in treating the non-lattice portion of a fuel assembly using the UMLEO code. For both regular and special fuel assemblies for the FNR core, shown in Figures II-1 and II-2, the lattice region consists of the active portions of fuel plates and associated clad and moderator. The non-lattice region includes the inactive portions of fuel plates and associated water, the side plates, inter-assembly water gap (sides only), and (for special assemblies) the central waterhole and control rod guides. While UMLEO will treat the fuel, clad, and moderator of the lattice explicitly, the non-lattice region must be homogenized by volume weighting.

For the UMLEO code to include the effects of the non-lattice region on the total cell spectrum, the user must input a non-lattice fraction (NLF) and a non-lattice peaking factor (NLPF). The NLF is computed readily as:

$$NLF = (\text{non-lattice area})/(\text{total assembly area})$$

where the total assembly area is determined by the grid plate pitch. The NLPF is defined (in UMLEO) as the ratio of the average thermal flux in the non-lattice region to the average thermal flux in the moderator region. Accurate values of the

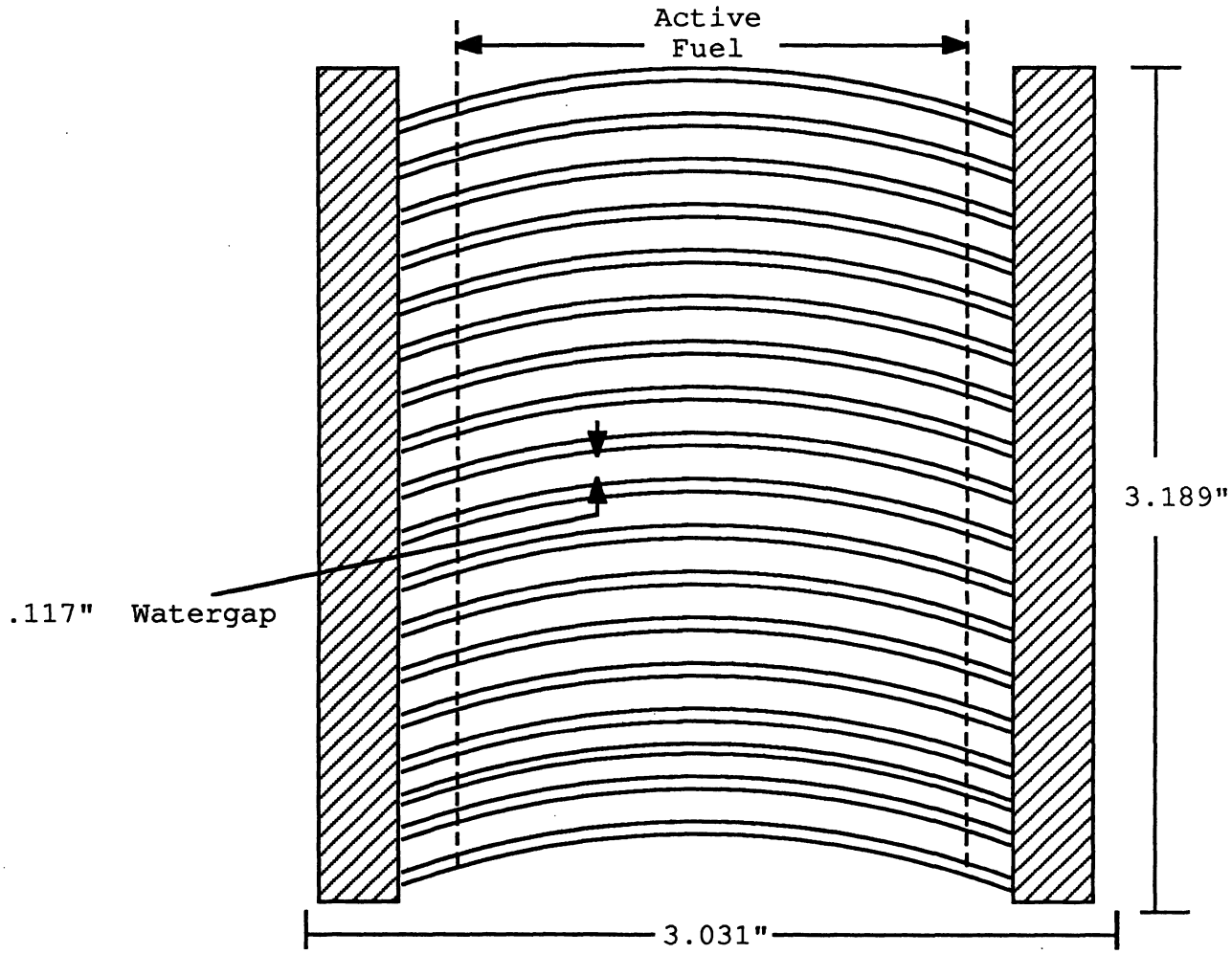

Figure II-1. FNR Regular Fuel Element

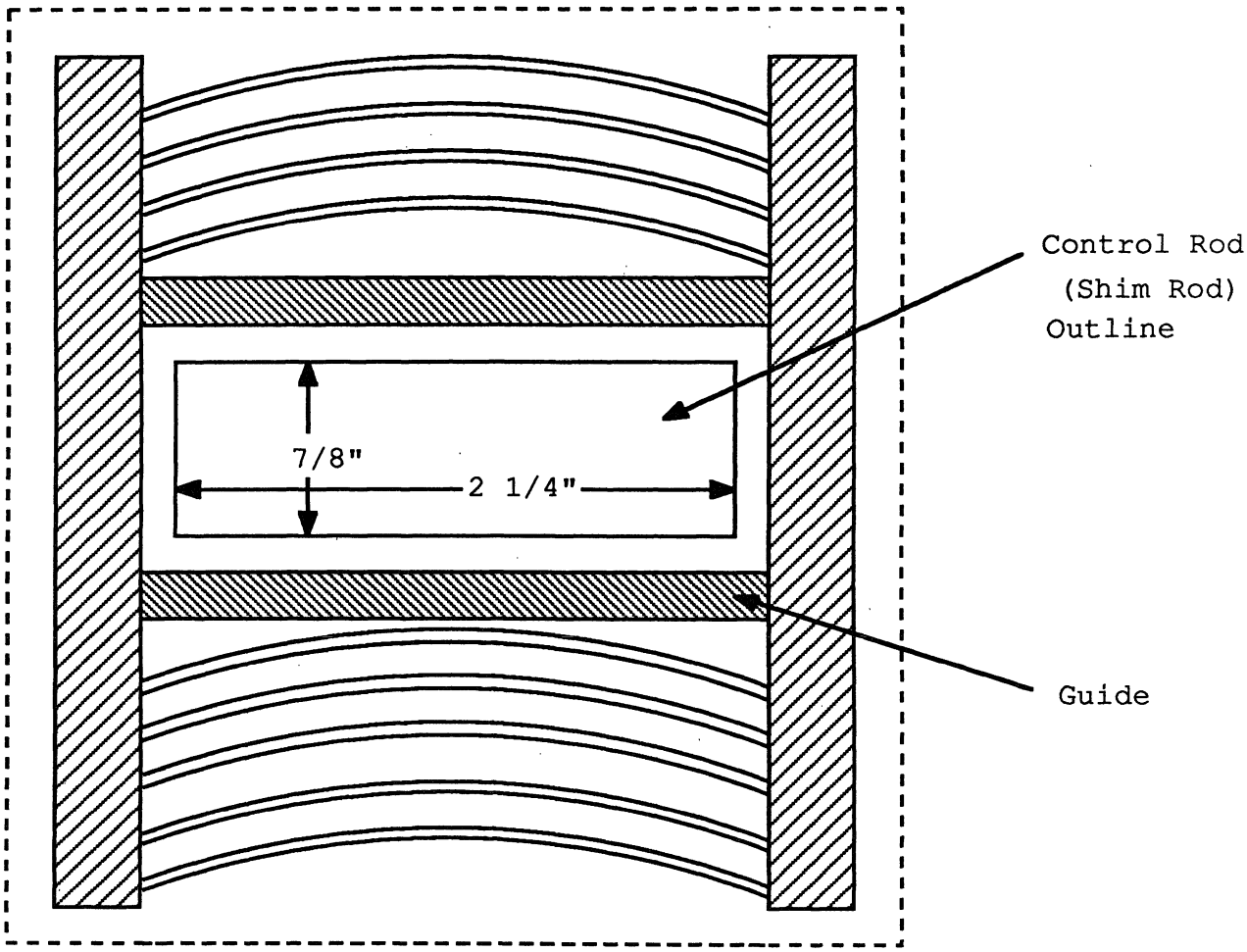

Figure II-2. FNR Special Fuel Element

NPLF must be obtained from more sophisticated calculations and Table II-8 includes some results from these calculations. For regular assemblies, which have a small NLF, 1-D total cell calculations with the HAMMER code and 2-D fine-mesh UM2DB calculations (with explicit representations of fuel plates and water channels) both yield a NLPF of essentially 1.0. However, for special assemblies, the NLF is equal to

Table II-8. NLPF Calculations for HEU FNR Fuel

Geometry	Code	Mesh Points	NLPF
Regular Assembly:			
1-D Unit Cell	HAMMER	18	1.008
2-D 1/4 Assembly	UM2DB	63 x 38	1.005
Special Assembly:			
1-D 4/9 Assembly	HAMMER	20	1.30
1-D 1/2 Assembly	UM2DB	63	1.292
2-D 1/4 Assembly	UM2DB	63 x 38	1.154
Penn State Assembly:			
2-D 1/4 Assembly	UM2DB	63 x 38	0.993

0.588 and the geometry requires a 2-D approach. One-dimensional calculations for a half-assembly with the HAMMER code, with explicit representation of four or five fuel plates and non-lattice region, yields a NLPF significantly greater than that predicted by a fine-mesh 2-D UM2DB calculation for the equivalent configuration.

Our conclusion is that 2-D fine-mesh assembly level calculations are necessary to determine the appropriate NLPF for input to UMLEO.

•Uranium Isotope Concentrations

HEU fuel can contain measurable amounts of ^{234}U and ^{236}U due to both the enrichment process and the use of some reprocessed fuel. Table II-9 shows uranium isotope concentrations for typical batches of FNR fuel. Although

Table II-9. Uranium Isotopic Concentrations for Typical FNR Fuel Elements

Isotope	Natural Uranium	FNR Fuels		
		93% Alloy	93% UAl_x	93% Penn State
U-234	0.0055%	1.00%	0.61%	1.00%
U-235	0.720 %	93.17%	93.19%	93.26%
U-236	---	0.50%	0.42%	0.50%
U-238	99.28 %	5.33%	5.78%	5.24%

^{234}U and ^{236}U yield more absorption than ^{238}U in HEU fuel, none of these is a significant absorber, as seen in Table II-10. For generality, we have included all uranium isotopes in the UMLEO input.

Table II-10. 93% FNR Alloy Fuel Neutron Loss Rates

Absorption	LEOPARD Unit Cell Calculation (%)	
	Beginning of Life	End of Life
H	10.3	12.9
O	0.55	0.59
Al	5.1	6.3
U-234	0.13	0.15
U-235	48.6	48.5
U-236	0.013	0.10
U-238	0.12	0.14
Xe	---	1.7
Sm	---	0.47
Pu-239	---	0.05
Fission Prod.	---	2.2
Leakage	35.01	26.9
TOTAL	100.0	100.0

•D_2O and H_2O Reflector

In order to obtain few-group constants for D_2O and H_2O reflectors, microscopic cross sections must be averaged over the core leakage spectrum, which is considerably softer than the in-core spectrum. This can be accomplished in an approximate manner using the UMLEO code with the reflector represented as a large non-lattice region. We have arbitrarily set the NLF at 0.5 and the NLPF at 1.0. However, we have found that the use of LEOPARD-generated cross sections for the reflectors in the FNR can have a significant (deleterious) effect on the predicted power distribution within the core. Therefore, we have chosen

to utilize the XSDRN code to generate reflector cross sections as discussed below. If XSDRN or similar code is not available, the approximate method described above using UMLEO may suffice.

As discussed elsewhere, D_2O cross sections are very sensitive to the amount of H_2O impurity present. We have used 0.25% H_2O impurity for all D_2O calculations, based upon information from the FNR supplier of D_2O.

2. HAMMER

The HAMMER code is a one-dimensional integral transport spectrum code used for accurate calculations, benchmarking and verification of cross section libraries [Jab73,Rot75], and difficult problems with strong spectral/spatial coupling. Our version of HAMMER is the recent EPRI version EPRI-HAMMER [Bar78], which utilizes a cross section data set based on the ENDF/B-IV cross section library.

Modifications to the HAMMER Code

Only minor modifications were needed to adapt the CDC version of the EPRI-HAMMER code to the University of Michigan computing system, which until 1986 utilized Amdahl computers, which are IBM-compatible. An additional edit was added to print and save 2-group and 4-group cross sections for separate material regions.

Verification of HAMMER

Three different methods were used to verify the HAMMER code. First, the code was compared with an older version of HAMMER [Sui67] which utilized ENDF/B-II data for typical HEU and LEU fuel. No significant discrepancies were found. Second, several TRX criticals were analyzed and compared with measured values. Table II-11 presents a comparison for one of the TRX slab criticals [Har70b]. The agreement is good, considering the difficulty of the problem, and is much better than similar results from the UMLEO code which have been shown in Table II-6. Third, HAMMER results for HEU, medium enrichment uranium (MEU), and LEU plate-type fuel were compared with results obtained from ANL [Woo79] using the VIM [Pra76] and EPRI-CELL [Cob75] codes. Table II-12 presents a representative comparison of these three codes. Based on these comparisons, we have concluded that the EPRI-HAMMER code is accurate and reliable for MTR-type fuel configurations.

Special Considerations for the FNR

For application of 0-D and 1-D codes to generate cross sections for fuel assemblies, a common approach is the total cell concept: an assembly is represented by a unit cell consisting of four regions -- fuel, clad, moderator and extra -- with non-lattice materials homogenized in the extra region. For integral transport codes (HAMMER, THERMOS,

Table II-11. EPRI-HAMMER Results for TRX Slab Critical

W/F=1.09			
Parameter†	Experiment††	HAMMER	% Diff.
ρ^{28}	1.21	1.91	-1.6
δ^{25}	0.124	0.133	7.5
δ^{28}	0.190	0.186	-2.1
CR*	1.387	1.342	-3.2
B^2	-0.0013	-0.00136	4.6
k†††	1.0	0.9982	-0.18

† ρ^{28} = $\frac{\text{U-238 epithermal capture}}{\text{U-238 thermal capture}}$

δ^{25} = $\frac{\text{U-235 epithermal capture}}{\text{U-235 thermal capture}}$

δ^{28} = $\frac{\text{U-238 fissions}}{\text{U-235 fissions}}$

CR* = $\frac{\text{U-238 captures}}{\text{U-235 fissions}}$

B^2 = critical buckling

†† WAPD-TM-931 (1970)

††† Measured value assumed to be 1.0; calculated value is based on EPRI-HAMMER run with measured critical buckling input

Table II-12. Selected Results from Comparison of VIM, EPRI-CELL and EPRI-HAMMER

Parameter	VIM	EPRI-CELL	% Diff*	HAMMER	% Diff*
HEU FUEL					
k_∞	1.7652 ± 0.0035	1.7650	-0.01	1.76447	-0.04
σ^{25}_{f4}	355.14 ± 0.73	359.34	1.2	361.39	1.7
σ^{28}_{a3}	27.12 ± 0.078	27.683	2.1	25.951	-4.3
MEU FUEL					
k_∞	1.7149 ± 0.0032	1.7208	0.34	1.7171	0.18
σ^{25}_{f4}	347.19 ± 0.81	350.78	1.0	352.94	1.7
σ^{28}_{a3}	12.86 ± 0.29	12.01	-6.6	12.387	-3.7
LEU FUEL					
k_∞	1.6603 ± 0.0031	1.6656	0.32	1.6598	-0.03
σ^{25}_{f4}	339.84 ± 0.88	342.82	0.9	344.60	1.4
σ^{28}_{a3}	6.87 ± 0.12	6.51	-5.2	6.808	-0.90

Note: * % Difference from VIM

EPRI-CELL, etc.), the total cell concept works well only if the extra region comprises a small fraction of the total assembly. This is not true of FNR special assemblies, and an assembly-level representation is required instead of the simple total cell approach.

The reasoning behind this recommendation can be seen in Figure II-3. A total cell representing a special assembly would result in a very "loose" lattice with little streaming between fuel plates. In the actual lattice, there is tight coupling between the fuel plates and virtually no (thermal) streaming across the large water hole. To represent this in HAMMER, the clad, fuel and moderator are represented explicitly for four unit cells next to 4/9 of the water hole. This is essentially a "slice" through 4/9 of a special assembly, with an additional side plate region.

C. Diffusion Theory Calculations

1. UM2DB

The 2DB code [Lit69] is a production level multigroup diffusion code for 2-D geometry. It was developed for fast reactor applications and has the capability to deplete individual isotopes with spatial dependence. The code accepts as input microscopic cross sections for an arbitrary number of isotopes which are then "mixed" to form macroscopic cross sections for materials which are assigned to specific geometric regions, or zones. Thus, a zone defines a

FNR Special Assembly

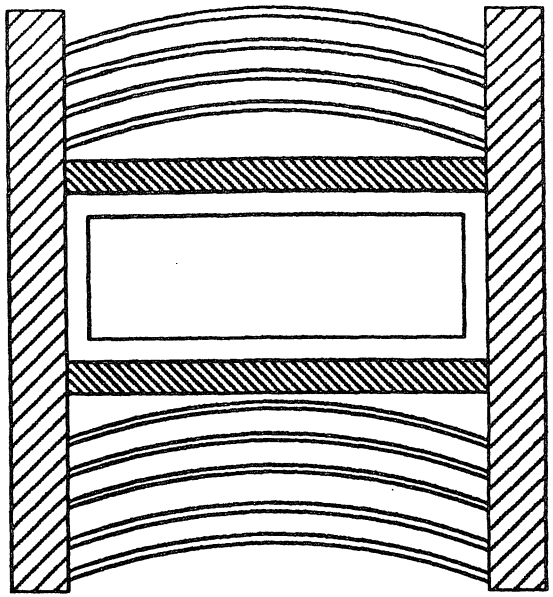

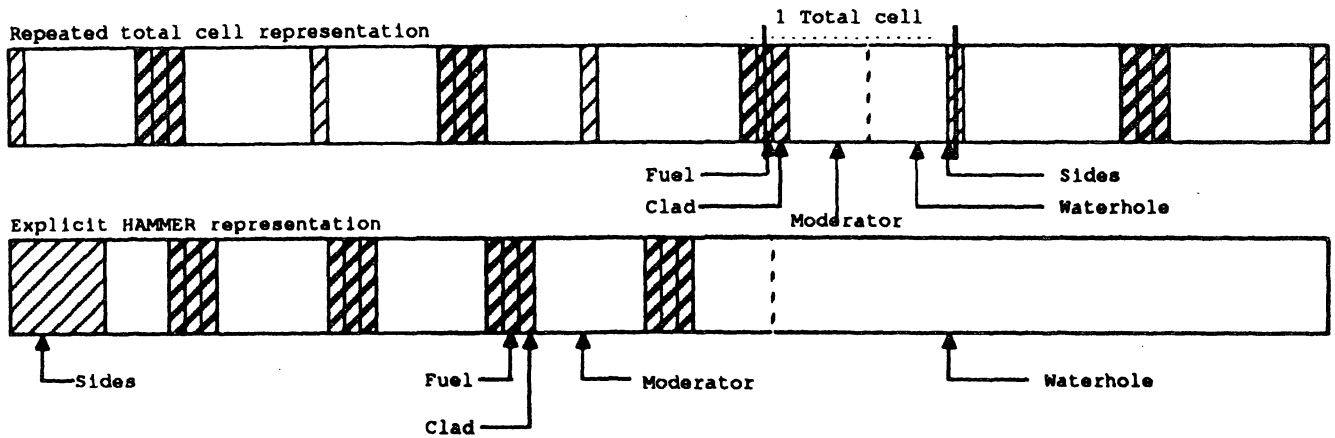

Figure II-3. Total cell vs. Explicit Representation of FNR Special Assembly.

"depletion region" and the isotopes within a particular zone are depleted in accordance with the specified power level and flux calculated for that zone. Macroscopic cross sections are then calculated by summing the products of the computed isotopic number densities and corresponding microscopic cross sections. For example, given nuclides i = 1,2, ..., L_I in a particular zone I, the macroscopic absorption cross section for zone I, group g is calculated:

$$\Sigma_{ag}^{I} = \sum_{i=1}^{L_I} \sigma_{ag}^{i} N_I^{i}$$

where $N_I{}^i$ = number density of nuclide i in zone I,

$\sigma_{ag}{}^i$ = microscopic absorption cross section for nuclide i, group g, and

L_I = number of nuclides in zone I.

The original 2DB code does not allow for changes in the microscopic cross sections as a function of depletion.

In addition to a depletion capability, 2DB has a wide variety of input options typical of a production level MGD code, including various criticality search options in addition to the usual k_{eff} calculation. Transverse bucklings may be input as a function of energy group and geometric zone and either x-y, r-z or r-θ geometry is allowed.

Modifications to 2DB

Although the 2DB code is an excellent tool for 2-D diffusion calculations, we found it necessary to make numerous modifications to the code to account for the special requirements for the FNR analyses. The paragraphs below describe in some detail the principal changes made to the 2DB code. Since these modifications have been quite extensive, the modified version of 2DB has been renamed UM2DB. (It should be noted that previous reports have referred to the UM2DB code as 2DBUM.)

•Macroscopic Depletion Capability

As noted above, the 2DB code does not allow for changes in the microscopic cross sections as a function of depletion. This is a reasonable model for fast reactor analyses, where many energy groups may be utilized and microscopic cross sections for a particular group tend to be reasonably constant; however, this is inappropriate for thermal reactor analyses, where the thermal spectrum changes significantly with depletion. For example, Figure II-4, taken from results of a UMLEO depletion calculation, is a plot of the spectrum averaged microscopic thermal fission cross section in ^{235}U as a function of fuel burnup. As can be seen, the microscopic cross section can change by as much as 1.5% over the fuel lifetime which translates into a significant change in the multiplication factor and power distribution.

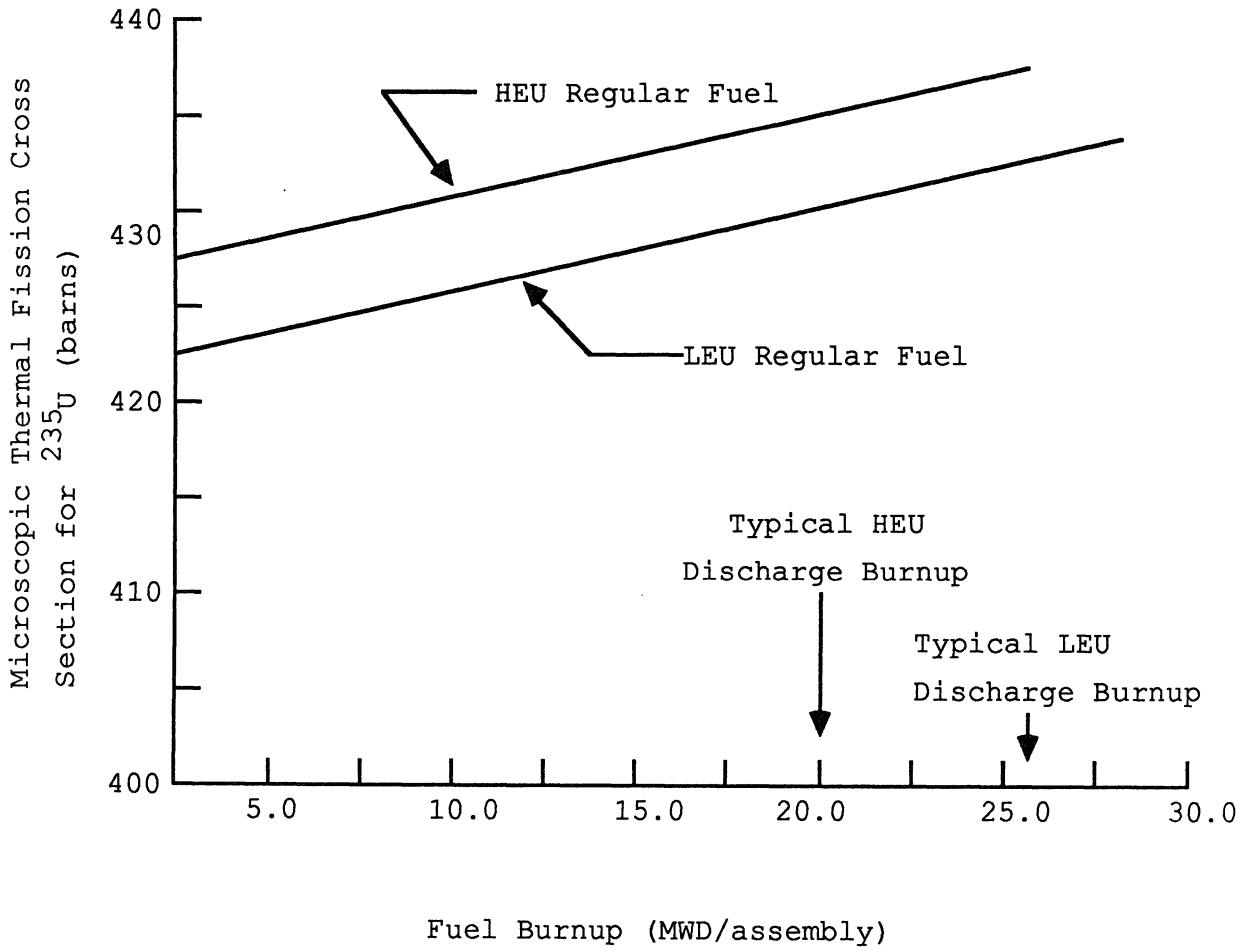

Figure II-4. Cross Sections generated by the UMLEO Code

The magnitude of this change cannot be ignored, and one of the first modifications to 2DB was to incorporate burnup dependence of the cross sections. The typical approach utilized in commercial codes is the PDQ-Harmony [Cal67,Bre65] method wherein microscopic cross sections are input as tablesets, with different cross sections for different values of user-specified independent variables, such as fuel burnup, fuel temperature or moderator temperature. Multi-axis interpolation schemes are then used to generate a microscopic cross section for a given isotope in specific zone -- once the burnup, fuel temperature, etc. of the zone are known from the previous time step. Thus, the microscopic cross section is interpolated from the tableset for every isotope in each zone and the zonal macroscopic cross section is accumulated using the isotopic number densities for that zone determined from the depletion portion of the diffusion-depletion calculation.

Unfortunately, this approach is somewhat unwieldy for a research reactor such as the FNR where the fuel configuration changes on a weekly and sometimes daily basis. The computational costs associated with accounting for isotopic depletion effects in several hundred fuel elements in a continuous shuffle between the core and the pool storage area was thought to be restrictive, even without the burden of depletion-dependent microscopic cross sections. Therefore,

an alternative scheme was developed based on parameterizing macroscopic cross sections. This method is based on generating a library of macroscopic cross sections as a function of depletion, or any other parameter (e.g., fuel temperature or moderator temperature), and then interpolating the appropriate macroscopic cross section for a specific zone using the burnup of that zone. The zone burnup is calculated from the results of the diffusion calculation, which yields the neutron flux as a function of spatial position.

Specifically, the following quantities are defined:

BU = burnup (MWD/T)

Σ_{ag}^{F} = macroscopic cross section of type a for group g, fuel type F

a = absorption, fission, etc.

In general, Σ_{ag}^{F} is a function of burnup, namely: $\Sigma_{ag}^{F} = \Sigma_{ag}^{F}(BU)$ due to depletion of isotopes i =1,2,...N_I in fuel region F as well as the burnup dependence of the microscopic cross sections, σ_{ag}^{i}, for these isotopes due to the spectrum changes. The former is of course the major effect but, as noted above, the latter cannot be ignored.

Since the UMLEO code has a depletion capability, one can obtain macroscopic cross sections as a function of depletion directly from the UMLEO output. Assuming the depletion steps in the UMLEO calculation correspond to the burnups BU_0, BU_1, ... BU_T (in MWD/T), then a hypothetical Σ_{ag}^{F} might appear

as in Figure II-5. The "tableset" of macroscopic cross sections, $\Sigma_{ag}^{F} = \Sigma_{ag}^{F}(BU)$ can then be interpolated within to find an arbitrary $\Sigma_{ag}^{F}(BU)$ for a zone that is comprised of fuel type F that has a known burnup (BU). This interpolation is depicted schematically in Figure II-5.

A few observations are in order:

(1) Since the depletion of a given zone determines the macroscopic cross section for that zone, this scheme allows for spatially-dependent depletion effects. Thus, even in the case where the same fuel is assigned to every zone I in the core, the diffusion calculation will yield a spatially-varying flux, hence a spatially varying burnup which will result in different macroscopic cross sections for each zone in general.

(2) The key assumption in this model is that the macroscopic cross sections, Σ_{ag}^{F}, are a function only of the burnup, and not of the path followed to reach that burnup. Hence, fuel depleted at 100% power for 1 day would obtain the same cross section as fuel depleted at 1% power for 100 days. Since isotopic production and loss rates can be sensitive functions of power level (e.g., xenon) and fuel temperature and the thermal spectrum is affected directly by moderator temperature, this model may seem at first glance to be inadequate. However, this is an extreme example and the temperature variations in the FNR are quite mild (fuel and

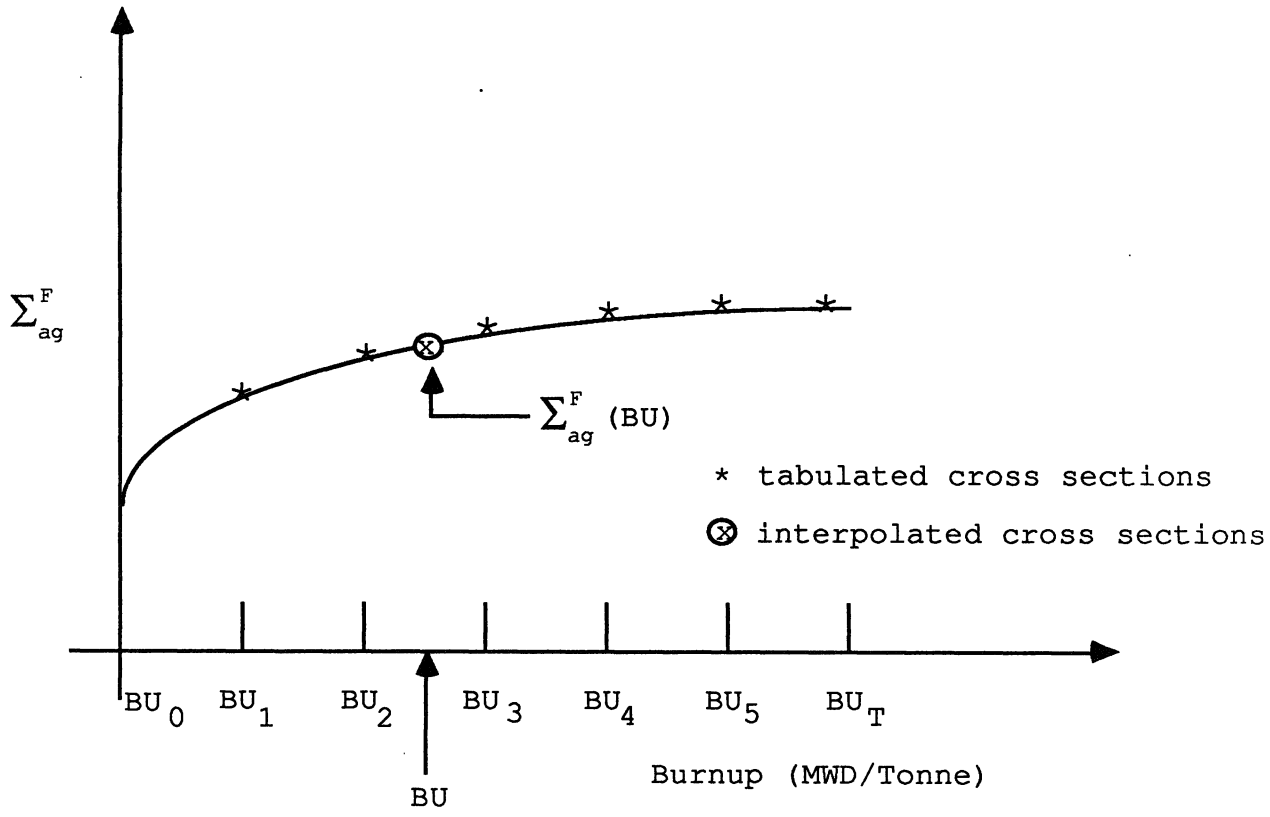

Figure II-5. Macroscopic Cross Section Interpolation

moderator temperatures in the range of 100°F-130°F) and xenon has been accounted for separately, as discussed below. Therefore, this model appears to be adequate, at least for low power research reactors such as the FNR.

The specific approach is to construct a burnup library of cross sections for each type of fuel element expected in the calculation. For example, regular and special elements for both LEU and HEU fuel, would yield a total of four library materials (F = 1,2,3,4) in order to perform a FNR mixed core simulation. The user assigns the library materials to UM2DB materials, which are in turn assigned to geometric zones. This intermediate assignment is necessary to allow shuffling of fuel elements in and out of the core and still allowing each element to be associated with its own burnup. The diffusion calculation is performed for the initial core configuration (which can be a depleted core because an initial burnup distribution can be input) and the material averaged powers, P_I(MW), are calculated using the input power level and calculated flux distribution. Knowing the time step, Δt, the burnup of material I is found:

$$BU_I(t+\Delta t) = \kappa P_I + BU(t)$$

where BU is the burnup of the material I at the beginning of the time step and κ is a conversion factor that depends on the initial uranium loading in the specific zone.

Given BU_I for a given material, or zone, the corresponding macroscopic cross section is interpolated from the appropriate library material tableset via quadratic Lagrangian interpolation. The scheme is to choose the two burnup points BU_a and BU_b that bracket BU_I and then a third point BU_c that is the closest among the remaining burnup points. The Lagrangian interpolation formula [Abr65] then yields the following for the interpolated cross section:

$$\Sigma_{ag}^{I} = \Sigma_{ag}^{a} \frac{(BU_I - BU_b)(BU_I - BU_c)}{(BU_a - BU_b)(BU_a - BU_c)} + \Sigma_{ag}^{b} \frac{(BU_I - BU_c)(BU_I - BU_a)}{(BU_b - BU_c)(BU_b - BU_a)}$$

$$+ \Sigma_{ag}^{c} \frac{(BU_I - BU_a)(BU_I - BU_b)}{(BU_c - BU_a)(BU_c - BU_b)}$$

where $\Sigma_{ag}{}^{a}$, $\Sigma_{ag}{}^{b}$ and $\Sigma_{ag}{}^{c}$ are the UMLEO generated macroscopic cross sections at burnups BU_a, BU_b and BU_c, respectively.

In practice, we have experienced one problem with the quadratic interpolation. The rapid variations in the macroscopic cross sections in the first 50 hours or so after startup can lead to erroneous interpolated cross sections due to the attempt to fit a quadratic through these points. We have, therefore, forced a linear interpolation for burnups in this range. Also, the option to treat xenon separately (see below) will alleviate this problem.

To verify the correct implementation of the interpolation scheme, Figure II-6 depicts the difference in k_∞ for a HEU fuel element as predicted by UMLEO and UM2DB as a function of burnup. The UM2DB calculation utilized a 2x2 homogeneous mesh with a burnup library generated by the UMLEO calculation. The UM2DB calculation utilized zero current boundary conditions on all sides and the input time steps and power level are consistent with the UMLEO calculation. The agreement between the two calculations are very close and is not a function of depletion, as is to be expected, and indicates that the macroscopic depletion methodology is correct.

•Treatment of Xenon

The build-up of xenon with depletion and its dependence on power level cannot be handled by the macroscopic depletion approach because the UMLEO generated macroscopic cross sections are based on the equilibrium xenon level, once the xenon reaches this level (usually 40-50 hours). Thus, if an element is removed from the core and then inserted at a later date, it will have its equilibrium xenon "built-in" (incorrectly) to its cross sections, which would have a significant effect on the core criticality at the beginning-of-cycle (BOC). In addition, fuel elements at different core locations with different power levels will still have the same built-in xenon number density from UMLEO.

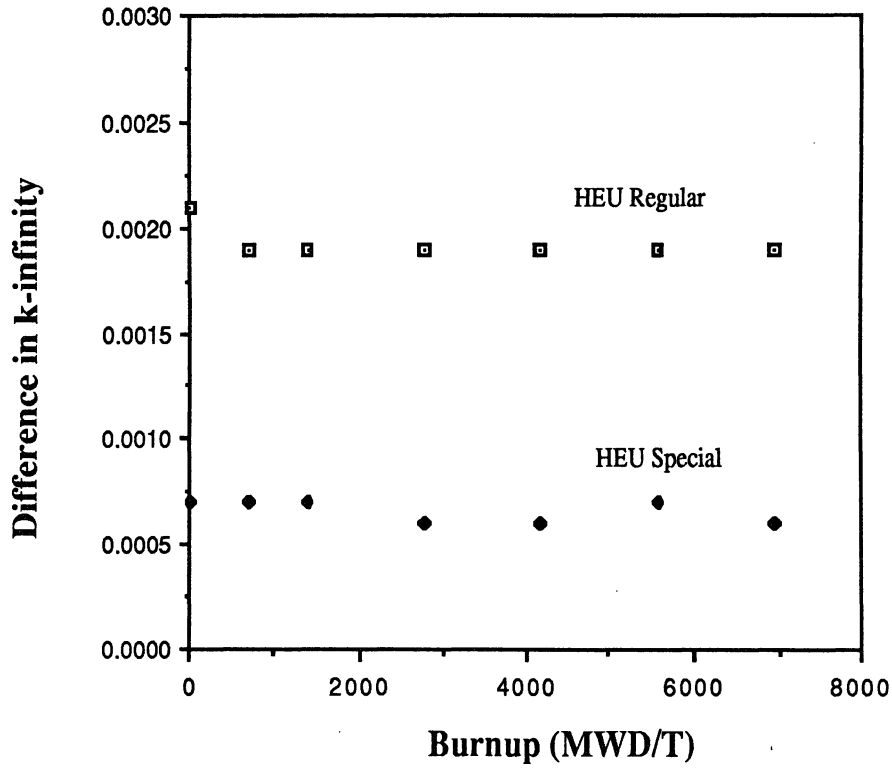

Figure II-6. Comparison of Macroscopic Depletion in UM2DB vs. UMLEO Depletion for HEU Fuel (Regular and Special)

To account for these xenon effects properly, an option has been added to treat xenon within the UM2DB calculation in three different ways:

(1) **Normal** - ignore the xenon effect and use the usual interpolated macroscopic cross section (which is based on the UMLEO-calculated equilibrium xenon level).

(2) **Equilibrium xenon** - use the flux and power level for the zone in question and compute the equilibrium xenon number density,

$$N_x^{eq} = \frac{(\gamma_I + \gamma_x)\ P^I}{\lambda_x + \sigma_{xg}^I \phi^I}$$

where γ_I and γ_x are the fission yields for ^{135}I and ^{135}Xe, respectively, λ_I and λ_x are the corresponding decay constants, P^I is the fission rate in zone I, ϕ^I is the average thermal flux in zone I, and $\sigma_{xg}{}^I$ is the interpolated microscopic absorption cross section for ^{135}Xe in zone I. The ^{135}Xe macroscopic cross section for zone I is then determined

$$\Sigma_{xg}^I = N_x^{eq} \sigma_{xg}^I$$

and added to the "xenon-free" macroscopic cross section, which is interpolated for zone I. The difference here is

that this xenon level is a function of the spatial power level determined in UM2DB rather than the average power level used in UMLEO as in option (1) above.

(3) **Time-dependent xenon** - the same as option (2) except rather than using equilibrium xenon levels, the actual xenon-iodine equations are solved explicitly as a function of time for each zone, taking into account the local power and flux levels. Given the xenon and iodine number densities at time $t=t_n$, the xenon and iodine number densities at time $t_{n+1}=t_n+\Delta t$ may be determined (for each zone I):

$$I_{n+1} = I_\infty + (I_n - I_\infty)e^{-\lambda_I \Delta t}$$

$$X_{n+1} = X_\infty + (X_n - X_\infty)e^{-\lambda_x^e \Delta t} + \frac{\lambda_I (I_n - I_\infty)(e^{-\lambda_I \Delta t} - e^{-\lambda_x^e \Delta t})}{\lambda_x^e - \lambda_I}$$

where

$$I_n = N_I(t_n)$$

$$X_n = N_X(t_n)$$

$$I_\infty = N_I^{eq} = \gamma_I P^I / \lambda_I$$

$$X_\infty = N_X^{eq}, \text{ and}$$

$$\lambda_x^e \equiv \lambda_x + \sum_g \sigma_{ag}^x \phi_g$$

As with the second option above, the local burnup of the zone is used to interpolate the microscopic xenon cross sections and "xenon-free" macroscopic cross sections for that zone.

The total macroscopic cross sections are then calculated for each zone using these quantities.

•Miscellaneous Modifications

Many additional changes to the 2DB code have been made over the duration of this project, hence necessitating the name change to UM2DB. These changes are briefly described below:

•An "overlay" input option was added to simplify the construction of a mesh with several different zone types. The idea is that subsequent zone definitions override earlier definitions, which makes it somewhat easier to generate a full core description from scratch.

•The names of all variables in the code were changed to mnemonics which resemble their purpose. For example, the old "K7" fission spectrum array is now denoted "CHI". This has greatly simplified checking and modifying the code.

•The FIDO free-format input processor (used by ANISN, DOT, MORSE, etc.) was incorporated to simplify input setup and reduce input errors.

•Memory storage space was reduced by a factor of about two for many problems through rearrangement and consolidation of many large arrays. All array storage is now in one large container array which is created dynamically by UM2DB during execution. (2START, a previously used separate code to acquire storage dynamically, is now obsolete.)

•The inner iteration coding was rewritten to follow the procedure outlined for the DIF3D code [Fer77]. Also, cross section subscripts were interchanged to avoid the need to copy cross sections to a temporary array for the inner iterations. These changes resulted in decreases in total CPU time by factors of 2-4 for typical problems. Improvements in the outer iteration acceleration scheme were not made.

•The edit capabilities were generalized and included in UM2DB as a standard edit module. With only minimal additional input, a user can obtain detailed absolute and relative reaction rate edits for one or more combinations of zones. This allows both detailed global and local results to be obtained easily from only one computer run.

•The format of the UM2DB binary cross-section burnup library created by the UMLEO/LINX package was modified to increase its generality and reduce the UM2DB user input. All information pertinent to the burnup library (such as number of burnup steps, group structure, etc.) is now included in the library and need not be entered in the UM2DB input. This reformatting facilitated such improvements as allowing different numbers of burnup steps for different materials, allowing direct access reading rather than sequential, the inclusion of both two and four group cross-sections in the same library, and reducing the core storage requirements for the UM2DB code.

•A preliminary version of an input and reference manual for UM2DB was written. Currently, this manual describes all necessary and optional input to the UM2DB code, without detailing the theory or computational methods. This manual is machine-readable and is transmitted on magnetic tape along with the UM2DB code to installations requesting the UM code package.

Table II-13 summarizes the various changes that have been incorporated into the UM2DB code during this project.

Verification of the 2DB Code

With UMLEO cross section sets in the modified 2DB code, several critical experiments were simulated and the results compared with measurements. A comparison of measured and calculated core eigenvalues and RMS deviation between measured and calculated flux or power distribution is given in Table II-14 for three representative cases: Case A is loading 33 of the Oak Ridge Bulk Shielding Reactor (BSR) [Joh57], a clean core configuration. Cases B and C are typical FNR depleted cores. The fuel burnup distribution for Case B is shown in Figure II-7 and a comparison of measured and calculated assembly power distributions is shown in Figure II-8. Further comparison of core eigenvalue and flux distributions for more recent FNR core configurations is given in Section V.

Table II-13. Modifications to 2DB

Modification	Purpose	Method
determine macroscopic cross sections by interpolation based on local fuel burnup	model fuel number density changes and spectrum effects due to local fuel depletion	-- quadratic Lagrangian intperpolation in cross section tableset from UMLEO at each depletion step -- major input options added, extra memory and scratch file
space-dependent xenon	xenon feedback	N^{Xe} determined from local power and flux levels σ_a interpolated as a function of local fuel depletion Σ_a^x added to Xe-free
dynamic memory allocation	reduced core storage requirements	system routines acquire only needed space
interface with LEOPARD	reduced input setup	A special preprocessor (LINX) converts UMLEO cross sections sets to the UM2DB input format
FIDO input processor	free-format input with many options	total revision of input routines
recoding of inner iteration routines	reduce CPU time by factor of four	use of precomputed constant arrays to eliminate redundant calculations
inproved edits and output	detailed analysis of reaction rates, neutron balance	neutron conservation equations
complete recoding and updating of entire code	improve and clarify coding , reduce storage and CPU time, consolidate all changes	mnemonic variable names, structured programming, improved code logic
$\sigma_{sg\to g}$, σ_{ag} relation	eliminate numerical inaccuracy when σ_{ag} is small	$\sigma_{sg\to g}$ computed in UM2DB form: $\sigma_{sg\to g} = \sigma_{tg} - \sigma_{ag} - \sum_{g'} \sigma_{sg\to g'}$
overlay input option	simplify mesh generation	added input option

Table II-14. Experimental and Calculated Results for Several Reactor Configurations

Case	Mesh/Group Structure	Core Reactivity		RMS Deviation[1] (thermal flux or assembly power)
		Measured	Calculated	
A (BSR #33)	6x6/2 group	1.006	1.009	11.3%[3]
	6x6/4 group	1.006	1.004	10.1%[3]
	12x12/2 group	1.006	1.012	7.8%[3]
B (FNR #67)	6x6/2 group	1.001	1.007[2]	9.3%[4]
C (FNR 1977 critical)	2x2/2 group	1.000	1.000[2]	----
	6x6/2 group	1.000	1.000[2]	----

Notes

1. RMS deviation = $\sqrt{\frac{1}{N-1}\sum_{i}\left(\frac{\text{calc-exp}}{\text{exp}}\right)_i^2}$

2. Corrected for measured xenon worth

3. Thermal flux deviation at 17 locations

4. Assembly power fraction deviation at 42 locations

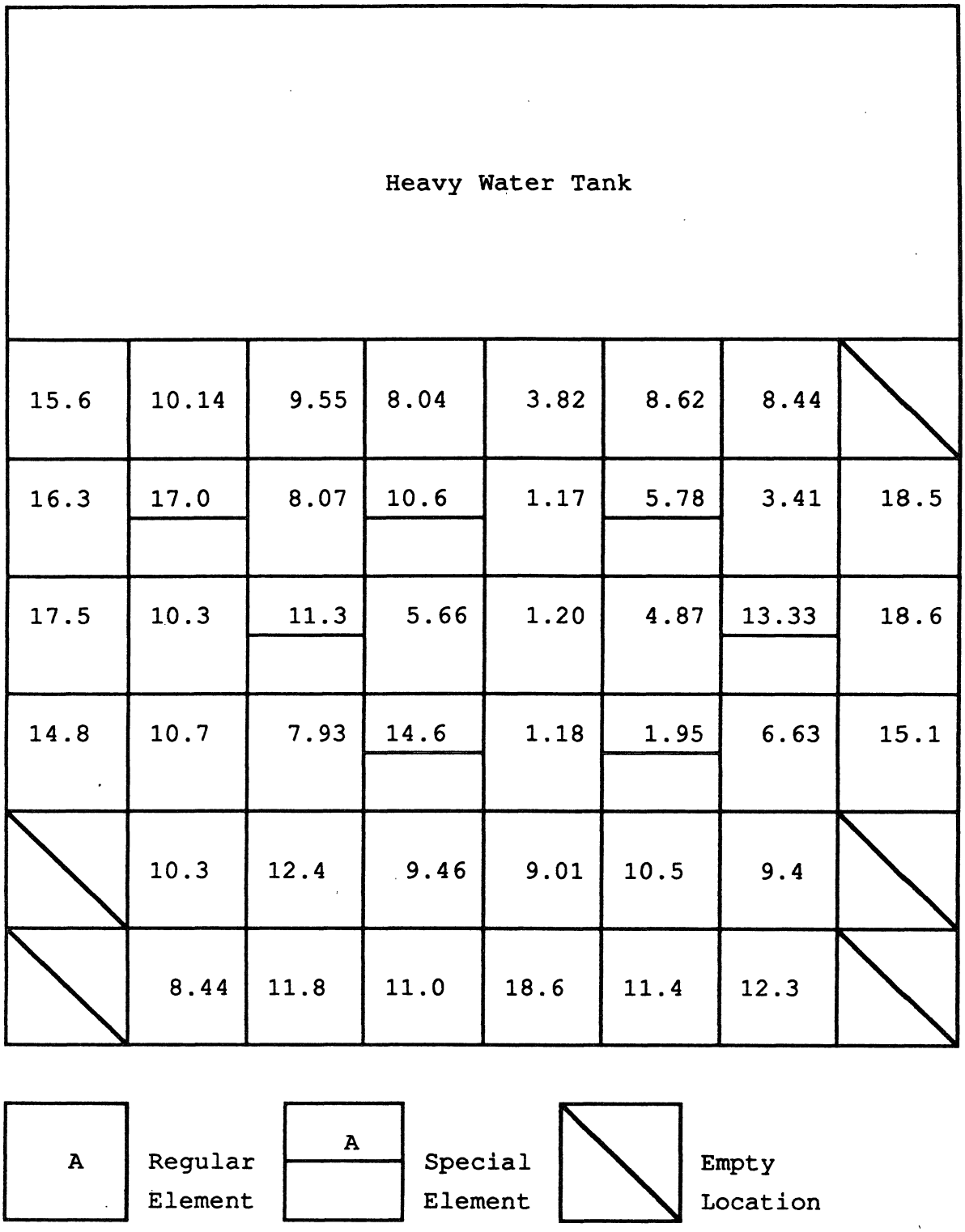

A: Assembly Burnup (MWD/assembly)

Figure II-7. Fuel Burnup Distribution for FNR Cycle 67

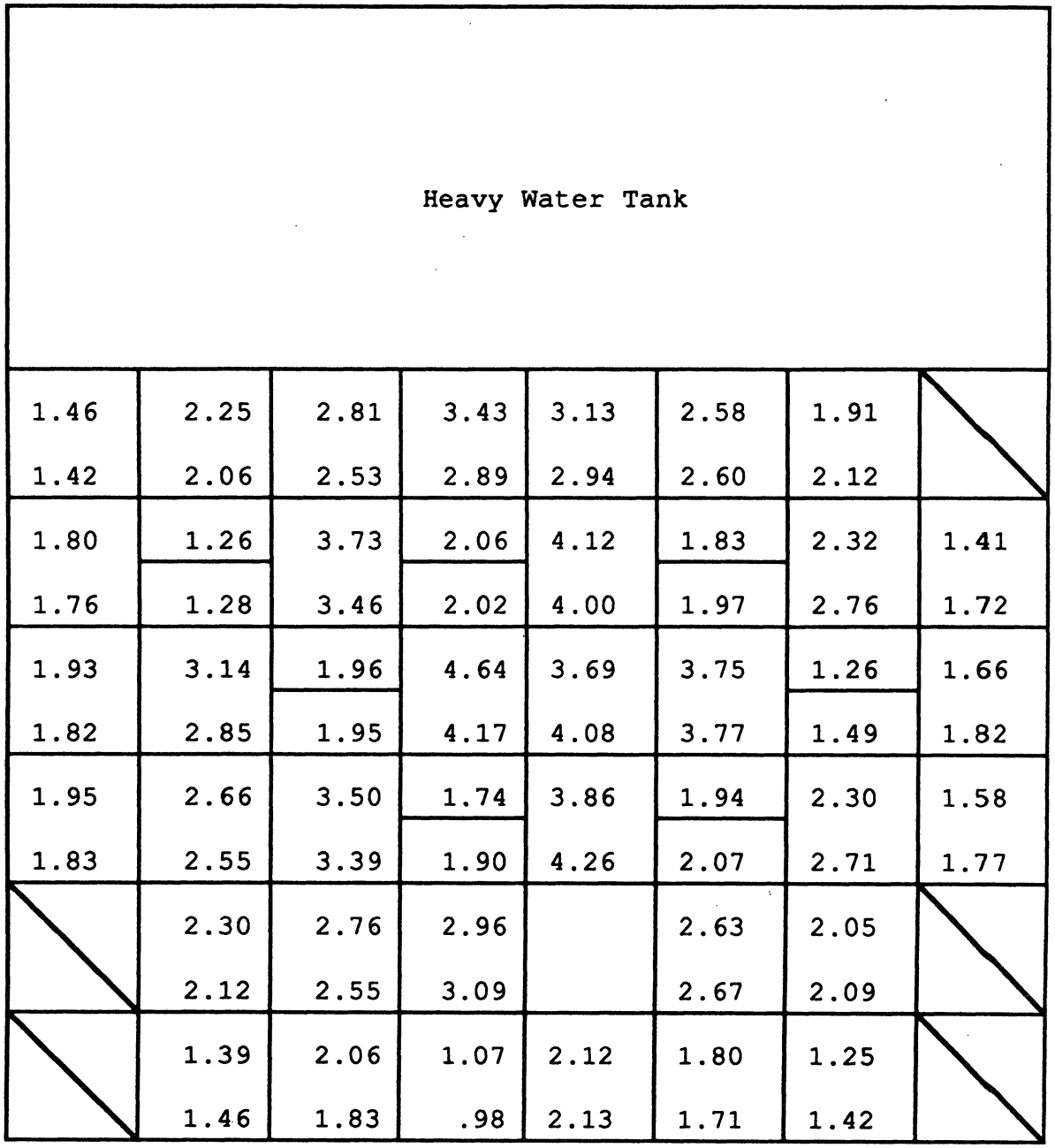

A: Assembly Power (%), Measured

B: Assembly Power (%), Calculated

Figure II-8. Experimental and Calculated Power Distributins for FNR Cycle 67 [rms deviation = 9.3%]

Special Considerations for the FNR

•Number of Energy Groups

Nearly all analyses have been carried out with two neutron energy groups--one fast and one thermal, with a cutoff at 0.625 eV. Analysis of the BSR with four energy groups (three fast, one thermal) yielded only marginal improvement in core eigenvalue and thermal flux distribution (see Table II-14) and the use of four energy groups was deemed to be not worth the added expense for routine calculations.

•Spatial Mesh

Three different spatial meshes, shown in Figure II-9, have been used for FNR simulation: A 2x2 mesh per assembly, or homogeneous mesh, is used for inexpensive survey calculations. This mesh makes no distinction between active and non-active portions of an assembly, and thus cannot give detailed flux distributions. It has, however, proved to be reasonably accurate in computing core reactivity and assembly-averaged power distributions. Most of the detailed FNR analyses have utilized a 6x6 mesh per assembly. This discrete mesh structure allows explicit representation of active and non-active regions, as well as waterholes and control rods. To check the adequacy of the 6x6 mesh structure, several benchmark calculations (see Table II-14) were run using a 12x12 mesh per assembly, confirming the

FNR Fuel Assemblies

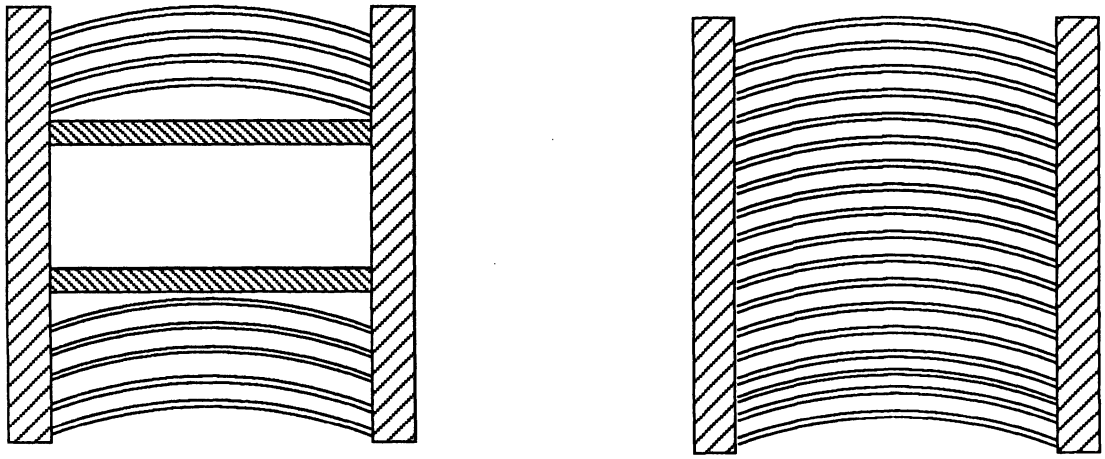

SPECIAL REGULAR

UM2DB Mesh per Assembly

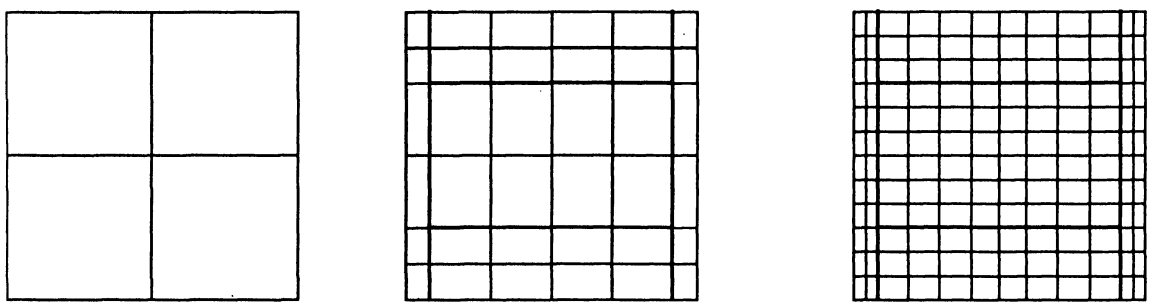

2 X 2 HOMOGENEOUS 6 X 6 DISCRETE 12 X 12 DISCRETE

Figure II-9. UM2DB Mesh Description

adequacy of the 6x6 mesh for most calculations. These 12x12 calculations are generally too expensive for routine use.

•Boundary Conditions

Zero-flux boundary conditions were used on all four boundaries for calculations without symmetry. To ensure that these boundary conditions would not affect the in-core flux, the core and heavy water tank were surrounded by 30-35 cm of water. This water thickness was chosen to be large enough so that the arbitrary nature of the boundary was of no consequence.

•Transverse Buckling

For 2-D x-y calculations, the leakage in the axial direction (z) is accounted for with a transverse buckling B^2, which is an input variable to UM2DB. This transverse buckling has an obvious impact on the predicted core multiplication factor, especially for a small, high leakage core such as the FNR. There are many approaches to determining an appropriate buckling (or set of bucklings, since UM2DB allows for zone- and group-dependent bucklings), and Section II.E.2 discusses the effort to evaluate these methods and arrive at a set of bucklings for the FNR.

2. UM3DB

Effort was expended over the last two years of the LEU project to develop a three-dimensional version of the two-dimensional diffusion theory code UM2DB. This capability is

needed to analyze control rod worths, axial depletion effects, and flux distributions in the core and D_2O tank. Because the UM2DB code has been a successful tool for 2-D global diffusion-depletion calculations of the FNR it was decided to incorporate the three dimensional capability into UM2DB rather than modifying an existing 3-D code (e.g., PDQ-7 [Cal67], VENTURE [Von75] and 3DB [Har70a] are operational on MTS) to include the various enhancements that have been made to UM2DB over the years, such as the macroscopic depletion scheme.

The approach is similar to the 3DB algorithm. Planes have been added to treat the third dimension and an iteration over planes is included to converge the 3-D solution. The inner iterations still involve the calculation for one plane, with appropriate terms added to account for the interaction with neighboring planes. Extensive changes were needed for the input routines to allow the specification of axial zones as well as changes to allow edits over the axial zones. The modified code, named UM3DB, has been tested extensively, including comparisons with the original version of 3DB, benchmark calculations of an IAEA test problem, and comparisons with UM2DB for a mid-core FNR problem. These test calculations are described in more detail below.

•Comparisons with 3DB

The 3DB code [Har70a] has been operational on MTS for several years and can be used for static 3-D analysis. The 3DB code package received from Argonne Code Center included a sample case for a simple 1/8-reactor consisting of a homogeneous fast reactor with a blanket. A two group description was used and three different meshes were calculated -- 2x2x2, 4x4x4 and 10x10x10. The results are tabulated in Table II-15, where it is evident that the codes compare very well. Although only multiplication factors are compared in Table II-15, the point-wise fluxes also agree to within four decimal points for all cases.

Table II-15. Comparison of UM3DB and 3DB Multiplication Factors

Mesh	k_{eff}	
	UM3DB	3DB
2 x 2 x 2	1.15890	1.15890
4 x 4 x 4	1.06187	1.06188
10 x 10 x 10	1.02167	1.02172

•IAEA Test Problem

The Argonne Benchmark Problem Book [Anl66] contains benchmark problems for many different neutronic configurations, including a 3-D static diffusion theory problem. This problem is a severe test of a 3-D code, since it consists of a quarter core with several fully inserted control rods and one partially inserted control rod, reflected by water on all sides. Figure II-10, taken from [Anl66], depicts the configuration.

Table II-16 summarizes the results for the benchmark problem. The UM3DB calculation predicts a multiplication factor that agrees to within 0.01% of the reference solution which utilized a Richardson-extrapolation of several VENTURE runs, as summarized in Table II-16. The UM3DB calculation employed a relatively crude mesh (17x17x29) and the lack of edits for that particular run did not allow a determination of local quantities such as peak-to-average power density.

•FNR Test Problem

Since the objective of the 3-D capability is the analysis of the FNR, UM3DB has been applied to a typical FNR configuration which has been calculated with UM2DB. The particular configuration examined was the LEU core on September 16, 1983 (Cycle 229A). The UM3DB thermal fluxes were normalized to yield the same core average as calculated by UM2DB. Figure II-11 summarizes the resultant assembly-

Benchmark Source Situation

Identification: 11

Date Submitted: June 1976 By: R.R. Lee (CE)
D.A. Meneley (Ontario Hydro)
B.Micheelsen (Riso-Denmark)
D.R. Vondy (ORNL)
M.R. Wagner (KWU)
W. Werner (GRS-Munich)

Date Accepted: June 1977 By: H.L. Dodds, Jr. (U. of Tenn.)
M.V. Gregory (SRL)

Descriptive Title: Multi-dimensional (x-y-z) LWR Model

Suggested Functions: Designed to provide a severe test for the capabilities of coarse mesh methods and flux synthesis approximations

Configuration: Three-dimensional configuration including space dimensions and region numbers: 2 Figures

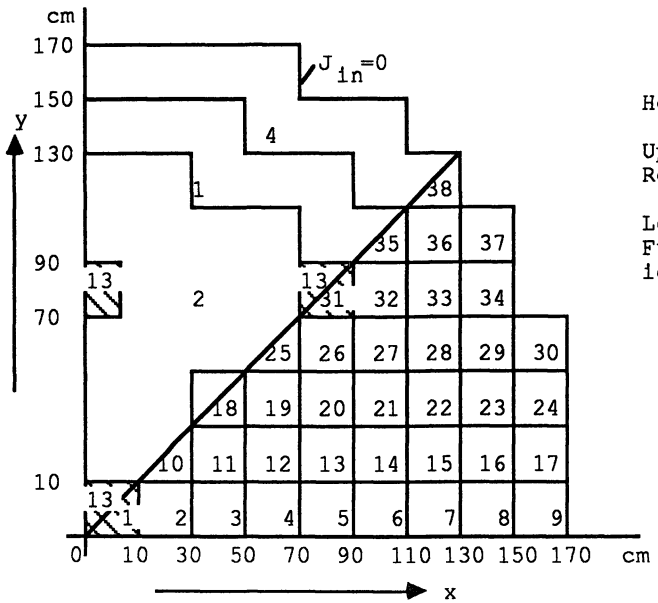

Horizontal Cross Section

Upper Octant:
Region Assignments

Lower Octant:
Fuel Assembly identification

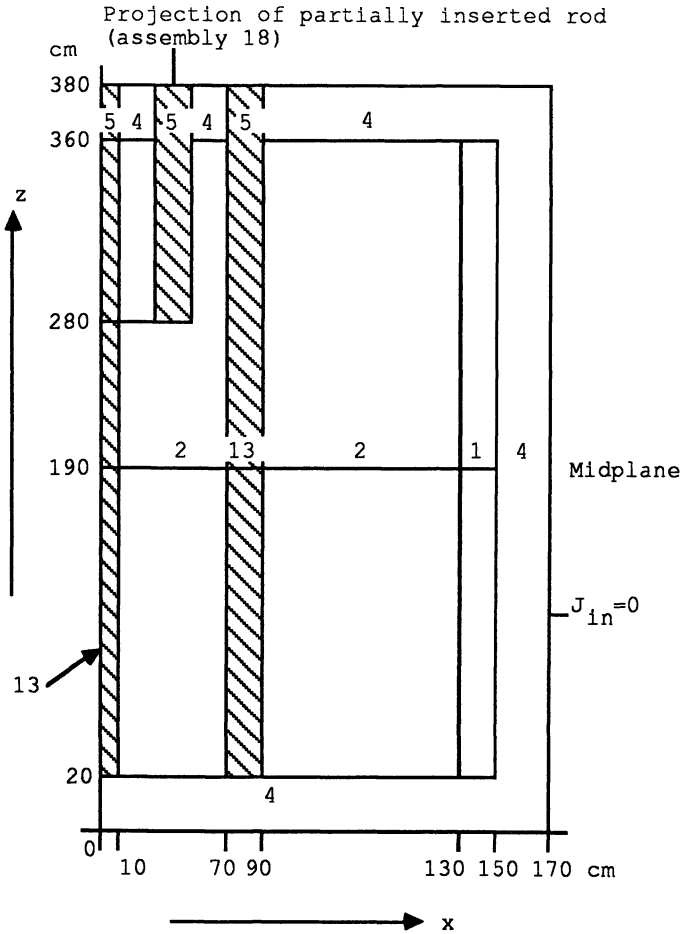

Vertical Cross Section, y = 0

Boundary Conditions:

Extneral Boundaries: Vacuum, no incoming current
Symmetry Boundaries: Reflection, no net current

Figure II-10. IAEA Benchmark Problem Configuration (from [ANL66])

Table II-16. 3-D, 2-Group IAEA Benchmark Problem Results (Non-return External Boundary Conditions)

Mesh Points [Total Unknowns]	Multiplication Factor	Peak-to-Average Power Density	IBM-360/91 Processor Time (min.)
VENTURE			
9x9x10 [1,620]	1.03176	2.3765	0.3 to 1
17x17x19 [10,982]	1.02913	2.5672	1.6 to 5
34x34x38 [87,856]	1.02864	2.5035	49
68x68x76 [702,848]	1.02887	2.4081	192
102x102x114 [2,372,112]	1.02896	2.3780	360†
Extrapolated	1.02903	2.354	
UM3DB			
17x17x29 [16,762]	1.02897	----	4††

Notes: † IBM 195

†† Amdahl 5860

UM3DB versus UM2DB
Assembly-Averaged Thermal Flux (10^{13} n/cm^2-s)

(UM3DB Flux normalized to total UM2DB flux in core)

UM2DB	Flux
UM3DB	Flux
UM2DB	ϕ_1/ϕ_2
UM3DB	ϕ_1/ϕ_2

-(Fast to Thermal Flux Ratio)

Average Thermal Flux over Portions of Heavy Water Tank

location	UM2DB	UM3DB
Back	.98	1.06
Center	1.35	1.42
Front	1.60	1.64
k_{eff} --	1.0238	1.0235

Heavy Water Tank

	.983 .988	1.20 1.21	1.41 1.42	1.38 1.39 2.50 2.50	1.28 1.28	1.03 1.03	1.81 1.81 .462 .463
.750 .751	1.05 1.05	1.48 1.48	A 2.40 2.40	1.73 1.73	C 2.19 2.19	1.17 1.17	.817 .815
1.03 1.03 1.35 1.35	1.11 1.11	2.11 2.11	1.79 1.79	1.69 1.69 2.76 2.76	1.60 1.60	1.17 1.17	.837 .833 2.16 2.16
1.50 1.50	.948 .949	1.26 1.26	B 2.09 2.09	1.52 1.52	1.93 1.92	1.08 1.08	1.90 1.89
7.85 7.85 .292 .292	1.66 1.67	.878 .879	1.04 1.04	1.05 1.05 2.46 2.46	.965 .963	.729 .726	1.15 1.14 .394 .394
2.58 2.58	.678 .679	1.17 1.17	1.53 1.53	1.61 1.60	1.42 1.41	.989 .984	.489 .486

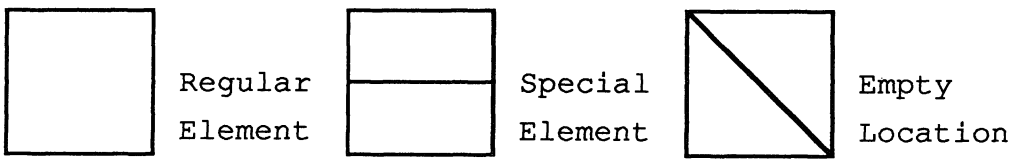

Figure II-11. Comparison of Assembly-Averaged Thermal Flux Distributions for UM3DB and UM2DB.

averaged thermal flux distribution for the core and reflectors (D_2O and H_2O) as well as fast-to-thermal flux ratios for selected regions. As can be seen, the agreement is very good within the core and significant deviations between UM2DB and UM3DB do not occur until well into the D_2O tank where one might expect differences between 2-D and 3-D predictions due to the non-separability of the flux in the D_2O tank. As a further indication of the non-separability of the flux in the reflectors, Figure II-12 summarizes the quarter-height and half-height thermal fluxes predicted by UM3DB in the core and reflectors. As can be seen, the difference in the thermal flux at these two axial locations is significantly larger in the reflector regions (5-10%) than in the core regions (0-2%). This indicates a substantial difference in the axial profiles in the reflector and core regions, hence, indicating the importance of the 3-D capability.

D. Transport Theory Calculations

The 1-D discrete ordinates transport codes ANISN [Eng67] and XSDRN [Gre69] were utilized to calculate MGD cross sections for ex-core regions such as the H_2O and D_2O reflectors. These calculations required no additional capabilities and no modifications were necessary for either ANISN or XSDRN. In addition, the 1-D integral transport code HAMMER [Bar78] and the 2-D discrete ordinates code TWOTRAN

UM3DB Thermal Flux Edit (10^{13} n/cm^2-s)
(UM3DB flux normalized to total UM2DB flux in core)

1/4-Height 1/2-Height 1/4|1/2	(Fast-to-Thermal Flux Ratio)

D_2O Tank

Location	UM3DB 1/4-Height	UM3DB 1/2-Height	UM2DB
Back	1.16	1.06	.976
Center	1.55	1.42	1.35
Front	1.77	1.64	1.60

Heavy Water Tank

	1.00 .988	1.23 1.21	1.44 1.42	1.41 1.39 2.48/2.50	1.30 1.28	1.05 1.03	1.82 1.81 .46/.46
.749 .751	1.05 1.05	1.48 1.48	a 2.41 2.40	1.73 1.73	c 2.19 2.19	1.17 1.17	.813 .815
1.03 1.03	1.10 1.11	2.10 2.11	1.78 1.79	1.68 1.69 2.76/2.76	1.59 1.60	1.16 1.17	.830 .833
	.944 .949	1.25 1.26	b 2.08 2.09	1.51 1.52	1.91 1.92	1.07 1.08	
		.874 .879	1.04 1.04	1.05 1.05 2.46/2.46	.957 .963	.722 .726	1.13 1.14 .39/.39

Regular Element

Special Element

Empty Location

Figure II-12. UM3DB Calculated Thermal Fluxes.

[Lat73] were utilized to calculate effective MGD cross sections for the FNR control rods. Again, no modifications were needed to either HAMMER or TWOTRAN although an "executive" code (ROD) was written to allow automatic sequential execution of the UMLEO, HAMMER, TWOTRAN, and UM2DB codes to generate the depletion-dependent (depletion of the fuel in the special element containing the control rod) cross sections for the control rod. The ROD code is described in Section E.1 below, which discusses the control rod calculation methodology in some detail.

E. Special Calculations

The sections above described the generic reactor analysis methods that have been developed and/or implemented on the UM computer system for the analysis of the FNR. In general, these methods are based on well-accepted production-level codes that are publicly available. However, there are a number of special calculations that are unique to the FNR and which involve more than a straightforward application of these codes. The following sections discuss these topics in more detail:

- control rod cross sections (integral and differential)
- transverse buckling
- lumped fission product correlation (CINDER)
- ex-core cross section generation

- effective delayed neutron fraction β_{eff}
- fuel cycle calculations

1. Control Rod Calculations

The three shim-safety rods for the FNR are made of boron stainless steel containing 1.5% natural boron by weight. The composition and dimensions are given in Table II-17. These rods are essentially black to thermal neutrons and cause a drastic thermal flux depression when inserted. Since fine-mesh transport theory calculations for the whole core are prohibitively expensive, a method was developed to obtain effective few-group constants for control regions to be utilized in standard UM2DB calculations. The methods developed have shown high accuracy in simulating measured rod worths for the FNR core. The basic approach is to utilize HAMMER to perform the spectrum calculation for the initial rod-fuel environment configuration. Space-dependent cross sections from the HAMMER calculation are then used in TWOTRAN in a 4-group discrete ordinate calculation of the actual 2-D control rod-fuel configuration. Reaction rates from the TWOTRAN calculation are then matched in a corresponding UM2DB calculation by varying the control rod absorption cross sections. In essence, this method is similar to a cross section "fixing" code such as MO-807 [Rut67], although the actual determination of effective

Table II-17. FNR Shim-Safety Control Rod Descriptions

Composition	Boron Stainless Steel -- 1.5 w/o natural boron
Dimensions	2.1984 cm x 5.6683 cm x 61 cm
Element	Number Density* (atoms/b-cm)
^{10}B	0.001108
^{11}B	0.005184
Fe	0.05644
Ni	0.0113
Cr	0.0164

*Based on composition and density of boron stainless steel from [And62].

cross sections is performed graphically. The following sections describe this analysis procedure in more detail.

•Step 1 - HAMMER Analysis (spectrum)

The generation of few-group constants to accurately represent a control rod is complicated by two problems: First, the methods and approximations in diffusion codes are unreliable in regions of steep flux gradients. Second, the strong spectral/spatial coupling induced by a control rod necessitates careful selection of a spatial mesh. Both of these problems arise in the analysis of the FNR rods.

Since HAMMER is a one-dimensional code and since the FNR rods are many thermal mean free paths thick, a cylindrical geometry was chosen to generate cross-sections for the rod and adjacent water. Since the rods are essentially black to thermal neutrons, it was deemed most important to preserve the rod surface area rather than volume. The geometry chosen is shown in Figure II-13. For this calculation, the fuel, clad, and moderator were treated as a homogeneous mixture.

The thermal analysis section of the HAMMER code provides two options for the thermal integral transport calculation:

(1) The standard option, due to Honeck [Hon60], is the basis of the THERMOS code [Hon62]. Using this option, the region-to-region transport kernels are computed by a "ray-tracing" technique, and an approximation is applied to the Bickley-Naylor functions [Bic35] involved.

(2) The second option, due to Carlvik [Car65], is the basis for the FLURIG code. In this method, a transformation of variables results in a "slicing" technique which makes use of Gaussian quadrature to evaluate the collision probabilities. No function approximations are made.

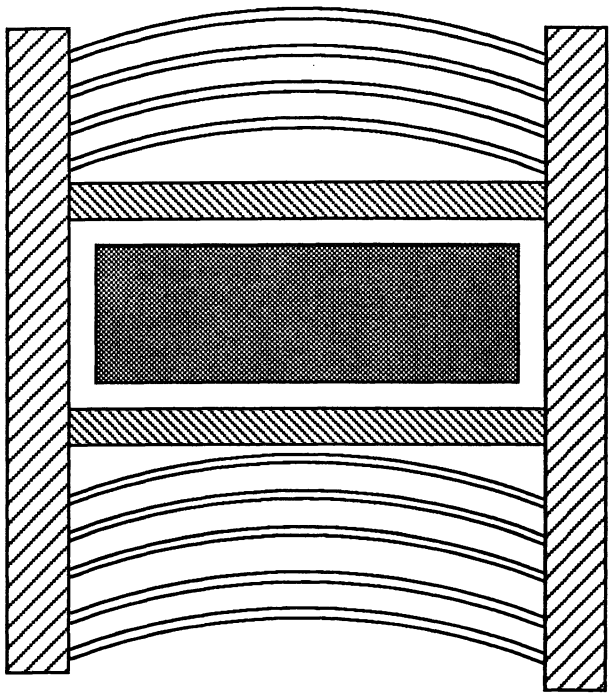

ACTUAL SPECIAL ELEMENT
(CONTROL ROD INSERTED)

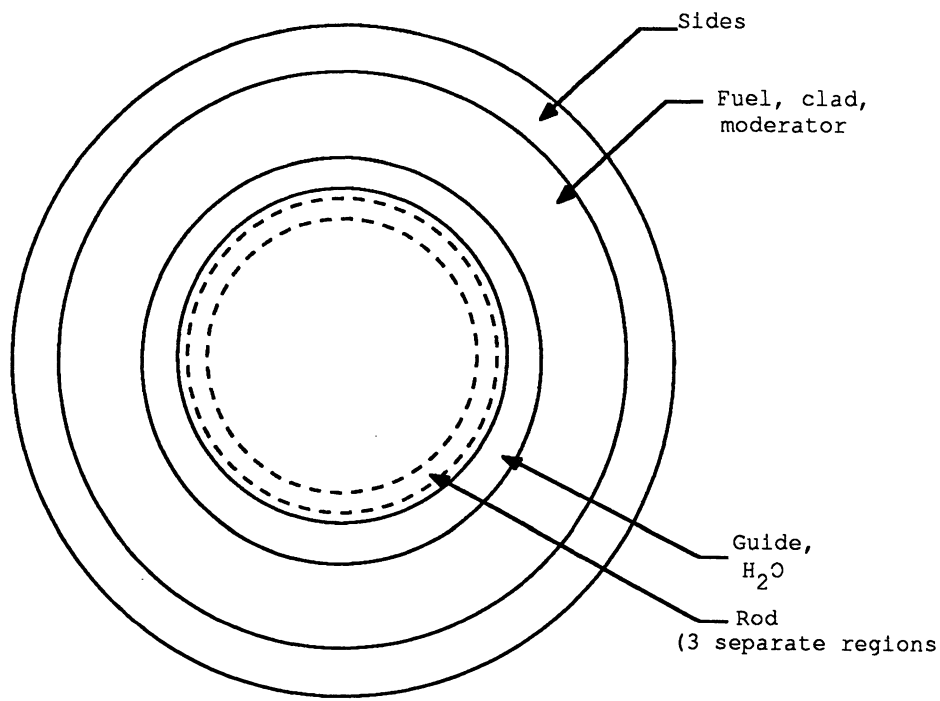

EQUIVALENT CYLINDRICAL GEOMETRY

FIGURE II-13. Hammer Geometry for Cylindricized FNR Special Assembly with Rod

In our study, both methods were tried for a cylindricized control assembly and yielded different results. Varying the mesh spacing and examining intermediate results led us to the conclusion that the numerical scheme using the first approach is not reliable for FNR control rods. The approximations used in computing the transport kernels between the internal regions in the control rod give inaccurate results for large, black absorbers. Additionally, using either a reflecting boundary or a "scattering ring" produced non-physical flux profiles near the outer boundary.

Due to the strong spectral/spatial coupling, it is not proper to represent the control rod by one set of few-group cross sections. This is readily apparent in Figure II-14 where the spectrum is shown as function of radial position. By trial and error, it was found that representing the rod by three distinct regions, with separate cross sections for each, was sufficient to allow a one thermal-group TWOTRAN discrete ordinates calculation to closely match the 30-group HAMMER thermal flux profile. The TWOTRAN calculations were performed with cross sections obtained from the corresponding HAMMER calculation. A typical comparison is shown in Figure II-15. The three regions of the control rod are a surface layer 0.1 cm thick, a second layer 0.3 cm thick and the third region consisting of the remaining central region of the rod. Most of the thermal absorption occurs in the two outer

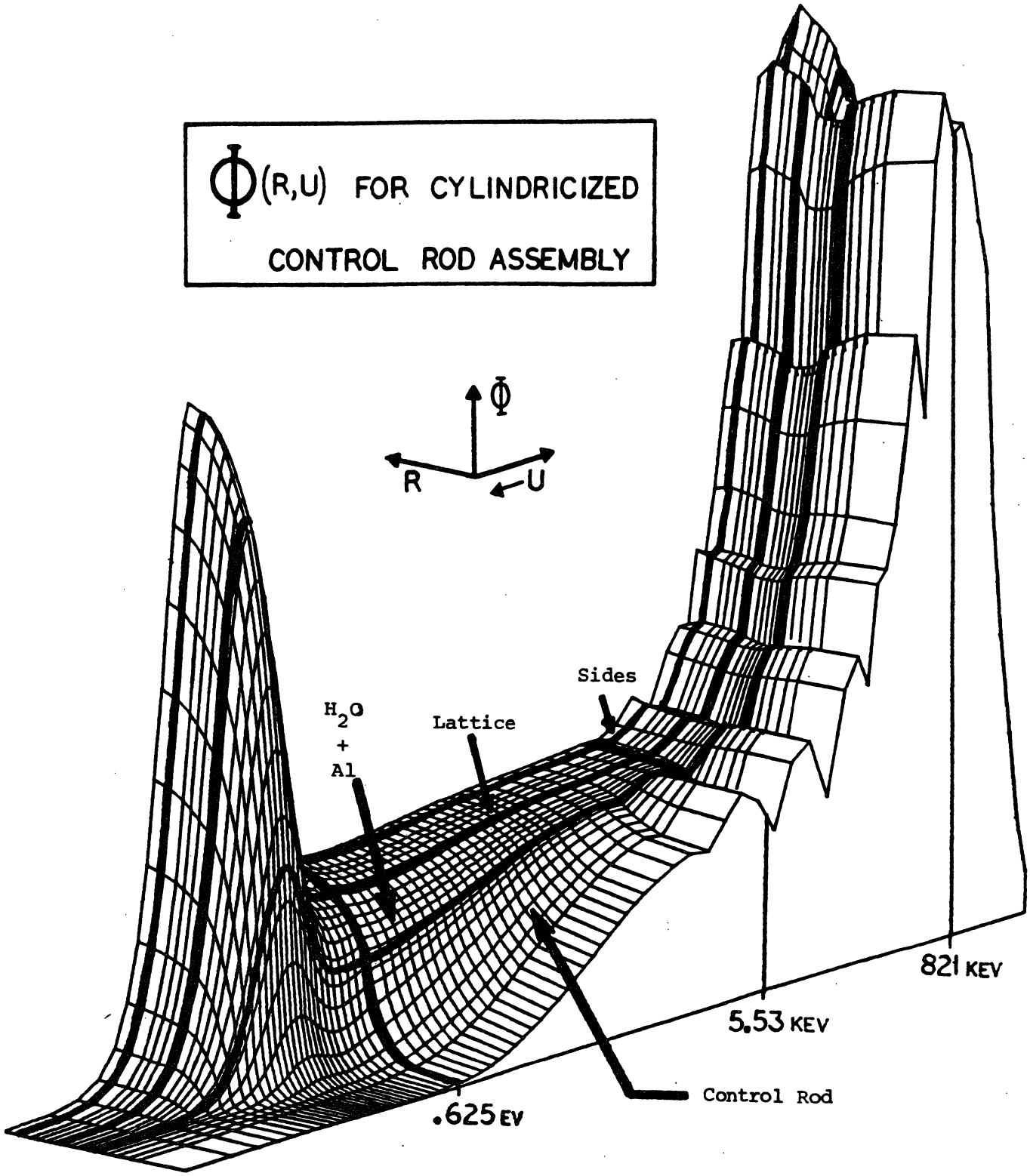

Figure II-14. Flux Spectra as a Function of Position in the Cylindricized FNR Special Assembly with Rod

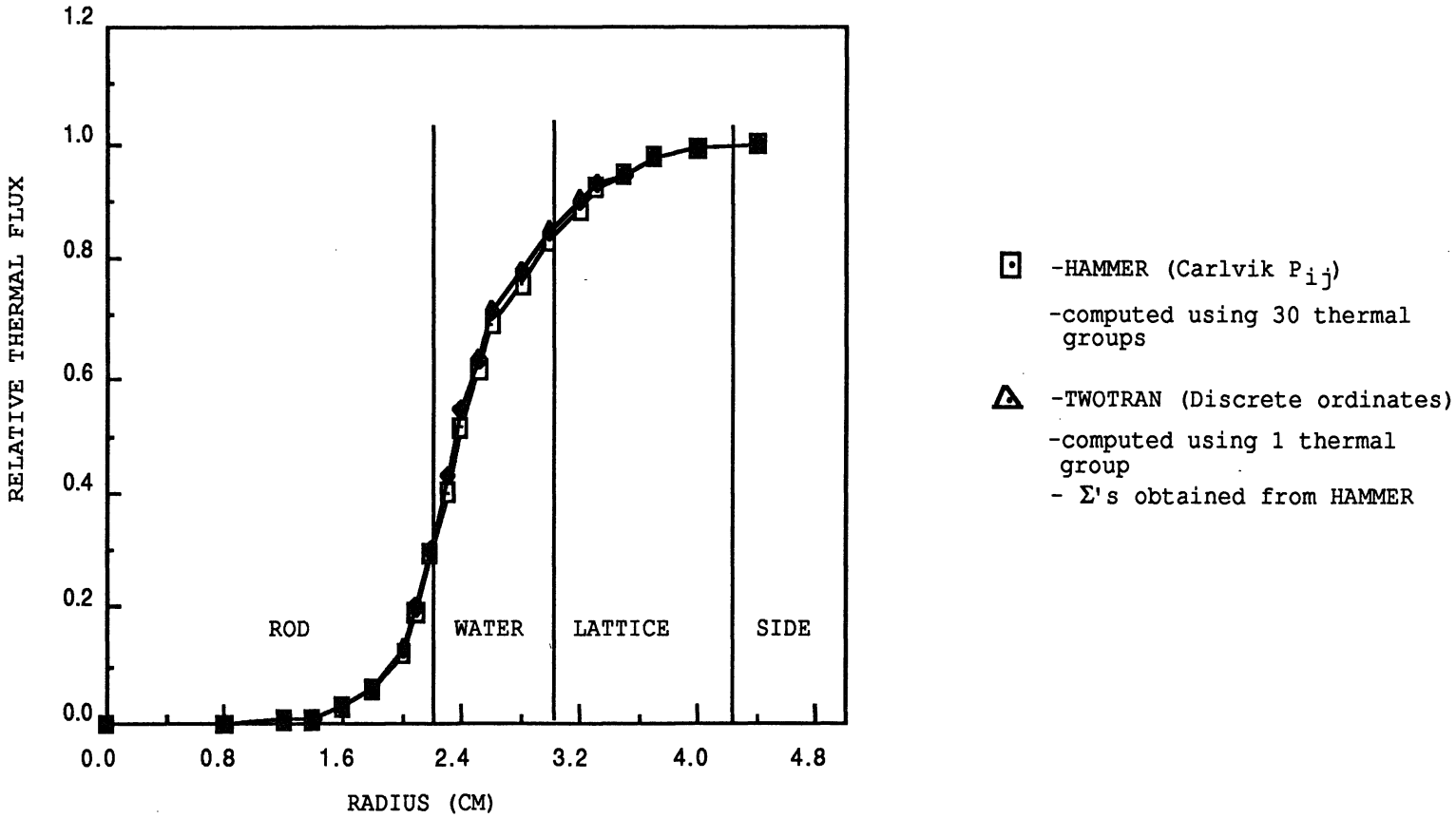

Figure II-15. Comparison of Thermal Flux for Cylindricized FNR Assembly with Rod: HAMMER vs. TWOTRAN

layers, with few thermal neutrons reaching the central region.

The selection of mesh spacing is very important for integral transport codes, which usually assume a flat flux in each mesh region. It is necessary to cluster the mesh points in areas of steep flux gradients, a task that must be done manually through trial and error.

•Step 2 - TWOTRAN Calculation (reaction rates)

The control rod cross sections obtained from HAMMER are not suitable for direct diffusion theory calculations. The strong absorption in the rod and the steep gradients at its boundaries grossly violate the underlying assumptions of diffusion theory. Direct use of the HAMMER-generated absorption cross sections results in an over-prediction of the neutron absorption rate in the control rod. In addition, the HAMMER representation of the control rod geometry as a cylindrical geometry would introduce errors due to this poor spatial model. To remedy this problem, HAMMER cross sections for the rod, neighboring lattice, and surrounding fuel assemblies are used in a fine-mesh TWOTRAN calculation. TWOTRAN is then used to predict the absorption rate ratios (control rod region/lattice region) for both thermal and fast energy groups.

•Step 3 - UM2DB Calculation (Cross Section Fitting)

Using the same mesh structure (6x6 per assembly) as for eventual whole core calculations, the problem is rerun with the UM2DB code. Both fast and thermal absorption cross sections for the rod are then adjusted until the UM2DB-predicted absorption rate ratios match those of the benchmark TWOTRAN calculation. The resulting "effective control region" cross sections are then used in global UM2DB calculations with the control rod inserted and withdrawn to determine the control rod worth. This entire procedure is summarized pictorially in Figures II-16 through II-21:

(i) Figure II-16: Four HAMMER calculations are needed to develop few-group constants.

(ii) Figure II-17: The HAMMER constants are used in a fine-mesh transport calculation of a special assembly (with rod) surrounded on each side by one half of a regular assembly, with reflecting boundaries. The same problem is repeated using diffusion theory and the standard 6x6 mesh/assembly. (The rod and surrounding water must be homogenized.)

(iii) Figure II-18: The diffusion theory calculation is repeated, using different values for the thermal absorption cross section of the control region (rod + surrounding water). From a plot of the ratio R_2 of thermal absorption in the control region to that in the

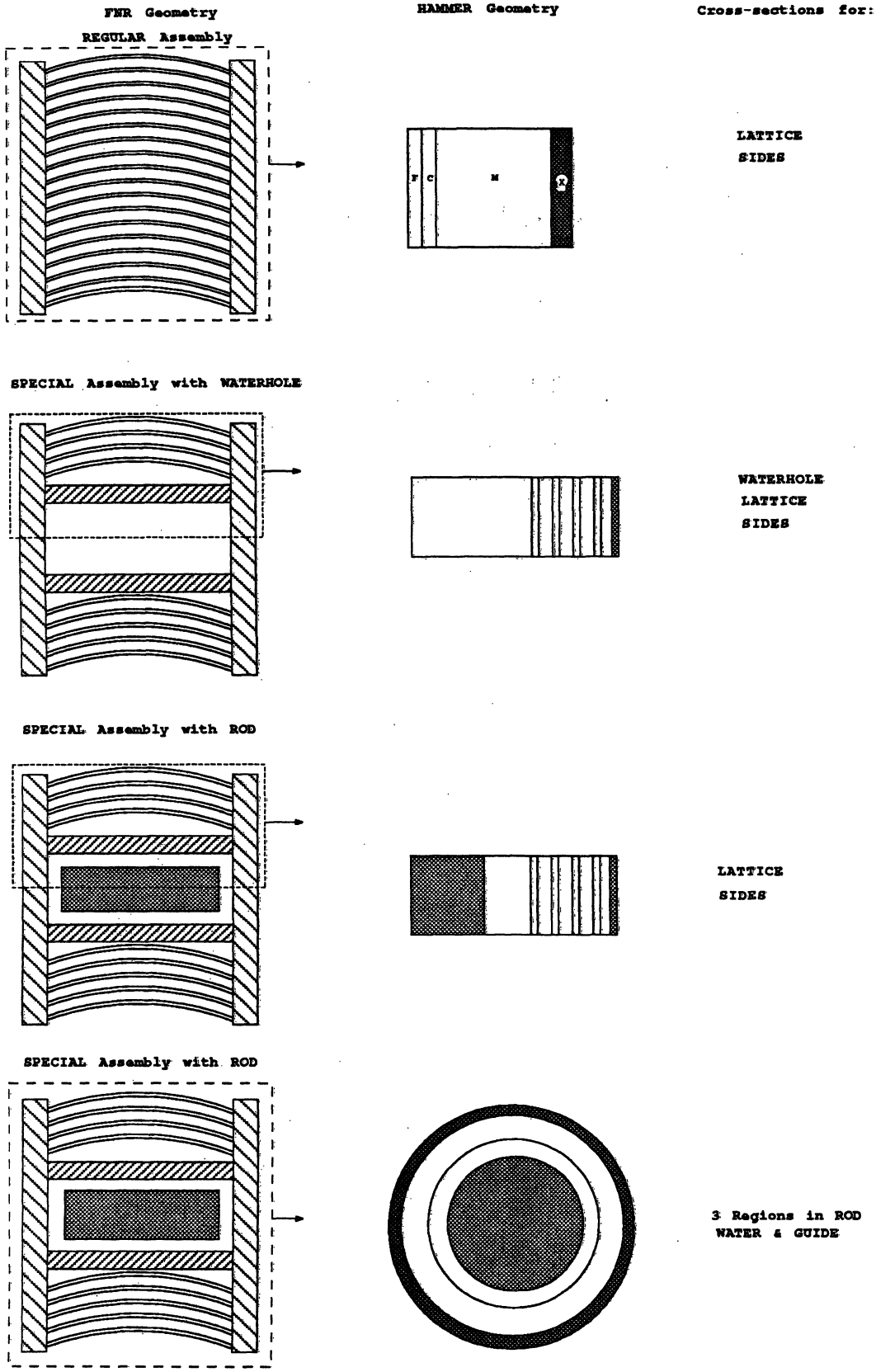

Figure II-16. Geometry for HAMMER Calculations

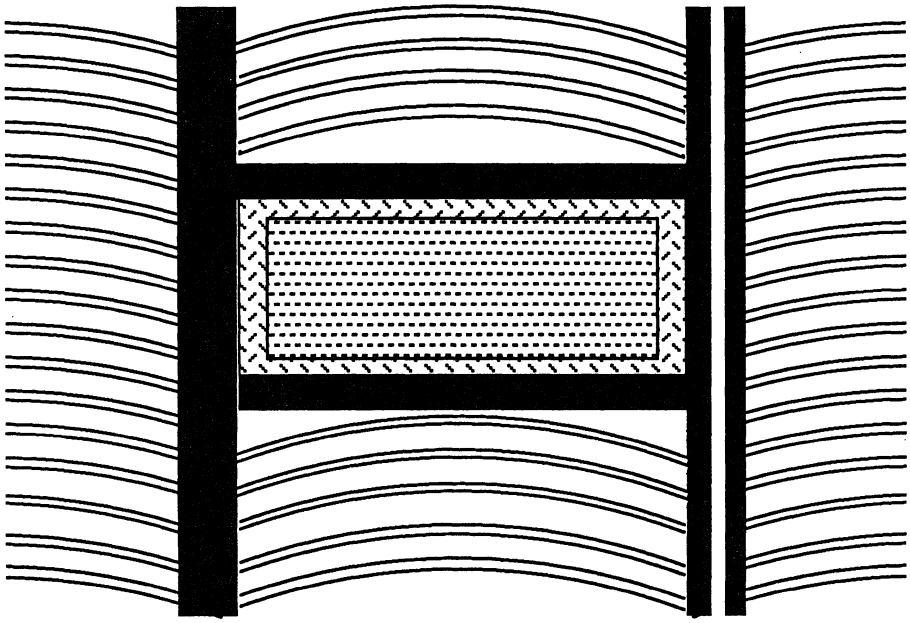

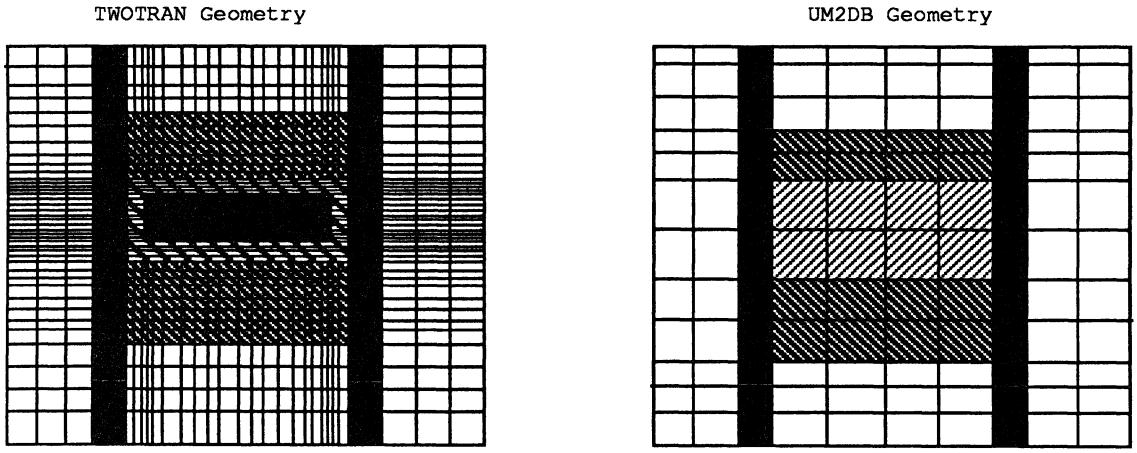

Figure II-17. Geometry for Determination of Effective Absorption Cross Sections of Control Region for use in UM2DB

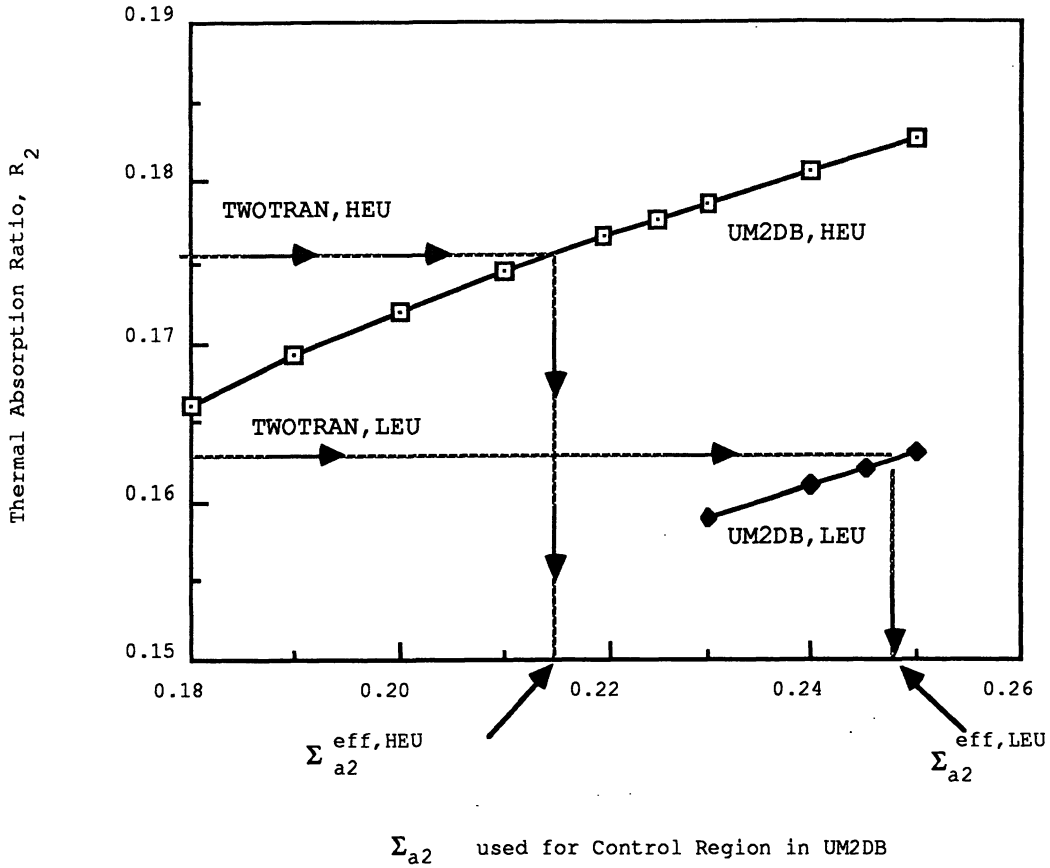

$$R_2 = \frac{\text{thermal absorption in control region}}{\text{thermal absorption in lattice regions}}$$

for geometry shown in Figure II-17

Figure II-18. Determination of Effective Thermal Absorption Cross Section

lattice regions, an effective thermal absorption cross section for the control region is selected which yields R_2 equal to the value obtained from the TWOTRAN run.

(iv) Figure II-19: A similar procedure is followed to determine an effective fast absorption cross section of the control region.

(v) Figure II-20: The thermal flux distribution is shown for a whole-core UM2DB calculation without control rod, used to obtain k_{eff} for the unrodded core.

(vi) Figure II-21: The thermal flux distribution is shown for a whole-core UM2DB calculation using the effective control region cross sections to simulate an inserted control rod. From this run, k_{eff} is obtained for the rodded configuration.

(vii) By using k_{eff} for the rodded and unrodded cores, the reactivity worth of the control rod is determined.

The accuracy of this procedure is demonstrated in Table II-18, where computed and measured rod worths are compared for FNR Cycle 67. Other rod worth comparisons are also given in Section V.C. It should be noted that this procedure is moderately expensive -- <u>one</u> calculation of control rod reactivity worth requires 4 HAMMER calculations, one fine-mesh TWOTRAN calculation (involving 4 assemblies),

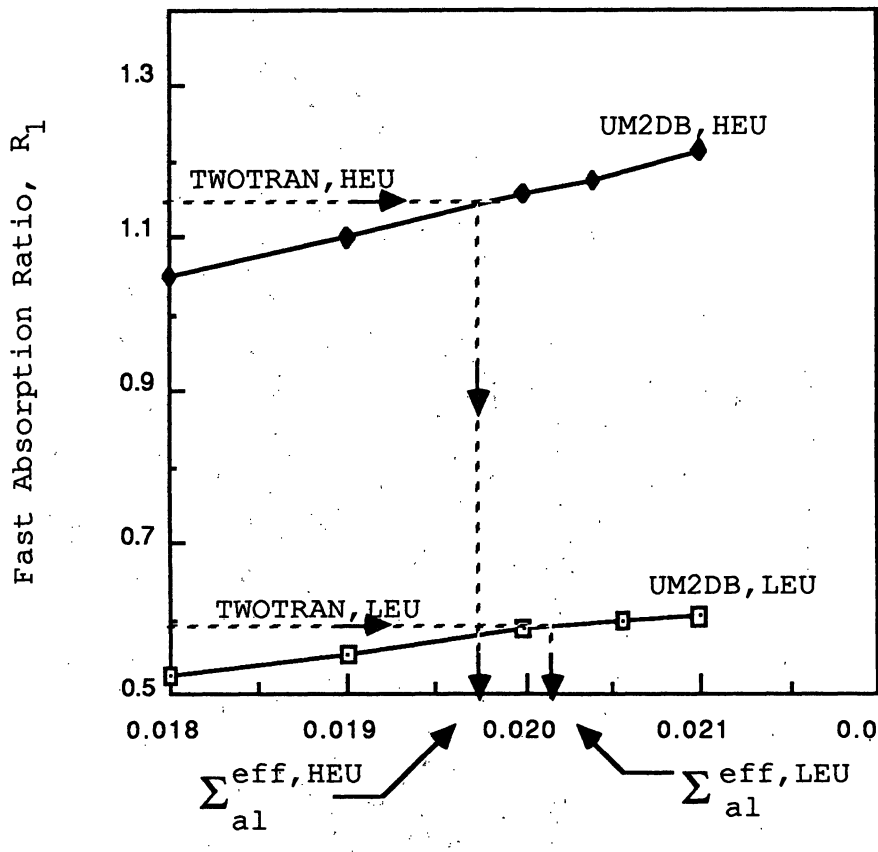

Σ_{al} used for Control Region in UM2DB (cm^{-1})

$$R_1 = \frac{\text{fast absorption in control region}}{\text{fast absorption in lattice regions}}$$

(for geometry shown in Figure II-17)

Figure II-19. Determination of Effective Fast Absorption Cross Section for Control Region.

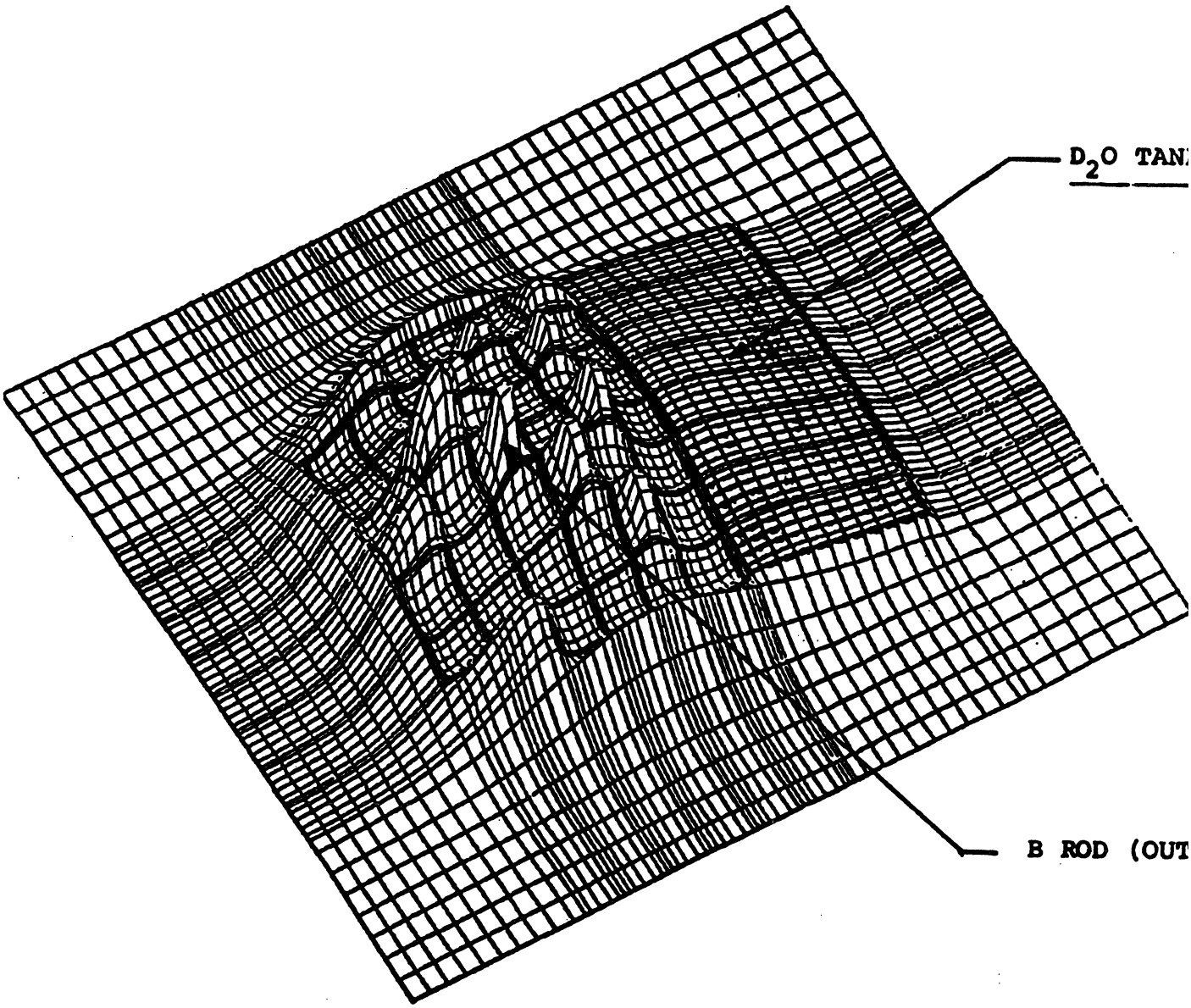

Figure II-20. Thermal Flux Profile in the FNR with Rods Out - UM2DB Calculation for Cycle #67 (1971).

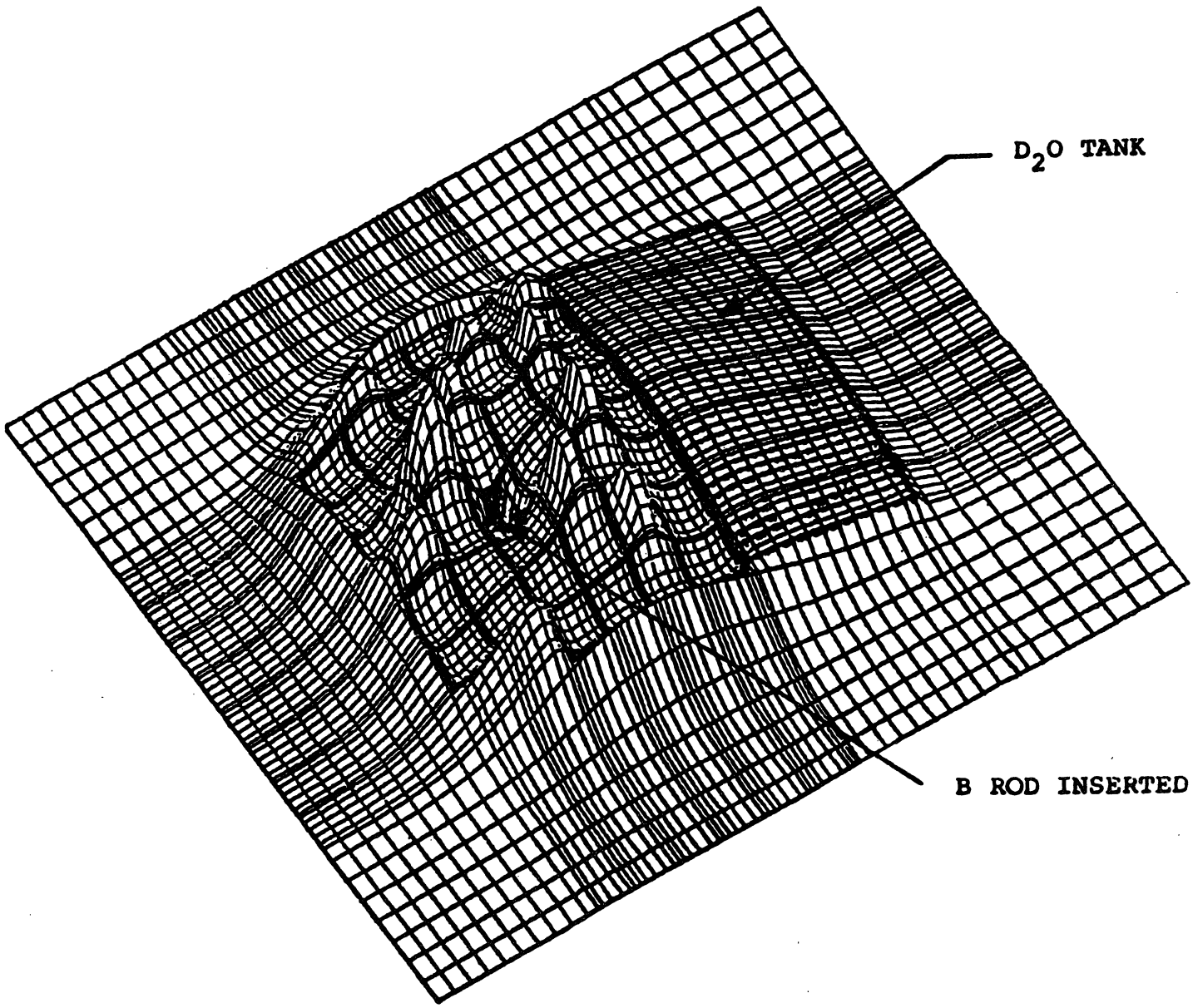

Figure II-21. Thermal Flux Profile with B Rod Inserted - UM2DB Calculation for Cycle #67 (1971).

Table II-18. Control Rod Reactivity Worth for FNR 67

Rod Location	Local Fuel Burnup (%)	Rod Worth (% Δ k/k)	
		Measured	Calculated
A	16	2.22	2.20
B	24	2.11	2.11
C	6	1.72	1.73
Total		6.05	6.04

several small UM2DB calculations (involving 4 assemblies), and two whole-core 6x6 mesh/assembly UM2DB calculations.

Although the entire procedure could be repeated for different values of fuel depletion, it was found that, for the FNR, the effective cross sections used for the control rod region were not sensitive to fuel burnup. Thus, to account for fuel depletion, only the first three HAMMER calculations in Figure II-16 are needed; the effective control cross sections need not be recomputed. This is done by linking HAMMER with the spectrum-depletion code UMLEO described below. The effective control cross sections must, however, be recomputed for LEU fuel. Figures II-18 and II-19 illustrate the substantial effect on control rod cross sections due to the change in fuel from HEU to LEU.

•The ROD Code

The computational scheme for FNR control rod worth analysis described above requires the use of the HAMMER code to generate special assembly cross sections both with and without a control rod. To include the effects of fuel depletion on control rod worth, HAMMER calculations must be done for several special assembly burnups. Two schemes were considered for accomplishing this: The first, adding a depletion capability to HAMMER, was clearly unacceptable due to the extremely high computer costs, long development time, and major rewrite of HAMMER that would be required. The second, linking the UMLEO and HAMMER codes to allow HAMMER calculations at any UMLEO burnup step, was implemented via the development of the ROD code. This code is a sophisticated supervisor program which dynamically loads and runs the UMLEO code for a special or regular assembly depletion run, saves the resulting isotopic number densities at each burnup step, sets up HAMMER input for user-specified burnup steps, dynamically loads and runs the HAMMER code, and then reformats the HAMMER generated cross sections into a burnup library suitable for the UM2DB code. Since the HAMMER code performs the spectrum calculation only for a specified input buckling (passed from the UMLEO code by the ROD code) and does not iterate to criticality, the ROD code checks the HAMMER eigenvalue. If the HAMMER eigenvalue is not

sufficiently close to 1.0, the ROD code interactively asks the user for a new buckling and then reruns the HAMMER code. This interactive iteration approach was chosen to avoid the high cost of modifying HAMMER to perform criticality searches. For the case of a special assembly with control rod inserted, the ROD code makes a normal UMLEO depletion run (i.e., no rod), estimates the critical buckling of a rodded special assembly using an empirical correlation, and then runs the HAMMER code for a rodded special assembly.

The entire calculational sequence of the ROD code is moderately expensive (about an order of magnitude greater than a standard UMLEO depletion run) but has been used to generate cross section burnup libraries for use in both HEU and LEU control rod worth analysis.

The ROD code performs many system-dependent functions related to disk file manipulation, dynamic program loading and linking, and interaction with the user via terminal input/output. As such, the code is *not* exportable to other computer systems not having both IBM Fortran and the Michigan Terminal System (MTS) operating system. Additionally, certain features of the FNR fuel assembly geometry are hardwired into the code, precluding its general use.

2. Transverse Buckling Calculations

Two-dimensional diffusion theory calculations for a small reactor such as the FNR are sensitive to the input buckling

used to model neutron leakage in the axial direction. The sensitivity of FNR calculations to buckling is a consequence of the importance of leakage which accounts for approximately one-third of the neutron losses. Because of the importance of this factor, a substantial effort was made to determine an appropriate buckling, or set of bucklings, for the FNR.

The following methods for determining bucklings were developed and evaluated during the project:

- Calculate from core height and reflector savings
- Calculate to match experimental and calculated core eigenvalues
- Calculate to match eigenvalues in finite cylinder and infinite cylinder calculations of the FNR
- Calculate to match thermal flux profiles in infinite cylinder and finite cylinder calculations of the FNR
- Determine from 3-D assembly calculations
- Determine from results of 3-D full core diffusion calculation (VENTURE/3DB)

The last method is the preferred approach although some of the earlier methods were used in the initial phase of the project due to the lack of a 3-D capability. Table II-19 summarizes the results of all of these approaches. Details of these methods may be found in [Ker80] and [Ker81]. The following discussion pertains to the VENTURE/3DB 3-D

Table II-19. Buckling Calculations

Method	Buckling ($\times 10^{-3}cm^{-2}$)	Comments
Reflector Savings and Core Height	2.0 1.6	Thermal group constants only One group constants
Matching Eigenvalue (Exp. vs. Calc.)	2.0	June, 1977 critical experiment
Matching Power Distribution (Exp. vs. Calc.)	1.7 - 1.8	FNR Cycle 67
Matching Eigenvalue (R-Z vs. R)	1.72 1.14	Core and H_2O reflector D_2O reflector
Matching Thermal Flux (R-Z vs. R)	1.82 1.14	Core and H_2O reflector D_2O reflector
3-D Assembly Calculation	1.721 1.720 1.76	Heterogeneous Assembly: Lattice Non-lattice Homogenous Assembly
3-D Full Core Calculation	1.76 1.65 1.66 1.10	Core Center H_2O reflector D_2O reflector: Fast Flux Thermal Flux

full-core calculations to determine the transverse buckling for use in 2-D x-y calculations of the FNR using UM2DB.

Since the purpose of the transverse buckling is to account for the missing direction in a calculation with lower

dimensionality, an obvious approach is to perform the 3-D calculation and edit out the buckling directly from the 3-D flux distribution. This allows the determination of group- and zone-dependent bucklings, which can be input to UM2DB. This approach was taken using the VENTURE code (and later the UM3DB code) to determine a set of group-dependent bucklings that give good agreement between 2-D and 3-D calculations. The VENTURE axial geometry had 28 planes with 14 planes in the core region. The bucklings were edited by an integration over the central six core planes as illustrated in Figure II-22. Integration over this particular volume gave a slightly better agreement between 2-D and 3-D flux profiles at the core midplane and calculated core eigenvalues. The results of the 2-D and 3-D flux and eigenvalue calculations are compared in Table II-20.

Table II-20. 2-D vs. 3-D Flux and Eigenvalue Comparisons

Code	Geometry	RMS Deviation in Midplane Thermal Flux	Core Eigenvalue
VENTURE	X-Y-Z	Reference	1.0258
UM2DB	X-Y	0.10%	1.0256

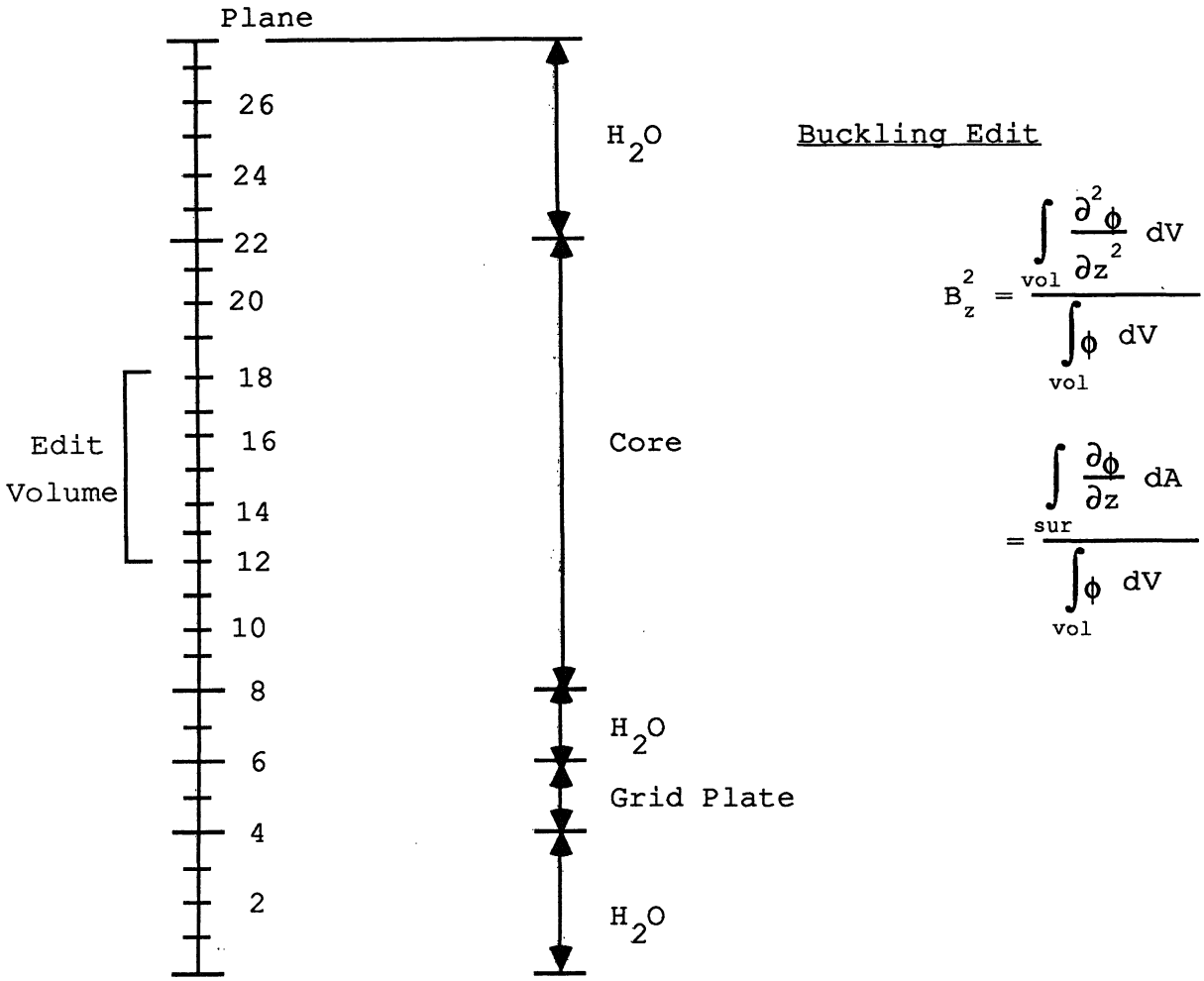

Figure II-22. Axial Geometry for 3-Dimensional VENTURE Calculation

These VENTURE generated bucklings were utilized as the reference bucklings for the UM2DB calculations until the middle of 1985, when the UM3DB code was used to generate a new set of bucklings. The reason for this effort was the relatively poor comparison between core eigenvalues predicted by UM2DB and UM3DB with one axial fuel burnup zone. This bias, approximately 0.4%, was thought to be due to an overestimation of the transverse bucklings. Using the procedure described above with the VENTURE code, the UM3DB code was used to generate a new set of bucklings for the June 8, 1983 LEU core. By using this new set of bucklings, the bias was reduced to less than 0.01%. Figure II-23 tabulates the transverse bucklings editted from the UM3DB calculation. This figure also appears as Figure B-2 in Appendix B.

Another set of axial bucklings was calculated from a UM3DB run for the May 29, 1982, HEU core (FNR cycle 212B) using the same procedures as above. Several calculations for the May 29, 1982 HEU core were performed using the UM3DB and UM2DB codes, and the results are presented in Table II-20. The results for the June 8, 1983 LEU core are also included in Table II-20 for the purpose of comparison.

For the UM3DB runs, the FNR core was represented with a 2x2 mesh per assembly in the x-y plane (a total of 38x34 meshes) and 31 axial meshes, including 14 meshes for the active fuel region. For the UM2DB runs, the FNR core was

Heavy Water (0.2~0.3m)			1.64 1.67				
Heavy Water (0.1~0.2m)			1.64 1.67				
Heavy Water (0~0.1m)			1.66 1.16	Aluminum (6mm)		1.66 1.07	
1.68 1.59	1.66 1.56	1.67 1.58	1.68 1.60	1.69 1.61	1.69 1.61	1.68 1.59	1.69 1.61
1.71 1.70	1.72 1.70	1.73 1.72	a 1.75 1.74	1.75 1.74	c 1.75 1.74	1.73 1.71	1.72 1.70
1.73 1.71	1.74 1.72	1.77 1.76	1.79 1.78	1.77 1.76	1.76 1.75	1.74 1.72	1.72 1.71
1.73 1.71	1.75 1.74	1.79 1.79	b 1.81 1.84	1.78 1.78	1.76 1.74	1.73 1.72	1.72 1.71
1.74 1.73	1.76 1.75	1.78 1.77	1.79 1.78	1.77 1.76	1.74 1.73	1.73 1.72	1.73 1.72
1.72 1.70	1.75 1.74	1.77 1.76	1.76 1.75	1.75 1.73	1.73 1.72	1.73 1.72	1.72 1.71

Water Reflector

1.71	
1.67	

Regular Element

Special Element

xx	Fast group ($10\ m^{-2}$)
xx	Thermal group ($10\ m^{-2}$)

Figure II-23. Axial Buckling Map for the FNR Core

Table II-21. Eigenvalue Comparison for the FNR Core

Method	Eigenvalues	
	5/29/82 HEU Core	6/8/83 LEU Core
UM3DB, 2x2 mesh/assembly	1.0519	1.0437
UM2DB, 2x2 mesh/assembly Bucklings from UM3DB	1.0517	1.0437
UM2DB, 2x2 mesh/assembly Bucklings from VENTURE	1.0491	1.0395
UM2DB, 6x6 mesh/assembly Bucklings from VENTURE	1.0461	1.0364

represented with a 2x2 or 6x6 mesh per assembly in the x-y plane (a total of 38x34 meshes or 72x70 meshes, respectively). As expected, the biases of 0.27% ~ 0.42% between the UM2DB and UM3DB eigenvalues were reduced to 0.02% or less.

A difference of approximately 0.30% between the UM2DB runs, with a 2x2 mesh per assembly and a 6x6 mesh per assembly, but with the same bucklings was due to different cross sections used for special fuel elements in the HEU and LEU cores. Cell-average cross sections from the UMLEO code were used for the 2x2 cases, while discrete cross sections from the HAMMER code were used for the 6x6 cases.

The UM2DB eigenvalues are compared in Table II-22 with improved axial bucklings for both the HEU and LEU cores, using a 6x6 mesh per assembly with assembly average fuel

Table II-22. UM2DB Eigenvalues for the FNR Core

Core	Measured ρ_{ex}(%Δk/k)	Eigenvalue		Absolute Bias (%Δk/k)	
		Bucklings from VENTURE	Bucklings from UM3DB	Bucklings from VENTURE	Bucklings from UM3DB
Dec., 1981 Critical LEU	0.45	1.0039	1.0079	-0.29[1]	0.10[1]
May, 1982 Full Power HEU	3.29	1.0498	1.0524	1.33[1]	1.56[2]
March, 1983 Critical Mixed	0.10	1.0136	1.0163	1.01[1]	1.28[1]
June, 1983 Critical LEU	0.00	1.0047	1.0085	0.11[1,2]	0.48[1,2]
June, 1983 Full Power LEU	3.29	1.0365	1.0406	0.10[1,2]	0.48[1,2]
Oct., 1983 Full Power Mixed	3.02	1.0399	1.0427	0.68[2]	0.94[2]

[1] Corrected for power defect of 0.23% Δk/k
[2] Corrected for samarium reactivity worth of 0.13% Δk/k

burnups estimated through direct UM2DB depletion runs. In determining the absolute bias between the calculated and measured eigenvalues, some minor corrections were made for power defect and samarium reactivity worths. For mixed core configurations, the HEU bucklings were used. Table II-22 indicates that there still remains a substantially higher eigenvalue bias for the configurations containing highly depleted HEU fuel elements than for LEU configurations with fresh or slightly depleted fuel elements.

3. Lumped Fission Product Correlation

As a means to account for the poisoning effect of fission products easily and efficiently, the UMLEO code calculates lumped fission product cross sections at each burnup step. The cross sections, expressed in terms of barns per fission, represent the sum of the cross sections in all individual fission product nuclides except ^{135}Xe and ^{149}Sm, which are handled explicitly in UMLEO. The aggregate cross section for the thermal group is determined with a third order polynomial in fuel burnup. In the fast energy range, only the epithermal (group 3) cross section is considered, again with a polynomial that is second order in burnup. These empirical correlations originally in UMLEO were intended for only slightly enriched fuel (approximately 3%), and were originally used in FNR neutronic analyses for the FNR with a crude adjustment to account for the higher enrichment of the

LEU and of HEU fuels. This adjustment was to scale the burnup used in the empirical correlation by the ratio $\varepsilon/3.0$, where ε is the enrichment to be used with UMLEO (e.g., 93) and 3.0 corresponds to the slightly-enriched fuel that the original correlation is predicated upon. This accounts for the first-order effect due to the convention that burnup is given in terms of energy per metric tonne of total uranium, but does not account for the differences in the fission product yield for HEU, LEU, and slightly-enriched LWR fuel.

In an effort to verify and improve the calculation of the lumped fission product cross section, the EPRI-CINDER code [Eng76] was used. The EPRI-CINDER code calculates fission product concentrations, effective cross sections, and other quantities based upon fuel composition, fluxes and power level with a point isotopic depletion model. The user chooses between two options, an 84-chain fission product library and a 12-chain fission product library. The 12-chain library accounts for the eleven most predominant chains and creates a 12th "effective" fission product chain to account for the remaining chains. The 12-chain library is intended for use in spatial depletion calculations and in general, gives results almost identical to the 84-chain library, except for calculated effective resonance integrals.

The code has been modified to run on the Amdahl computer at the University of Michigan. Originally written for a CDC

6600 machine, the code requires a greater exponent capacity than the Amdahl permits. The algorithm used to calculate the nuclide concentrations includes intermediate products which are accumulated over several nuclides. These products become so small as to be outside the limits of the machine (underflow/overflow). Since the algorithm is complicated by extensive roundoff controls, the simplest solution was to multiply the time step length, power and decay constants by a (very large) constant factor as soon as they are read as input. Thus, the intermediate quantities become manageable while the calculated number density remains unchanged.

To determine the accuracy of this 'fix', sample cases have been run using the unaltered code on the CDC 6600 at Michigan State University through the MERIT computer network. The results of these cases have been compared with the results of identical cases run with the modified code. In addition, comparisons between the altered code and summary tables printed in the EPRI-CINDER code manual have been made. Small differences occurred in several quantities, none greater than 0.2% in magnitude, while other results were unchanged.

Simulation of PWR fuel with 2.6% ^{235}U by both the EPRI-CINDER and UMLEO codes indicates significant disagreement in the fission product cross sections obtained by the two codes. The value calculated by the UMLEO code for the epithermal absorption cross section, σ_3, is nearly

50% greater at the beginning of life and 20% greater after a fuel burnup of 20,000 MWD/tonne, compared with EPRI-CINDER values. The thermal absorption cross section σ_0, for neutron energy of 0.025 eV, shows even larger disagreement -- nearly 60% over the entire depletion history.

Comparison of results from the original CINDER code [Eng62] (the predecessor to EPRI-CINDER), EPRI-CINDER and UMLEO simulations of 3.4% enriched PWR fuel indicates that the correlation incorporated into the UMLEO code was probably based upon calculations with the original CINDER code or a program similar to it. The CINDER and UMLEO results agree quite well with one another but not with those of EPRI-CINDER. The EPRI-CINDER results, with an ENDF/B-IV database for fission products, are expected to be more accurate than the old CINDER calculations. This has been verified by an EPRI-CINDER simulation of a detailed experiment [Gun75] performed to measure the fission product poisoning in ^{233}U fuel irradiated in the Material Testing Reactor. The EPRI-CINDER results agree fairly well with the experimental data. Figures II-24 and II-25 show the experimental and calculated values for the fission product resonance integral and thermal absorption cross section, respectively, as a function of irradiation time.

As in the case of the PWR type fuel calculations, the simulation of the four primary FNR fuel types -- HEU and LEU,

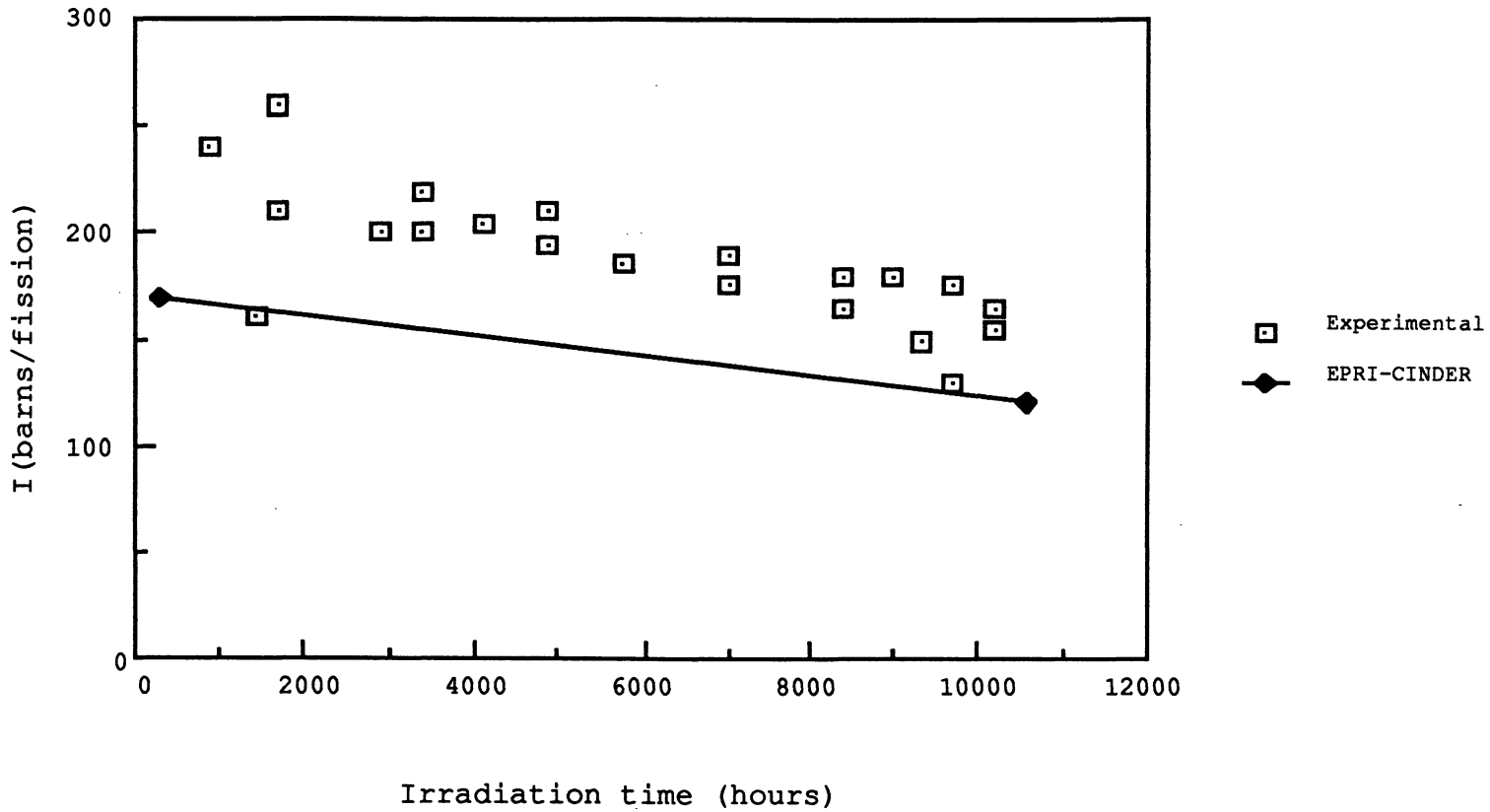

Figure II-24. Lumped Fission Product Resonance Integral for U-233.

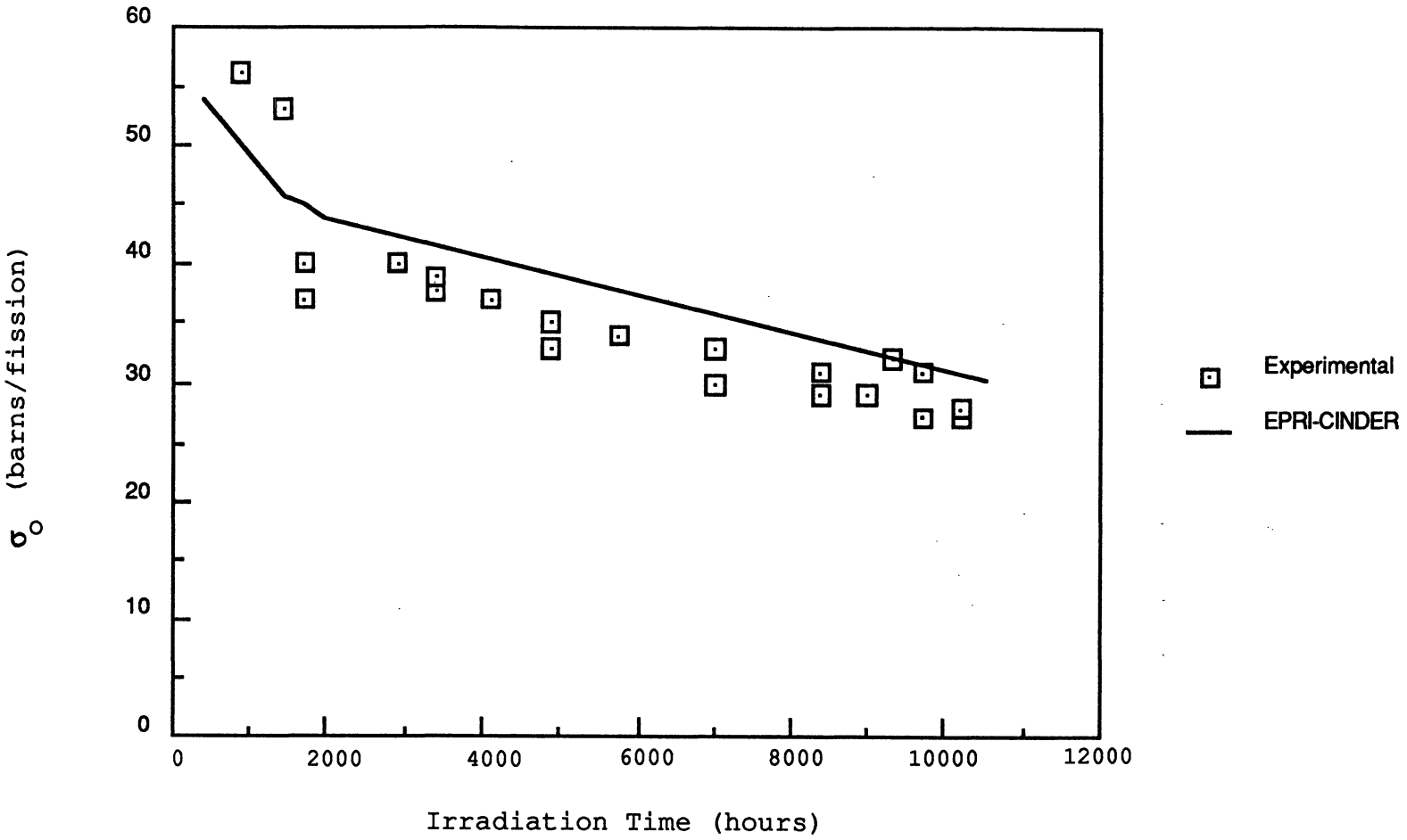

Figure II-25. Lumped Fission Product Thermal Absorption Cross Section for U-233.

regular and special fuel elements -- by the two codes, UMLEO and EPRI-CINDER, yield significant disagreement in the calculated fission product cross sections as seen in Figures II-26 through II-29. Note that the UMLEO correlation used produces only one curve for each enrichment, whether for a special or regular fuel element. The UMLEO cross sections are larger than the EPRI-CINDER results, as much as 90% in the case of the HEU regular fuel element. Because of this drastic discrepancy, new UMLEO lumped fission product cross section correlations have been formulated based on the results of the EPRI-CINDER code.

In the new fission product correlations for the UMLEO code, cross sections are correlated as a function of fuel burnup, where burnup is given in units of MWD/tonne of ^{235}U rather than the traditional units of MWD/tonne of uranium. This yields more precise and more flexible correlations than with the traditional definition for burnup, and the same correlation can be used for both HEU and LEU fuel. Figures II-26 through II-29 plot fission product absorption cross sections for all four groups versus fuel burnup in MWD/tonne of ^{235}U.

The actual correlations in the form of polynomials were derived from the burnup-dependent absorption cross sections plotted in the figures. In the case of the fast group cross sections, σ_1, σ_2 and σ_3, the data for all four fuel types

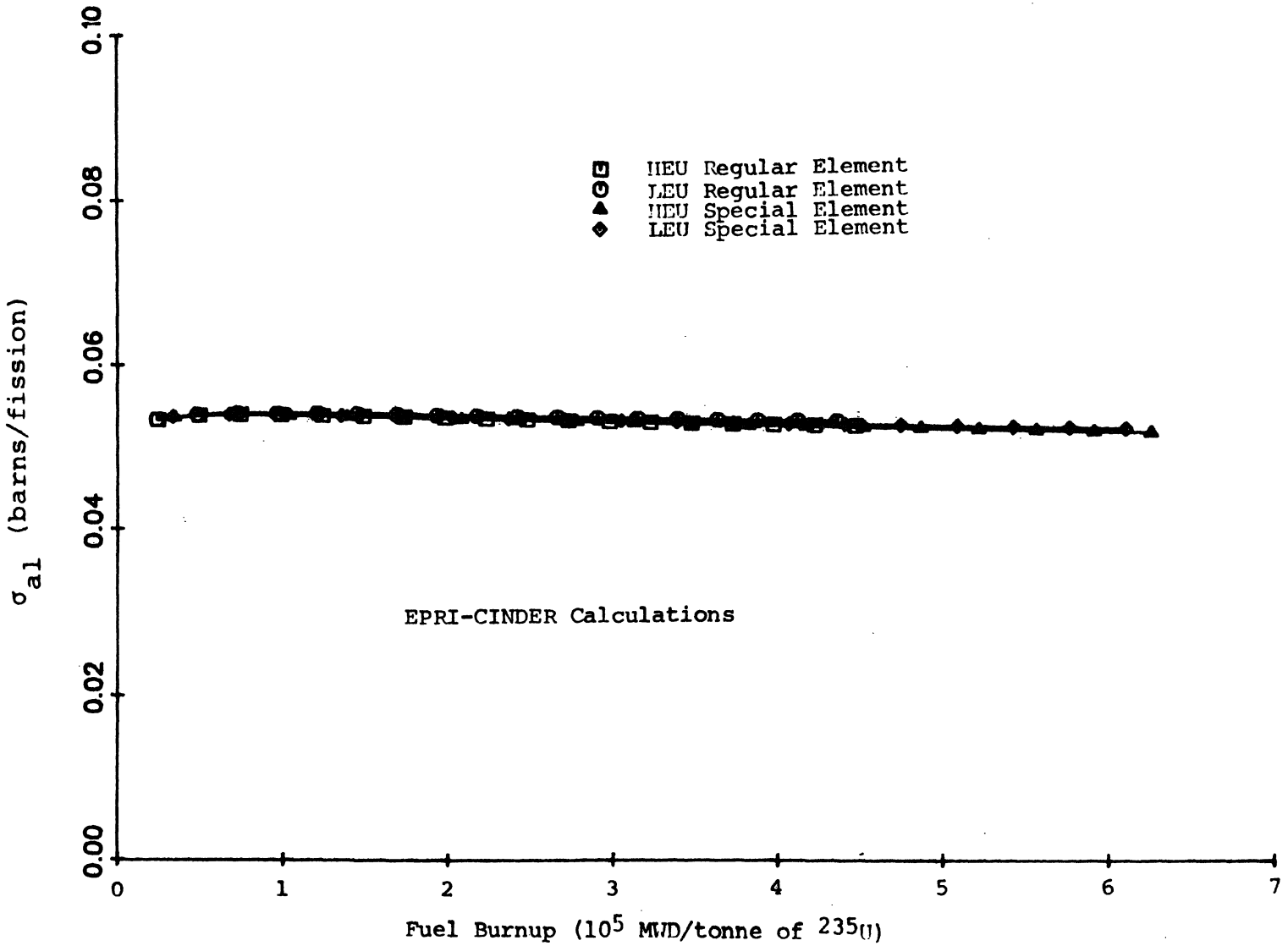

Figure II-26. Fission Product Absorption Cross Section - Group 1.

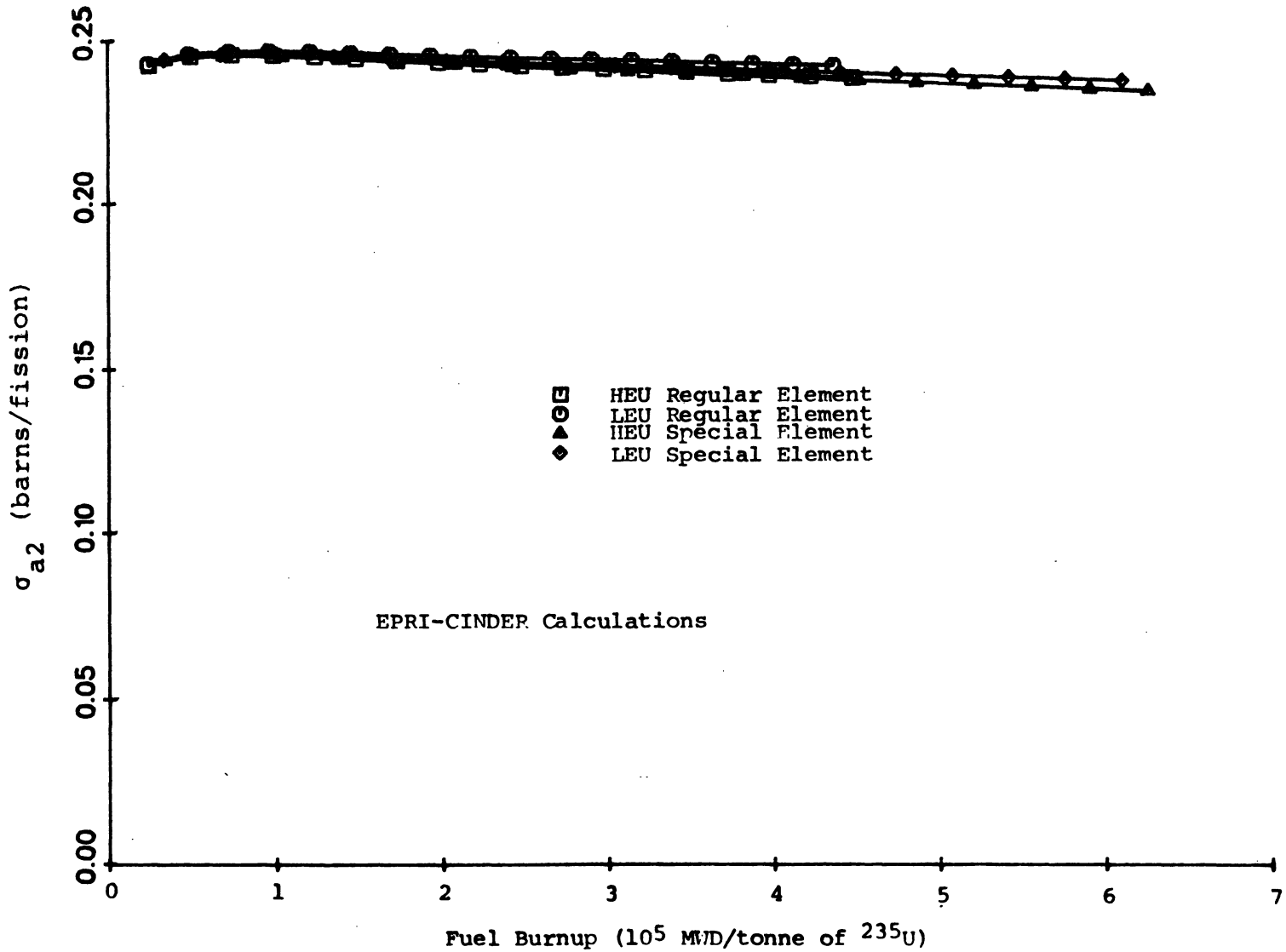

Figure II-27. Fission Product Absorption Cross Section - Group 2.

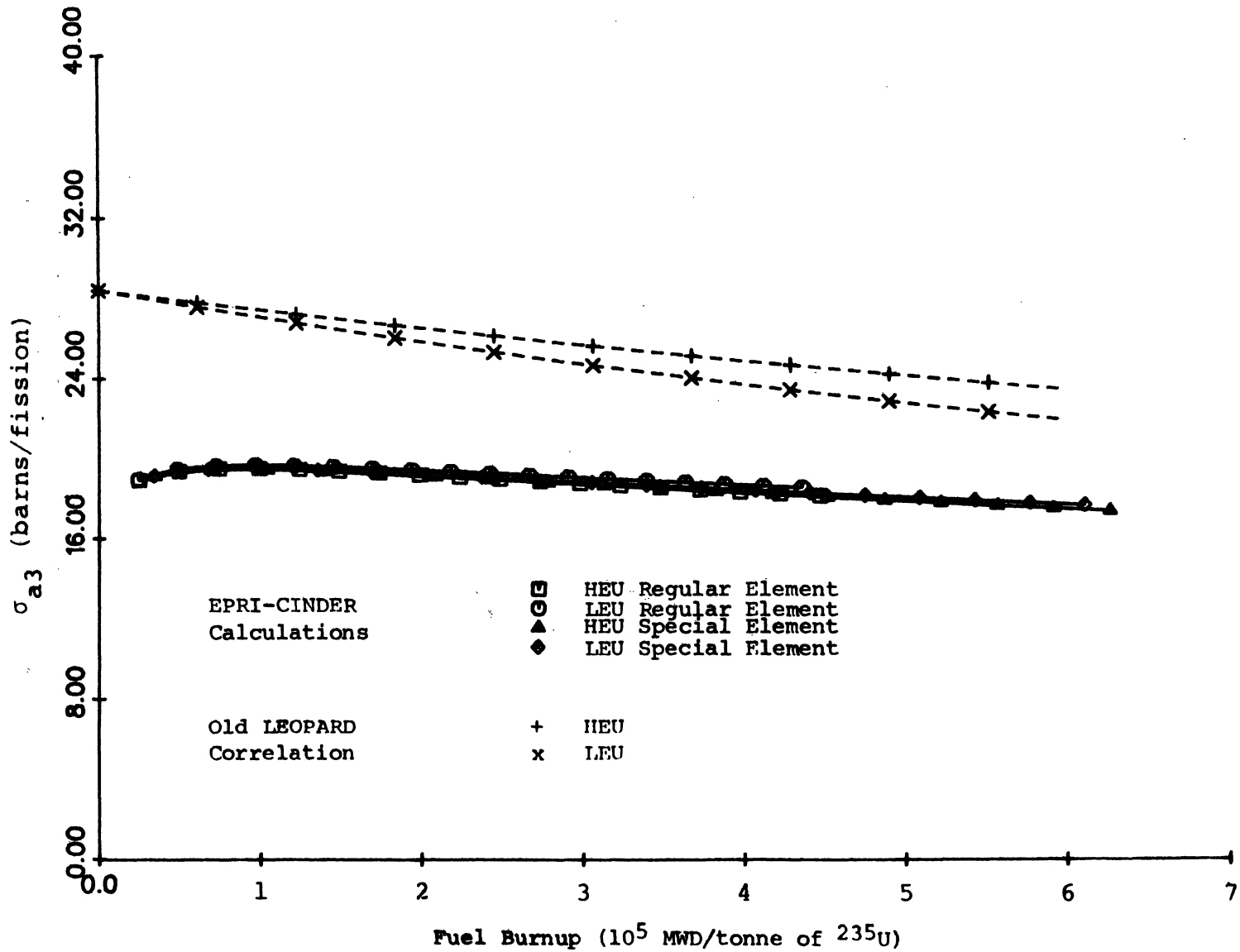

Figure II-28. Fission Product Absorption Cross Section - Group 3.

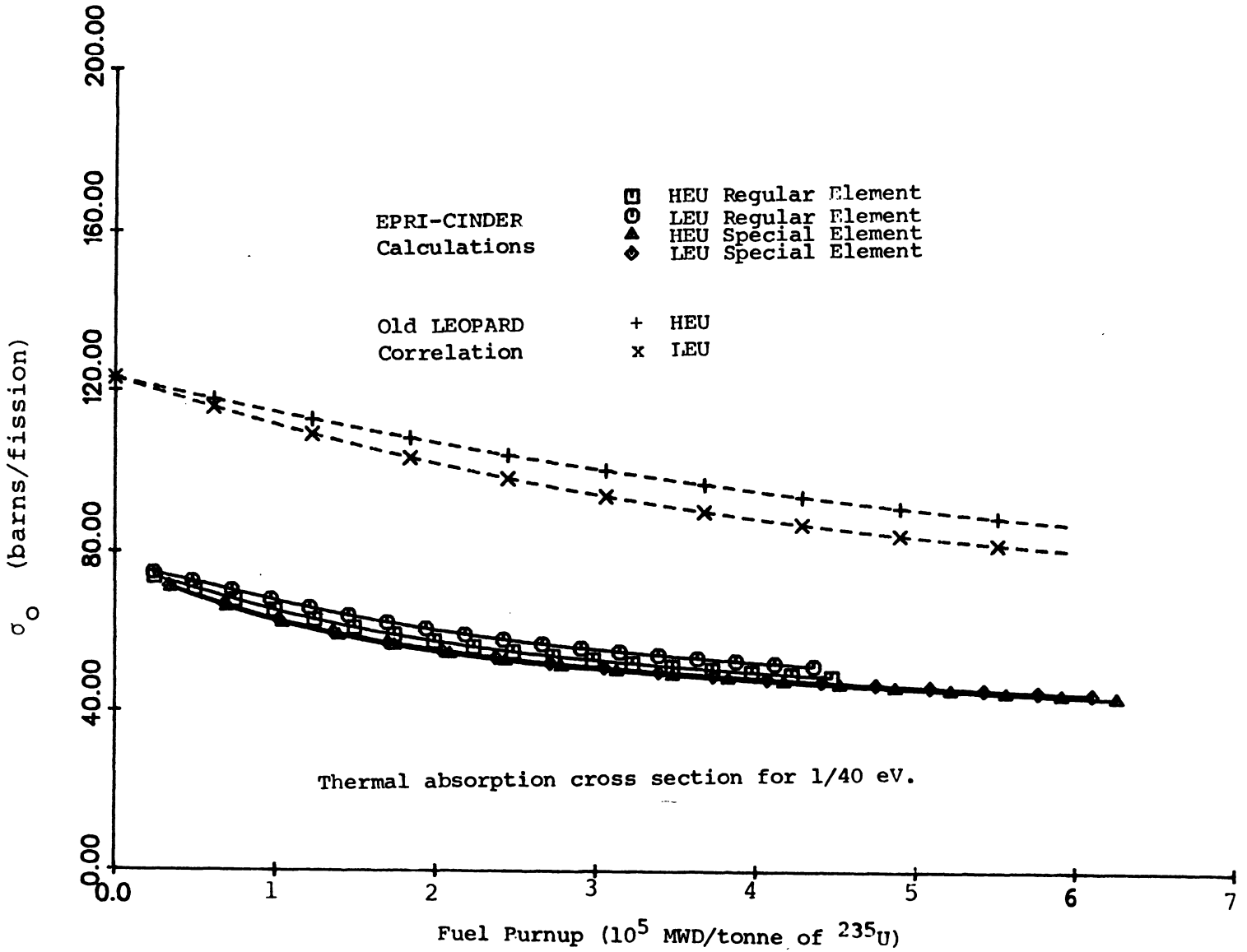

Figure II-29. Fission Product Absorption Cross Section - Group 4 (Thermal).

were used together to derive a single correlation for each group. For the thermal cross section, σ_0, because the differences between the fuel types are relatively large, only the data for the HEU special fuel element were used to correlate the burnup dependence.

Another correlation to represent the differences between fuel types was derived by taking advantage of the different amounts of fuel and water present in the various fuel types. This correlation takes the form:

$$\sigma_0(r) = \sigma_{0,HS}\, C_1 \{1 + C_2 \exp(-C_3 r)\}$$

where r is the ratio of the number density of hydrogen atoms to that of ^{235}U atoms in the unit cell at the beginning of life and $\sigma_{0,HS}$ is the thermal cross section for the HEU special fuel element obtained as a polynomial in fuel burnup units of MWD/tonne of ^{235}U. The constants C_1, C_2 and C_3 are determined by using the values for σ_0 for the four fuel types at a burnup of 100,000 MWD/tonne of ^{235}U. The lumped fission product correlations derived in our study are simple but sufficiently accurate. The maximum deviation between the correlations and the EPRI-CINDER results is observed to be about 4% for low fuel burnup (where the resultant cross section is also small) for the LEU regular element, with the deviations usually less than 1% for all four groups and four

fuel types.

With the new fission product correlations, UMLEO calculations were performed to generate few-group constants for the UM2DB code. Comparison of the eigenvalues calculated by the UM2DB code with those of the identical test cases with a library utilizing the old burnup correlation indicates the effect is small but significant. The test case simulated the June 1977 HEU critical experiment, with the old correlations yielding an eigenvalue of 1.0139 compared with a value of 1.0182 obtained with the new correlations.

The HEU and LEU batch core depletion tests illustrate the differences more completely, for fuel depletion is the basis of the correlation. The difference in the eigenvalue for the two correlations increases almost linearly with fuel depletion. The eigenvalues with the new correlations are greater than those with the old as a consequence of the overprediction in the absorption cross sections by the old correlations. At the end of life at 200 days depletion, the differences amount to 0.68% for the HEU and 0.54% for the LEU core.

The new UMLEO fission product correlations duplicate the EPRI-CINDER results quite well for the four FNR fuel types analyzed, thus eliminating a known deficiency of the UMLEO code. The overall effect of the new lumped fission product

correlation on the infinite medium multiplication factor for HEU fuel can be seen in Figure II-30.

4. Ex-Core Cross Section Generation

This section of the report describes the calculation of the ex-core cross sections used for the analysis of the FNR HEU and LEU cores. Section II.B.1 described the original method for determining ex-core cross sections with the UMLEO code as used in the early phase of the project. It was found later that the in-core and ex-core power distributions as well as the core eigenvalue depend sensitively upon the values used for the heavy-water tank cross sections, so this work was begun to determine more accurate ex-core cross sections by means of a one-dimensional transport code calculation with the XSDRN code [Gre69].

The structure of the heavy water tank is complicated by numerous beam tube void cans and cylindrical penetrations filled with light water [Ker80]. The calculation of the core power distributions with the UM2DB code requires region averaged, 2-group cross sections for each of the ex-core zones.

The region-averaged cross sections have been determined by means of several codes in the SCALE package [Wes80], including CSAS, NITAWL and XSDRN. The CSAS code is used initially to set up the input for the remaining codes in the package. The geometrical configuration of the problem is

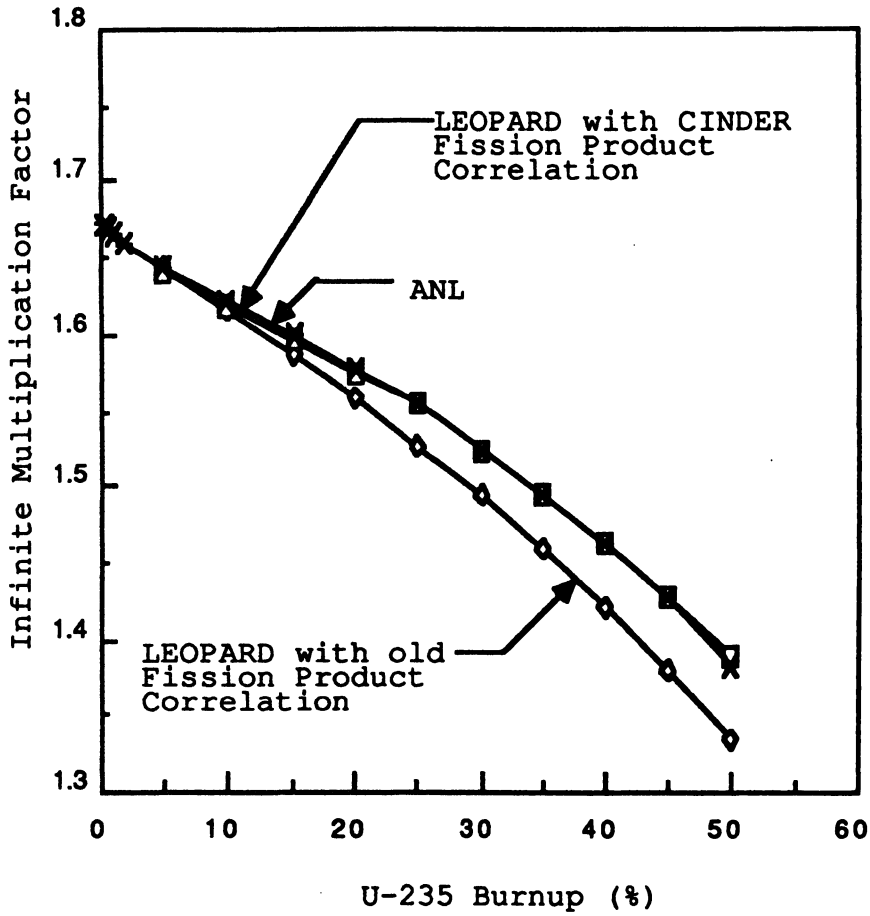

Figure II-30. Infinite Medium Multiplication Factor for HEU Fuel versus U-235 Burnup

shown in Figure II-31. In the core region, the core is homogenized by volume averaging the number densities for batch HEU and batch LEU cores from the data given in Table C-2 of [Ker81]. The core and reflector regions are then modelled in one-dimensional slab geometry, as is shown in Figure II-31. A 38.1 cm region of light water simulates the reflector region on the south side of the core. The core region consists of a homogenized mixture of LEU or HEU fuel, clad and moderator, with a thickness corresponding to five rows of fuel elements in the north-south direction. The water gap between the core and the heavy water tank and the aluminum wall of the heavy water tank are also represented. The heavy water tank is approximately modelled by dividing it into three zones of equal volume, and voids are homogenized into the zones. The actual void fractions for the three heavy water zones in the south-north direction are 0.126, 0.090 and 0.058, respectively. This three zone model of the heavy water tank was used to account more accurately for the spatial distribution of the voids, and to account for the spatial dependence of the neutron spectrum, which depends very sensitively on distance into the D_2O tank. The light water reflector on the north side of the core is included as a 20cm region of light water. The cylindrical light water

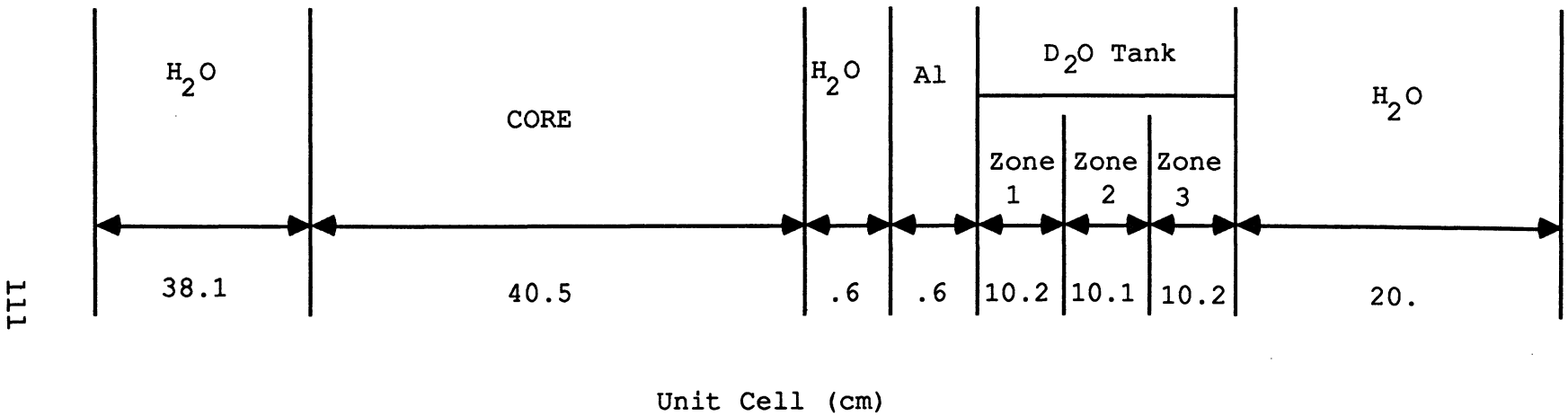

Figure II-31. D_2O-Core Geometry Used in XSDRN Calculation

penetrations into the heavy water tank are neglected in the generation of average cross sections for the heavy water tank.

The NITAWL code is used to perform the resonance calculations for the uranium isotopes by means of the Nordheim Integral Treatment. The NITAWL code also processes the master cross section libraries into a format accessible by the XSDRN code, the one-dimensional discrete ordinates transport theory code. The master library contains 123 energy groups -- 93 fast groups and 30 thermal groups.

The spectral calculations and cross section weighting are performed by the XSDRN code, with the geometry of Figure II-31. A P-3, S-8 calculation is performed in 123 energy groups with a total of 35 spatial meshes, including 12 meshes in the core and 9 meshes in the heavy water tank. Transverse leakage is accounted for with a geometric buckling. XSDRN determines weighted cross sections by spectrally and spatially weighting the microscopic cross sections for each isotope for each spatial zone of the problem. The group structures are defined as follows. For the 2-group cross section generation, group 1 extends from 14.92 MeV to 0.6552 eV, and group 2 extends from 0.6552 eV to 0.004742 eV. For the 4-group cross section generation, group 1 extends from 14.92 MeV to 820.9 KeV, group 2 from 820.9 KeV to 5.531 KeV,

group 3 from 5.531 KeV to 0.6552 eV, and group 4 from 0.6552 eV to 0.004742 eV.

The XSDRN code produces fine-group transport cross sections by integrating the P-1 component of the scattering cross section over the current as follows:

$$\sigma_{tr}(E) = \sigma_t(E) - \frac{\int_0^\infty dE' \, \sigma_1(E' \rightarrow E) J(E')}{3J(E)}$$

A zone-averaged leakage spectrum is defined as follows for the determination of the fine- and coarse-group transport cross sections:

$$L_{j,g} = \int_j d\underline{r} \int_g dE \, L(\underline{r}, E) / V_j$$

where g is the fine group index, V_j is the volume for zone j and $L(\underline{r},E)$ is the leakage spectrum calculated by the code. Coarse-group transport cross sections are then determined for each zone j by weighting the fine group transport cross sections over the leakage spectrum as follows:

$$\sigma_{tr,G} = \frac{\sum_g L_g \sigma_{tr,g}}{\sum_g L_g}$$

where g is the coarse group index and the sum is taken over all of the fine groups contained in the coarse group.

Macroscopic reflector cross sections are then determined for input to the UM2DB code by multiplying the microscopic

cross sections by the appropriate number densities for each zone. The 2-group cross sections for the ex-core regions computed with the XSDRN code are compared with those calculated with the UMLEO code in Table II-23.

Several differences can be noted in the cross section comparisons given in Table II-23. The fast group absorption cross sections for aluminum, light water and heavy water are significantly overpredicted by the old UMLEO library. The use of the ENDF/B-IV library with the UMLEO code has improved results for aluminum and light water, but UMLEO is still inaccurate in computing heavy water cross sections. The fast group absorption cross section is over predicted by an order of magnitude by the UMLEO code. This is partly due to the inclusion of voids in the XSDRN calculations, and partly due to the spatial dependence of the spectral effects, which cannot be adequately modelled with the UMLEO code. The XSDRN downscatter cross section for heavy water was found to be strongly dependent on the flux spectrum, and much larger than the UMLEO results.

The decrease in the fast absorption cross section of heavy water and the increase in the downscatter cross section of heavy water led to a change in the thermal flux distribution in the heavy water tank, as can be seen in Figure II-32. The thermal flux peak is significantly

Table II-23. 2-Group Ex-Core Cross Section Comparison (cm^{-1})

Zone	Code	Group 1			Group 2		
		Σ_a	Σ_{tr}	$\Sigma_{s,g-1\rightarrow g}$	Σ_a	Σ_{tr}	$\Sigma_{s,g-1\rightarrow g}$
HEU, Aluminum	LEO OLDLIB	7.803E-4 [1]	.1138	0.0	9.556E-3	.09088	5.515E-5
	LEO ENDF/B-IV	3.498E-4	.1085	0.0	9.586E-3	.08780	1.463E-4
	XSDRN 123 GP	3.933E-4	.1164	0.0	1.051E-2	.09367	2.296E-4
HEU, Light Water	LEO OLDLIB	8.691E-4	.2776	0.0	.01853	2.112	.05267
	LEO ENDF/B-IV	4.914E-4	.2932	0.0	.01830	2.073	.05314
	XSDRN 123 GP	5.372E-4	.2726	0.0	.01845	2.867	.05963
HEU, Heavy Water	LEO OLDLIB	4.698E-4	.1803	0.0	6.651E-5	.3075	5.465E-3
	LEO ENDF/B-IV	3.312E-4	.1823	0.0	6.535E-5	.2957	5.473E-3
	XSDRN 0-10cm	5.785E-5	.2045	0.0	5.817E-5	.3373	6.746E-3
	XSDRN 10-20cm	4.084E-5	.2265	0.0	6.222E-5	.3528	1.113E-2
	XSDRN 20-30cm	4.286E-5	.2416	0.0	6.668E-5	.3682	1.568E-2
LEU, Aluminum	LEO OLDLIB	7.719E-4	.1141	0.0	1.041E-2	.09172	4.844E-5
	LEO ENDF/B-IV	3.528E-4	.1088	0.0	1.051E-2	.08872	1.317E-4
	XSDRN 123 GP	3.847E-4	.1169	0.0	1.043E-2	.09355	2.169E-4
LEU Light Water	LEO OLDLIB	7.415E-4	.2636	0.0	.01781	2.009	.04738
	LEO ENDF/B-IV	4.318E-4	.2760	0.0	.01781	1.992	.04731
	XSDRN 123 GP	5.320E-4	.2704	0.0	.01841	2.869	.05856
LEU, Heavy Water	LEO OLDLIB	4.721E-4	.1800	0.0	6.513E-5	.3058	5.391E-3
	LEO ENDF/B-IV	3.335E-4	.1820	0.0	6.467E-5	.2947	5.388E-3
	XSDRN 0-10cm	5.814E-5	.2044	0.0	5.768E-5	.3366	6.514E-3
	XSDRN 10-20cm	4.080E-5	.2265	0.0	6.217E-5	.3517	1.103E-2
	XSDRN 20-30cm	4.275E-5	.2417	0.0	6.633E-5	.3672	1.565E-2

[1] Read as 7.803×10^{-4}

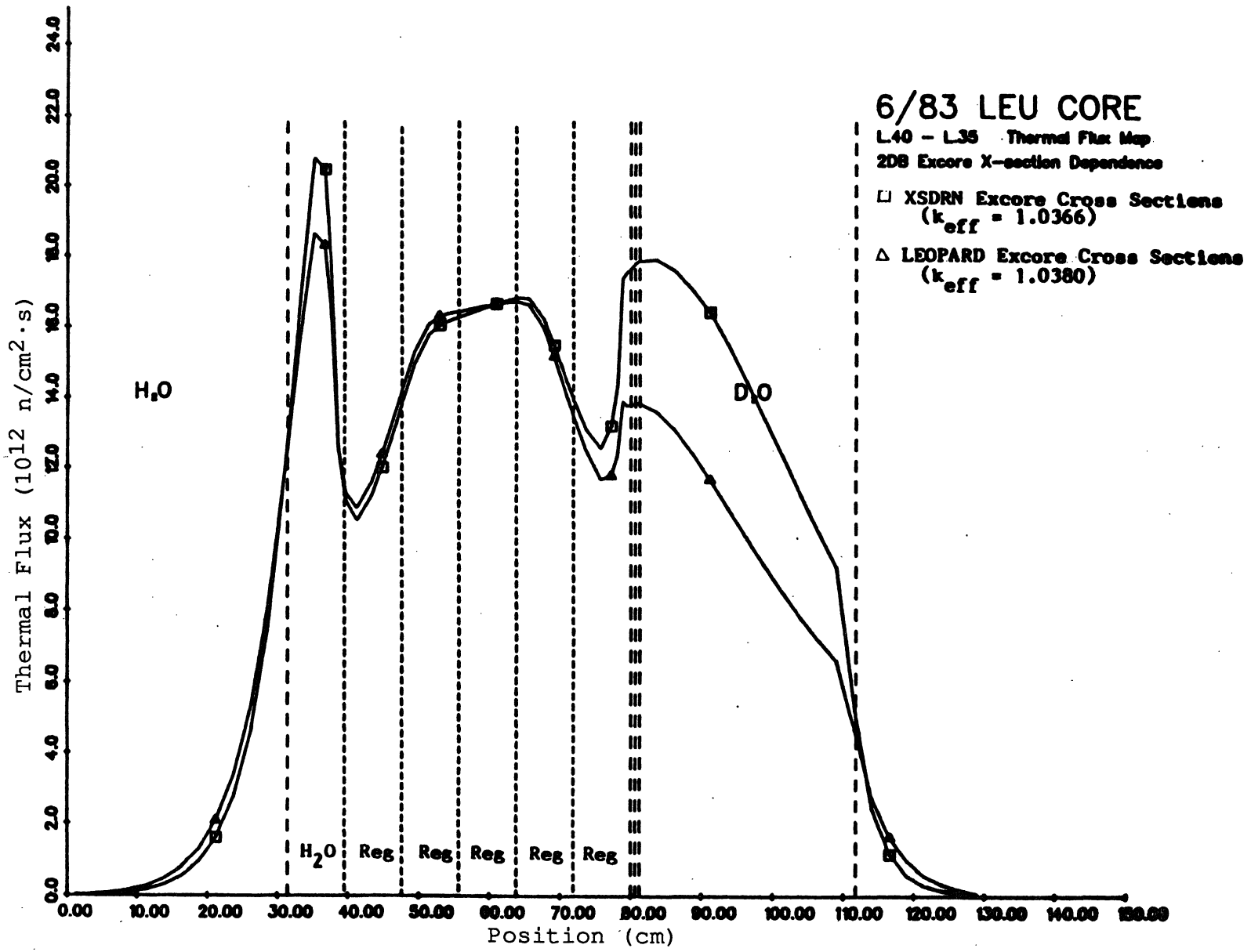

Figure II-32. D_2O-Core Thermal Flux Distribution

larger in the D_2O tank when the XSDRN cross sections are used in the UM2DB calculations.

5. Effective Delayed Neutron Fraction

This section describes the methodology for calculation of the effective delayed neutron fraction, β_{eff}, for the FNR core. Three different methods were used in this study: a) first order perturbation theory, b) eigenvalue method, and c) non-leakage probability method. The eigenvalue method is based on the work of Kaplan and Henry [Kap60] and the application of this method to the FNR configuration is described in [Mor81,Ker81].

The third method [Coo62] involves writing the non-leakage probability, P_f, of fission neutrons as:

$$P_f = (1-\beta)P_p + \beta P_d$$

where β is the actual delayed neutron fraction and P_p and P_d are the respective probabilities that the prompt and delayed neutrons will not escape while slowing down. Substituting this equation into the time-dependent diffusion equation for the neutron scalar flux ϕ including the precursor balance equations, and taking the inner product of the terms in the resulting equations with the adjoint flux, ϕ^*, we obtain:

$$\beta_{eff} = \beta\langle\varphi^*, P_d R\phi\rangle / \langle\phi^*, P_f R\phi\rangle$$

where < > indicates an integral over the reactor and R is the production operator. Since the term $R\phi$ is proportional to power, the ratio of the inner products can be interpreted as the ratio of the probability of non-leakage of delayed neutrons from the core region to the corresponding non-leakage probability for any fission neutrons. Thus, β_{eff} can be obtained as:

$$\beta_{eff} = \beta \langle P_d \rangle / \langle P_f \rangle$$

Two-dimensional calculations for FNR configurations indicate that method (a) with four energy groups, underpredicts β_{eff} by 2~3% compared with methods (b) and (c). The results from the latter two methods are in agreement with one another to within 1%. To resolve the difference between method (a) and methods (b) and (c), further effort was undertaken to perform first order perturbation calculations with a larger number of energy groups. By modifying the UMLEO code, six-group cross sections were obtained, with the second and third groups in the standard UMLEO structure replaced by four groups. A first order perturbation calculation with the six-group cross sections indicates a reduction, by a factor of two, of the difference noted earlier in the β_{eff} values calculated.

The values of β_{eff}/β calculated for several FNR configurations are summarized in Table II-24. In addition to showing the differences due to different calculational methods, Table II-24 also indicates that the ratio of β_{eff}/β decreases as the core size increases. Direct eigenvalue or non-leakage probability calculations with a perturbed fission spectrum, accounting explicitly for the delayed neutron spectrum, have not been performed for the 39 element equilibrium core configurations. For both the HEU and LEU configurations, in this case, first order perturbation theory calculations only were performed. Based on comparisons between the perturbation theory and eigenvalue results obtained for the batch core configurations, values of the correction factor, β_{eff}/β, obtainable with the eigenvalue method were estimated to be 1.139 and 1.132 for the HEU and LEU equilibrium core configurations, respectively. Based on calculations performed to date, the effective delayed neutron fraction for the LEU core is expected to be slightly smaller than the corresponding value for the HEU core.

Table II-24. Effective Delayed Neutron Fraction for the FNR

Core Configuration	Calculational Method	Number of Groups	β_{eff} / β
25 element HEU batch core	perturbation	4	1.136
	eigenvalue	2	1.164
	non-leakage probability	2	1.154
31 element HEU batch core	perturbation	4	1.123
	perturbation	6	1.136
	eigenvalue	2	1.153
	non-leakage probability	2	1.144
39 element HEU equilibrium	perturbation	4	1.114
	eigenvalue*	2	1.139
39 element LEU equilibrium	pertubation	4	1.107
	eigenvalue*	2	1.132

* Estimated value

6. Fuel Cycle Calculations

•Batch and Equilibrium Core Models

To provide meaningful and comprehensive comparisons of HEU and LEU fuels, it is necessary to model both the intrinsic fuel properties and the FNR operating conditions. For this purpose, two core configurations were analyzed for both fuels. The first configuration is a batch core consisting of fresh fuel assemblies, while the second configuration is an equilibrium core. The batch core configuration allows a comparison of undepleted HEU and LEU fuels fresh cores at beginning-of-life (BOL) as well as a comparison of average depletion effects obtained by depleting the batch core with no fuel shuffling. The equilibrium core allows comparison of depletion characteristics and shutdown margin for conditions typical of FNR operation, where fuel shuffling takes place every week or so. The batch core model illustrated in Figure II-33 has 31 fresh regular fuel elements, and four fresh special fuel elements without control rods. The configuration is symmetric about the north-south midplane and was analyzed using a half-core model.

Although the FNR core configuration and fuel shuffling pattern are, in practice, determined by operational requirements, an equilibrium core model was developed to

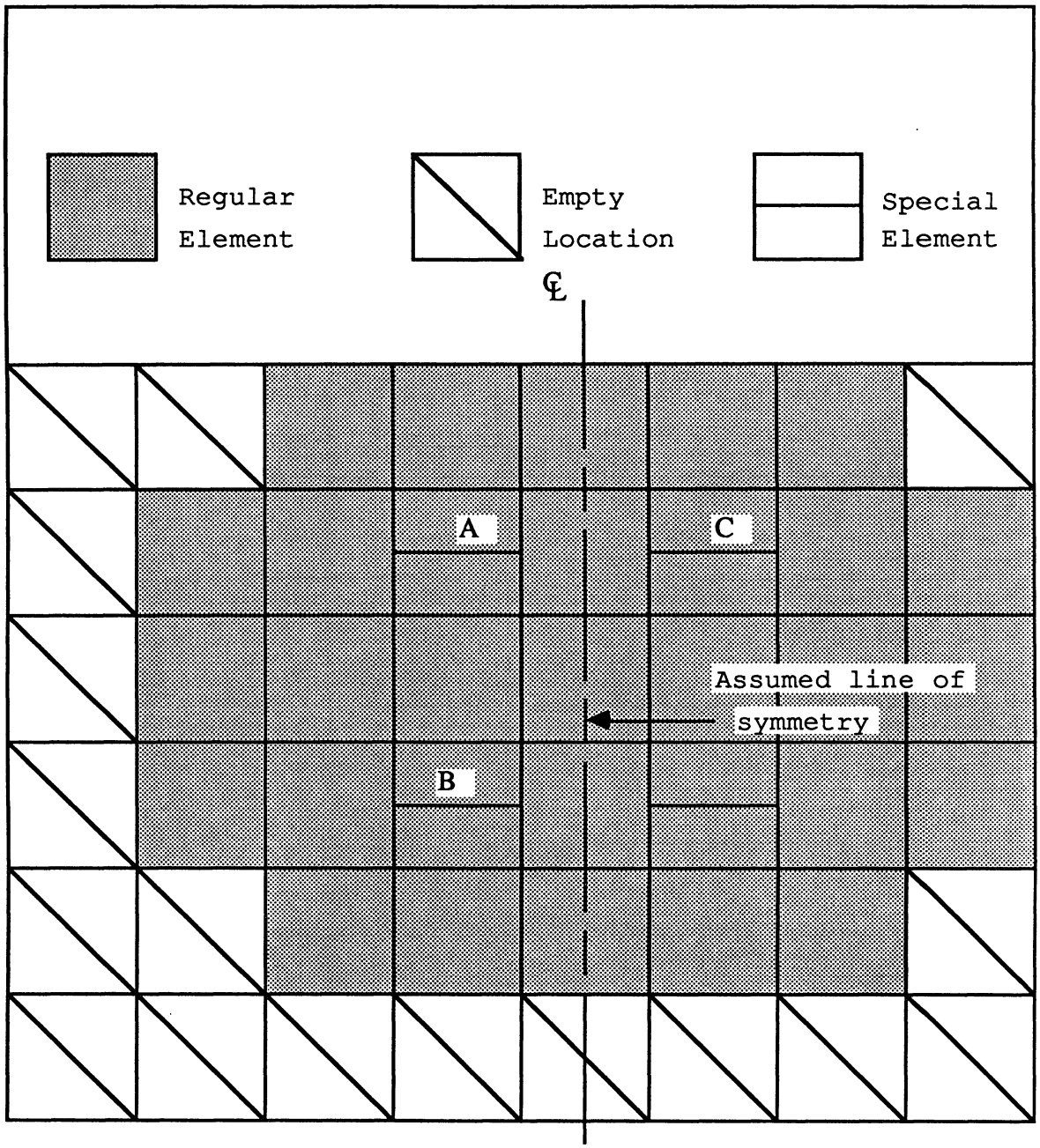

Figure II-33. Batch Core Configuration

allow a meaningful comparison of operating characteristics for the HEU and the LEU cores. The equilibrium core shown in Figure II-34 uses an in-out shuffling scheme with fresh elements loaded at the core center and moved outward as they deplete. This scheme maximizes the reactivity worth at the core center, thus maximizing the control rod worth to achieve the required 2.5% $\Delta k/k$ shutdown margin. To compare different fuel types in the equilibrium core, the end-of-cycle (EOC) k_{eff} was preserved between different cases. Preserving EOC k_{eff} provides the most realistic comparison of different fuel types because it attempts to model actual FNR operation where a core is depleted until the shim rods are nearly fully withdrawn. Along with preserving the EOC k_{eff}, the core size is also maintained constant. These two criteria essentially determine the maximum fuel burnup for a given fuel design. To achieve any higher burnup would require that the core size be increased in order to maintain criticality. Once the maximum fuel burnup is determined by preserving k_{eff} with a fixed core size, calculations must be performed to verify that the core configuration has the required 2.5% $\Delta k/k$ shutdown margin. Although the fuel burnup and power distribution are roughly constant during each equilibrium cycle, our equilibrium core

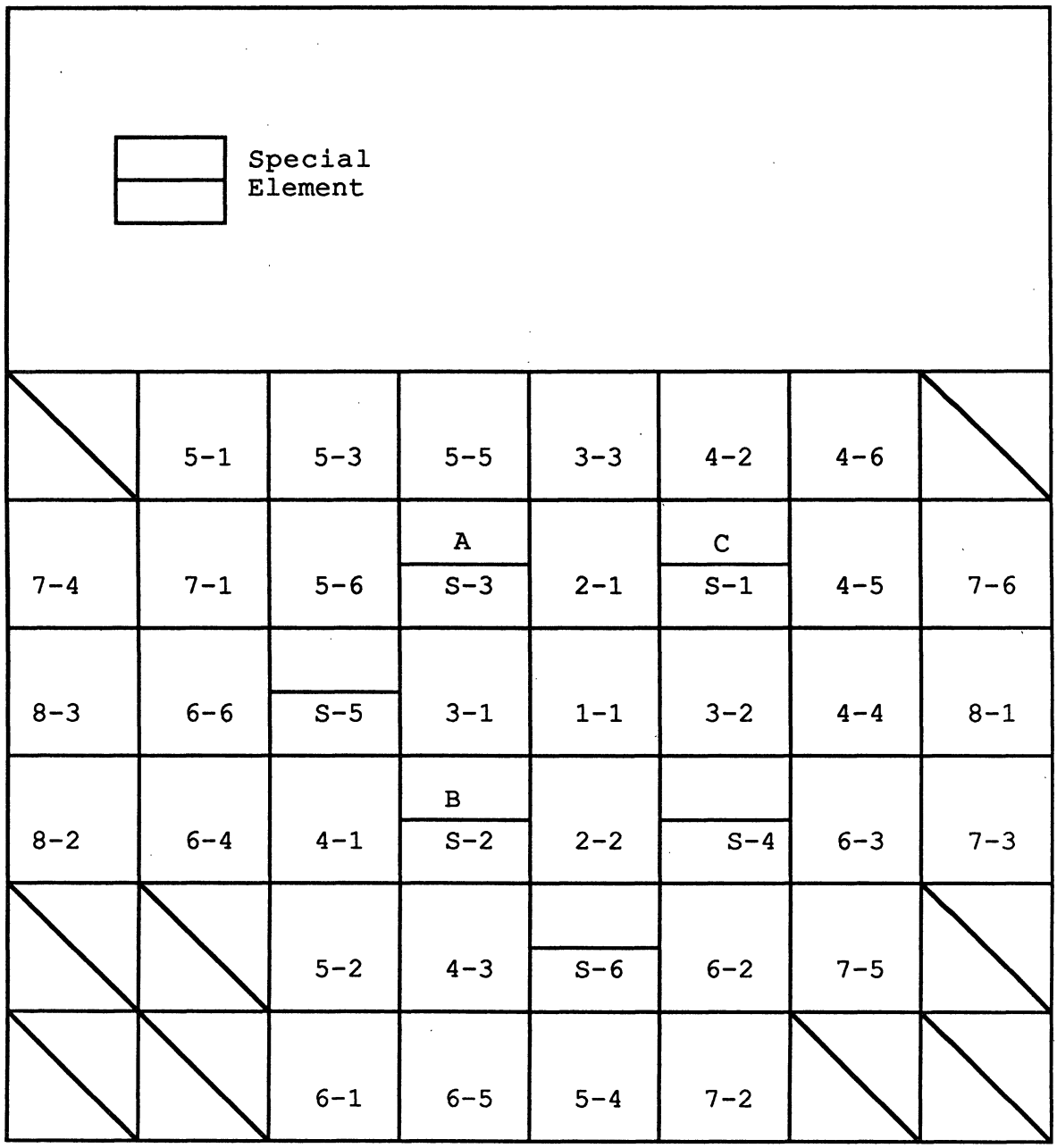

Figure II-34. Equilibrium Core Loading Zones

configuration is chosen in such a way that the core configuration repeats every sixth cycle.

The shuffling pattern in the equilibrium cycle divides the 33 regular fuel element locations into eight loading zones as shown in Figure II-34. Each regular element loading zone corresponds to core locations having nearly equal fuel burnup, although not necessarily equal burnup rates. New fuel is loaded into Zone 1 and depleted fuel is discharged from Zone 8. At the start of each cycle, one new element is loaded into Zone 1 and the element in Zone 1 is moved to Zone 2. The fuel shuffling continues to Zone 8 where elements are discharged. The eight zone shuffling pattern for the regular elements is shown in Figure II-35.

The shuffling pattern for the special fuel elements is different because there are six special element locations. A new special element is added and a depleted element is discharged only every sixth cycle. With this shuffling pattern a new special element is placed in Special Zone 1 at the start of cycle 1. The element removed from Special Zone 1 is placed in an ex-core storage for one cycle and then placed in Special Zone 2 at the start of cycle 2. The sequence continues until the start of cycle 6 when the element from storage is placed into Special Zone 6 and a depleted special element is discharged from the core.

Regular Fuel Elements

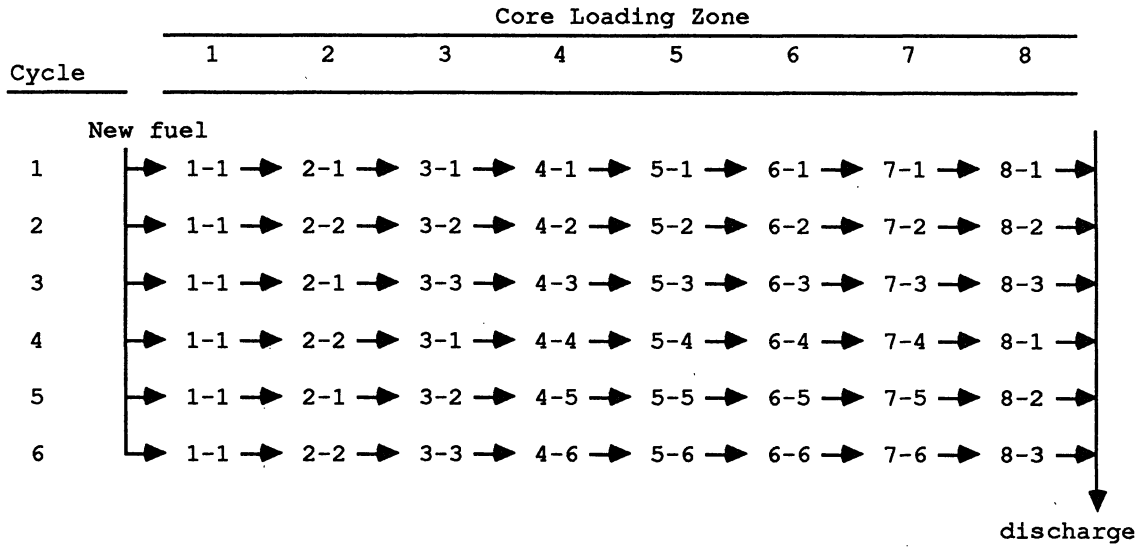

Speical Fuel Elements

Cycle	Storage		Core Loading Zone		Storage
1	New fuel	→	S-1	→	X_1
2	X_1	→	S-2	→	X_2
3	X_2	→	S-3	→	X_3
4	X_3	→	S-4	→	X_4
5	X_4	→	S-5	→	X_5
6	X_5	→	S-6	→	Discharge

Figure II-35. Equilibrium Core Shuffling Scheme

This shuffling pattern for special elements is also shown in Figure II-35.

•Characteristics of the Equilibrium Core Model

The equilibrium core model was designed to be typical of the actual FNR operation. Many characteristics of the FNR operation are well represented in the equilibrium core analysis. In fact, a modified version of the equilibrium core shuffling scheme has been implemented at the FNR and has proven to be a practical and efficient scheme for loading fuel elements. Nonetheless, there are differences between the equilibrium core model and actual FNR operation. These differences exist mainly because the FNR operation is more varied than the equilibrium model. Fuel elements do not need to be shuffled in any fixed pattern and the core configuration does not repeat periodically. This section describes characteristics of the equilibrium model and actual FNR configurations, and also explains important differences between equilibrium analysis and actual operation.

To verify the usefulness of the equilibrium model, Table II-25 presents a comparison of the calculated equilibrium core parameters and actual core parameters based on FNR operation. The comparisons indicate that the proposed equilibrium cycle represents a reasonably practical configuration for comparing the HEU and LEU fuel

Table II-25. Comparison of Equilibrium Core and Actual FNR Parameters

	Operating Experience*	HEU Equilibrium
Operating Cycle Length (days)	17.6	----
Equilibrium Cycle Length (days)	----	11.0
Average Number of Fuel Element Shuffles per Day	0.82	0.80
Average Discharge Burnup (MWD/element)		
Regular	19.4	19.2
Special	19.5	16.9
Calculated k_{eff}		
Range	1.022 - 1.026	1.020 - 1.032
Average	1.024	1.025
Shim Rod Worth (%Δk/k)		
Rod A	2.20	2.08
Rod B	2.21	2.24
Rod C	2.00	2.17
Total	6.41	6.49

* Averaged from October, 1978 to November, 1979.

designs. On the average, fuel elements are shuffled just as often in both cores. The calculated control rod worths for the equilibrium core compare well with the rod worths measured in the FNR.

The cycle length comparisons for the equilibrium and operating cores in Table II-25 point out a difference between analytic models and actual operations. In the equilibrium core model, cycle length is determined by the discharge fuel burnup over the regular and special fuel elements. In contrast, the FNR operating cycle length is the time interval between shim rod calibrations, which are required by technical specifications whenever more than three fuel elements are shuffled. In calculations comparing the HEU and LEU fuels, the parameter most indicative of the time between control rod calibrations, or operating cycle length, is the burnup reactivity change rate rather than the equilibrium core cycle length. With a constraint on the allowable core excess reactivity, the length of time the core can be maintained critical, without shuffling more than three fuel elements thereby requiring rod recalibration, is determined by the fuel burnup reactivity change rate.

F. Overall Verification

This section discusses the results of using the UM reactor analysis code package to analyze the IAEA research reactor benchmark problem [IAE80]. The detailed specifications for the benchmark problem are given in Table II-25 and Figure II-36. Briefly, it corresponds to a 10MWth, 6x5 element core at several uniform depletion steps. The reactor core is reflected by graphite on two opposite sides and surrounded by light water. Standard MTR elements with 23 fuel plates are utilized, with uranium enrichments of 93%, 45% and 20%, corresponding to a ^{235}U content of 280, 320 and 390 grams per element, respectively. This benchmark problem has already been calculated by seven international research institutions and their results are summarized in [IAE80]. Analyses have been performed for both the HEU and LEU cores and compared with the results obtained by the other research institutions. The MEU configuration was not analyzed although the procedure is the same as with the HEU and LEU cases.

Table II-26. Specifications for the IAEA Research Reactor Benchmark Problem (after [IAE80])

AIMS: Comparison of the different calculation methods and cross-section data sets used in different laboratories, limited conclusions for real conversion problems.

Specifications for the Methodical Benchmark-Problem

Data and Specifications Agreed Upon:

Active Core Height: 600mm
Extrapolation Length: 80mm (in 80mm distance from the core, the cosine-shaped flux goes to zero)
X-Y Calculations only

Space at the grid plate per fuel element: 77mm x 81mm

Fuel element cross-section: 76mm x 80.5mm inlcuding support plate
76mm x 80.0mm without support plate

Meat dimensions: 63mm x 0.51mm x 600mm

Aluminum-canning: $\rho_{Al} = 2.7g \cdot cm^{-3}$

Number of fuel plates per fuel element: 17 identical plates, each 1.27mm thick

Identification of the remaining plate positions of the control element:
4 plates of pure aluminum $\rho_{Al} = 2.7g \cdot cm^{-3}$, each 1.27mm thick in the position of the first, the third, the twenty-first, and the twenty-third standard plate position; water gaps between the two sets of aluminum plates.

Specifications of the different fuels (UAl_x-Al Fuel) for HEU, MEU, LEU corresponding to the previous definitions:

HEU:
- Enrichment 93 w/o (weight %) U-235
- 280g U-235 per fuel element, which corresponds to 12.174g U-235 per each fuel plate
- 21 w/o of uranium in the UAl_x-Al
- only U-235 and U-238 in the fresh fuel

MEU:
- Enrichment 45 w/o U-235
- 320g U-235 per fuel element (23 plates)
- 40 w/o of uranium in the UA_x-Al
- only U-235 and U-238 in the fresh fuel

LEU:
- Enrichment 20 w/o U-235
- 390g U-235 per fuel element (23 plates)
- 72 w/o of uranium in the UAl_x-Al
- only U-235 and U-238 in the fresh fuel

Total power: 10 MW_{th} (power buildup by 3.1×10^{10} fission/Joule)

Thermal hydraulic data: Water temperature 20°C
Fuel temperature 20°C
Pressure at core height 1.7 bar

Xenon state: Homogeneous xenon content corresponding to average power density

Results: k_{eff}; fluxes and flux ratios along the two symmetry-axes of the core in three groups and for begin of cycle (BOL) and end of cycle (EOL), respectively.

$\phi_{thermal}$ with $0 \text{ eV} < E_n < 0.625 \text{ eV}$

$\phi_{epithermal}$ with $0.625 \text{ eV} < E_n < 5.531 \text{ keV}$

ϕ_{fast} with $E_n > 5.531 \text{ keV}$

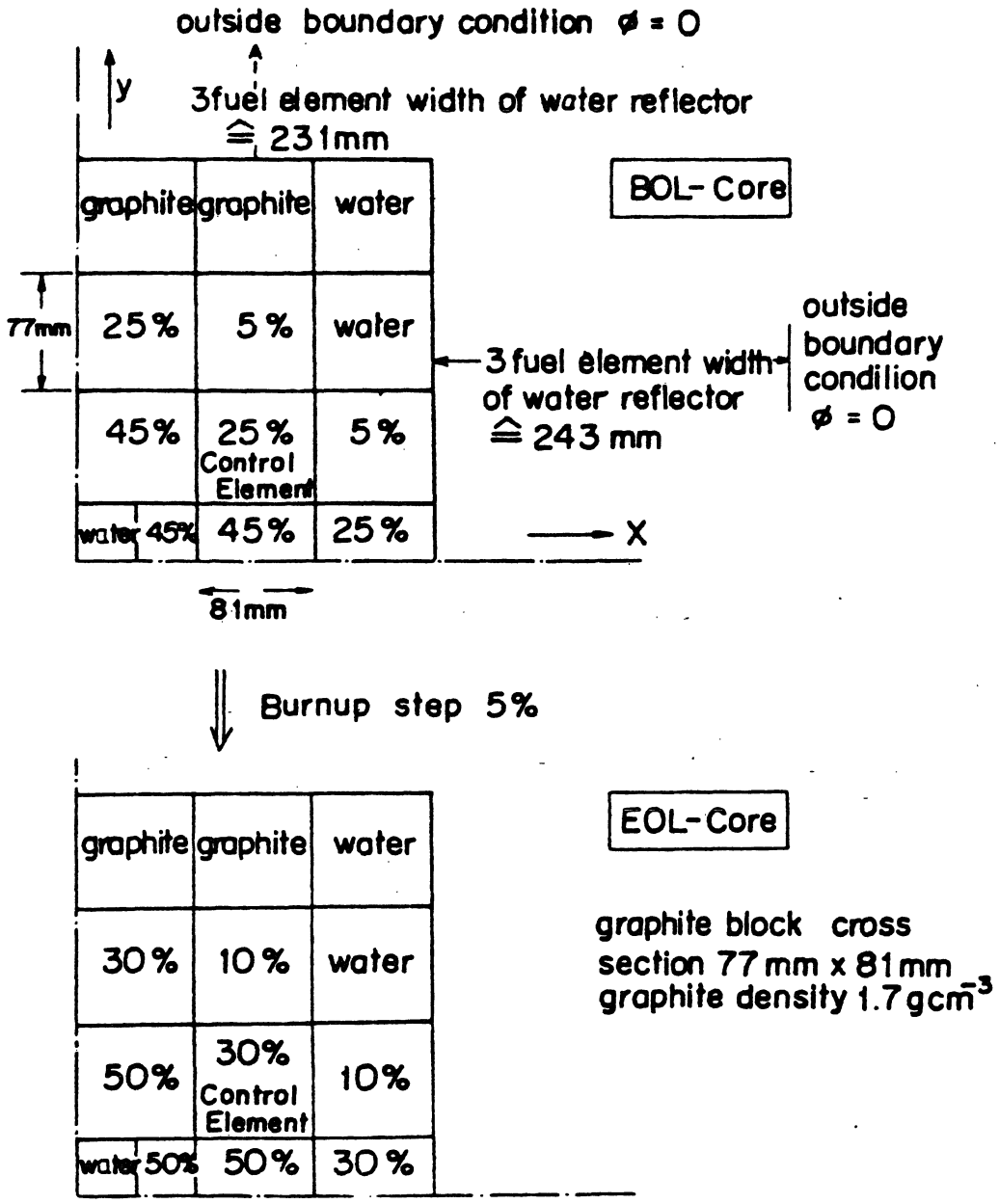

Burnup definition : (%) means the percentage of loss of the number of U 235 - Atoms

METHODICAL BENCHMARK
10 MW CASE
CORE CROSS SECTION

Figure II-36. Core Cross Section for the IAEA Research Reactor Benchmark Problem

1. Fuel and Control Element Cross Section Calculations

Macroscopic cross sections were generated as a function of burnup (in percentage loss of the number of ^{235}U atoms) by the UMLEO code with the ENDF/B-IV library. The unit cell geometries for UMLEO are based on the specifications given in Table II-26. Figure II-37 illustrates the unit cell geometries for both the fuel and the control elements. The extra region, or non-lattice regions, in Figure II-37 for both the fuel element and the control element include the aluminum in the fuel plates beyond the width of the fuel meat, the water beyond the fuel meat, the aluminum support plates and the water surrounding the fuel element. Moreover, the non-lattice region for the control element includes the central water channel for the control rod as well as the aluminum side plates forming the channel.

Table II-27 presents the infinite medium multiplication factors for the fuel element as a function of ^{235}U burnup for both HEU and LEU cores. The table includes results obtained by UMLEO and Argonne National Laboratory (ANL). The UMLEO code utilized the ENDF/B-IV library with the fission product correlation based on the EPRI-CINDER code.

The data in Table II-27 are plotted in Figure II-38, where it is evident that the UMLEO results agree very well

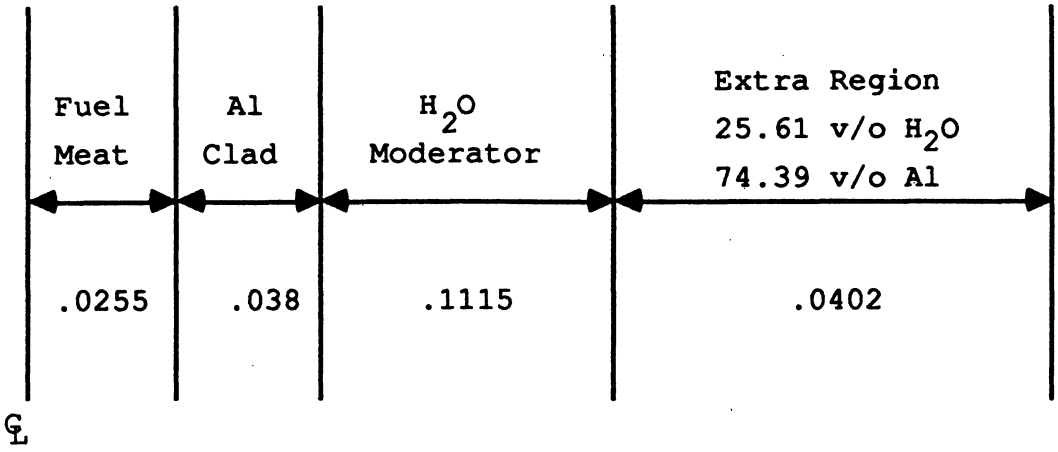

Fuel Element (cm)

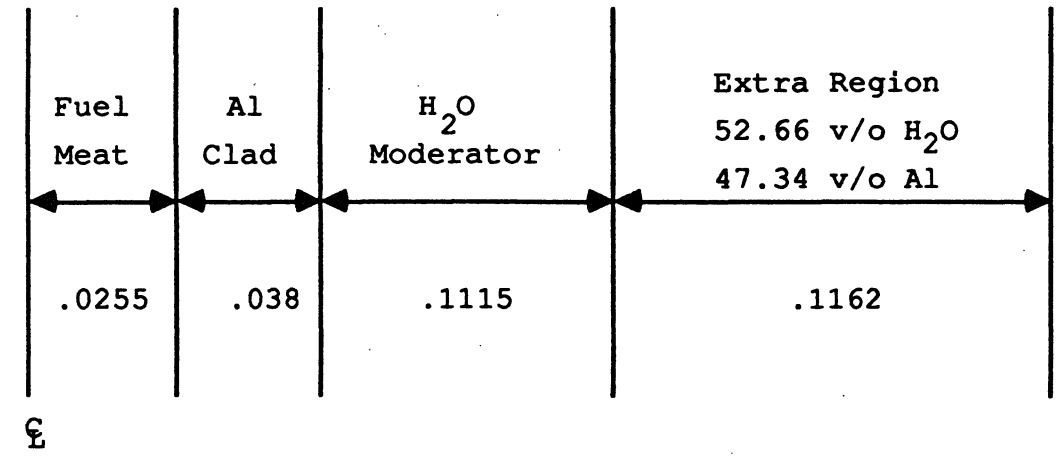

Control Element (cm)

Figure II-37. Fuel and Control Element Unit Cell Geometries Used for UMLEO Calculations (HEU and LEU Cores)

Table II-27. Infinite Medium Multiplication Factors for HEU and LEU Fuel

U-235 Burnup (%)	k_∞ - HEU Core			k_∞ - LEU Core		
	UMLEO	ANL	%Diff.	UMLEO	ANL	%Diff.
0.0	1.7432	1.7370	+.36	1.6551	1.6548	+.018
5.0	1.6427	1.6370	+.35	1.5643	1.5641	+.013
10.0	1.6203	1.6165	+.24	1.5434	1.5445	-.071
15.0	1.5979	1.5953	+.16	1.5224	1.5241	-.112
20.0	1.5745	1.5728	+.11	1.5005	1.5026	-.140
25.0	1.5494	1.5485	+.06	1.4773	1.4797	-.162
30.0	1.5225	1.5223	+.01	1.4529	1.4554	-.172
35.0	1.4932	1.4936	-.03	1.4270	1.4296	-.182
40.0	1.4608	1.4620	-.08	1.3989	1.4018	-.207
45.0	1.4247	1.4269	-.16	1.3688	1.3719	-.226
50.0	1.3842	1.3876	-.25	1.3356	1.3394	-.284

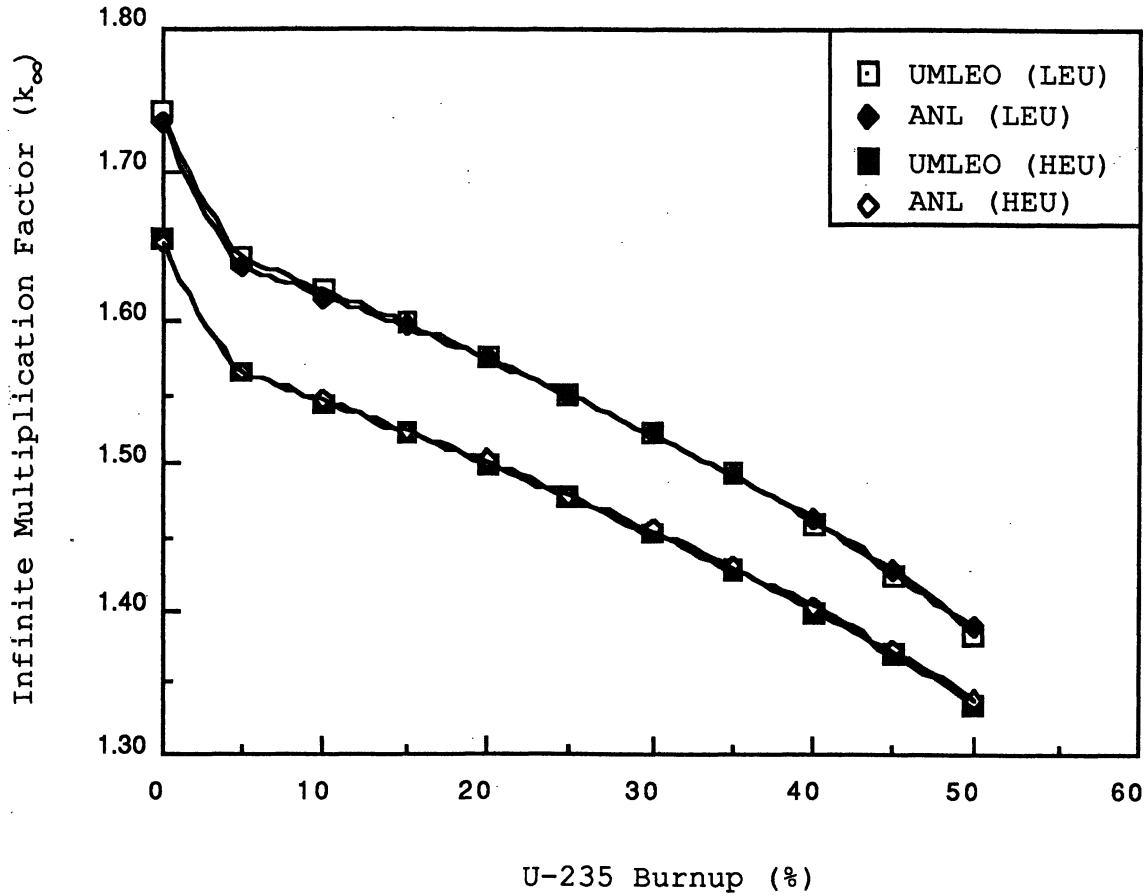

Figure II-38. Infinite Medium Multiplication Factors for HEU and LEU Fuel versus U-235 Burnup

with the ANL predictions. This comparison seems reasonable because EPRI-CINDER was used by ANL for the depletion analysis. Therefore, UMLEO was used to generate the 2-group cross section libraries for both the fuel and control elements. An earlier ENDF/B-IV version of UMLEO with an old fission product correlation tended to underestimate the infinite medium multiplication factor compared with the ANL result, as seen earlier in Figure II-30.

In addition to the comparison of k_∞, UMLEO atom densities in the fuel meat, as a function of ^{235}U burnup, are compared in Tables II-28 and II-29 with the results calculated by ANL. Again the UMLEO results compare very well with the ANL results.

2. Reflector Cross Section Calculations

Separate UMLEO calculations were performed to generate the macroscopic cross sections for the light water reflector, the central flux trap and the graphite reflector. The problem configuration and the corresponding unit cell used in these UMLEO calculations are shown in Figure II-39. The macroscopic cross sections for these regions are taken from the non-lattice edits (corresponding to the extra region in Figure II-37) of UMLEO and are assumed to be independent of burnup. Both 3-group and 2-group cross sections are tabulated in Table

Table II-28. Atom Densities in the Fuel Meat versus ^{235}U Burnup -- HEU Fuel

^{235}U Burnup (%)	Atom Densities (1/b-cm)							
	^{135}Xe	^{149}Sm	^{235}U	^{236}U	^{238}U	^{239}Pu	^{240}Pu	^{241}Pu
LEOPARD								
0.0	0.0	0.0	1.6179E-3	0.0	1.2020E-4	0.0	0.0	0.0
5.0	1.7072E-8[1]	1.4167E-7	1.5370E-3	1.3485E-5	1.1973E-4	4.4223E-7	8.2701E-9	1.4831E-10
10.0	1.6472E-8	1.3831E-7	1.4560E-3	2.6911E-5	1.1923E-4	8.5342E-7	3.1717E-8	2.1173E-9
25.0	1.4095E-8	1.1567E-7	1.2134E-3	6.6279E-5	1.1769E-4	1.8227E-6	1.6748E-7	3.6986E-8
30.0	1.3279E-8	1.0815E-7	1.1324E-3	7.9144E-5	1.1716E-4	2.0612E-6	2.2867E-7	6.0327E-8
45.0	1.0760E-8	8.5706E-8	8.8971E-3	1.1677E-4	1.1549E-4	2.5373E-6	4.3137E-7	1.7023E-7
50.0	9.8972E-9	7.8257E-8	8.0880E-4	1.2900E-4	1.1490E-4	2.6169E-6	5.0156E-7	2.1671E-7
ANL								
0.0	0.0	0.0	1.6179E-3	0.0	1.2020E-4	0.0	0.0	0.0
5.0	1.7094E-8	1.3393E-7	1.5370E-3	1.3468E-5	1.1973E-4	4.3769E-7	8.5690E-9	3.7780E-10
10.0	1.6416E-8	1.2824E-7	1.4561E-7	2.6885E-5	1.1923E-4	8.4775E-7	3.3247E-8	2.9955E-9
25.0	1.4034E-8	1.0755E-7	1.2134E-3	6.6298E-5	1.1768E-4	1.8002E-6	1.7889E-7	3.9914E-8
30.0	1.3219E-8	1.0069E-7	1.1325E-3	7.9139E-5	1.1715E-4	2.0304E-6	2.4357E-7	6.4686E-8
45.0	1.0709E-8	8.0131E-8	8.8985E-4	1.1672E-4	1.1546E-4	2.4799E-6	4.5967E-7	1.7615E-7
50.0	9.8497E-9	7.3282E-8	8.0895E-4	1.2890E-4	1.1486E-4	2.5535E-6	5.3381E-7	2.2312E-7

[1]Read as 1.7072×10^{-8}

Table II-29. Atom Densities in the Fuel Meat versus ^{235}U Burnup -- LEU Fuel

^{235}U Burnup (%)	Atom Densities (1/b-cm)							
	^{135}Xe	^{149}Sm	^{235}U	^{236}U	^{238}U	^{239}Pu	^{240}Pu	^{241}Pu
LEOPARD								
0.0	0.0	0.0	2.2536E-3	0.0	8.9003E-3	0.0	0.0	0.0
5.0	2.3069E-8[1]	2.0549E-7	2.1409E-3	1.9572E-5	8.8869E-3	1.1947E-5	2.3550E-7	1.2866E-8
10.0	2.2463E-8	2.0214E-7	2.0283E-3	3.8977E-5	8.8728E-3	2.3050E-5	8.9287E-7	9.8727E-8
25.0	1.9980E-8	1.7514E-7	1.6901E-3	9.5929E-5	8.8278E-3	4.9988E-5	4.6847E-6	1.3058E-6
30.0	1.9084E-8	1.6580E-7	1.5776E-3	1.1442E-4	8.8118E-3	5.6892E-5	6.3610E-6	2.1013E-6
45.0	1.6197E-8	1.3693E-7	1.2396E-3	1.6839E-4	8.7596E-3	7.1711E-5	1.2029E-5	5.6320E-6
50.0	1.5164E-8	1.2704E-7	1.1268E-3	1.8584E-4	8.7405E-3	7.4734E-5	1.4028E-5	7.1105E-6
ANL								
0.0	0.0	0.0	2.2536E-3	0.0	8.9005E-3	0.0	0.0	0.0
5.0	2.3023E-8	1.9168E-7	2.1409E-3	1.9458E-5	8.8878E-3	1.1374E-5	2.4226E-7	1.3277E-8
10.0	2.2410E-8	1.8634E-7	2.0282E-3	3.8844E-5	8.8741E-3	2.2042E-5	9.2957E-7	1.0474E-7
25.0	1.9879E-8	1.6193E-7	1.6902E-3	9.5651E-5	8.8304E-3	4.7478E-5	4.8797E-6	1.3596E-6
30.0	1.8970E-8	1.5346E-7	1.5775E-3	1.1410E-4	8.8147E-3	5.3906E-5	6.6116E-6	2.1811E-6
45.0	1.6051E-8	1.2717E-7	1.2395E-3	1.6778E-4	8.7635E-3	6.7549E-5	1.2411E-5	5.7635E-6
50.0	1.5012E-8	1.1813E-7	1.1269E-3	1.8504E-4	8.7447E-3	7.0314E-5	1.4434E-5	7.2364E-6

[1]Read as 2.3069×10^{-8}

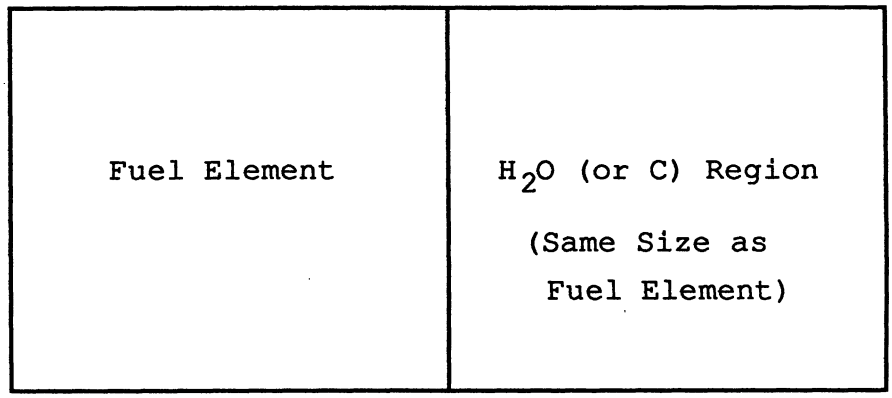

Problem Cross Section

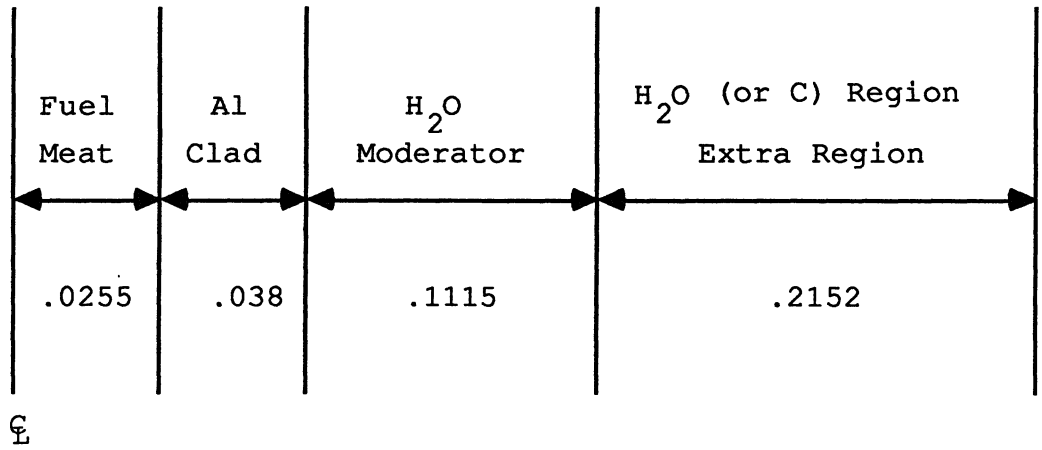

Unit Cell (cm)

Figure II-39. Reflector Unit Cell Geometry Used for UMLEO Calculations

II-30 for the HEU core and in Table II-31 for the LEU core. Results from another institution were not available, and these cross sections are included for reference.

We have also run the 1-D discrete ordinates codes XSDRN-PM and ANISN for the global 1-D (i.e., y-direction in Figure II-36) core calculations to generate another set of macroscopic cross sections for the reflectors. The results from these calculations are also given in Table II-29. For the treatment of anisotropic scattering, a P-1 model was used in these calculations based on earlier calculations which indicated very little difference between the P-1 and P-3 calculations.

The results calculated by ANL (for 3-group) and by Switzerland EIR (for 2-group) are included in Table II-30. In general, there is reasonable agreement between the ANISN and XSDRN-PM results except for the diffusion coefficients D, where the different weighting schemes have a large effect on the resultant coefficients. Also, the agreement between UMLEO and ANL is reasonable, except for $\Sigma_{a,1}$ for graphite. Since this cross section has very little effect on the overall results, we have not examined this in more detail. Overall, the comparison seems reasonable.

Table II-30. 2- and 3-Group Ex-Core Cross Section Comparison for HEU Fuel

Model	Light Water Reflector									
	Group 1		Group 2		Group 1[4]		Group 2		Group 3	
	D	Σ_a	D	Σ_a	D	Σ_a	D	Σ_a	D	Σ_a
XSDRN-PM[1]	1.121	5.182E-4[5]	0.153	1.872E-2	1.502	1.960E-4	0.561	1.019E-3	0.153	1.872E-2
ANISN[2]	0.824	5.183E-4	0.129	1.872E-2	1.186	1.960E-4	0.559	1.020E-3	0.129	1.872E-2
UMLEO[3]	1.154	4.231E-4	0.168	1.800E-2	1.402	2.029E-4	0.597	0.918E-3	0.168	1.800E-2
ANL	--	--	--	--	1.729	2.271E-4	0.569	1.002E-3	0.147	1.901E-2
SWITZERLAND	1.152	4.876E-4	0.165	1.780E-2	--	--	--	--	--	--
	Graphite Reflector									
XSDRN-PM[1]	1.435	3.518E-5	0.828	2.048E-4	1.646	4.757E-5	0.942	1.106E-5	0.828	2.048E-4
ANISN[2]	1.193	3.541E-5	0.828	2.049E-4	1.382	4.791E-5	0.943	1.107E-5	0.828	2.049E-4
UMLEO[3]	1.327	2.962E-5	0.876	2.134E-4	1.546	3.832E-5	0.873	1.156E-5	0.876	2.134E-4
ANL	--	--	--	--	1.334	1.160E-5	0.876	1.297E-5	0.842	2.510E-4
SWITZERLAND	1.402	0.586E-5	0.886	1.962E-4	--	--	--	--	--	--

[1] Diffusion coefficient obtained by collapsing the transport cross section through leakage spectrum weight

[2] Diffusion coefficient based on flux-weighted transport cross section.

[3] Diffusion coefficient collpased through flux weighting

[4] Energy Boundaries

	XSDRN-PM/ANISN	UMLEO/ANL/SWITZERLAND
Group 1:	3.0 keV < E_n < 20.0 MeV	5.53 keV < E_n < 10.0 MeV
Group 2:	0.8 eV < E_n < 3.0 keV	0.625 eV < E_n < 5.53 keV
Group 3:	0.00001 eV < E_n < 0.8 eV	0.0 eV < E_n < 0.625 eV

[5] Read as 5.182×10^{-4}

Table II-31. 2- and 3-Group Ex-Core Cross Sections for LEU Fuel

Reflector	Group 1		Group 2		Group 1		Group 2		Group 3	
	D	Σ_a	D	Σ_a	D	Σ_a	D	Σ_a	D	Σ_a
Water	1.148	4.116E-4[2]	0.175	1.745E-2	1.381	2.018E-4	0.606	8.988E-4	0.175	1.745E-2
Graphite	1.417	2.860E-5	0.930	1.881E-4	1.643	3.696E-5	0.926	1.044E-5	0.930	1.881E-4

[1] Energy Boundaries

5.53 keV < E_n < 10.0 MeV
0.6525 eV < E_n < 5.53 keV
0 eV < E_n < 0.625 eV

[2] Read as 4.116×10^{-4}

3. Reactor Core Calculations

The quarter core calculations were performed with the UM2DB code, for the geometry shown in Figure II-36. The fluxes were normalized to a power of 2.5 MW for the quarter core, represented by 12 mesh intervals in the x-direction and 13 in the y-direction.

Table II-32 presents the UM2DB effective multiplication factors for the HEU core at three different burnup stages: the fresh core, beginning-of-life (BOL) core and end-of-life (EOL) core (which are shown in Figure II-36). Since more than one set of cross sections are available for reflectors, there are three cases examined in Table II-32: the UMLEO results were used for both reflectors in case 1, the XSDRN-PM results for both reflectors in case 2, and the UMLEO results for the light water reflector with the XSDRN-PM results for the graphite reflector in case 3. It has been noted that the eigenvalue differences between case 2 and case 3 are larger than those between case 1 and case 3, indicating that the light water reflector has more of an effect on the core calculations than the graphite reflector, as expected.

Table II-32. UM2DB Eigenvalue Calculation for IAEA Benchmark Problem

Burnup Stage	UM2DB Eigenvalue		
	UMLEO*	XSDRN-PM**	UMLEO/XSDRN-PM***
Fresh	1.1877	1.1709	1.1842
BOL	1.0355	1.0204	1.0323
EOL	1.0132	0.9985	1.0101

* Case 1: LEOPARD H_2O and graphite reflector cross sections

** Case 2: XSDRN-PM H_2O and graphite reflector cross sections

*** Case 3: LEOPARD H_2O reflector cross sections and XSDRN-PM graphite reflector cross sections.

The effective multiplication factors calculated by the seven international research centers are given in Tables II-33 and II-34, where UMLEO-generated cross sections are used for both graphite and light water reflector regions. Following the lead of [IAE80], wherein the German results are chosen as the reference case, the comparison of effective multiplication factors is presented again in Tables II-35 and II-36. As can be seen, the deviations from each other are small, typically less than 1% $\Delta k/k$.

It is clear from these results that the analysis of the IAEA benchmark core using the UM code package agrees very well with the results of the seven international research centers.

Table II-33. Summary of Effective Multiplication Factors - HEU Core

Burnup Stage	Eigenvalue Calculation (HEU Core)							
	UM2DB	Germany (INTERATOM)	USA (ANL)	Switz. (EIR)	Austria (OSCAE)	France (CEA)	Argen. (CNEA)	Japan (JAERI)
Fresh	1.1842	1.1888	1.1834	1.1939	1.1966	1.2020	1.2002	1.1810
BOL	1.0323	1.0328	1.0233	1.0368	1.0320	1.0404	1.0377	1.0420
EOL	1.0101	1.0101	1.0004	1.0138	1.0090	1.0170	1.0143	1.0220

Table II-34. Summary of Effective Multiplication Factors - LEU Core

Burnup Stage	Eigenvalue Calculation (LEU Core)							
	UM2DB	Germany (INTERATOM)	USA (ANL)	Switz. (EIR)	Austria (OSCAE)	France (CEA)	Argen. (CNEA)	Japan (JAERI)
Fresh	1.1701	1.1683	1.1683	1.1594	1.1813	1.1870	1.1815	1.1834
BOL	1.0301	1.0278	1.0213	1.0178	1.0320	1.0394	1.0332	1.0578
EOL	1.0108	1.0091	1.0014	1.0000	1.0120	1.0191	1.0130	1.0412

Table II-35. Comparison of Effective Multiplication Factors - HEU Core

Burnup Stage	Absolute Bias (%Δ k/k)							
	Germany (INTERATOM)	UM2DB	USA (ANL)	Switz. (EIR)	Austria (OSCAE)	France (CEA)	Argen. (CNEA)	Japan (JAERI)
Fresh	1.1888	-0.39	-0.45	0.43	0.66	1.11	0.96	-0.66
BOL	1.0328	-0.05	-0.92	0.39	-0.08	0.74	0.47	0.89
EOL	1.0101	0.0	0.96	0.37	-0.11	0.68	0.42	1.18

Table II-36. Comparison of Effective Multiplication Factors - LEU Core

Burnup Stage	Absolute Bias (% Δ ρ)							
	Germany (INTERATOM)	UM2DB	USA (ANL)	Switz. (EIR)	Austria (OSCAE)	France (CEA)	Argen. (CNEA)	Japan (JAERI)
Fresh	1.1683	0.15	0.00	-0.76	1.11	1.60	1.13	1.29
BOL	1.0278	0.22	-0.63	-0.97	0.41	1.13	0.53	2.92
EOL	1.0091	0.17	-0.76	-0.90	0.29	0.99	0.39	3.18

III. DEMONSTRATION EXPERIMENTS

The demonstration experiments program was designed to characterize the FNR in sufficient detail to discern and quantify the neutronic differences between the HEU and LEU cores. In this section, we report the results of the comparative measurements of:

- the in-core spectra measured at a point in the core,
- the subcadmium flux distributions obtained from self-powered detector mappings and wire activations both in the core and in the reflectors,
- the leakage flux intensities measured at beam ports, and
- the spectrum of the leakage flux measured at a beam port.

These experiments are sufficient to identify significant changes in the in-core and ex-core neutron intensities and spectra. The comparisons which are presented are between equilibrium HEU cores, and LEU cores which have not reached equilibrium. However, the latest LEU measurements reported (December 1984-June 1985) were performed on a core which approximates the LEU equilibrium core configuration.

A. In-core Spectral Measurements

In this section, we present the unfolded HEU and LEU spectra. Since the refined saturated activities may be more important to some readers than even the unfolded results, some comments on these data are also presented. Although we have a variety of unfolding approaches at our disposal, we shall limit our discussion to two

unfolding techniques -- the semi-empirical method and the integral unfolding method [Weh84].

1. Thermal and Epithermal Activation

Multiple foil activations were performed at a sample holder in both the HEU and the LEU cores. Prior to presenting the data, a few words of caution are necessary. Figure III-1 shows the core configurations present for these measurements. Note that the HEU measurements were made in a large, equilibrium core. In contrast, the LEU measurements were made in a small, clean core, also shown in Figure III-1. Because of the differences in the core sizes, one must be careful not to erroneously attribute the absolute differences in flux intensities (or activities) solely to the enrichment differences.

Table III-1a shows the saturated activities per unit target nucleus for non-threshold reactions measured at the sample holder in an HEU core. The uncertainties in these values are difficult to determine precisely. This is because the expressions used to determine the saturated activity are nonlinear and can be quite complicated. However, the major factors which contribute to the uncertainty can be separated out, and the following expression can be used to obtain approximate values for the errors of a straightforward isotope production and decay scheme:

$$\delta A = [\delta m^2+\delta C^2+\delta P_s+\delta F^2+\delta L^2+\delta \varepsilon p^2+\delta S^2+\delta f^2+\delta Y^2+\delta \lambda^2]\cdot 5 + \delta_s .$$

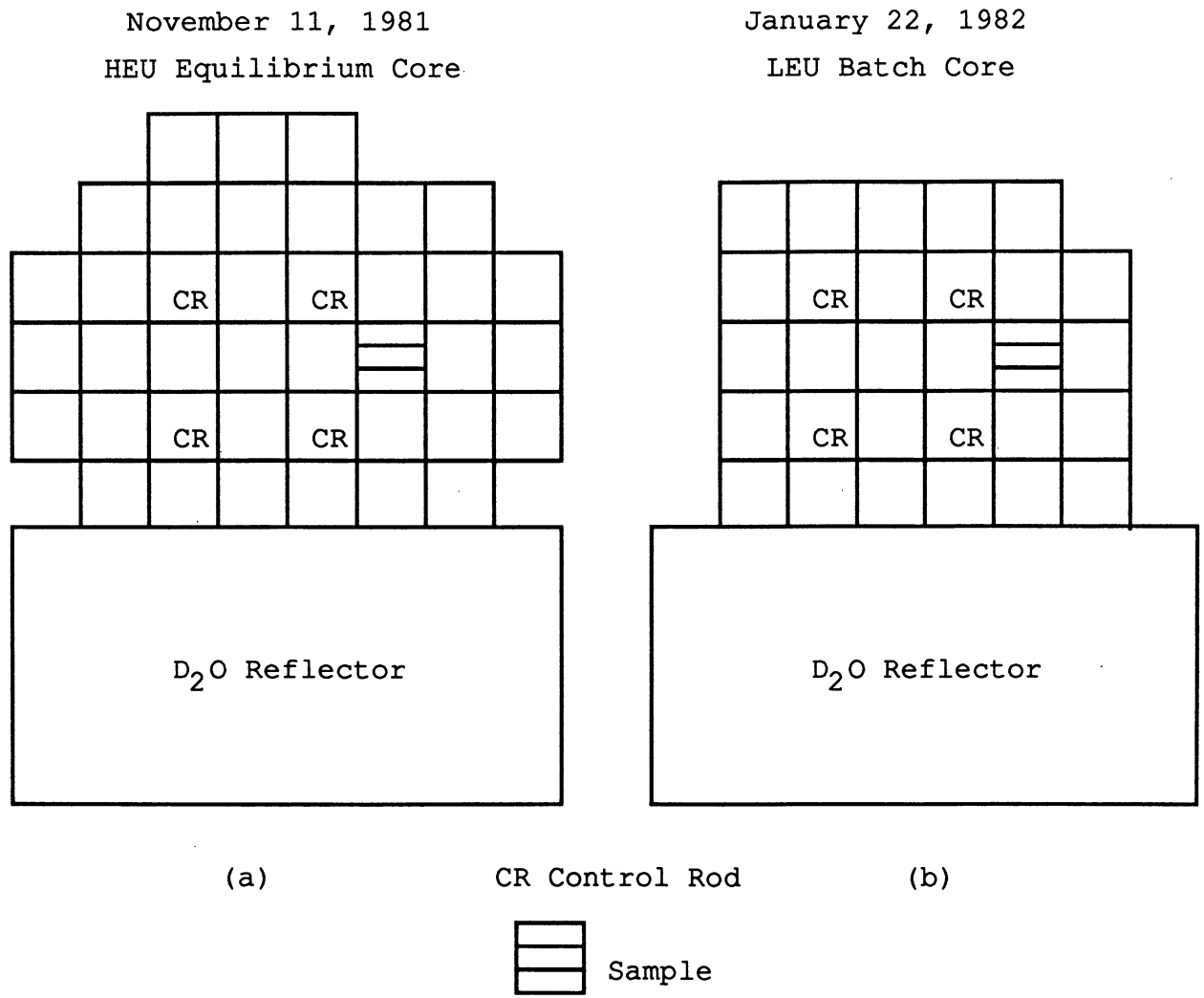

Figure III-1. Core Configurations for HEU and LEU Special Holder Measurements

Table III-1a. Saturated Activities for Reactions Dominated by the Thermal/ Epithermal Flux at the HEU Special Assembly Sample Holder

REACTION	BARE FOILS		CADMIUM COVERED FOILS		
	ACTIVITY (per sec.)	UNCERTAINTY (percent)	ACTIVITY (per sec.)	CADMIUM THICKNESS (mils)	UNCERTAINTY (percent)
$Fe^{58}(n,\gamma)$. (FP)	0.287-10[1]	4	0.209-11	20.	4
$Co^{59}(n,\gamma)$. (FP)	0.813-09	5	0.113-09	20.	5
$Au^{197}(n,\gamma)$	0.400-08	8	0.220-08	20.	4
$Cu^{63}(n,\gamma)$. (FP)	0.833-10	5	0.668-11[2]	20.	7
Mn^{55} (n,γ)	0.249-09	5	-	-	-
$Ag^{109}(n,\gamma)$	0.101-09	8	0.273-10	20.	8
$Ta^{181}(n,\gamma)$	-	-	0.622-09	20.	8
$W^{186}(n,\gamma)$	0.828-09	8	0.239-09	20.	8
$U^{238}(n,\gamma)$	0.270-09	9	0.234-09	20.	9
Na^{23} (n,γ)	-	-	0.484-12	40.	11
U^{235}(n,fission)	0.106-07	10	-	-	-
Pu^{239}(n,fission)	0.185-07	10	-	-	-
$Th^{232}(n,\gamma)$	-	-	0.720-10	20.	8
Sc^{45} (n,γ)	0.470-09	8	0.167-10	20.	7
$Lu^{176}(n,\gamma)$	0.724-07	7	0.130-08	20.	6
$Dy^{164}(n,\gamma)$	0.414-07	6	0.571-09	20.	7
$Dy^{156}(n,\gamma)$	0.167-08	5	0.106-08	20.	5
Mo^{98} (n,γ)	-	-	0.108-10	20.	10
Zr^{94} (n,γ)	-	-	0.547-12	20.	4
Zn^{64} (n,γ)	-	-	0.250-11	20.	5
Zn^{68} (n,γ)	-	-	0.352-12	20.	10
Zr^{96} (n,γ)	-	-	0.810-11	20.	10

(1) Read as 0.287×10^{-10}

(2) The Cu^{64} branching ratio is uncertain by 10-30% according to the literature. Our evaluations have shown this uncertainty must be much lower. The cadmium ratio should be reliable since it is independent of the branching ratio.

Table III-1b. Saturated Activities for Reactions Dominated by the Thermal/ Epithermal Flux at the LEU Special Assembly Sample Holder

REACTION	BARE FOILS		CADMIUM COVERED FOILS		
	ACTIVITY (per sec.)	UNCERTAINTY (percent)	ACTIVITY (per sec.)	CADMIUM THICKNESS (mils)	UNCERTAINTY (percent)
$Fe^{58}(n,\gamma)$. (FP)[1]	0.263-10	5	0.219-11	25.	5
$Co^{59}(n,\gamma)$. (FP)	0.806-09	5	0.120-09	25.	5
$Cu^{63}(n,\gamma)$. (FP)	-	-	0.778-11	25.	6
$Mn^{55}(n,\gamma)$ (FP)	0.261-09	7	0.243-10	25.	5
$Au^{197}(n,\gamma)$	0.373-08	8	0.224-08	20.	8
$Ag^{109}(n,\gamma)$	0.103-09	8	0.341-10	20.	8
$U^{238}(n,\gamma)$	-	-	0.232-09	25.	6
U^{235}(n,fission)	0.960-08	8	0.470-09	25.	8
Pu^{239}(n,fission)	0.180-07	8	0.590-09	25.	8
$Th^{232}(n,\gamma)$	-	-	0.800-10	25.	5
$Sc^{45}(n,\gamma)$	0.499-09	6	-	-	-

(1) The abreviation "FP" means the measurements were made at full power (2MW).

Table III-1c. Saturated Activities for Reactions Dominated by the Thermal/Epithermal Flux at the LEU Special Assembly Sample Holder (Modified Core)

REACTION	BARE FOILS		CADMIUM COVERED FOILS		
	ACTIVITY (per sec.)	UNCERTAINTY (percent)	ACTIVITY (per sec.)	CADMIUM THICKNESS (mils)	UNCERTAINTY (percent)
$Au^{197}(n,\gamma)$	0.428-8	8	0.209-8	20.	8
$Ag^{109}(n,\gamma)$	0.906-9	8	0.216-10	20.	8
$Ta^{181}(n,\gamma)$	0.905-9	6	0.566-9	20.	6
$W^{186}(n,\gamma)$	0.947-9	6	-	-	-
$Sc^{45}(n,\gamma)$	0.519-9	7	0.168-10	20.	7
$Lu^{176}(n,\gamma)$	0.751-7	6	-	-	-
$Dy^{164}(n,\gamma)$	0.430-7	6	0.462-9	20.	7
$In^{115}(n,\gamma)$	-	-	0.292-8	20.	8
$Cu^{63}(n,\gamma)$	0.792-10	5	0.624-11	20.	7
$Mn^{55}(n,\gamma)$	0.242-9	5	0.166-10	20.	7

The symbols are defined in Table III-2, and the prefix δ implies the relative error in the quantity. In accordance with the ICRU guidelines, the term δ_S is defined to be the maximum conceivable systematic uncertainty in the measurement. Table III-2 shows the factors considered in assessing the magnitudes of the uncertainties, along with representative values. Note that we have chosen to quote the uncertainties at the 95% confidence level, so that these values correspond to approximately twice (1.96) the conventional standard error. These estimates may appear significantly too large since several completely independent measurements of the same activity normally agreed to well within the quoted uncertainties. But for the determination of an absolute activity, both the relatively large systematic uncertainty in the absolute efficiency of the detector and the absolute power level can dominate. In addition, while many of the other factors are frequently small, the quadrature sum of several of these uncertainties together may not be insignificant. In light of our experiences, it would be quite surprising to find absolute activity measurements quoted with uncertainties on the order of one or two percent. Tables III-1a and III-1b also show the estimated uncertainties in the measured activities. The full power measurements are noted using the initials "FP". Since these measurements do not require a power calibration factor, they have lower uncertainties associated with them. As mentioned above, the

Table III-2. Factors Used in Assessing the Uncertainty in the Activities

Consideration	Symbol	Typical Error (%)
Irradiation Conditions		
1. Power reproducibility (full power)	δP_s	2%
Power calibration (low power)		6%
2. Power ramp corrections	δF	1-2%
3. Foil positioning errors		1-2%
Nuclear Parameters		
1. Half-life	$\delta\lambda$	1%
Effective half-life (Co^{58})		4%
2. Gamma branching ratios	δf	1-20%
3. Number densities, isotopic abundance	δN_i	1%
4. Fission yields	δY	6-20%
Mass Determination	δm	
1. Mass measurements		0-1.2%
2. Fissile/fertile material composition		1-3%
3. Alloy compositions		1-2%
Counting Parameters		
1. Counting Statistics	δC	1-2%
2. Absolute efficiency of detector	$\delta \varepsilon^p$	1%
3. Count rate corrections	δL	<3-6%
4. Sample geometry corrections	δS	1-10%
5. Irradiation, counting, and wait times		<1%

Note: Errors are quoted for the 95% confidence level.

absolute copper activities should be viewed with caution since the gamma branching ratio has a large uncertainty quoted in the literature.

The saturated activities presented in Table III-1a are used directly for our unfolding of the flux. For some readers, the saturated activities may be most useful since these can be used as benchmarks for other unfolding approaches. However, recall that we have incorporated the effects of self-shielding in the cross sections instead of correcting the activities. Thus, users wishing to employ these activities in their own calculations must apply self-shielding corrections.

Table III-1b presents the activities which were measured in the clean LEU core presented in Figure III-1, along with an estimate of the uncertainty in these values. Note that we have chosen to present only those reactions which were used in the unfoldings. That is, we have not included those reactions whose decay schemes or cross sections have very large uncertainties (such as the Dy^{157} capture reaction). Table III-1c presents the activities measured in an even more compact LEU core. In this case, the four fuel elements along the far right column of the LEU core shown in Figure III-1 were removed. Since the larger LEU core shown in Figure III-1 is more comparable to the HEU core, we have chosen the data of Table III-1b as being representative of the LEU fuel.

Table III-3 presents a comparison of the measured cadmium ratios for six reactions measured in HEU and LEU fuel. Through

Table III-3. Comparison of Cadmium Ratios for HEU and LEU Foils Measured at the Sample Holder

Reaction	Power (FP/LP)[1]	HEU Cadmium Ratio		LEU Cadmium Ratio		Cadium Fraction Ratio (HEU/LEU)	
		Measured	Predicted	Measured	Predicted	Measured[3]	Predicted
Fe^{58} (n,γ)	FP	13.7	9.0	12.0	8.0	1.15	1.14
Co^{59} (n,γ)	FP	7.2	6.5	6.7	5.9	1.08	1.12
Au^{197}(n,γ)	LP	1.8	1.74	1.7	1.66	1.23	1.12
Ag^{109}(n,γ)	LP	3.7	3.3	3.0	3.0	1.34	1.14
Mn^{55} (n,γ)	LP	15.2[2]	12.9	10.7	10.3	1.46	1.28
Cu^{63} (n,γ)	LP	12.5	10.	10.3[4]	8.9	1.23	1.16

(1) The abreviations FP and LP stand for full-power and low-power measurements.

(2) The Mn^{55} HEU cadmium ratio has a large uncertainty due to a 15% uncertainty in the cadmium covered activity. This activity was not used for unfolding.

(3) The low power values have a larger uncertainty (12-15%) due to the additional uncertainty introudced in the power calibration.

(4) The LEU bare copper data have a large uncertainty and are not used for unfolding.

comparison of the HEU and LEU measured values, it is apparent that the LEU spectrum is measurably harder than the HEU spectrum. This can also be seen in the final column of Table III-3 which shows the ratio of the HEU to LEU cadmium fractions. The cadmium fraction is the cadmium ratio minus one, and is crudely representative of the ratio of the subcadmium to epicadmium fluxes. Since the ratio of the cadmium fractions is a ratio of ratios, the uncertainty in these values is rather large, i.e. 10-15%. Nevertheless, the data consistently indicates the harder nature of the LEU spectrum.

Table III-3 also shows the cadmium ratios which are predicted from the spectra calculated with the HAMMER code. The effects of self-shielding have been included in these calculations, so the measured and calculated cadmium ratios can be directly compared. These comparisons are quite interesting since they show that the calculated spectrum is too hard compared to what the measurements indicate. This is most likely due to deficiencies in our analytic model. The HAMMER code performs a unit cell calculation with reflective boundary conditions. As a result, the effect of leakage on the spectrum is neglected. Since leakage tends to soften a spectrum, the calculated spectrum should be too hard. This is precisely what is observed. Since it is not critical that our calculated spectra agree precisely with our measurements, we have not pursued this further. However, it would be interesting to perform a similar calculation (for example, using ANISN) with a vacuum boundary condition for comparison.

Table III-4a presents a comparison of bare and cadmium covered saturated activities measured at the center of an HEU core in a regular fuel element, and in the special sample holder in an HEU core. The HEU core center measurements were made at 1 MW in the core configuration shown in Figure III-2. Since these two sets of measurements were made at different core positions in cores with different fuel configurations, the absolute activities cannot be meaningfully compared. However, from an examination of the cadmium ratios, the spectrum can be seen to be slightly harder at the core center, as correctly predicted by the HAMMER calculations. The second half of Table III-4a shows threshold reaction data. While we shall compare the HEU and LEU threshold reaction data in Section 2 below, it is interesting to compare the data measured in a regular fuel element to that measured in the special fuel assembly sample holder. The HEU core center data has been normalized to the special sample holder data for comparison. The normalization factor was chosen to be the average value of the ratio of measured activity at the holder to the activity measured at the core center. If the fast spectrum is the same at both of these locations, then the normalized activities should be the same for the holder and core center measurements. The agreement between these data is remarkably good, and indicates that above a few MeV the fast spectrum in the special holder cannot be very different from the fast spectrum in a regular fuel element. While this is also expected based on the HAMMER results, it is nevertheless an

Table III-4a. Comparison of HEU Saturated Activities at the Special Assembly Holder Versus Core Center

Reaction	HEU Holder		HEU Core Center	
	Bare	Cadmium Covered	Bare	Cadmium Covered
Non-Threshold Reactions				
$Fe^{58}(n,\gamma)$	0.287-10	0.209-11	0.141-10	0.152-11
$Cu^{63}(n,\gamma)$	0.833-10	0.668-11	0.453-10	0.467-11
$Ag^{109}(n,\gamma)$	0.101-09	0.273-10	0.540-10	--
Normalized Threshold Reactions				
$Ti^{46}(n,p)$	--	0.157-12	--	0.160-12
$Ti^{47}(n,p)$	--	0.273-10	--	0.239-12
$Ti^{48}(n,p)$	--	0.422-14	--	0.439-14
$Fe^{54}(n,p)$	--	0.117-11	--	0.116-11
$Al^{27}(n,p)$	--	0.961-14	--	0.937-14
$Zr^{90}(n,p)$	--	0.105-14	--	0.104-14
$Ni^{58}(n,p)$	--	0.151-11	--	0.150-11
$Ni^{58}(n,p)$	--	--	--	0.309-16

(1) These measurements were made on another (see Figure III-2(a)) equilibrium HEU core, but at 1 Megawatt. The measured saturated activities at the center of this core are normalized to the sample holder data as described in the text.

Table III-4b. Comparison of LEU Saturated Activities at the Special Assembly Holder Versus Core Center

Reaction	LEU Holder		LEU Core Center[1]	
	Bare	Cadium Covered	Bare	Cadium Covered
Non-Threshold Reaction Measurements				
$Fe^{58}(n,\gamma)$	0.263-10	0.219-11	0.251-10 0.217-10[4]	0.293-11 0.279-11[4]
$Cu^{63}(n,\gamma)$	0.806-09	0.120-09	0.808-09[2] 0.838-09	0.158-09[2] 0.175-09
Threshold Reaction Measurements[3]				
$Fe^{54}(n,p)$	--	0.128-11	--	0.127-11
$Co^{59}(n,p)$	--	0.217-13	--	0.226-13
$Co^{59}(n,2n)$	--	0.301-14	--	0.306-14
$Ti^{46}(n,p)$	--	0.174-12	--	0.185-12
$Ti^{47}(n,p)$	--	0.330-12	--	0.303-12
$Ti^{48}(n,p)$	--	0.445-14	--	0.490-14
$Ni^{58}(n,p)$	--	0.178-11	--	0.181-11

(1) These LEU measurements were made on a different LEU core (2/9/84) shown in Figure III-3a.

(2) These LEU measurements were made on a different LEU core (5/10/83) shown in Figure III-3b.

(3) The saturated activities for the core were decreased by a factor of .595 in order to compare with the sample holder values. The core activities have an uncertainty of 5-10%.

(4) These LEU measurements were made on a different LEU core (10/7/83). Other LEU iron cadmium ratios measured at the core center (6/27/83) vary from 8.0-8.3.

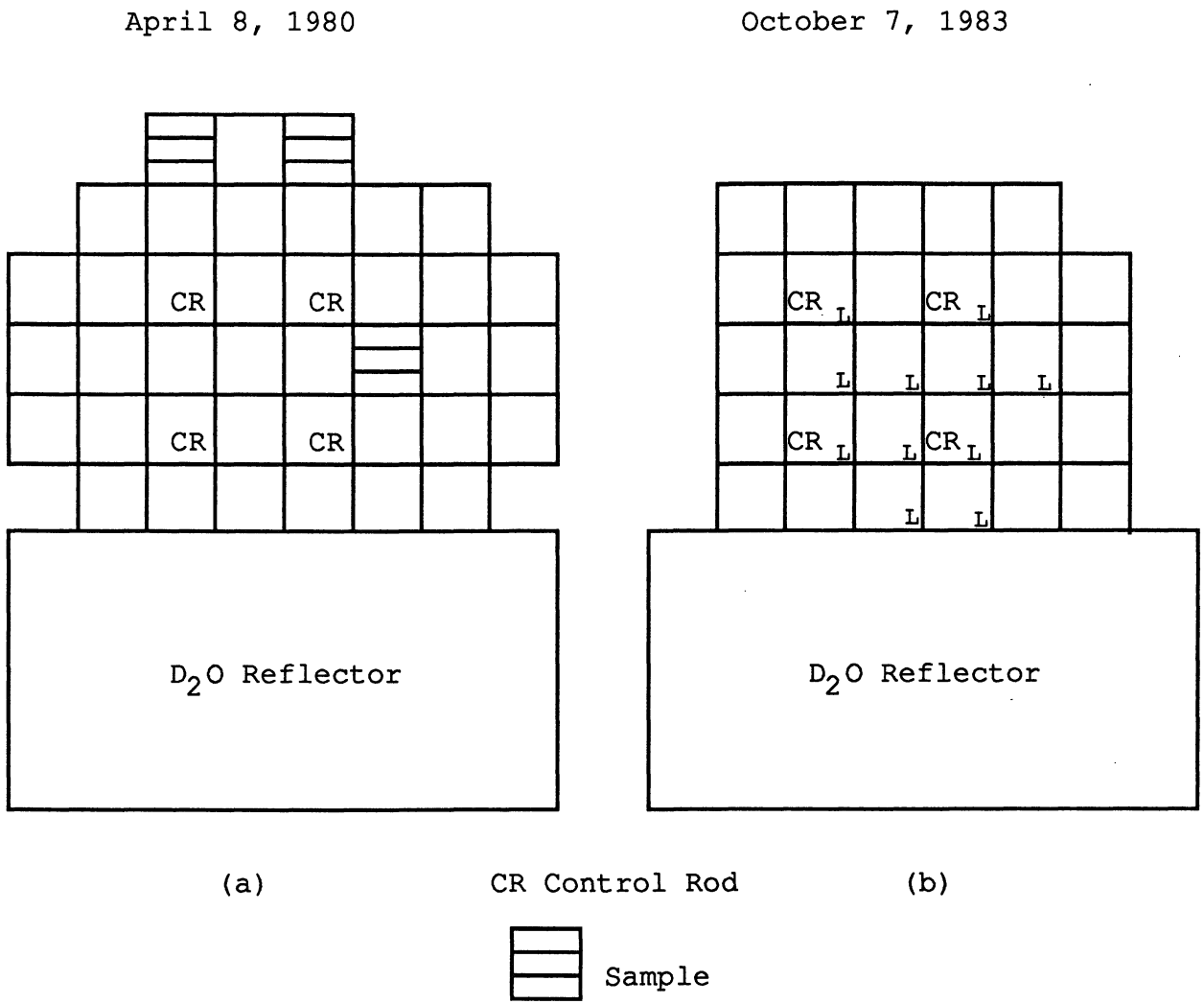

Figure III-2. Core Configurations for HEU and LEU Regular Assembly Measurements

experimental verification of our assumptions, as well as adding credibility to the accuracy of the measurements.

Table III-4b presents a comparison of bare and cadmium covered saturated activities measured at the center of an LEU core (shown in Figure III-3(a)) and at the special assembly sample holder in the LEU core shown in Figure III-1. These measurements also confirm that the spectrum is slightly harder at the core center, as expected. The measured threshold reaction data for the center of the LEU core was normalized to the LEU special holder data as described above. The LEU core center data have a greater uncertainty than the corresponding LEU holder data due to a larger uncertainty in the absolute detector efficiency. As a result, the 3.1% root-mean-squared difference between the LEU core center and LEU special holder of the threshold reaction data is larger than for the equivalent HEU data discussed above. Nevertheless, this data provide another verification that the spectrum above a few MeV will not be different from the spectrum at the core center.

Table III-5 shows the average cadmium ratios for iron for both HEU and LEU cores measured in the sample holder, at the core center, and in the heavy and light water reflectors. It is significant that the ratio of the HEU to LEU cadmium fractions are the same for the core and the sample holder. This corroborates our expectation that any spectral shift present at the core center will also be present at the sample holder. Note that there is no spectral change observed in the heavy water reflector, and it is

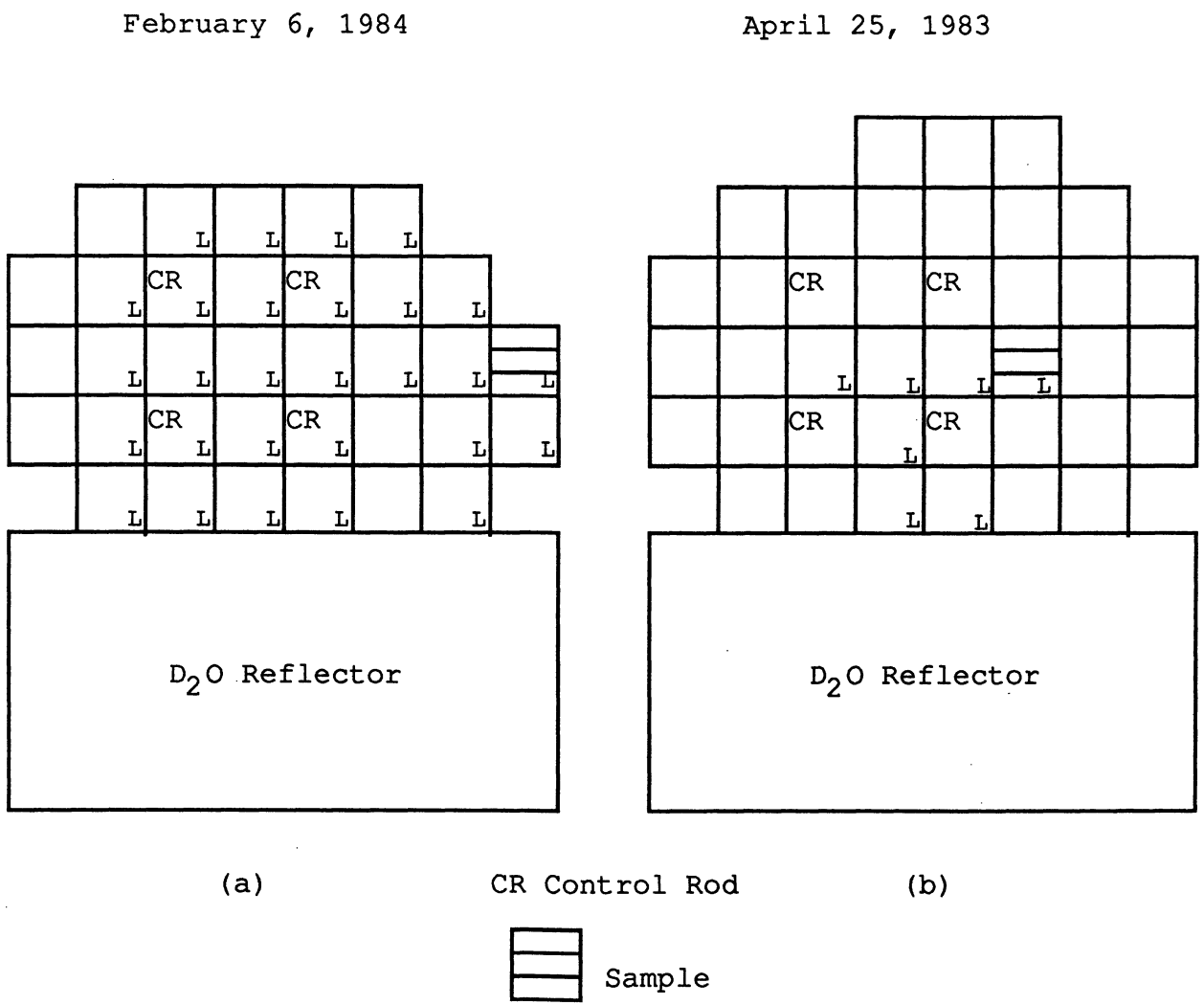

Figure III-3. Core Configurations for Additional LEU Measurements

Table III-5. Average Iron Cadmium Ratios for HEU and LEU Cores

Core Fuel	Sample Holder	Core [1]	D_2O [2] Reflector	H_2O [3] Reflector
HEU Fuel	13.7	9.5	20.	--
LEU Fuel	12.0 [5]	8.4	20.	26.
Cad. Fraction [4] Ratio (HEU/LEU)	1.15	1.15	1.0	--

(1) Measured between fuel plates of a regular fuel element in the center of the core. Quoted cadmium ratios are an average of 3 HEU and 2 LEU measurements made in the core.

(2) The heavy water reflector is adjacent to the edge of the core. Measurements were made 5 cm radially into the heavy water reflector.

(3) Measurements were made 2.5 cm away from the core boundary in the light water reflector.

(4) The cadmium fraction is the cadmium ratio minus one.

(5) For comparison, the cadmium ratio in the center of a water-filled special assembly was measured to be 20.

doubtful that any change would be observed in the light water reflector.

Table III-6 compares the subcadmium fluxes measured in the sample holder, using each of six capture reactions. The purpose here is to compare the consistency of the cross sections and flux measurements. The measured-to-calculated ratio is determined from:

$$\frac{A_b - A_c}{\int_0^\infty \sigma(E)\,G(E)\,[1-E_2\{t(E)\}]\,\phi(E)\,dE}$$

where A_b and A_c are the measured bare and cadmium covered saturated activities per unit target nucleus, $\sigma(E)$ is the reaction cross section, $G(E)$ is the self-shielding factor, $t(E)$ is the thickness of the cadmium cover measured in mean free paths, E_2 is an exponential integral, and $\phi(E)$ is energy-dependent flux calculated by HAMMER. Note that to within a multiplicative constant, the denominator is the effective subcadmium cross section. While the resulting agreement shown in Table III-6 is remarkably good for most of the reactions, we do find that iron is displaced from the average by about 10%. This difference is also corroborated by measurements made at the center of HEU and LEU cores which showed the iron subcadmium flux to be 16% larger than predicted by copper, and 7% larger than the value determined from cobalt. All of our previous measurements [Weh83a,Weh83b] which have made use of the

Table III-6. Comparison of Subcadmium Fluxes Measured by Different Reactions

REACTION	HEU MEASURED/CALCULATED	LEU MEASURED/CALCULATED
$Fe^{58}(n,\gamma)$	1.11	1.14
$Co^{59}(n,\gamma)$	1.01	1.02
$Au^{197}(n,\gamma)$	0.97	0.95
$Ag^{109}(n,\gamma)$	1.02	1.02
$Mn^{55}(n,\gamma)$	-	1.02
$Cu^{64}(n,\gamma)$	0.97	-

iron cross section will give a subcadmium flux which is about 10% too high. Thus, we conclude that the ENDF/B-IV iron capture cross section may be approximately 10% too small at thermal energies. [Note: The ENDF/B-V iron cross section is approximately 3% larger at thermal energies.]

2. Fast Flux Reaction Rate Data Measured in HEU and LEU Cores

Threshold reaction data have already been presented in Tables III-4a and III-4b for the center of the HEU and LEU cores. We have seen that there is negligible evidence that the fast spectrum will be different in the sample holder than in a regular

fuel element. In this section, we shall compare HEU and LEU threshold reaction data measured in the sample holder, and can assume that these comparisons are valid for regular fuel elements. Table III-7 presents a comprehensive set of threshold reaction data for measurements made in the special assembly sample holders for the HEU and LEU cores shown in Figure III-1. After normalizing the HEU and LEU solid holder data, the data agree to within a standard deviation of 5%. This is significant because it again confirms that down to approximately 0.5 MeV, there will be very little spectral difference between the HEU and LEU cores.

Also shown in Table III-7 is data taken in the air-filled sample holder in the LEU core shown in Figure III-2b. This data has a larger uncertainty associated with it, but includes the interesting $Pt^{195}(n,n')$ reaction. This reaction has a very low threshold energy (~0.1 Mev), and will be helpful in defining the spectrum below 1 MeV when the cross section is known to greater precision. If the hollow holder data are normalized to the LEU solid holder data, the two data sets agree to within a standard deviation of 8.8%. While this agreement is not as impressive as the comparison above, it implies that the solid aluminum around the threshold foils does not significantly perturb the fast spectrum. The shielding correction is given by:

$$G(E) = \frac{1 - 2E_3\{\Sigma(E)t\}}{2\Sigma(E)t}$$

Table III-7. Saturated Activities for Reactions Dominated by the Fast Flux

Reaction	HEU Solid Holder	LEU Solid Holder	LEU Hollow Holder
$Fe^{54}(n,\alpha)$	0.115-13	0.132-13	---
$Fe^{54}(n,p)$	0.117-11	0.128-11	0.101-11
$Fe^{56}(n,p)$	---	0.173-13	0.108-13
$Al^{27}(n,\alpha)$	0.961-14	0.112-13	0.742-14
$Ti^{46}(n,p)$	0.157-12	0.174-12	0.120-12
$Ti^{47}(n,p)$	0.273-12	0.330-12	0.236-12
$Ti^{48}(n,p)$	0.422-14	0.445-14	0.308-14
$Zn^{64}(n,p)$	0.484-12	0.503-12	0.322-12
$Mg^{24}(n,p)$	0.215-13	0.225-13	0.135-13
$Ni^{58}(n,p)$	0.151-11	0.178-11	0.112-11
$Zr^{90}(n,2n)$	0.105-14	0.117-14	---
$Np^{237}(n,fission)$	0.234-10	0.265-10	---
$U^{238}(n,fission)$	0.432-11	0.490-11	---
$Th^{232}(n,fission)$	0.113-11	0.132-11	---
$In^{115}(n,n')$	---	0.307-11	0.279-11
$Pt^{195}(n,n')$	---	---	0.518-12
$V^{51}(n,\alpha)$	---	0.290-15	---
$Co^{59}(n,p)$	---	0.217-13	---
$Mn^{55}(n,2n)$	---	0.390-14	---
$Ni^{60}(n,2n)$	0.251-13[1]	0.405-13	---
$Ni^{58}(n,2n)$	---	0.532-16	---
$Co^{59}(n,2n)$	---	0.301-14	---
$Cu^{63}(n,\alpha)$	0.600-14	---	---
$Al^{27}(n,p)$	---	0.635-13	---
$Rh^{103}(n,p)$	0.155-15	---	---

[1]Measured value has a 20% uncertainty associated with it.

where $\Sigma(E)$ is the macroscopic total cross section for aluminum, and t is the mean chord length for the solid holder. Using this expression, one can show that the perturbation of the solid aluminum holder on the fast flux should be negligibly small. Thus, the agreement between the hollow holder data and the solid holder data is not unexpected.

3. Thermal and Epithermal Unfolded Spectra

The unfolded HEU and LEU spectra are presented in this section. The semi-empirical unfolding technique was chosen for the deconvolutions since this approach allows the experimentalist to construct the unfolded spectrum on a foil-by-foil basis. The advantage of this approach is clearly shown in the discussion of the LEU spectrum below. Since both the LEU and HEU deconvolutions share the same unfolding parameters, we shall discuss our unfolding philosophy once prior to the presentation of both sets of results.

The semi-empirical technique iteratively refines the spectrum until the specified convergence criteria are met. Based on experience, we have chosen to limit the maximum number of allowed iterations to convergence to 15, and have defined convergence to occur when the average deviation between the measured and calculated activities is 5% or less. These criteria may appear too relaxed since the fitting residue would continue to decrease if the number of iterations were allowed to increase. However, our experience has shown that past a certain point, the unfolded spectra may develop spurious structure by radically changing the

flux in energy groups which have relatively little impact on the foil activities -- such as between 10 keV and 0.5 MeV. In order to compensate for these unphysical peaks and/or valleys, the spectra are normally "smoothed" (sometimes quite heavily) since one expects the flux to be fairly smooth. For instance, the flux at an energy group may be defined to be the average of several points on either side of the group. While the smoothing washes out these erroneous excursions, the resulting spectrum may not necessarily be a better approximation to the true spectrum. However, by limiting the maximum number of iterations, and defining convergence to have occurred when the average difference between the measured and calculated (based on the unfolded spectrum) activity is 5%, the generation of spurious structure caused by the unfolding technique can be avoided. Because of this conservative approach, the spectra do not need to be heavily "smoothed" to remove unphysical features.

In the spectra which are presented below, we have chosen to use Monte Carlo error analysis techniques. In this approach, the activities, cross sections, and input spectrum are randomly perturbed to within predefined limits, and then this new unfolding problem is solved. This scheme is repeated 10-20 times, and the results are used to generate the estimates of the uncertainties in the unfolded flux. While the limits of the perturbations on the cross sections and activities are the known uncertainties in these values, appropriate uncertainty limits for the input spectrum are more difficult. It is our belief that the input flux at any one

group is known a priori to within a factor of 2-10. This is an order of magnitude smaller than the inverse sensitivity method would predict. By limiting the input flux perturbations to these lower limits, our quoted uncertainties are believed to be more realistic.

We have chosen to unfold the detailed fast spectrum separately from the thermal and epithermal spectrum. This is desirable since there is too much activation data to perform a complete flux unfolding with an associated error analysis. This will not affect the accuracy of the thermal and epithermal fluxes which are presented. We have performed the thermal and epithermal flux unfoldings with all the measured threshold reactions, but without the error analysis, and then compared this result to the unfoldings with only a few threshold reactions. The addition of these threshold reactions does not change the HEU thermal and epithermal results presented below. For the LEU thermal and epithermal spectrum below, the inclusion of all measured threshold reactions increased the integral fast flux above 1 MeV by 4.0% above the result quoted below, but does not alter the shape or the magnitude of the spectrum below 1 MeV.

The results of the HEU thermal and epithermal unfoldings are shown in Tables III-8 and III-9 and Figure III-4. Table III-8 shows the non-threshold reactions which were used and the energy span in which 90% of the activity is produced. Also shown is a comparison of the measured activity to the activity calculated with

Table III-8. Comparison of HEU Unfolded Activities with Measured Activities

Reaction	Foil Cover Type	Energy Limits 90% Activity		Calculated Unfolded Activity	Ratio Measured to Calculated Activities	Deviation Measured from Calculated
		Lower (MeV)	Upper (MeV)			
FE58(N,G)FE59	Cadmium	8.291E-07	3.509E-04	2.140E-12	0.9768	-2.32
CO59(N,G)CO60	Bare	9.315E-09	1.079E-04	7.993E-10	1.0172	1.72
CO59(N,G)CO60	Cadmium	1.476E-06	1.488E-04	1.143E-10	0.9885	-1.15
AU197(N,G)AU198	Bare	1.626E-08	6.016E-06	4.062E-09	0.9848	-1.52
AU197(N,G)AU198	Cadmium	4.324E-06	1.725E-05	2.231E-09	0.9859	-1.41
U238(N,G)U239	Bare	4.288E-08	1.231E-04	2.760E-10	0.9780	-2.20
U238(N,G)U239	Cadmium	6.963E-06	1.426E-04	2.210E-10	1.0600	6.00
TH232(N,G)TH233	Cadmium	2.237E-05	1.882E-03	7.176E-11	1.0033	0.33
CU63(N,G)CU64	Bare	8.689E-09	3.934E-07	8.938E-11	0.9711	-2.89
MN55(N,G)MN56	Bare	8.620E-09	2.507E-07	2.564E-10	0.9711	-2.89
SC45(N,G)SC46	Bare	8.361E-09	1.496E-07	4.831E-10	0.9729	-2.71
SC45(N,G)SC46	Cadmium	5.184E-07	3.425E-05	1.721E-11	0.9702	-2.98
LU176(N,G)LU177	Bare	1.882E-08	1.618E-07	7.652E-08	0.9462	-5.38
LU176(N,G)LU177	Cadmium	1.315E-06	9.030E-05	1.352E-09	0.9614	-3.86
DY164(N,G)DY165M	Bare	7.923E-09	1.118E-07	4.308E-08	0.9609	-3.91
DY164(N,G)DY165M	Cadmium	3.895E-07	4.106E-06	5.483E-10	1.0414	4.14
NA23(N,G)NA24	Cadmium	7.758E-07	3.164E-03	4.817E-13	1.0049	0.49
U235(N,F)FSPR	Bare	7.657E-09	1.480E-07	1.065E-08	0.9956	-0.44
PU239(N,F)FSPR	Bare	1.042E-08	3.176E-07	1.797E-08	1.0296	2.96
AG109(N,G)AG110M	Bare	1.148E-08	5.926E-06	9.801E-11	1.0305	3.05
AG109(N,G)AG110M	Cadmium	2.738E-06	2.933E-04	2.762E-11	0.9884	-1.16
TA181(N,G)TA182	Cadmium	3.252E-06	2.386E-04	6.188E-10	1.0051	0.51
W186(N,G)W187	Bare	1.072E-08	1.847E-05	9.007E-10	0.9192	-8.08
W186(N,G)W187	Cadmium	6.513E-06	2.854E-05	2.345E-10	1.0193	1.93
NP237(N,F)FSPR	Cadmium	6.754E-01	4.171E+00	2.343E-11	0.9990	-0.10

Table III-9. HEU Unfolded Sample Holder Thermal and Epithermal Flux

Group	Energy (MeV)	Differential Flux		Integral Flux			
				Above E		Below E	
		(n/cm^2-sec-MeV)	δ(%)	(n/cm^2-sec)	δ(%)	(n/cm^2-sec)	δ(%)
1	1.00E-10	9.803E+18	9.1	6.355E+13	6.6	8.917E+09	9.1
2	1.00E-09	1.020E+20	7.2	6.355E+13	6.6	9.399E+11	7.2
3	1.00E-08	2.255E+20	5.8	6.262E+13	6.7	3.922E+12	6.1
4	2.30E-08	2.435E+20	4.6	5.963E+13	7.0	1.059E+13	5.1
5	5.00E-08	1.736E+20	2.8	5.296E+13	7.7	1.514E+13	4.1
6	7.60E-08	8.782E+19	7.8	4.842E+13	8.4	1.851E+13	2.9
7	1.15E-07	3.545E+19	10.5	4.505E+13	9.0	2.041E+13	2.6
8	1.70E-07	1.510E+19	15.9	4.315E+13	9.4	2.167E+13	2.8
9	2.55E-07	7.429E+18	17.5	4.189E+13	9.5	2.262E+13	3.1
10	3.80E-07	4.240E+18	9.1	4.093E+13	9.5	2.340E+13	3.1
11	5.50E-07	2.698E+18	8.0	4.016E+13	9.6	2.425E+13	3.0
12	8.40E-07	1.656E+18	10.0	3.931E+13	9.7	2.497E+13	3.1
13	1.27E-06	1.006E+18	19.1	3.859E+13	9.9	2.555E+13	3.3
14	1.90E-06	6.744E+17	6.2	3.801E+13	10.2	2.615E+13	3.3
15	2.80E-06	4.411E+17	10.4	3.741E+13	10.4	2.676E+13	3.2
16	4.25E-06	2.860E+17	4.9	3.680E+13	10.6	2.735E+13	3.1
17	6.30E-06	1.958E+17	8.0	3.620E+13	10.7	2.791E+13	3.1
18	9.20E-06	1.343E+17	12.1	3.564E+13	10.9	2.843E+13	3.2
19	1.35E-05	8.374E+16	21.2	3.513E+13	11.1	2.905E+13	3.0
20	2.10E-05	5.481E+16	15.7	3.450E+13	11.1	2.955E+13	2.8
21	3.00E-05	3.986E+16	5.7	3.400E+13	11.1	3.016E+13	2.7
22	4.50E-05	2.564E+16	14.6	3.339E+13	11.3	3.080E+13	2.5
23	6.90E-05	1.739E+16	13.4	3.276E+13	11.4	3.134E+13	2.3

Table III-9 (cont.)

Group	Energy (MeV)	Differential Flux		Integral Flux			
				Above E		Below E	
		(n/cm^2-sec-MeV)	δ(%)	(n/cm^2-sec)	δ(%)	(n/cm^2-sec)	δ(%)
24	1.00E-04	1.341E+16	7.8	3.221E+13	11.5	3.181E+13	2.3
25	1.35E-04	1.062E+16	6.5	3.174E+13	11.7	3.218E+13	2.3
26	1.70E-04	7.718E+15	10.5	3.137E+13	11.8	3.255E+13	2.2
27	2.20E-04	6.116E+15	29.3	3.101E+13	11.9	3.285E+13	2.1
28	2.80E-04	4.802E+15	26.9	3.071E+13	12.3	3.317E+13	2.1
29	3.60E-04	3.725E+15	11.6	3.038E+13	12.6	3.349E+13	2.0
30	4.50E-04	2.912E+15	18.1	3.007E+13	12.6	3.383E+13	2.0
31	5.75E-04	2.322E+15	17.3	2.972E+13	12.6	3.426E+13	1.9
32	7.60E-04	1.816E+15	16.2	2.930E+13	12.6	3.461E+13	1.9
33	9.60E-04	1.449E+15	19.1	2.895E+13	12.7	3.504E+13	2.0
34	1.27E-03	1.174E+15	22.0	2.851E+13	12.7	3.540E+13	2.0
35	1.60E-03	1.034E+15	24.8	2.816E+13	12.6	3.575E+13	2.1
36	2.00E-03	9.497E+14	31.5	2.780E+13	12.6	3.626E+13	2.3
37	2.70E-03	7.179E+14	29.6	2.729E+13	12.7	3.665E+13	2.6
38	3.40E-03	4.550E+14	18.6	2.690E+13	12.8	3.711E+13	2.7
39	4.50E-03	3.126E+14	11.6	2.645E+13	12.8	3.742E+13	2.8
40	5.50E-03	2.211E+14	12.4	2.614E+13	12.9	3.780E+13	2.8
41	7.20E-03	1.691E+14	11.1	2.576E+13	13.1	3.815E+13	2.8
42	9.20E-03	1.397E+14	13.7	2.540E+13	13.3	3.853E+13	2.8
43	1.20E-02	1.194E+14	16.1	2.502E+13	13.5	3.889E+13	2.9
44	1.50E-02	1.026E+14	16.0	2.466E+13	13.6	3.932E+13	3.0
45	1.90E-02	7.602E+13	14.9	2.424E+13	13.6	3.984E+13	3.1
46	2.55E-02	5.127E+13	16.4	2.372E+13	13.7	4.019E+13	3.2

Table III-9 (cont.)

Group	Energy (MeV)	Differential Flux		Integral Flux			
				Above E		Below E	
		(n/cm^2-sec-MeV)	δ(%)	(n/cm^2-sec)	δ(%)	(n/cm^2-sec)	δ(%)
47	3.20E-02	4.169E+13	16.2	2.337E+13	13.7	4.052E+13	3.3
48	4.00E-02	4.238E+13	17.9	2.303E+13	13.8	4.104E+13	3.4
49	5.25E-02	3.957E+13	20.0	2.252E+13	13.9	4.154E+13	3.6
50	6.60E-02	2.842E+13	18.6	2.201E+13	14.1	4.216E+13	3.9
51	8.80E-02	2.246E+13	19.1	2.140E+13	14.2	4.264E+13	4.0
52	1.10E-01	2.128E+13	19.9	2.091E+13	14.3	4.317E+13	4.2
53	1.35E-01	1.836E+13	20.2	2.039E+13	14.5	4.362E+13	4.4
54	1.60E-01	1.579E+13	20.9	1.993E+13	14.6	4.408E+13	4.5
55	1.90E-01	1.562E+13	21.3	1.947E+13	14.7	4.454E+13	4.7
56	2.20E-01	1.538E+13	21.5	1.902E+13	14.9	4.506E+13	4.9
57	2.55E-01	1.497E+13	21.2	1.849E+13	15.1	4.557E+13	5.1
58	2.90E-01	1.444E+13	20.4	1.798E+13	15.3	4.600E+13	5.2
59	3.20E-01	1.369E+13	19.2	1.756E+13	15.4	4.654E+13	5.4
60	3.60E-01	1.261E+13	19.3	1.701E+13	15.6	4.705E+13	5.5
61	4.00E-01	1.150E+13	20.7	1.651E+13	15.7	4.762E+13	5.6
62	4.50E-01	1.127E+13	22.7	1.593E+13	15.7	4.819E+13	5.7
63	5.00E-01	1.177E+13	24.5	1.537E+13	15.7	4.878E+13	5.7
64	5.50E-01	1.194E+13	26.2	1.478E+13	15.6	4.937E+13	5.8
65	6.00E-01	1.163E+13	27.6	1.418E+13	15.5	5.007E+13	5.9
66	6.60E-01	1.115E+13	28.9	1.348E+13	15.4	5.074E+13	6.0
67	7.20E-01	1.055E+13	30.0	1.282E+13	15.3	5.136E+13	6.0
68	7.80E-01	9.825E+12	31.1	1.219E+13	15.3	5.195E+13	6.1
69	8.40E-01	9.076E+12	32.1	1.160E+13	15.3	5.267E+13	6.2

Table III-9 (cont.)

Group	Energy (MeV)	Differential Flux		Integral Flux			
				Above E		Below E	
		(n/cm^2-sec-MeV)	δ(%)	(n/cm^2-sec)	δ(%)	(n/cm^2-sec)	δ(%)
70	9.20E-01	8.330E+12	30.9	1.089E+13	15.6	5.332E+13	6.4
71	1.00E+00	7.271E+12	26.1	1.023E+13	15.9	5.473E+13	6.6
72	1.20E+00	6.083E+12	22.1	8.819E+12	16.7	5.591E+13	6.7
73	1.40E+00	5.174E+12	21.4	7.646E+12	17.6	5.690E+13	6.8
74	1.60E+00	4.360E+12	27.3	6.659E+12	18.5	5.769E+13	6.9
75	1.80E+00	3.862E+12	40.9	5.863E+12	17.7	5.835E+13	7.0
76	2.00E+00	3.334E+12	42.8	5.206E+12	14.9	5.919E+13	7.1
77	2.30E+00	2.685E+12	28.4	4.361E+12	9.6	5.993E+13	7.1
78	2.60E+00	2.096E+12	14.8	3.626E+12	6.8	6.055E+13	7.1
79	2.90E+00	1.593E+12	11.0	3.007E+12	6.1	6.119E+13	7.0
80	3.30E+00	1.228E+12	10.9	2.361E+12	5.7	6.170E+13	6.9
81	3.70E+00	9.752E+11	8.4	1.853E+12	5.8	6.209E+13	6.8
82	4.10E+00	8.074E+11	7.8	1.463E+12	6.5	6.240E+13	6.8
83	4.50E+00	6.478E+11	6.6	1.157E+12	7.1	6.270E+13	6.7
84	5.00E+00	5.005E+11	7.4	8.501E+11	7.8	6.294E+13	6.7
85	5.50E+00	3.739E+11	9.1	6.113E+11	8.1	6.312E+13	6.7
86	6.00E+00	2.555E+11	9.3	4.319E+11	8.1	6.329E+13	6.6
87	6.70E+00	1.536E+11	9.0	2.608E+11	8.6	6.339E+13	6.6
88	7.40E+00	9.188E+10	9.1	1.589E+11	10.0	6.346E+13	6.6
89	8.20E+00	5.222E+10	9.8	8.985E+10	13.0	6.350E+13	6.6
90	9.00E+00	2.788E+10	11.1	5.098E+10	18.4	6.353E+13	6.6
91	1.00E+01	1.427E+10	10.9	2.529E+10	30.8	6.354E+13	6.6
92	1.10E+01	7.400E+09	16.6	1.229E+10	51.8	6.355E+13	6.6

Table III-9 (cont.)

Group	Energy (MeV)	Differential Flux		Integral Flux			
				Above E		Below E	
		(n/cm^2-sec-MeV)	δ(%)	(n/cm^2-sec)	δ(%)	(n/cm^2-sec)	δ(%)
93	1.20E+01	3.780E+09	36.8	5.767E+09	80.6	6.355E+13	6.6
94	1.30E+01	1.997E+09	65.6	2.738E+09	110.5	6.355E+13	6.6
95	1.40E+01	1.138E+09	96.5	1.382E+09	135.4	6.355E+13	6.6
96	1.50E+01	7.630E+08	126.5	7.643E+08	153.4	6.355E+13	6.6
97	1.60E+01	6.406E+08	153.9	4.485E+08	165.2	6.355E+13	6.6
98	1.70E+01	5.339E+08	171.7	2.540E+08	171.9	6.355E+13	6.6
99	1.80E+01	4.308E+08	181.8	1.263E+08	172.1	6.355E+13	6.6
100	1.90E+01	1.434E+08	145.6	3.712E+07	145.6	6.355E+13	6.6

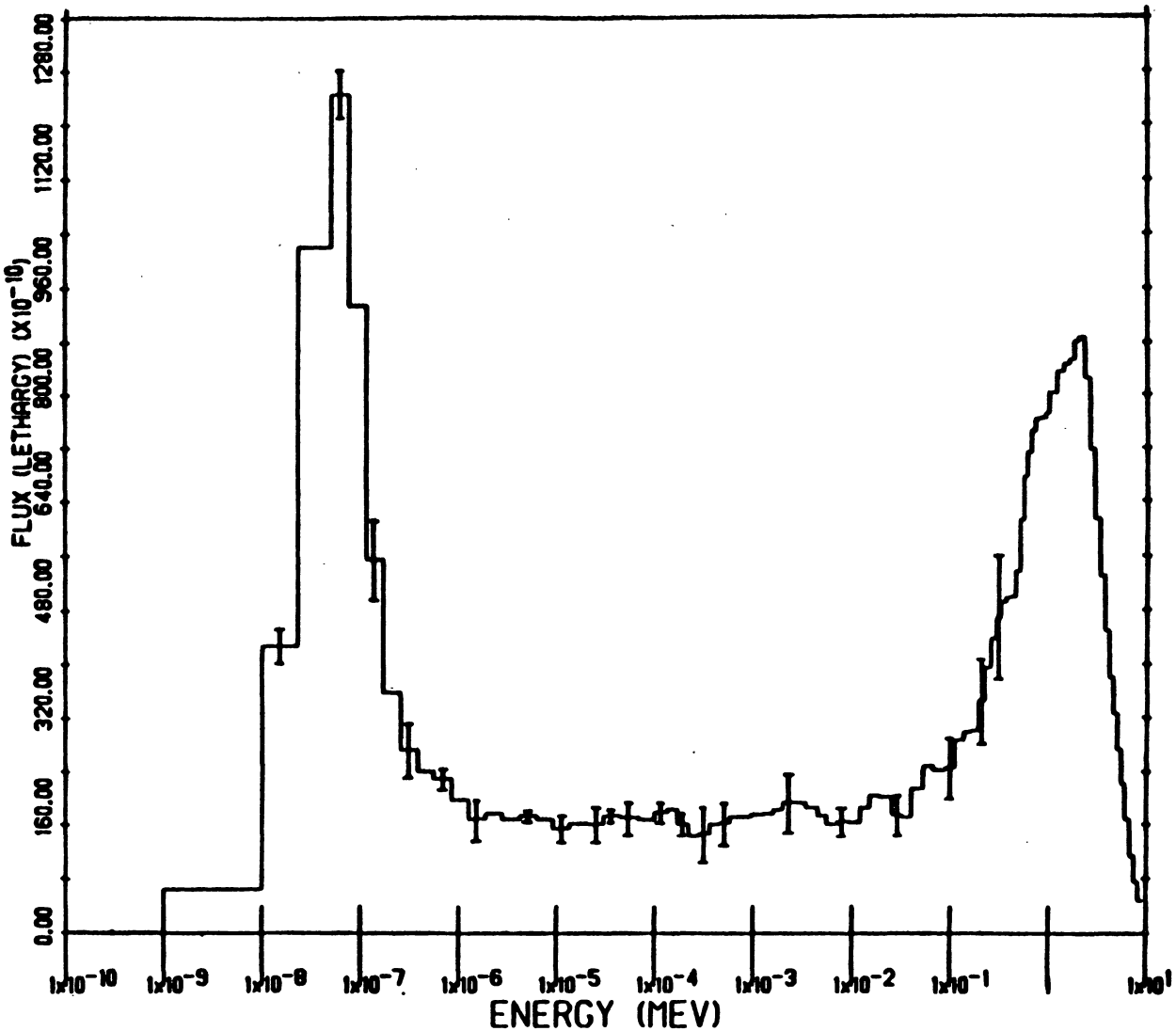

Figure III-4. FNR Unfolded HEU Spectrum.

the unfolded spectrum. The final column shows the percentage deviation of the measured activity from the calculated activity. Note that with very few exceptions, this agreement is quite acceptable (<5%). One particularly interesting result is the $Fe^{58}(n,\gamma)$ cadmium covered data shown in the first row of Table III-8. This datum is fit reasonably well by the unfolded spectrum. This implies that the iron capture reaction inconsistency shown in Table III-6 is probably not related to an error in the isotopic abundance, but is more likely attributable to the cross section we have used. Kirk [Kir81] have also noted the limited accuracy of the $Fe^{58}(n,\gamma)$ cross section.

Figure III-4 shows the measured HEU spectrum with the lethargy dependent flux plotted on a linear scale. This spectrum is harder than the HAMMER calculated spectrum, as expected. We shall defer comments about the physical meaning of the small fluctuations in the resonance energy region until after presenting the LEU results. However, without the rather substantial corrections discussed for self-shielding, gamma counting, and power calibrations, the spectrum would have large oscillations which would require considerable smoothing to remove. Table III-9 presents the values for the measured HEU differential and integral fluxes, as well as their uncertainties. Note that the uncertainties in the differential flux tend to vary significantly between groups for energies above 0.25 eV and below 10 keV. These fluctuations are probably due to the presence of resonances in these groups which

serve to enhance the sensitivity of the measurements there. For instance, the effect of the gold resonance at 4.9 eV is evidenced by a sharply lower uncertainty in that energy group. At energies above 9 MeV, the uncertainty in the unfolded flux increases dramatically. This is caused by the limited number of reactions which were used to provide sensitivity in this energy region. In the next section we shall present more accurate measurements of the differential fast fluxes. The last four columns of Table III-9 show the integral fluxes above (and including), and below (and including) each energy group. These results will be used later to compare the broad group fluxes in the HEU and LEU cores. In summary, based on the agreement between the measured and calculated activities, and the reasonable shape of the spectrum, we have accepted these results as the measured HEU spectrum. Since it has been our experience that the solution of the unfolding problem using one technique is also recognized as a solution using other techniques, we have not compared these results with the results using other approaches.

The LEU thermal and epithermal flux unfoldings highlight the advantage of using our interactive unfolding approach. Using all the data shown in Table III-1b, there were large unphysical fluctuations in the unfolded flux between 0.2 and 10 keV. To understand the source of this problem, we began with the twelve reactions with measured to calculated deviations less than five percent, and iteratively added a reaction and then performed the

unfolding. Each unfolded spectrum can be used as the input spectrum for the next foil addition. Figure III-5 shows the results when the cadmium covered manganese data is entered. This activity was calculated to be about 6% too large using the spectrum predicted by the remaining activation data. The dashed curve represents the initial input spectrum, and the solid curve is the resulting solution spectrum. The fraction of the total cadmium covered manganese activity produced in each energy group is also shown superimposed as a dashed curve upon the input and solution spectra. The majority of the manganese activity is produced in the 337 eV resonance, and to a lesser extent in the 1.080 keV resonance. Since the flux was well determined in the group containing the 337 eV resonance, the differential flux had to be perturbed more substantially in those groups which were not well determined. Note the significant perturbation which has occurred to the spectrum above 50 keV to compensate for only a 6% discrepancy between the measured and calculated manganese activity. This is a pathological problem with reactor spectral unfolding. As the number of measured activities increases, the consistency of the activities and cross sections must increase to prevent such magnified perturbations.

Table III-10 shows the non-threshold reactions which were used in the final LEU fittings. The fit is not as impressive as the HEU unfolding, but still meets the convergence criteria which were defined. Table III-11 presents the LEU results in a comparable

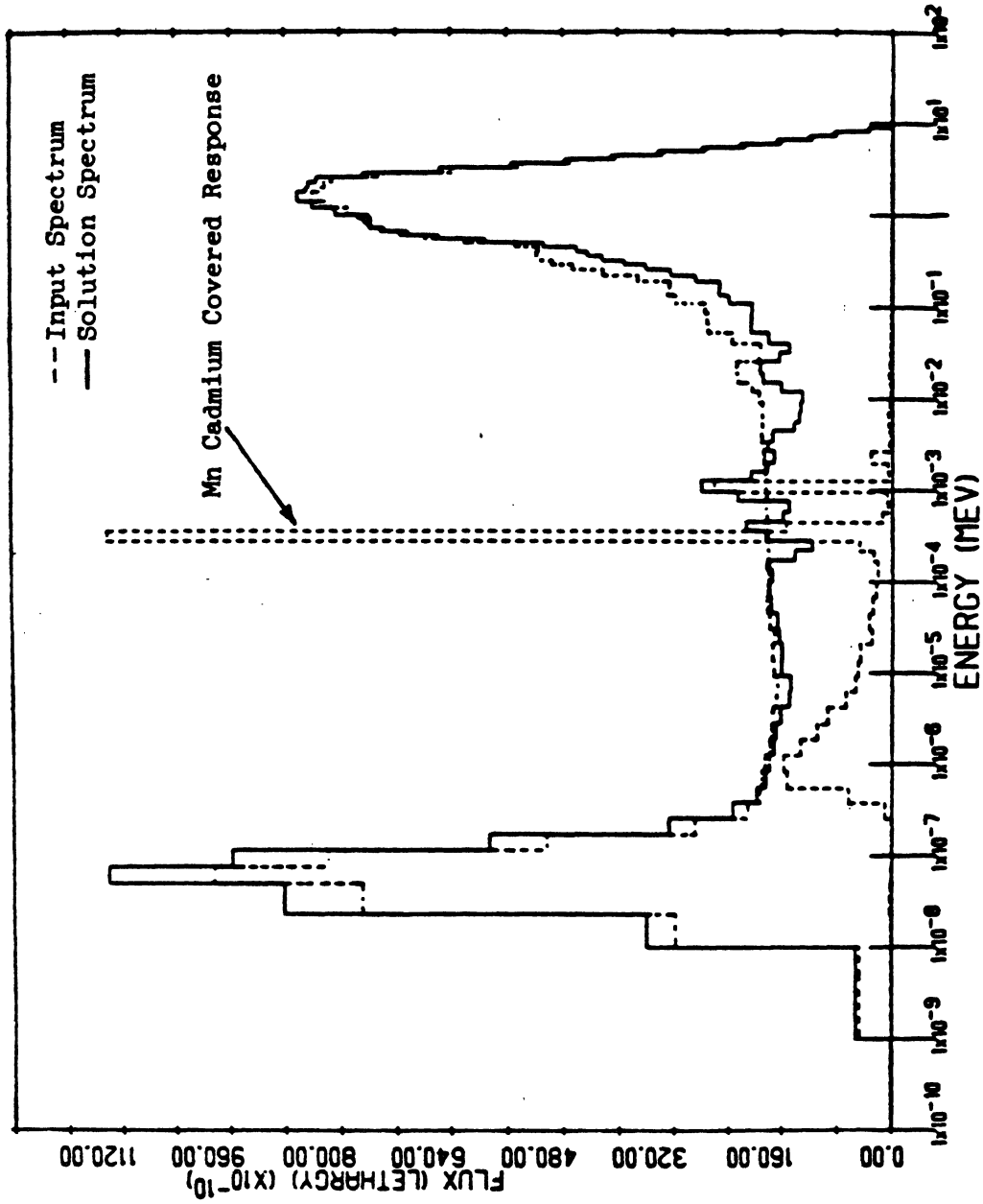

Figure III-5. Iterative Unfolding Example Using Mn.

Table III-10. Comparison of LEU Unfolded Activities with Measured Activities

Reaction	Foil Cover Type	Energy Limits 90% Activity		Calculated Unfolded Activity	Ratio Measured to Calculated Activities	Deviation Measured from Calculated (%)
		Lower (MeV)	Upper (MeV)			
U235(N,F)FSPR	Bare	8.042E-09	1.551E-07	1.058E-08	0.9077	-9.23
PU239(N,F)FSPR	Bare	1.094E-08	3.155E-07	1.798E-08	1.0013	0.13
U235(N,F)FSPR	Cadmium	7.997E-07	3.628E-03	4.523E-10	1.0392	3.92
PU239(N,F)FSPR	Cadmium	4.080E-07	1.541E-03	5.710E-10	1.0333	3.33
NP237(N,F)FSPR	Cadmium	6.760E-01	4.098E+00	2.642E-11	1.0029	0.29
CU63(N,G)CU64	Cadmium	1.044E-06	7.603E-03	8.056E-12	0.9657	-3.43
MN55(N,G)MN56	Bare	9.130E-09	2.997E-07	2.569E-10	1.0159	1.59
CO59(N,G)CO60	Bare	9.926E-09	1.109E-04	8.058E-10	1.0003	0.03
CO59(N,G)CO60	Cadmium	2.104E-06	1.492E-04	1.201E-10	0.9990	-0.10
FE58(N,G)FE59	Bare	9.260E-09	7.367E-07	2.369E-11	1.1102	11.02
FE58(N,G)FE59	Cadmium	1.135E-06	3.521E-04	2.349E-12	0.9323	-6.77
U238(N,G)U239	Cadmium	7.013E-06	1.720E-04	2.377E-10	0.9759	-2.41
TH232(N,G)TH233	Cadmium	2.257E-05	1.850E-03	7.920E-11	1.0101	1.01
AU197(N,G)AU198	Bare	1.711E-08	6.031E-06	4.066E-09	0.9296	-7.04
AU197(N,G)AU198	Cadmium	4.321E-06	1.367E-05	2.245E-09	0.9980	-0.20
AG109(N,G)AG110M	Bare	1.207E-08	6.012E-06	9.852E-11	1.0404	4.04
SC45(N,G)SC46	Bare	8.795E-09	1.531E-07	4.807E-10	1.0382	3.82

Table III-11. LEU Unfolded Sample Holder Thermal and Epithermal Flux

Group	Energy (MeV)	Differential Flux		Integral Flux			
				Above E		Below E	
		(n/cm^2-sec-MeV)	δ(%)	(n/cm^2-sec)	δ(%)	(n/cm^2-sec)	δ(%)
1	1.00E-10	9.438E+18	8.7	6.878E+13	4.8	8.211E+09	8.7
2	1.00E-09	9.878E+19	6.7	6.877E+13	4.8	8.750E+11	6.7
3	1.00E-08	2.201E+20	5.9	6.791E+13	4.8	3.691E+12	6.0
4	2.30E-08	2.424E+20	5.3	6.509E+13	5.0	1.015E+13	5.5
5	5.00E-08	1.809E+20	4.7	5.863E+13	5.4	1.480E+13	5.3
6	7.60E-08	1.001E+20	3.9	5.398E+13	5.9	1.865E+13	4.9
7	1.15E-07	4.156E+19	4.9	5.013E+13	6.3	2.089E+13	4.4
8	1.70E-07	1.603E+19	14.7	4.789E+13	6.5	2.222E+13	4.0
9	2.55E-07	7.438E+18	20.4	4.656E+13	6.5	2.315E+13	3.7
10	3.80E-07	4.236E+18	13.8	4.563E+13	6.6	2.389E+13	3.5
11	5.50E-07	2.716E+18	7.8	4.489E+13	6.8	2.470E+13	3.4
12	8.40E-07	1.758E+18	8.0	4.408E+13	6.9	2.546E+13	3.4
13	1.27E-06	1.147E+18	8.8	4.332E+13	7.1	2.618E+13	3.3
14	1.90E-06	7.787E+17	7.7	4.261E+13	7.2	2.689E+13	3.3
15	2.80E-06	5.036E+17	7.7	4.189E+13	7.4	2.765E+13	3.3
16	4.25E-06	2.967E+17	5.9	4.114E+13	7.6	2.826E+13	3.2
17	6.30E-06	1.926E+17	8.1	4.052E+13	7.8	2.884E+13	3.1
18	9.20E-06	1.371E+17	13.6	3.994E+13	7.9	2.947E+13	3.0
19	1.35E-05	8.975E+16	10.0	3.932E+13	8.0	3.014E+13	2.9
20	2.10E-05	6.403E+16	12.7	3.864E+13	8.1	3.071E+13	2.9
21	3.00E-05	4.646E+16	14.7	3.807E+13	8.1	3.139E+13	2.8
22	4.50E-05	3.090E+16	10.5	3.739E+13	8.2	3.214E+13	2.9
23	6.90E-05	2.110E+16	8.9	3.664E+13	8.2	3.281E+13	2.9

Table III-11 (cont.)

Group	Energy (MeV)	Differential Flux		Integral Flux			
				Above E		Below E	
		(n/cm^2-sec-MeV)	δ(%)	(n/cm^2-sec)	δ(%)	(n/cm^2-sec)	δ(%)
24	1.00E-04	1.446E+16	12.1	3.597E+13	8.4	3.332E+13	2.9
25	1.35E-04	1.144E+16	9.2	3.546E+13	8.6	3.372E+13	2.9
26	1.70E-04	7.277E+15	15.5	3.506E+13	8.8	3.410E+13	2.8
27	2.20E-04	5.089E+15	59.8	3.468E+13	8.9	3.439E+13	2.7
28	2.80E-04	5.719E+15	21.7	3.439E+13	9.1	3.483E+13	2.7
29	3.60E-04	5.275E+15	12.9	3.395E+13	9.3	3.529E+13	2.7
30	4.50E-04	3.062E+15	16.1	3.350E+13	9.3	3.567E+13	2.7
31	5.75E-04	2.179E+15	20.8	3.311E+13	9.3	3.607E+13	2.8
32	7.60E-04	2.588E+15	22.5	3.271E+13	9.4	3.655E+13	2.8
33	9.60E-04	2.495E+15	31.4	3.223E+13	9.3	3.724E+13	2.9
34	1.27E-03	1.461E+15	21.0	3.155E+13	8.9	3.769E+13	3.0
35	1.60E-03	1.002E+15	17.8	3.109E+13	8.8	3.809E+13	3.1
36	2.00E-03	7.157E+14	20.3	3.069E+13	8.8	3.858E+13	3.2
37	2.70E-03	6.144E+14	17.8	3.020E+13	8.9	3.901E+13	3.3
38	3.40E-03	4.523E+14	17.1	2.977E+13	8.8	3.951E+13	3.4
39	4.50E-03	2.860E+14	15.7	2.927E+13	8.8	3.980E+13	3.4
40	5.50E-03	2.127E+14	16.3	2.898E+13	8.9	4.018E+13	3.4
41	7.20E-03	1.696E+14	16.0	2.860E+13	9.1	4.053E+13	3.4
42	9.20E-03	1.343E+14	19.8	2.825E+13	9.2	4.090E+13	3.4
43	1.20E-02	1.251E+14	17.5	2.788E+13	9.3	4.127E+13	3.5
44	1.50E-02	1.184E+14	17.5	2.751E+13	9.4	4.174E+13	3.6
45	1.90E-02	9.383E+13	17.3	2.704E+13	9.4	4.235E+13	3.8
46	2.55E-02	6.265E+13	18.5	2.644E+13	9.5	4.275E+13	3.9

Table III-11 (cont.)

Group	Energy (MeV)	Differential Flux		Integral Flux			
				Above E		Below E	
		(n/cm^2-sec-MeV)	δ(%)	(n/cm^2-sec)	δ(%)	(n/cm^2-sec)	δ(%)
47	3.20E-02	4.736E+13	16.1	2.603E+13	9.5	4.313E+13	4.0
48	4.00E-02	4.530E+13	16.7	2.565E+13	9.5	4.369E+13	4.1
49	5.25E-02	4.124E+13	18.0	2.509E+13	9.6	4.425E+13	4.2
50	6.60E-02	3.189E+13	19.2	2.453E+13	9.5	4.496E+13	4.4
51	8.80E-02	2.491E+13	20.4	2.382E+13	9.5	4.551E+13	4.5
52	1.10E-01	2.365E+13	22.0	2.327E+13	9.5	4.611E+13	4.7
53	1.35E-01	2.063E+13	23.4	2.267E+13	9.4	4.663E+13	4.8
54	1.60E-01	1.716E+13	24.2	2.215E+13	9.3	4.715E+13	5.0
55	1.90E-01	1.656E+13	24.8	2.163E+13	9.3	4.766E+13	5.1
56	2.20E-01	1.603E+13	25.4	2.112E+13	9.3	4.823E+13	5.3
57	2.55E-01	1.528E+13	25.5	2.056E+13	9.3	4.877E+13	5.5
58	2.90E-01	1.450E+13	25.1	2.001E+13	9.4	4.922E+13	5.6
59	3.20E-01	1.358E+13	24.1	1.957E+13	9.5	4.977E+13	5.8
60	3.60E-01	1.234E+13	23.2	1.901E+13	9.6	5.028E+13	5.9
61	4.00E-01	1.109E+13	22.5	1.850E+13	9.7	5.085E+13	6.1
62	4.50E-01	1.070E+13	22.0	1.793E+13	9.9	5.141E+13	6.2
63	5.00E-01	1.104E+13	20.8	1.737E+13	10.0	4.198E+13	6.3
64	5.50E-01	1.111E+13	19.1	1.680E+13	10.1	5.256E+13	6.3
65	6.00E-01	1.075E+13	17.6	1.622E+13	10.2	5.324E+13	6.4
66	6.60E-01	1.024E+13	16.4	1.544E+13	10.4	5.388E+13	6.4
67	7.20E-01	9.632E+13	15.3	1.490E+13	10.6	5.449E+13	6.4
68	7.80E-01	8.947E+12	14.5	1.429E+13	10.8	5.505E+13	6.5
69	8.40E-01	8.250E+12	13.7	1.373E+13	11.0	5.575E+13	6.5

Table III-11 (cont.)

Group	Energy (MeV)	Differential Flux		Integral Flux			
				Above E		Below E	
		(n/cm^2-sec-MeV)	δ(%)	(n/cm^2-sec)	δ(%)	(n/cm^2-sec)	δ(%)
70	9.20E-01	7.623E+12	12.9	1.303E+13	11.2	5.639E+13	6.4
71	1.00E+00	6.908E+12	11.8	1.239E+13	11.5	5.785E+13	6.6
72	1.20E+00	6.076E+12	10.7	1.093E+13	12.3	5.914E+13	6.7
73	1.40E+00	5.393E+12	10.2	9.646E+12	13.1	6.028E+13	6.8
74	1.60E+00	4.762E+12	10.2	8.502E+12	13.9	6.129E+13	6.9
75	1.80E+00	4.198E+12	10.6	7.492E+12	14.7	6.218E+13	7.0
76	2.00E+00	3.696E+12	11.3	6.602E+12	15.4	6.335E+13	7.1
77	2.30E+00	3.203E+12	12.4	5.427E+12	16.5	6.437E+13	7.1
78	2.60E+00	2.632E+12	13.6	4.409E+12	17.6	6.521E+13	5.5
79	2.90E+00	1.998E+12	14.9	3.574E+12	18.7	6.605E+13	5.4
80	3.30E+00	1.498E+12	16.4	2.730E+12	19.9	6.668E+13	5.3
81	3.70E+00	1.159E+12	17.8	2.098E+12	21.0	6.717E+13	5.1
82	4.10E+00	9.044E+11	19.1	1.611E+12	22.0	6.755E+13	5.1
83	4.50E+00	6.841E+11	20.4	1.231E+12	22.9	6.791E+13	5.0
84	5.00E+00	5.049E+11	21.8	8.728E+11	23.9	6.817E+13	4.9
85	5.50E+00	3.674E+11	23.1	6.091E+11	24.9	6.836E+13	4.9
86	6.00E+00	2.505E+11	24.4	4.176E+11	25.7	6.855E+13	4.8
87	6.70E+00	1.618E+11	25.8	2.354E+11	26.7	6.866E+13	4.8
88	7.40E+00	1.033E+11	27.2	1.181E+11	27.6	6.875E+13	4.8
89	8.20E+00	3.978E+10	28.6	3.275E+10	28.6	6.878E+13	4.8

format to the HEU results presented in Table III-9. The uncertainties in these values are comparable to those presented for the HEU results. Figure III-6 shows the unfolded LEU thermal and epithermal fluxes. As with the HEU results, the spectrum above 1 MeV is unfolded in greater detail in the next section.

Figure III-7 compares the unfolded HEU and LEU spectra. The two spectra are normalized to have the same integral flux above 1 MeV. Beginning at 1 MeV and moving to lower energies, note the remarkable similarity between the spectra. In the region down to 0.1 MeV, this is principally a reflection of the agreement in the HAMMER calculated spectra since only the neptunium fission reaction has enough sensitivity in this region to alter the calculated spectra. In the region from 10 keV down to 10 eV, there is relatively good agreement in the shape of the spectrum. Both HEU and LEU spectra show identical depressions at about 0.2 keV for reasons which are not understood. Below 10 eV, the spectra begin to look distinct. It is in this region where the harder nature of the LEU spectrum becomes apparent. This may be related to the U^{238} capture cross section. While the U^{238} capture cross section has many resonances, principal resonances appear at 6.7, 10.2, and 20 eV. If a significant number of neutrons are absorbed in slowing down through these resonances, then one might expect the flux to be slightly lower in this region. In the thermal energy range, the significantly larger HEU thermal flux is quite apparent, and not unexpected.

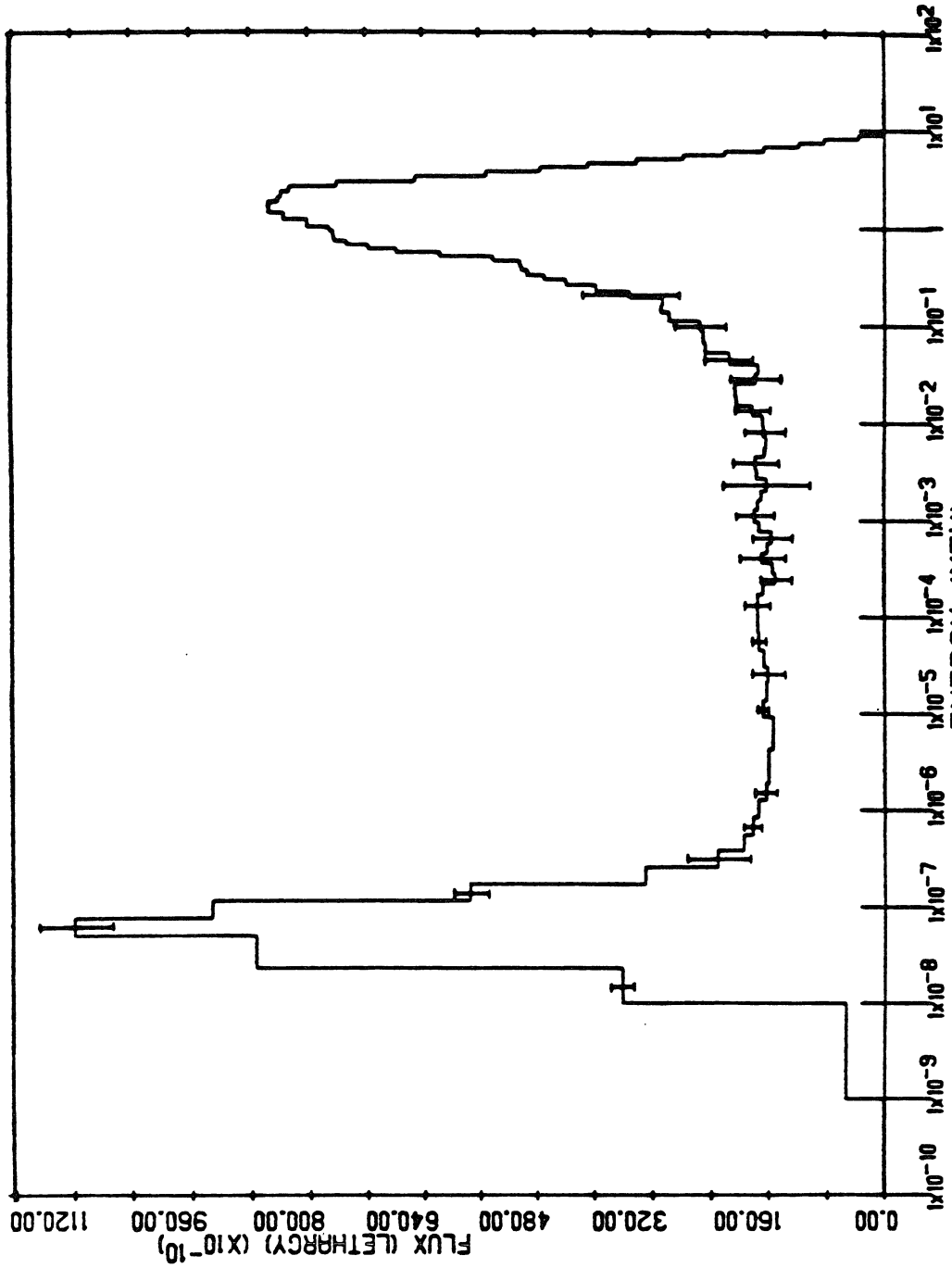

Figure III-6. FNR Unfolded LEU Spectrum.

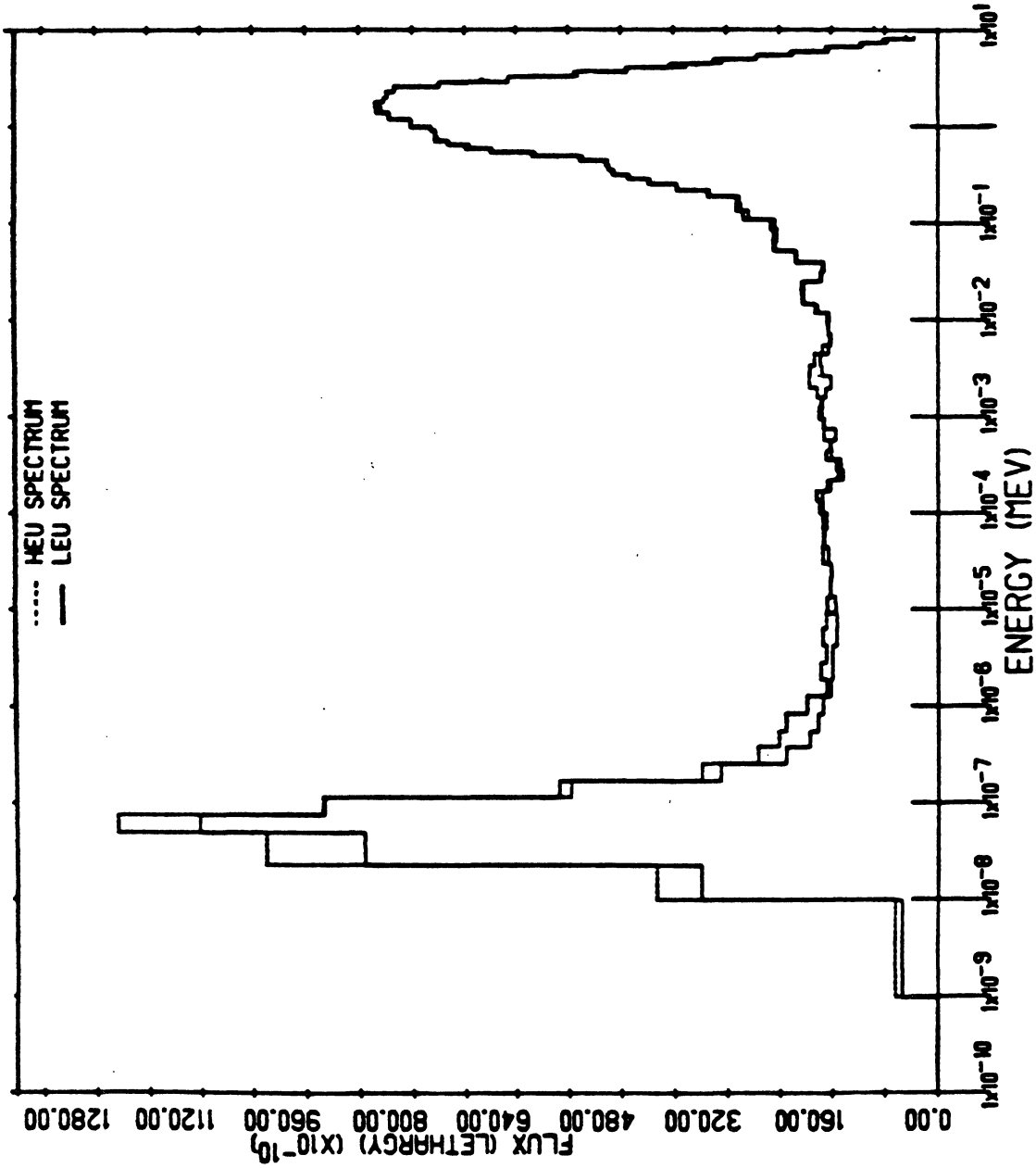

Figure III-7. Comparison of Normalized HEU and LEU Spectra.

Table III-12 compares the broad group integral fluxes for the HEU and LEU spectra. For each of the three broad groups, the integral flux and its uncertainty, and the fraction of the total integral flux are shown. The uncertainty in the collapsed broad group integral flux is smaller than the average of the uncertainties in the groups comprising it because of the strong correlations between groups. That is, if the differential flux is unfolded to be too large in one energy group, it will usually be too small in a nearby energy group so that the integral activity is close to being correct. Because of these correlations, the uncertainties in integral fluxes are usually much smaller than the uncertainties in the differential fluxes. For the fast flux, a large uncertainty in the integral flux is quoted based on the results shown in Tables III-9 and III-11. This is because we have used very few threshold foils in the unfoldings. In the next section, we shall show that the HEU fast flux is not different from the value presented in Table III-12, and the LEU fast flux is only 4% larger than the value presented here. Furthermore, the uncertainties in these fast flux values are much lower. The final column of Table III-12 shows the values of the HEU to LEU ratio of the integral fluxes normalized to the same fast flux. Note that the ratio of the subcadmium fluxes would increase to 1.22 using the better value for the LEU fast flux presented in the next section. This is slightly larger than the 1.19 value one would expect.

Table III-12. Broad Group Comparisons of Unfolded HEU and LEU Fluxes

Energy Region	HEU Results			LEU Results			Normalized Ratio HEU/LEU
	Integral Flux (10^{13})	δ(%)	Fraction of Total	Integral Flux (10^{13})	δ(%)	Fraction of Total	
ϕ_{sc} (E<.55 eV)	2.339	3.0	0.368	2.389	3.4	0.347	1.19±.03
ϕ_{epi} (.55 eV<E<1 MeV)	2.993	4.0	0.471	3.250	6.0	0.473	1.11
ϕ_{fast} (E>1 MeV)	1.023	15.9[1]	0.161	1.239	11.0[1]	0.180	1.00

(1) The actual uncertainty in this value is much smaller. These deconvolutions used only a few threshold reactions, and hence the results show a large uncertainty. The fast flux unfoldings used more reactions, and the integral fast fluxes differ slightly from these values.

4. Unfolded Fast Flux

The threshold reaction data shown in Table III-7 were used to unfold the HEU and LEU core fast fluxes. As expected, the HEU and LEU fast spectra showed the same general characteristics when they were unfolded. In the discussion which follows, we shall present the results of the LEU fast spectral unfolding, but note any differences from the HEU results.

For the fast flux unfolding, the energy region from 1 to 15 MeV was broken into 50 energy groups. A cross section library for this energy grid was developed for the threshold reactions. Not all of the measured threshold data reported in Table III-7 were used in the unfoldings. In particular, the $V^{51}(n,\alpha)$, $Mn^{55}(n,2n)$, $Ni^{59}(n,2n)$, $Np^{237}(n,fission)$, and $Mg^{24}(n,p)$ data were excluded from our final unfoldings. The $V^{51}(n,\alpha)$, $Mn^{55}(n,2n)$, and $Ni^{58}(n,2n)$ reactions were not used because the cross sections are not well known. When these cross sections are better determined, this data should be incorporated into the unfoldings. The $Np^{237}(n,fission)$ reaction is not included in the fast flux unfoldings reported here because 36% of the activity is produced below 1 MeV. We have performed fast flux unfoldings covering the energy range 0.5 MeV to 15 MeV using Np^{237}, and the measured fluxes are consistent with the data reported in Tables III-9 and III-11. This is expected since the same Np^{237} data was also used in both of those flux unfoldings. Finally, the $Mg^{24}(n,p)$ reaction was not included because the HEU and LEU solid holder measurements,

as well as the LEU hollow holder measurement, support a cross section which is 10% smaller in order to be consistent with other threshold reaction data covering nearly the same energy region.

Table III-13 shows the threshold reactions used, and the energy range of sensitivity to the flux for each case. These energy bands cover the region above 1.4 MeV completely, and their staggered positions imply the shape of the unfolded differential flux should be meaningful. In addition, the reaction rate per target nucleus which would be calculated using the unfolded flux is shown, along with a comparison with the measured activity. The average magnitude of the deviation is 3.7%, which is quite reasonable considering the uncertainties in the cross sections. We have allowed the number of iterations to increase to see if the fit would improve, but the solution changed only minimally. From this, we conclude that the solution is stable with respect to the number of iterations used. Furthermore, we have also employed two least squares unfolding methods (FERRET and STAYSL), but the shapes of the unfolded curves were not significantly different. As a result, we shall limit our discussion to the unfolded LEU results using the semi-empirical method (SANL). Table III-14 compares our deviations between measured and unfolded activities with those one would obtain from a more limited set of threshold data measured in the ORR [Gre79,Fri74]. It is interesting that the first three reactions, which represent some of our worst fit data, show the same type of disagreements after unfolding as the ORR data does.

Table III-13. LEU Unfolded Spectrum Activity Comparisons

Reaction	Cover Type	Energy Range for 90% Activity (MeV)		Unfolded Activity	Ratio of Measured to Unfolded Activities	Deviation of Measured from Unfolded (%)
		Lower	Upper			
IN115(N,N)IN115M	Cadmium	1.374E+00	5.001E+00	3.051E-12	1.0064	0.64
TH232(N,F)FSPR	Cadmium	1.565E+00	5.897E+00	1.213E-12	1.0881	8.81
U238(N,F)FSPR	Bare	1.570E+00	5.463E+00	5.231E-12	0.9366	-6.34
TI47(N,P)SC47	Cadmium	2.009E+00	6.391E+00	3.552E-13	0.9291	-7.09
NI58(N,P)CO58	Bare	2.322E+00	6.579E+00	1.657E-12	1.0739	7.39
ZN64(N,P)CU64	Cadmium	2.658E+00	6.407E+00	5.191E-13	0.9690	-3.10
FE54(N,P)54MN	Bare	2.669E+00	6.795E+00	1.254E-12	1.0207	2.07
AL27(N,P)MG27	Cadmium	3.847E+00	8.430E+00	6.711E-14	0.9462	-5.38
CO59(N,P)FE59	Bare	3.837E+00	8.512E+00	2.277E-14	0.9529	-4.71
TI46(N,P)SC46	Cadmium	4.250E+00	8.462E+00	1.652E-13	1.0530	5.30
NI60(N,P)CO60	Cadmium	5.318E+00	1.002E+01	4.013E-14	1.0092	0.92
FE54(N,A)CR51	Bare	5.483E+00	1.071E+01	1.234E-14	1.0695	6.95
FE56(N,P)MN56	Cadmium	5.669E+00	1.069E+01	1.739E-14	0.9950	-0.50
TI48(N,P)SC48	Cadmium	6.122E+00	1.181E+01	4.397E-15	1.0121	1.21
AL27(N,A)NA24	Cadmium	6.751E+00	1.168E+01	1.112E-14	1.0076	0.76
CO59(N,2N)CO58	Bare	1.153E+01	1.413E+01	2.994E-15	1.0053	0.53
ZR90(N,2N)ZR89	Cadmium	1.255E+01	1.450E+01	1.176E-15	0.9949	-0.51

Table III-14. Comparison of Deviations between Measured and Calculated Activities for FNR and ORR Unfoldings

REACTION	Deviation between Measured Activity and Unfolded Activity	
	FNR LEU	ORR
$Fe^{54}(n,\alpha)Cr^{51}$	7.	11.
$Ti^{47}(n,p)Sc^{47}$	-7.	-18.
$Ni^{58}(n,p)Co^{58}$	7.	6.
$Fe^{54}(n,p)Mn^{54}$	2.	5.
$Ti^{48}(n,p)Sc^{48}$	1.	-8.
U^{238}(n,fission)	-6.	8.

This type of similarity tends to strengthen our confidence in the measured activities, but raises questions about our cross sections.

Table III-15 presents the values of the differential unfolded flux, the associated uncertainty for each group (excluding the effects of errors in the cross sections), and the percentage difference between the input spectrum and the unfolded spectrum. We have deliberately separated out the effect of cross section errors on the uncertainty in the unfolded flux to illustrate the best possible results which could be obtained with accurate

Table III-15. Unfolded Differential Fast Flux

Group Number	Lower Energy (MeV)	Flux (n/cm^2-sec-MeV) Unfolded Spectra	Uncert. (%)	% Diff from input	Integral Flux Above E
1	0.100E+01	0.767E+13	16.0	-2.90	0.128E+14
2	0.125E+01	0.686E+13	12.0	-7.64	0.109E+14
3	0.150E+01	0.757E+13	9.3	-4.94	0.917E+13
4	0.175E+01	0.483E+13	7.2	0.86	0.773E+13
5	0.200E+01	0.424E+13	5.7	2.65	0.652E+13
6	0.225E+01	0.360E+13	4.1	2.93	0.546E+13
7	0.250E+01	0.296E+13	4.1	2.65	0.456E+13
8	0.275E+01	0.235E+13	4.4	3.32	0.382E+13
9	0.300E+01	0.196E+13	4.6	5.05	0.323E+13
10	0.325E+01	0.160E+13	4.8	5.83	0.276E+13
11	0.350E+01	0.137E+13	5.2	5.15	0.236E+13
12	0.375E+01	0.117E+13	5.7	3.60	0.201E+13
13	0.400E+01	0.100E+13	5.9	2.18	0.172E+13
14	0.425E+01	0.860E+12	5.8	1.70	0.147E+13
15	0.450E+01	0.750E+12	5.9	1.52	0.126E+13
16	0.475E+01	0.667E+12	5.6	0.86	0.107E+13
17	0.500E+01	0.579E+12	4.7	0.67	0.901E+12
18	0.525E+01	00496E+12	4.1	0.39	0.756E+12
19	0.550E+01	0.425E+12	4.5	0.77	0.632E+12
20	0.575E+01	0.364E+12	6.2	2.08	0.526E+12
21	0.600E+01	0.306E+12	6.8	3.70	0.435E+12
22	0.625E+01	0.250E+12	5.9	5.64	0.359E+12
23	0.650E+01	0.202E+12	5.6	7.72	0.296E+12
24	0.675E+01	0.165E+12	5.1	9.63	0.246E+12
25	0.700E+01	0.136E+12	4.6	11.35	0.204E+12
26	0.725E+01	0.113E+12	4.2	12.86	0.170E+12
27	0.750E+01	0.946E+11	4.4	14.27	0.142E+12
28	0.775E+01	0.797E+11	4.6	15.47	0.118E+12
29	0.800E+01	0.667E+11	4.5	16.52	0.985E+11
30	0.825E+01	0.553E+11	4.4	17.37	0.819E+11
31	0.850E+01	0.459E+11	4.4	18.07	0.680E+11
32	0.875E+01	0.382E+11	4.8	18.60	0.566E+11
33	0.900E+01	0.318E+11	5.8	19.00	0.470E+11
34	0.925E+01	0.265E+11	7.6	19.29	0.391E+11
35	0.950E+01	0.221E+11	9.6	19.50	0.325E+11
36	0.975E+01	0.183E+11	11.7	19.66	0.270E+11
37	0.100E+02	0.153E+11	13.8	19.86	0.224E+11
38	0.103E+02	0.127E+11	15.8	20.03	0.186E+11
39	0.105E+02	0.106E+11	17.0	19.80	0.154E+11
40	0.108E+02	0.894E+11	15.7	18.85	0.127E+11
41	0.110E+02	0.753E+11	13.2	17.86	0.105E+11
42	0.113E+02	0.634E+11	15.4	16.87	0.186E+10
43	0.115E+02	0.532E+10	19.0	16.06	0.703E+10
44	0.118E+02	0.443E+10	18.9	16.05	0.570E+10
45	0.120E+02	0.333E+10	12.9	18.45	0.459E+10
46	0.125E+02	0.225E+10	7.1	20.63	0.293E+10
47	0.130E+02	0.154E+10	5.8	22.05	0.180E+10
48	0.135E+02	0.105E+10	8.1	23.01	0.103E+10
49	0.140E+02	0.723E+09	10.8	23.60	0.509E+09
50	0.145E+02	0.294E+09	30.7	23.96	0.147E+09

activation data. However, we have performed the error analysis including estimates of the cross section uncertainties. For this case, the errors shown in Table III-15 increase by a factor of ~2-3.5. Thus, the uncertainty in the unfolded flux is dominated by the uncertainties in the cross sections. The uncertainty below 1.5 MeV is larger than at other energies because of the limited amount of foil coverage in this region. Also shown for reference in Table III-15 is the unfolded integral flux above each energy E. Table III-16 shows the errors associated with some integral fluxes. Note that the errors in the integral fluxes are less than the errors in the differential fluxes for reasons discussed earlier.

Table III-16. Analysis of Integral Flux Errors

Energy Range (MeV)		Integral Flux Uncertainty (%)	
From	To	no $\delta\sigma$	with $\delta\sigma$
1.5	15.0	2.56	8.24
1.5	4.0	3.60	10.31
4.0	6.0	4.44	11.52
6.0	9.0	4.47	7.60
9.0	12.0	9.66	24.80
12.0	15.0	7.08	15.13

Figure III-8 shows $\phi(E)$ versus energy for the calculated measured (solution) spectra. The input and solution spectra are normalized to give the same integral flux above 1 MeV. At 3.25 MeV, the unfolded flux shows a slight dip relative to the HAMMER input flux. Harris [Har67] attributed a dip in his proton recoil measurements to the oxygen elastic scattering resonance at about 3.5 MeV. Since our thermal and epithermal measured flux had a greater thermal to epithermal flux ratio than the calculations predicted, one might suspect the calculations were based on a model in which we underestimated the amount of water around the holder. If so, one might expect the measured flux to be slightly lower than the calculated flux at 3.5 MeV. From 4 to 6 MeV, the unfolded spectrum follows the shape of the HAMMER calculation reasonably well. It is interesting that integral fast spectrum measurements using threshold reactions have shown a large rise in the flux in this region relative to measurements made using other techniques. This has been the source of a controversy between direct differential measurements (e.g., proton recoil, time of flight) and integral measurements (i.e., foil activation) of the fission spectrum. Grundl [Gru68], McElroy [Mce69], and Fabry [Fab68] have independently reported a large (30%) "bulge" in the fast flux in the 3-6 MeV range, or an equivalent hardening in the "temperature" of the fission spectrum from ~1.29 MeV to 1.47 MeV. These early measurements used a much smaller set of threshold

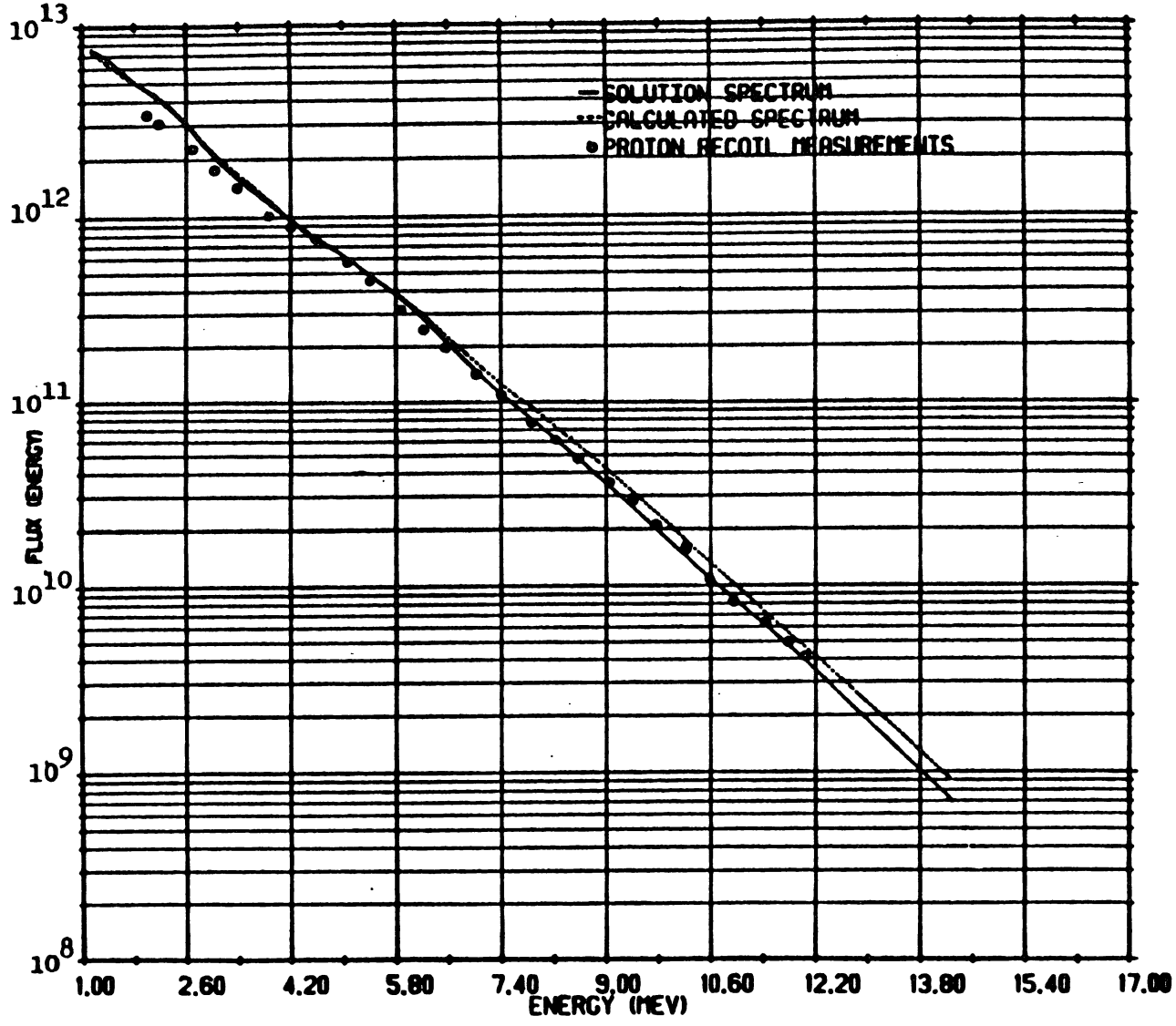

Figure III-8. FNR Measured and Calculated Fast Spectra.

reaction data than ours, and cross sections which were presumably less accurate.

Figure III-8 also shows Harris's proton recoil measurements for comparison. The calculations, unfolded spectrum, and proton recoil measurements agree at 4.5 MeV. It is interesting that our full spectral unfoldings using the newer ENDF-IV cross sections and a more comprehensive set of activation data still appears to show this deviation, although to a smaller extent. This tends to indicate that this controversy between direct differential measurements and integral methods (i.e., threshold activations), may be directly related to the accuracy of the cross sections known at that time. Above 7 MeV, the unfolded flux is significantly depressed relative to the calculated spectrum. It is impressive that a depression of the flux in this energy range was demanded by <u>all</u> of the five (six, if Mg^{24} is included) threshold reactions having sensitivity in this region. For this reason, it is difficult to dismiss this depression as an experimental error. For the HEU and the LEU hollow holder spectrum unfolded using the FERRET [Sch79], STAYSL [Per77], and SANL [Mce67] codes, this depression is also present. In this region, our calculated spectrum consists of a perturbed fission spectrum. The agreement between the measured proton recoil spectrum and the unfolded spectrum is quite good and lends credence to the shape of the unfolded results. Above 11 MeV, the agreement between the measured and calculated spectra remains poor. In this region, the (n,2n)

reactions are providing spectral sensitivity, so one would expect the unfolded results to be meaningful. Above 12 MeV, we do not have any proton recoil data to compare with our unfolded results. Overall, the unfolded spectrum is quite credible. Below 6 MeV, the unfolded spectrum agrees with the HAMMER calculated spectrum reasonably well, but at the lower energies, it deviates from the proton recoil data. Since there will be neutrons scattering down into these lower energies, one would expect the flux at these lower energies to be sensitive to the amount of water in the vicinity of the detectors. Thus, the unfolded flux should exceed the flux seen at the proton recoil spectrometer at lower energies. Above 6 MeV, the unfolded spectrum agrees well with the measured proton recoil data, but deviates from the calculated spectrum. This says that the particular extrapolation that we used to extend the HAMMER calculations was not appropriate, and does not reflect on the accuracy of that set of computer codes.

There are three conclusions we can draw from our fast flux unfolding efforts. First, we recognize that spectral unfolding does not provide the resolution which is available with the direct differential methods, such as proton recoil telescopes. This is inherent in the unfolding method and the shape of the cross sections. In practice, unfolding serves as a means for making refinements to one's best estimate of the spectrum to become more consistent with the integral activation measurements. Second, the unfolded solution does not appear to be significantly dependent

upon the method used for the unfolding. The spectral features described above were observed using all three unfolding methods. Solutions from one unfolding method were recognized as solutions to the other unfolding methods. This is not surprising since all methods attempt to minimize the difference between a measured and calculated activity. If one has a good first approximation to the spectrum, then the changes which must be introduced by the unfolding method will be small, and relatively independent of the technique used to infer the change.

Third, we have found the shape of the unfolded spectra to be relatively independent of the input spectrum in those energy regions where there is good foil coverage. We have tried moderately different input spectra for the region above 2 MeV to test this sensitivity, and the solution exhibited the same characteristics shown in Figure III-8. Furthermore, it is encouraging that the unfolded solution looks more like the previously measured spectrum rather than the input spectrum above 6 MeV. This indicates that the unfolded solution is more than just a reflection of the input spectrum. Finally, the accuracy of the high energy threshold reaction cross sections are currently the most significant obstacle to performing more precise fast flux unfoldings. Like the thermal and epithermal flux unfoldings, increasing the number of reactions used in the unfoldings may improve the resolution of the differential unfolded spectrum. However, because the cross sections are smoother and the energy

coverage more complete, one does not require the same amount of consistency between the measurements and cross section sets to prevent unphysical features in the unfolded spectrum. Thus, to some extent, unfolding the fast flux is an easier problem than unfolding the thermal and epithermal fluxes. But the error analysis has also shown that the accuracy of the unfolded spectrum is currently limited by the accuracy of the threshold cross sections. The errors in the differential fluxes have been estimated to be 15-40%, which is too large to expect to accurately see small perturbations in the spectrum. A complete set of threshold reactions (~15-20) with accurately known cross sections (~±3-5%) is probably required to be able to confidently unfold the differential fission spectrum with good precision and resolution. While the accuracy of many threshold cross sections has improved in the past 15 years, these conditions have still not been met. However, considering the difficulty of inferring differential quantities from integral measurements, it is impressive that the technique works even as well as it does.

5. Summary and Conclusions

The large number of reaction rate measurements has allowed a comparison of the consistency of the cross sections. For most reactions, there is a good agreement between the fluxes predicted using the measured activities and the cross sections. However, the iron capture reaction at thermal energies appears to be 10% too small when compared with the results of the measurements made using

cobalt, gold, silver, manganese, and copper foils. We have also noted in a separate work that there are inconsistencies in the gold total cross section at thermal energies which also need resolution. At higher energies, the $Mg^{24}(n,p)$ cross section yields a fast flux which is inconsistent with the results obtained using other threshold reactions. Based upon our measurements, this cross section should be decreased by 10%. The $Zn^{64}(n,p)$ cross section measured by Argonne National Laboratory is substantially different from the ENDF-IV evaluation. Since only the ANL cross section yields a reliable fast flux when applied to our measurements, we suggest the ANL cross section is more accurate. At very high energies (E>10 MeV), the accuracy of the cross sections in general is not particularly good. Precision measurements of the cross sections at these energies are difficult, but they are needed for more accurate deconvolutions of the high energy differential fast flux.

Regarding the unfolding methodology, we did not find much difference between the spectra determined with the semi-empirical and least squares unfolding techniques. This may have been because our initial estimate of the shape of the spectrum was too consistent with the activation measurements, so the amount of change required by the unfolding codes was not dramatic. We did, however, discover that the choice of the input spectrum normalization can affect the shape of the unfolded spectrum. This is an area which we believe has not been generally explored. The

interactive semi-empirical unfolding program we have used is similar to the SAND-II algorithm [Mce67], and has the advantages of speed, flexibility, convenience, and accuracy. It allows the user to graphically see the effects of each measured reaction rate on the unfolded flux, and provides a physical feel for the solution. The least squares methods we explored provide the mathematical guarantee of a minimum variance solution, and a rigorously correct error analysis. This latter advantage is the practical motivation for using the least squares techniques. However, while the error propagation is rigorous, the resulting errors are dependent upon knowledge of the uncertainties in the input spectrum, which are not well known. This is an area which has been receiving attention, and may make the least squares methods even more advantageous in the future.

The HEU and LEU spectra were found to be measurably different, particularly below the principal U^{238} capture resonances. For the same integral fast flux, the LEU integral subcadmium flux was measured to be 19±3% smaller than the HEU value. This corresponds almost exactly to the difference in the U^{235} number densities. Above 1 MeV, there were no measurable differences between the HEU and LEU spectrum. The unfolded fast spectrum agrees well with the measured proton recoil data above 4 MeV. A clean comparison of just these measured data is shown in Figure III-9 for reference. This level of agreement was achieved by using a large number of accurate threshold reaction data, recent ENDF-IV and -V cross

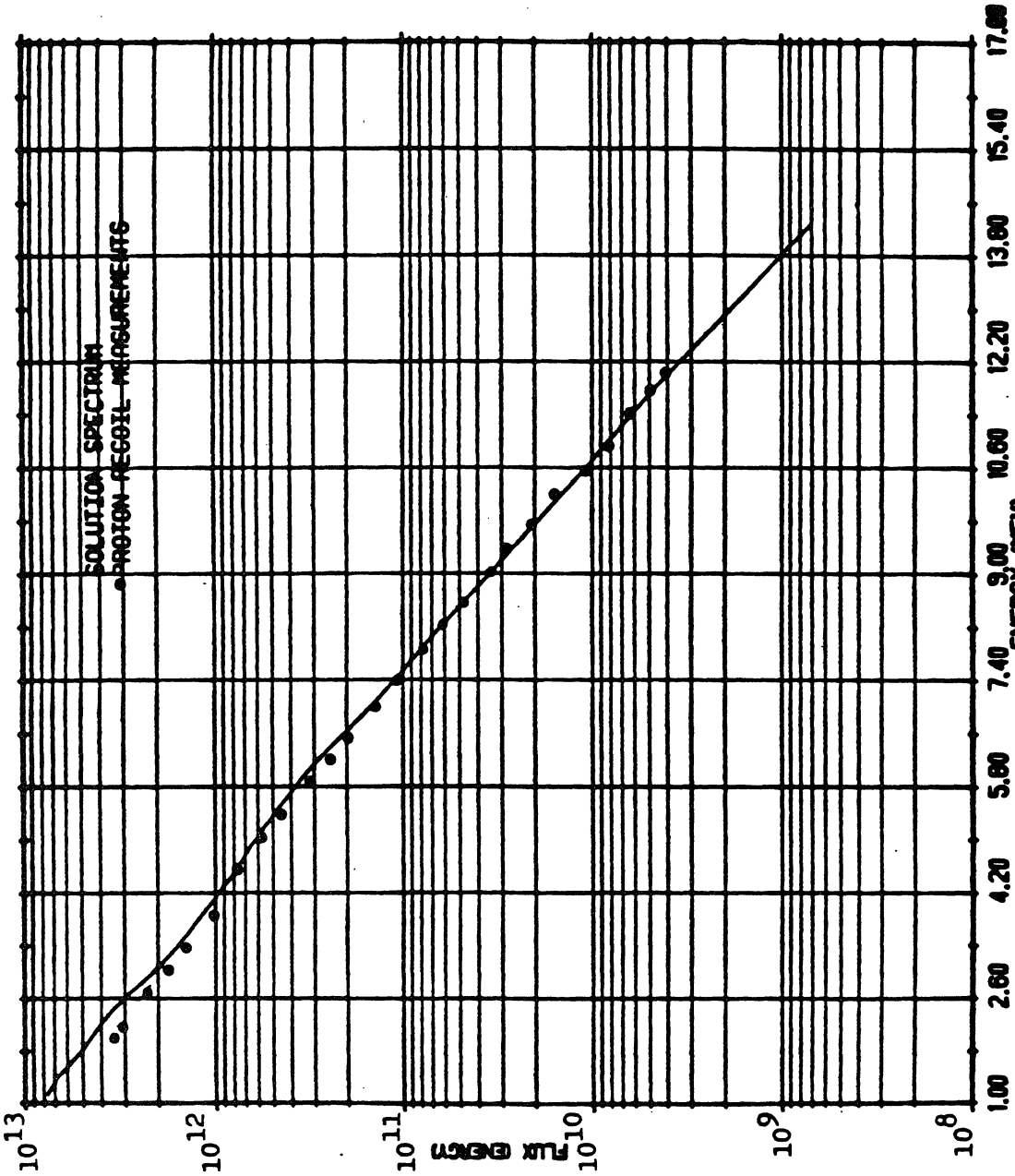

Figure III-9. FNR measured fast flux

sections, and the fact that the spectrum is sufficiently smooth (i.e., small second derivatives) at these energies so the lower resolution of the multiple foil method was not critical. From this, we conclude that the multiple foil method can be used to measure absolute differential fast spectra reasonably accurately.

B. Determination of SPND Sensitivity

1. SPND Detector Characteristics

The operating characteristics of a rhodium self-powered neutron detector (SPND) are discussed in [Hil64]. The SPND's used in these experiments have 0.020" diameter rhodium emitters, Al_2O_3 and MgO insulators, and 0.062" outer diameters. A background lead running the length of the detector cable was used to determine the background signal strength. Each detector is mounted on a 36" x 0.625" x 0.093" Inconel paddle for structural support. A 1.5" x 0.25" hole around the emitter reduces the perturbation caused by the paddle.

2. Measurements of the Detector Sensitivity

The SPND produces a direct current as its output signal. The net current signal is proportional to the reaction rate in the emitter, which in turn is proportional to the flux. The amount of current produced per unit flux is defined to be the sensitivity of the detector. More specifically, if f'_{sc} is the fraction of the net detector current I_{net} which would be produced by placing the detector into a flux with a subcadmium component ϕ_{sc}, then the subcadmium sensitivity is defined by:

$$S_{sc} \equiv \frac{f'_{sc} I_{net}}{\phi_{sc}}$$

To determine the detector sensitivity, the values of ϕ_{sc}, f'_{sc}, and I_{net} must be independently measured at the same location. These measurements were performed in the core and D_2O reflector, for both HEU and LEU fuels.

The net equilibrium current was determined by directly measuring the current (~50 nanoamps) coming from the emitter lead and subtracting the current measured at the background lead. Two rhodium SPND detectors with similar mountings were used during the course of these measurements. Calibrations performed in the core showed the detectors' measured net current were in good agreement.

The subcadmium current fraction was measured by activating bare and cadmium covered rhodium wires with the same diameter as the detector emitter. The wires were counted on a GeLi detector, and it can be shown that [Bal69a]

$$f'_{sc} \sim f_{sc} \equiv 1 - 1/CR$$

where CR is the cadmium ratio of rhodium. Measured values of f_{sc} are shown in Table III-17.

The subcadmium flux was determined by activating bare cadmium covered iron wires, and then counting the activities using a GeLi

Table III-17. Measured Subcadmium Correction Factor f_{sc}

	Position	HEU	LEU
L-35	Regular Fuel Element (Core Boundary, North Face)		.786
L-37	Regular Fuel Element (Core Center)	.791	.749
L-39	Regular Fuel Element (LEU South Face)		.795
L-40	Regular Fuel Element (HEU South Face)	.830	
L-67	Regular Fuel Element (Second Column from West Face)	.830	
L-57	Special Fuel Element (Third Column from West Face)		.860
H_2O	Water Reflector, Second Channel (Center Plane, South Face)	.930	.914
D_2O	Heavy Water Reflector (Position X) (Center Plane, North Face)	.895	.892
L-39	Special Fuel Element (Waterhole)	.913	

detector and ND6600 analyzer. Absolute efficiencies are determined from an NBS mixed radionuclide standard. The conversion from saturated activity A per unit nucleus to subcadmium flux is made using an LEU spectrum-averaged cross section calculated by a one-dimensional transport code as discussed further in Section V.A. Since

$$\phi_{sc} = \frac{A_b - A_c}{\sigma} ,$$

the sensitivity is directly proportional to this cross section, which in turn depends on the spectrum. While it is conventional to use a 2200 m/s cross section to obtain a sensitivity (S_{2200}) which is a current per "2200 m/s flux," the subcadmium flux is the true quantity of interest. Hence, a spectrum-averaged, subcadmium group cross section is used in the analysis.

To make these results more generally applicable, experiments were performed to separate out the effect of the paddle on the sensitivity. Inconel paddles which duplicated the detector support paddles were constructed and bare iron wires were attached. The loaded paddles were irradiated and the results of the activation were compared with bare iron wires irradiated without the paddle. The results show a 7% flux depression at the emitter caused by the paddle. Since the current from the emitter would be 7% larger without the paddle, the measured sensitivities have been increased by this amount.

Table III-18 shows the sensitivity determined from the measurements for the 2.54 cm long emitter with the effect of the support paddle removed. The subcadmium sensitivities measured in the HEU and LEU cores agree reasonably well. Since the HEU spectrum is softer in the core, this agreement would be even better if an HEU spectrum averaged cross section were used in the analysis. The subcadmium sensitivities measured in the heavy water reflector for HEU and LEU cores differ by ~ 16%, which is larger than expected. Comparing the average value of the sensitivity measured in the core to the average value measured in the heavy water reflector, it is clear that the detector is significantly more sensitive (~ 42%) in the reflector. Interestingly, this conclusion is still true even if the values were converted to conventional S_{2200} sensitivities.

Table III-18 also shows measured sensitivity values for an HEU core with an LEU element at the core center. It is interesting that the sensitivity in the LEU element agrees reasonably well with the value in an all-LEU core (~ 7% larger), and the D_2O sensitivity agrees reasonably well with the value measured on an all-HEU core (~ 7% larger).

Regarding the relative uncertainties, the LEU sensitivity values have been measured repeatedly and include additional measurements using the Co^{59} capture reactions. The ratio of the HEU core to D_2O-X values is also believed to be accurate, although it differs substantially (0.64 versus 0.79) from the equivalent LEU

Table III-18. Measured SPND Sensitivities at 1/4-Core Height for HEU, LEU, and Mixed Cores

Location Fuel Type	Iron Wire		Rh Wire	SPND	
	σ · (barns)	ϕ_{sc} (10^{13} n/cm^2-s)	f_{sc}	I_{net} (10^{-9} amps)	S_{sc} (1) (10^{-21} amps/ ϕ_{sc}-in)
Core Regular Element					
HEU	0.956	2.22	.81	47.78	1.87
LEU	0.952	1.76	.75	43.32	1.98
Mixed (2)	0.952	1.58	.75	41.60	2.11
Core Special Element					
HEU	1.023	----	.91	----	2.48
LEU	1.023	----	.86	----	2.48
Mixed	1.023	----	----	----	2.48
D_2O Reflector					
HEU	1.023	1.74	.90	52.67	2.92
LEU	1.023	2.16	.89	56.97	2.51
Mixed	1.023	1.68	.89	54.80	3.11
H_2O Reflector					
HEU	1.023	----	.93	----	2.53
LEU	1.023	----	----	----	2.53
Mixed	1.023	1.45	.93	36.90	2.53

(1) Rhodium emitters were 2.54 cm long and .0508 cm diameter; measured sensitivity increased by 7% to account for support paddle.

(2) LEU fuel element at center-of-core lattice position.

ratio. Table III-19 shows more recent measurements of the detector sensitivity, and indicates good agreement with the values presented in Table III-18.

3. Comparison with Previous Measurements

Table III-20 shows a compilation of previous measurements and calculations of the conventional S_{2200} sensitivity for rhodium SPND's similar to the ones used in these experiments. These values are also converted into subcadmium sensitivities for comparison with our measured values. These conversions were made by using the individual author's interpretation of the 2200 m/s flux, and multiplying by the appropriate ratio ϕ_{2200}/ϕ_{sc}.

The present measurements of the LEU core sensitivity are considerably lower than Warren's [War72] measurement (12%) and calculation (20%), but only about 3% lower than the measurements reported in [Kro75], [Bal69b] and [Deb72]. In the heavy water reflector, the present LEU measurement is about 4% higher than Warren's measurement, but about 25% larger than the values in [Kro75], [Bal69b] and [Deb72]. Thus in general, the heavy water sensitivity agrees reasonably well with Warren's measurements, while the sensitivity measured in the core is reasonably close to the other reported measurements.

4. Calculation of the Detector Sensitivity

The measured values for the sensitivity of the detector in the core disagree significantly both with Warren's calculation and the present measurement in the D_2O reflector. In order to identify

Table III-19. Core and D_2O Reflector Sensitivities for LEU Core of 8-4-84

Location	Foil	A(Sat)	ϕ_{sc} [1]	I(SPND)	f_{sc}	f_p	S (10^{-21} A/ϕ_{sc}-in)
L-37-18"	Fe(bare) Fe(cd)	1.62×10^{-11} 0.201×10^{-11}	1.49×10^{13}	38.1×10^{-9}	.75	1.07	2.05
D_2O-X-18"	Fe(bare) Fe(cd)[2]	1.98×10^{-11} 0.10×10^{-11}	1.84	48.3	.89	1.07	2.50
L-37-12"	Fe(bare) Fe(cd)[3]	2.19×10^{-11} 0.27×10^{-11}	2.02	48.6	.75	1.07	1.93
L-37-12"	Co(bare) Co(cd)	7.26×10^{-11} 1.56×10^{-11}	2.05	48.6	.75	1.07	1.91

(1) ϕ_{sc} is obtained by the difference in bare and cadmium saturated activities divided by the effective average activation cross section. For Fe, σ = .952b and for Co, σ =2.785b in the core. In D_2O for Fe, σ = 1.02b.

(2) Inferred from earlier cadmium ratio of 20.0.

(3) Inferred from measured value at 18".

Table III-20. Comparisons of SPND Sensitivities with Previously Quoted Values

Author	Emitter Dia. (mils)	S_{2200} (10^{-21} amps/ϕ_{2200} -cm)	S_{sc} (10^{-21} amps/ϕ_{sc} -cm)	
			Core	D_2O
Measurements				
Warren	.020	1.20	.89	.95
Kroon	.018	.91		
	.020	.99	.76	.80
Debair	.020	1.01		
Baldwin	.018	.96		
	.020	1.04(1)	.77	.83
This work (LEU)	.020	1.05		
D_2O	.020	1.25	.78	.99
Calculations				
This work(VIM-LEU)	.020	.99	.73	.78
D_2O		.98		
Warren	.020	1.31	.97	1.04
Laaksonen	.018	.75 (2)		
	.020	.88 (3)	.64	.68
Goldstein	.020	1.51	1.12	1.20

(1) Extrapolated to 20 mils based on Kroon's experiment.

(2) Value interpolated off graph at E_T = .030 eV.

(3) Extrapolation based on Laaksonen's estimate.

the source of these differences, an analytical model of the detector is developed below. If the detector is placed in a neutron flux, a new equilibrium signal will be produced which can be written as:

$$I_{net} = Ne \int_v P_\beta(\underline{r}) \int_0^\infty \sigma(E)\phi_p(\underline{r}, E)\, dE\, d\underline{r}$$

where e = electron charge, N = number density of nuclei in the emitter, and $\sigma(E)$ = the Rh^{103} activation cross section. $\phi_p(\underline{r},E)$ is the actual (perturbed) flux in the emitter at point $\underline{r}$ and energy E, $P_\beta(\underline{r})$ is the probability averaged over the beta spectrum that a beta emitted at point $\underline{r}$ will contribute to the detector current, and the spatial integral is over the volume V of the detector.

Since the ultimate goal is to determine the average unperturbed subcadmium flux ϕ_{sc} at the emitter's position without the detector present, it is convenient to define:

$$\beta_{sc} = \frac{\int_v P_\beta(\underline{r}) \int_o^{E_{cc}} \sigma(E)\ \phi_p(\underline{r},E)\ dE d\underline{r}}{\iint_{v\,o}^{E_{cc}} \sigma(E)\ \phi_p(\underline{r},E)\ dE d\underline{r}}$$

= average probability that a beta born in the emitter from a subcadmium reaction will contribute to the current

$$f'_{sc} = \frac{\int_v P_\beta(\underline{r}) \int_0^{E_{cc}} \sigma(E)\ \phi_p(\underline{r},E)\ dE d\underline{r}}{\int_v P_\beta(\underline{r}) \int_0^{\infty} \sigma(E)\ \phi_p(\underline{r},E)\ dE d\underline{r}} = \text{subcadmium current fraction}$$

$$f_p = \frac{\iint_{v\,o}^{E_{cc}} \phi_p(\underline{r},E)\ dE d\underline{r}}{\iint_{v\,o}^{E_{cc}} \phi_o(\underline{r},E)\ dE d\underline{r}} = \text{flux perturbation factor}$$

where $\phi_o(\underline{r},E)$ is the unperturbed flux which would be present at position $\underline{r}$ and energy E without the detector present, and

$$\sigma = \frac{\iint_{v\,o}^{E_{cc}} \sigma(E)\ \phi_p(\underline{r},E)\ dE d\underline{r}}{\iint_{v\,o}^{E_{cc}} \phi_p(\underline{r},E)\ dE d\underline{r}} = \text{subcadmium group cross section}$$

Using these definitions,

$$I_{net} = \frac{(NVe)\beta_{sc}\ \sigma f_p}{f'_{sc}} \langle \phi_{sc} \rangle$$

$$\text{where } \langle\phi_{sc}\rangle = \frac{1}{V}\int_{v}\int_{o}^{E_{cc}} \phi_o(\underline{r},E)\ dE d\underline{r}.$$

Thus,

$$\langle\phi_{sc}\rangle = \frac{f'_{sc}\ I_{net}}{(NVe)\ \beta_{sc}\ \phi f_p} \equiv \frac{f'_{sc}\ I_{net}}{S_{sc}}$$

where S_{SC} is defined to be the detector sensitivity. To calculate the sensitivity, one must then calculate the factors in:

$$S_{sc} = (NVe) \cdot \beta_{sc} \cdot \sigma \cdot f_p$$

for the detector.

(1) β_{SC}. Measurements [Bal69b] and calculations [Laa75,Deb72] of the beta escape probability indicate a value of 0.46 is appropriate for our spectrum and emitter geometry. This value is considerably smaller than Warren's [War72] calculated value. The SPND insulator space charge effect is calculated [Laa75,War72] to reduce this value by about 20%, which is reasonable since

measurements [Bal69a] on an 0.018" emitter show a 14% reduction. Thus, β_{sc} = 0.37 is adopted.

(2) σ, f_{sc}, f_p have been calculated using one-dimensional transport theory (ANISN) [Eng67], and three-dimensional Monte Carlo simulations (VIM) [Fil72] and are shown in Table III-21 for an LEU core. Because of the three dimensional capability, the VIM results are recommended, and compared in Table III-21 with previous calculations. On an absolute basis, the model underpredicts the core sensitivity by 6% and underpredicts the D_2O sensitivity by 21%. This agreement is quite reasonable for the core, and tends to support a measured core sensitivity which is lower than one would predict on the basis of Warren's model. The principal improvement comes from the lower values of β_{sc} and σ. The disagreement in the D_2O reflector calculations is disturbing, but reflects the difficulty in making calculations in a complex, heterogeneous D_2O reflector.

5. Concluding Remarks

As shown in Table III-18, the sensitivity of the rhodium SPND's measured in the FNR core (0.78 x 10^{-21} amps/ϕ_{sc}-cm) is lower than Warren's values reported in the literature for similar detectors. The sensitivities measured in HEU and LEU fuels agree reasonably well in the core (6% difference), but are 14% different in the D_2O reflector for reasons which are not known. The sensitivity measured in the core was substantially smaller than the values

Table III-21. Calculated SPND Sensitivities for LEU Fuel

Location	σ(barns)		f_p		f_{sc}			S_{sc} (10^{-21}A/ϕ_{sc}-in)	
	ANISN	VIM	ANISN	VIM	ANISN	VIM	MEAS.	ANISN	VIM
Core									
LEU Fuel	114.0	114.1	.747	.730	.80	.83	.75	1.90	1.86
D_2O Reflector	120.0	115.8	.719	.768	.89	.93	.89	1.92	1.98
H_2O Reflector		120.6		.733		.95	.93		1.97

measured in the heavy water reflector and in the light water reflector.

The analytic model predicts sensitivities which are in reasonable agreement with the measurements in the core, although it underestimates the observed sensitivity change between core and D_2O reflector. Comparing these results with the results of other approaches, this model offers an effective method for predicting subcadmium sensitivities of SPND's in the core.

C. Subcadmium Neutron Flux Measurements

1. Introduction

The FNR HEU-LEU Demonstration Experiments include a comprehensive set of experiments to identify and quantify significant operational differences between two nuclear fuel enrichments. One aspect of these measurements, the subcadmium flux profiling, is the subject of this section. The flux profiling effort has been accomplished through foil and wire activations, and by rhodium SPND mappings.

2. Activation Data

•Techniques

The irradiation of wires and foils in and around the FNR core provides information on the reactor flux. Irradiations in the core are made by taping the probe material to a thin (≈0.010") aluminum paddle approximately 30" long. In some cases, samples are enclosed by 0.020" cadmium capsules or tubing. The bare and cadmium covered probe materials are irradiated simultaneously,

mounted at the same core height, and separated in the horizontal plane by about an inch. The paddles are curved to facilitate insertion between two fuel plates (separation distance is 0.115"). A paddle stop rests on the top of the fuel plate and provides the axial reference point for the samples.

The heavy water tank on the north side of the core contains twelve 1" diameter, vertical tubes which penetrate into the tank. The majority of these penetrate to 8" below the top of the fuel plate. While these tubes are filled with H_2O, calculations indicate that the measurements are representative, within a few percent, of an unperturbed D_2O environment. Samples are activated in these tank penetrations by first securing the material to the outside of a 5/8" diameter aluminum rod or tube, and then lowering the holder to the bottom of the tank's vertical penetration. The samples are rotated during the irradiation to ensure uniform activations. In all cases, the reactor must be subcritical during both sample insertion and removal.

•Post-irradiation Handling and Counting

After the irradiations, the handling of the samples depends upon the activity and half-life of the activated material. For long-lived isotopes, such as Mn-54, the material is normally stored in the pool until ready for counting. For short-lived isotopes, such as Rh-104m, the samples must be expeditiously and remotely prepared for counting.

The counting of the activated samples is performed using GeLi

detectors. Wire samples are counted between two oppositely facing detectors multiplexed together. The sample is positioned by an automatic sample changer into a rotating, cylindrical plexiglass holder. Pulse pileup losses are accounted for with a precision pulser fed into the GeLi preamplifier. The amplified and multiplexed signals are counted using an ND 570 ADC and fed into an ND 6620 analyzer/computer for analysis. Absolute efficiencies can be determined with NBS and Amersham mixed point source standards through a cross calibration technique at a separate GeLi detector station. Background interference is made negligible for most gamma ray energies with 2-6" lead shielding around all detectors.

The counting data is processed to give a saturated activity per unit nucleus, A_{satn}, through the relationship:

$$A_{satn} = \frac{\lambda C_{net}\left(\frac{t_R}{t_L}\right)\{(\text{Pulser rate}\cdot t_L)/(\text{Pulser counts})\}}{\left(1-e^{-\lambda t_i}\right)\left(1-e^{-\lambda t_R}\right)\epsilon\left(1-e^{-\lambda t_w}\right)BR[m\cdot(a/o)\cdot N_{avo}/AW]}$$

where: λ = decay constant

C_{net} = net counts observed

t_l = detector live time

t_i = irradiation time

ϵ = absolute detector efficiency

BR = branching ratio

t_w = time between irradiation and counting

AW = atomic weight of element

N_{avo} = Avogadro's number

a/o = atom percent of parent isotope

m = sample weight

t_R = detector counting real time

Once the data is converted to saturated activity per nucleus, it can be further processed to give flux data by defining effective group cross sections. Define an effective activation cross section $\langle\sigma\rangle$ by:

$$\langle\sigma\rangle = \frac{\int_{o}^{E_{cc}} \sigma(E)\ \psi(E)\ dE}{\int_{E_a}^{E_b} \psi(E)\ dE}$$

where $\psi(E)$ is a computed spectrum. Then the group flux between E_a and E_b is:

$$\phi_{E_a}^{E_b} = \int_{E_a}^{E_b} \phi(E)\ dE = \frac{A_{satn}^{bare} - A_{satn}^{cadmium}}{\langle\sigma\rangle}$$

The subcadmium flux is then determined by choosing the limits of integration to be 0 to E_{cc}, where E_{cc} is the cadmium cutoff energy (~ 0.55 eV).

3. Experimental Results and Interpretations

•Single LEU Element Replacement

In a single element replacement experiment fresh HEU and LEU elements are alternately placed at the core center in an equilibrium HEU core. Iron wire activations were made along the full axial length of the elements, but for this experiment only bare wire activations were made. Figure III-10 shows the core geometry used. For operational convenience the fresh elements were simply interchanged between core center (L-37) and core edge (L-40).

An average was made of the saturated activities of the six one-inch wire segments symmetric about the core midplane, for both the HEU and LEU elements. Table III-22 gives the ratio of these averages for both iron wire reactions. The (n,p) threshold reaction responds to fast neutrons and suggests very little change

Table III-22. Single Element Replacement in Equilibrium HEU Core

Reaction	Ratio $\frac{\text{HEU Activity}}{\text{LEU Activity}}$
Fe-58(n,γ)Fe-59	1.19±0.036
Fe-54(n,p)Mn-54	1.00±0.031

in fission rate. The (n,γ) ratio is consistent with the degradation in low energy neutron intensity expected for the higher U-235 loading in the LEU element. This reaction has a small epicadmium contribution, not removed by cadmium covered

activations. Since it is anticipated that the LEU spectrum is somewhat harder than that of HEU, the HEU/LEU thermal flux ratio may be slightly larger than 1.19. However, this measured ratio is almost exactly equal to the ratio of the U^{235} masses.

•Rhodium SPND Flux Profiles

Many SPND maps have been obtained during the HEU/LEU comparison program. These have included partial or full profiles in the core, in the south H_2O reflector and in accessible positions of the D_2O north reflector. Activation results from Fe and Rh wires have been used to verify SPND profiles at specific points in both core and reflector. This verification has been particularly significant in a) comparing profile intensities from one core type to another, and b) comparing the core versus D_2O peak intensities in the profile of any given core.

A number of cores have been mapped: a) the large equilibrium HEU cores of dates May, 1979, September, 1979, August, 1980, November, 1981, and May, 1982. These cores should be closely equivalent in flux profile since loading patterns are essentially identical (see Figure III-11); b) three small LEU cores identified according to loading dates January 8, 1982, January 21, 1982, and April 16, 1982 (see Figures III-12 and III-13). The April LEU core is somewhat larger than the January LEU and shifted in east to west in loading geometry; c) the so-called "high leakage" HEU cores of July, August, September, and October, 1982 (see Figure III-14). These have the narrow five row North-South loading of the LEU cores

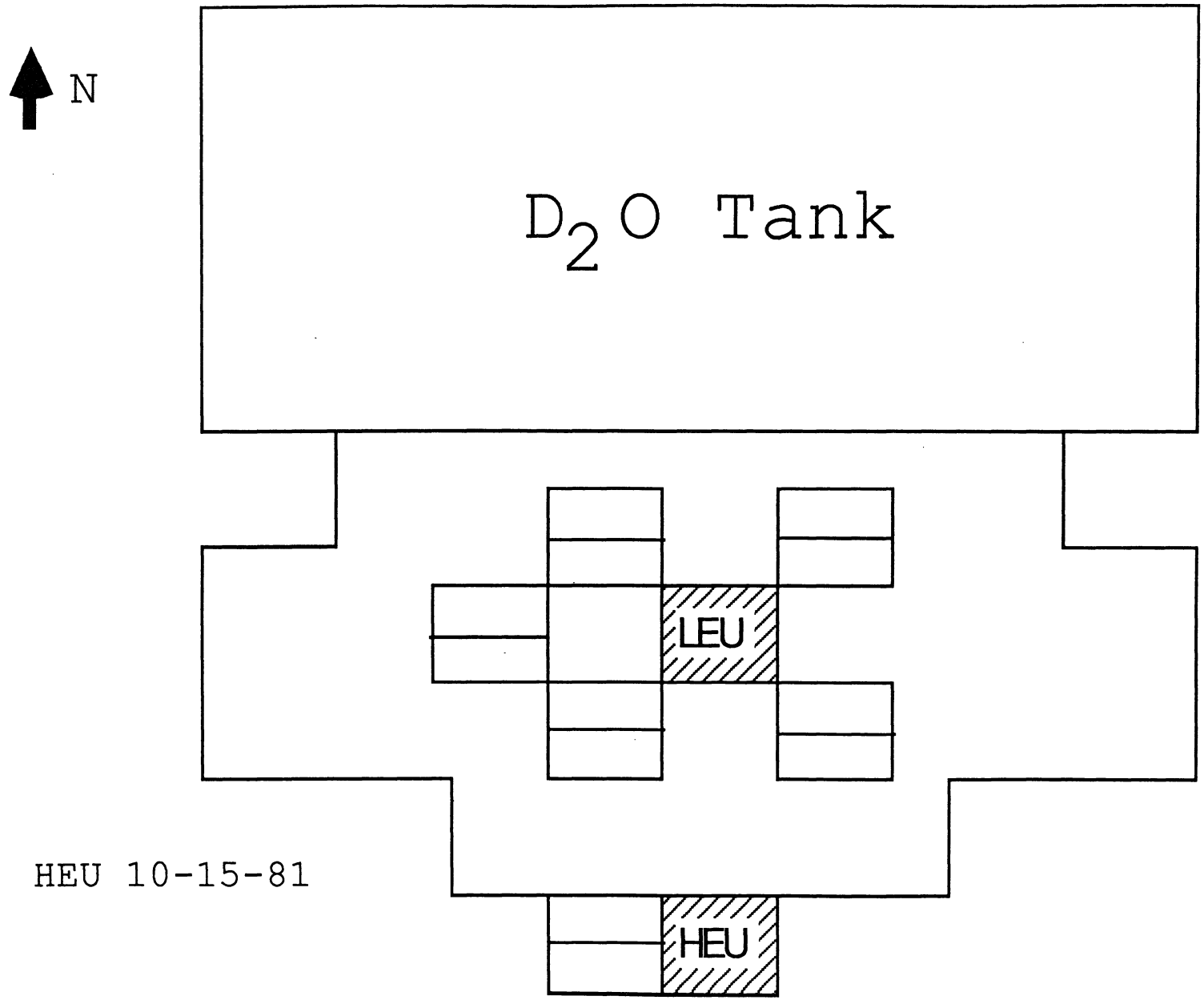

Figure III-10. Core Geometry for Single Element Replacement

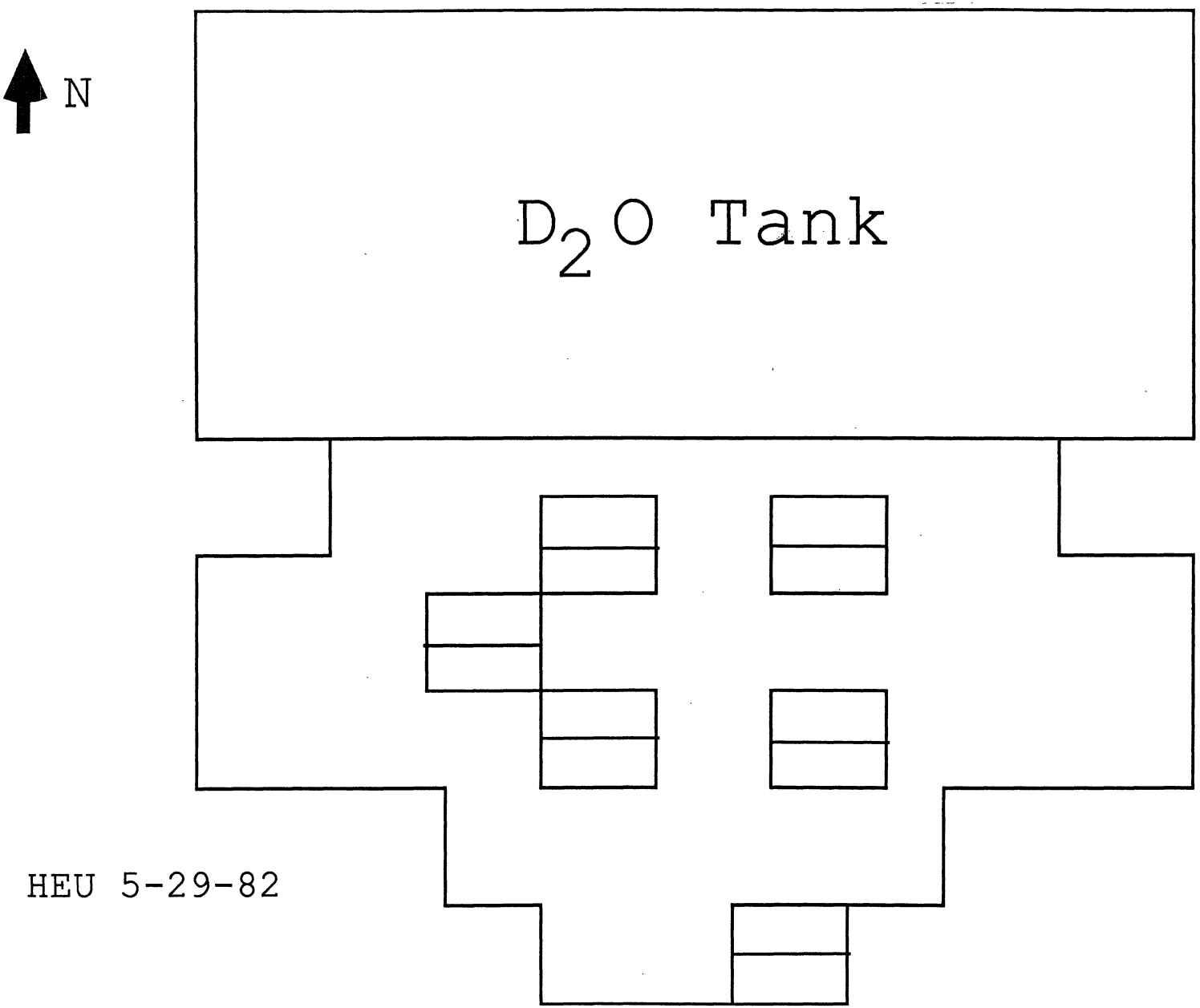

Figure III-11. HEU Normal Core Pattern. Special elements noted by ⊟

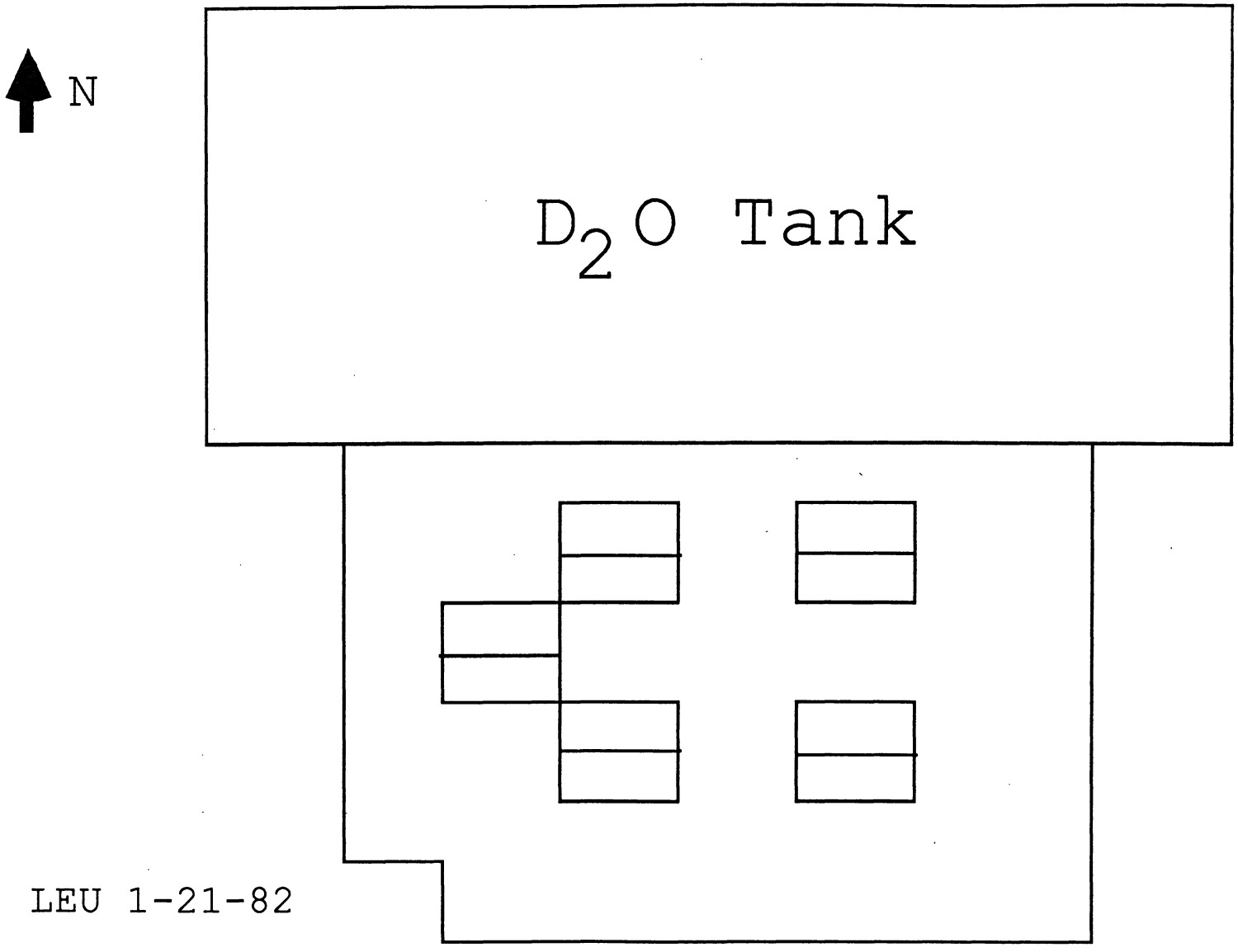

Figure III-12. LEU (1-21-82) Core Pattern.

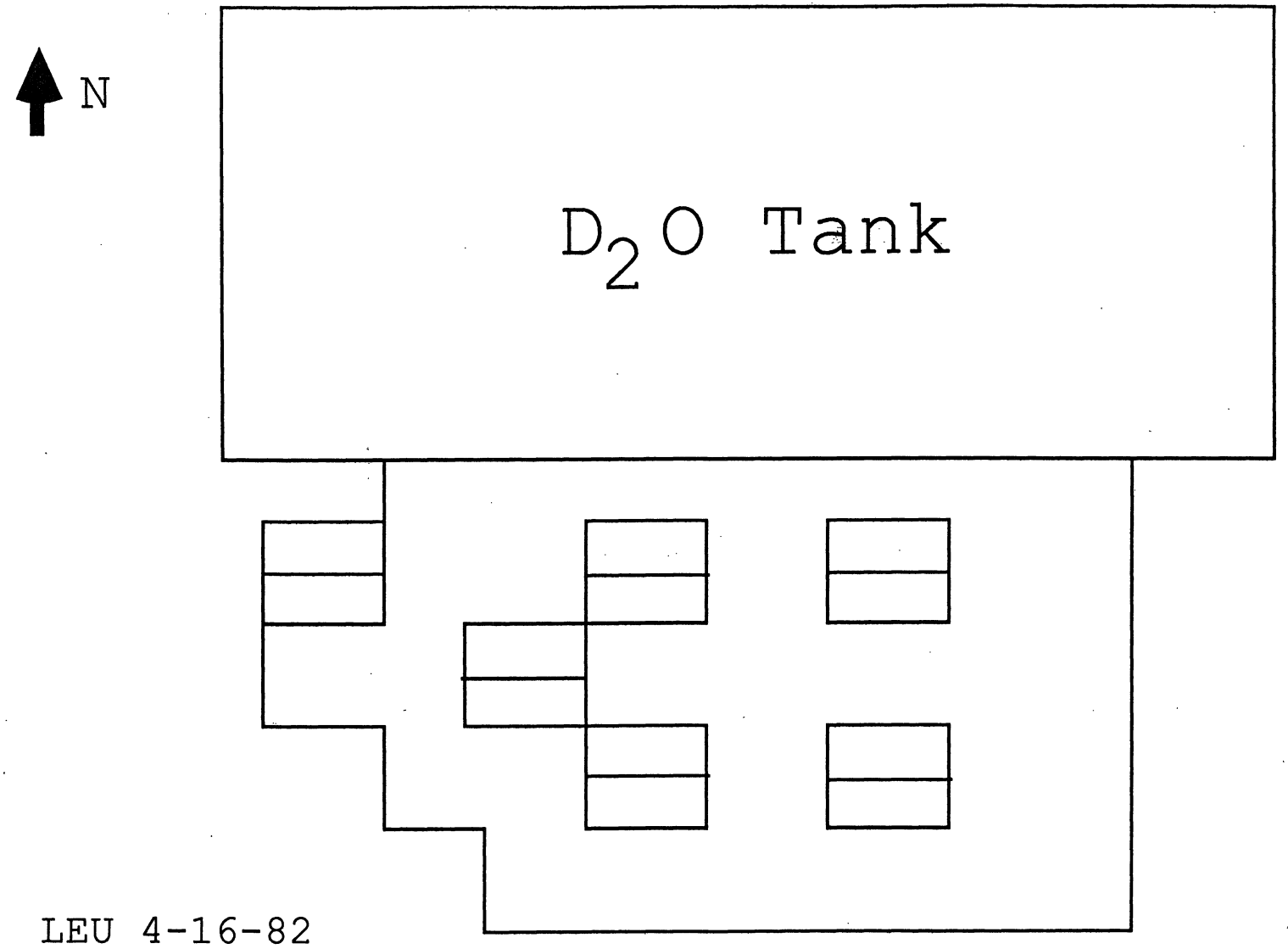

Figure III-13. LEU (4-16-82) Core Pattern.

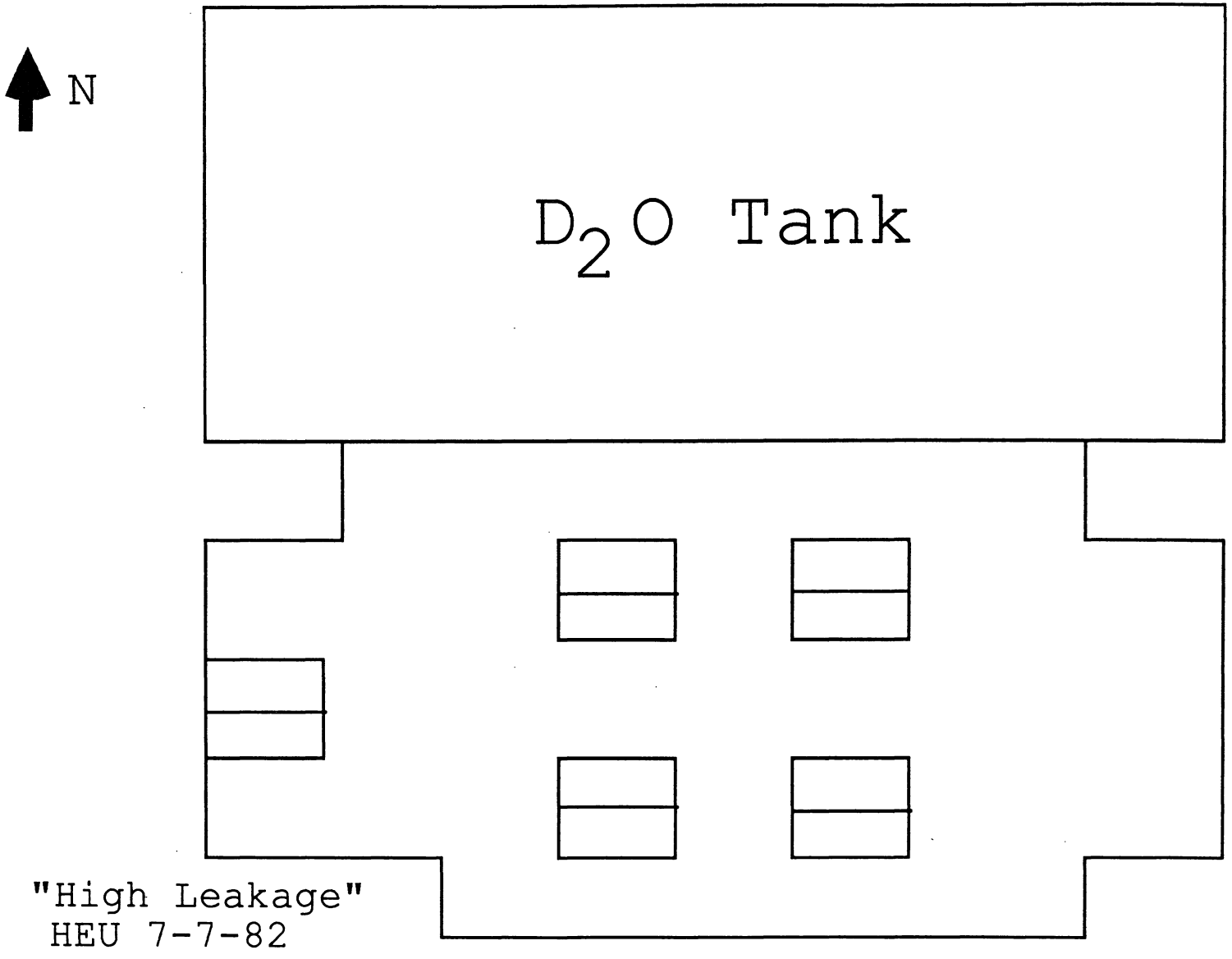

Figure III-14. "High Leakage" HEU Core Pattern (7-7-82)

and are intended to mock-up the LEU leakage conditions as nearly as possible. These will be designated simply as HL-HEU cores; and d) a near-equilibrium, 38-element LEU core designated as December, 1984 (see Figure III-15).

As described earlier, the geometry of the D_2O tank precludes making measurements beyond 8" below the top of the fuel plates. Furthermore, the SPND can extend down only to 6" below the top of the fuel plates because of its design. For mapping in a given horizontal plane fluxes must be extrapolated 6" for the quoted core midplane value. While there is a significant uncertainty in the value of the D_2O tank flux extrapolated to core midplane, the ratio for the core to D_2O tank fluxes should be reliable for the core 1/4-plane height. Since the back row of tank penetrations (i.e., farthest north, M-Q) do not extend as far into the tank, this data should be viewed with some suspicion. The D_2O tank penetrations are shown in Figure III-16.

In the light water reflectors, special assemblies were designed to allow SPND measurements at four fixed distances radially away from the core. These adapters were designed to fit snugly against adjacent fuel assemblies. But because the fuel plates are curved away from the SPND adapters, the radial position of the detector channels must be defined carefully.

Selected SPND current and subcadmium flux maps from three core loadings are given in Tables III-23 to III-28. The tables are arranged so that the 1/4, 1/2, 3/4 height fluxes are in vertical

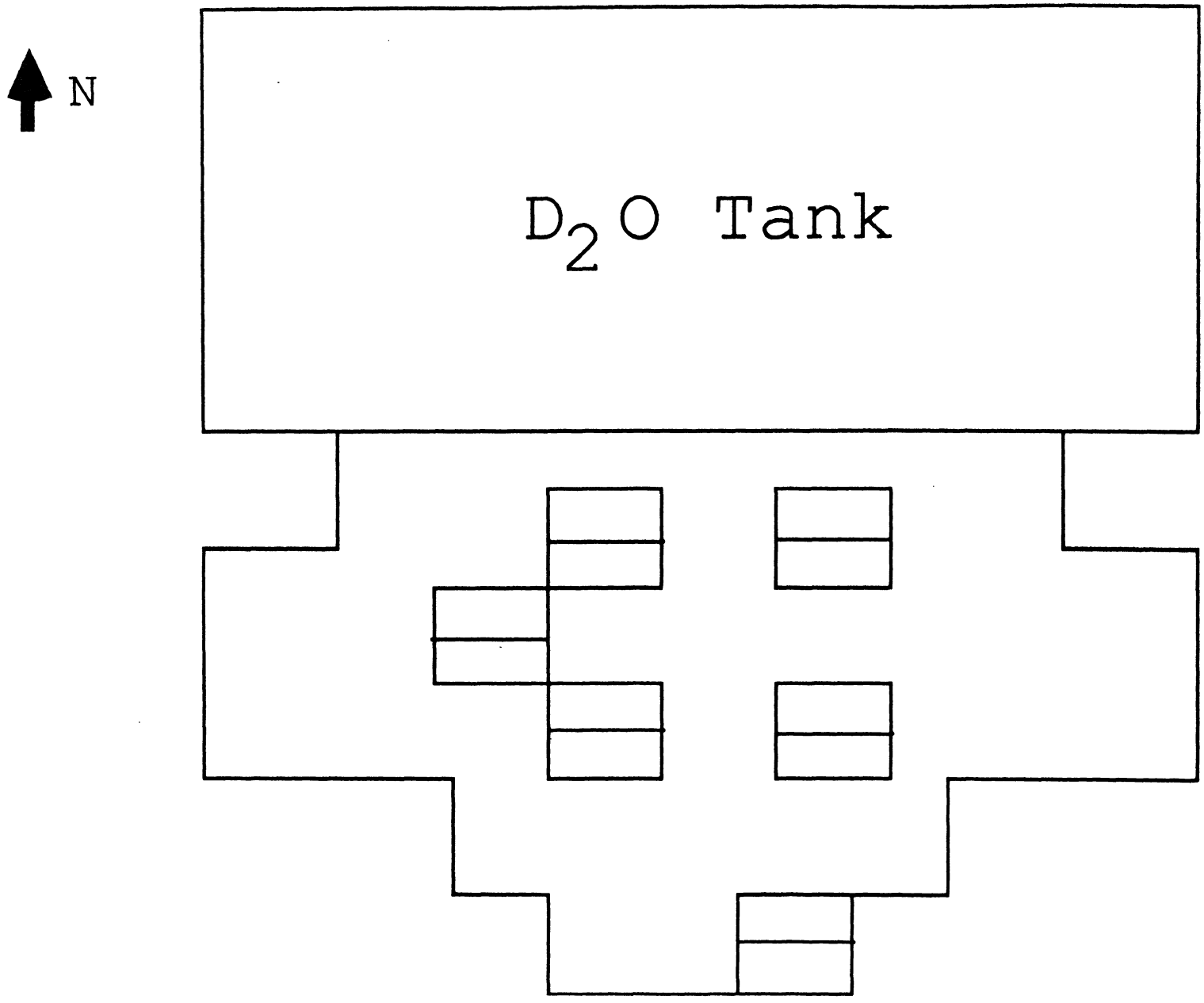

Figure III-15. LEU Core Pattern by 12/10/84

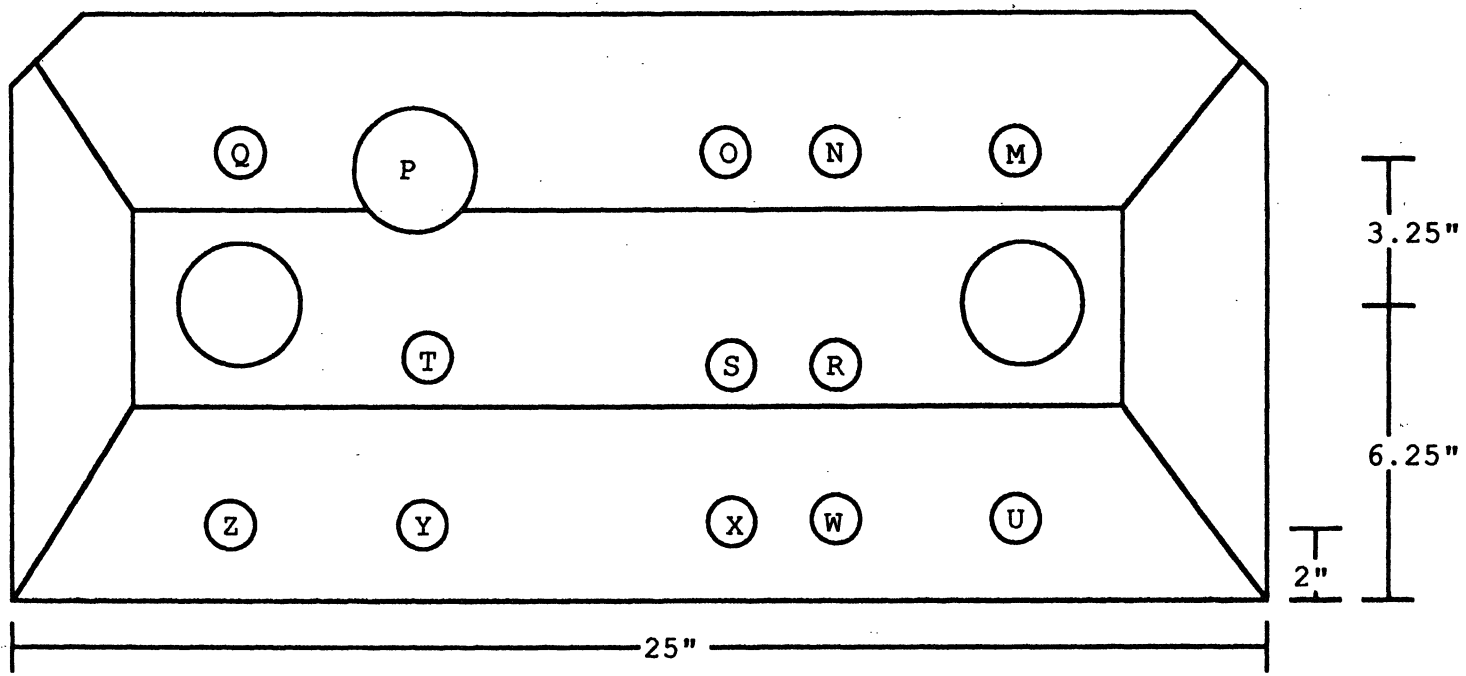

Figure III-16. D_2O Tank Penetration Geometry.

Current (10^{-8} amp) September 27, 1979

			O. 2.13 2.72		N. 2.16 2.76		
			S. 3.89 4.96		R. 3.52 4.52		
			X. 4.89 6.26		W. 4.79 6.13		
75	65 3.00	55 3.70	45 4.46	35 3.50 4.50 3.56	25 4.10	15 3.35	5
			A	5.44	C		
2.47	3.43	8.87	5.59	4.43 5.61 4.47	5.44	4.84	3.41
			B	5.14	CR		
		3.03	3.69	3.48 4.01 3.11	3.83	3.20	
				2.59	2.45		

Ch.	
1	2.77
2	2.72
3	2.35
4	1.98

Table III-23. SPND Net Current Measurements for HEU Core of 9/27/79.

ϕ_{sc} x 10^{-13} HEU 9/27/79

				O. 0.70 0.89		N. 0.71 0.91	
				S. 1.28 1.63		R. 1.15 1.48	
				X. 1.60 2.05		W. 1.57 2.01	
	1.41	1.74	2.09	1.60 2.06 1.63	1.92	1.57	
				2.49			
1.17	1.63	3.49	2.56	2.01 2.54 2.02	2.49	2.22	1.62
				2.35			
		1.44	1.69	1.59 1.84 1.42	1.75	1.52	
				1.23	1.16		

Water reflector →

1.09
1.07
0.92
0.78

Table III-24. SPND Subcadmium Flux Map for Equilibrium HEU Core of 9/27/79.

Current (10^{-8} amp) HEU May 29, 1982

X. 5.20 W. 4.96
6.64 6.37

75	65	55	45	35	25	15	5
				3.40 4.35 3.55			
			A	4.35 5.45 4.50	C		
2.00 2.50 1.90	3.10 3.95 3.05	7.25 9.20 7.40	4.35 5.50 4.45	4.65 5.90 4.80	4.20 5.45 4.45	3.60 4.65 3.70	2.60 3.30 2.70
			B	4.30 5.55 4.55	CR		
				3.60 4.65 3.75			
				No Data			

Table III-25. SPND Net Current Measurements for HEU Core of 5/29/82.

ϕ_{sc}x 10^{-13} HEU 5/29/82

				X. 1.71 2.18		W. 1.63 2.09	
				1.56 1.99 1.63			
				1.99 2.49 2.06			
0.95 1.19 0.90	1.47 1.88 1.45	2.86 3.62 2.91	1.99 2.52 2.04	2.10 2.67 2.17	1.92 2.49 2.04	1.65 2.13 1.69	1.23 1.57 1.28
				1.97 2.54 2.08			
				1.65 2.13 1.72			
				No Data			

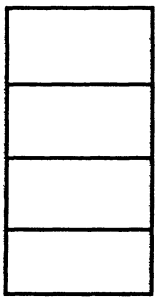

Table III-26. SPND Subcadmium Flux Map for Equilibrium HEU Core of 5/29/82.

Current (10^{-9}amps) LEU 12/20-21/84

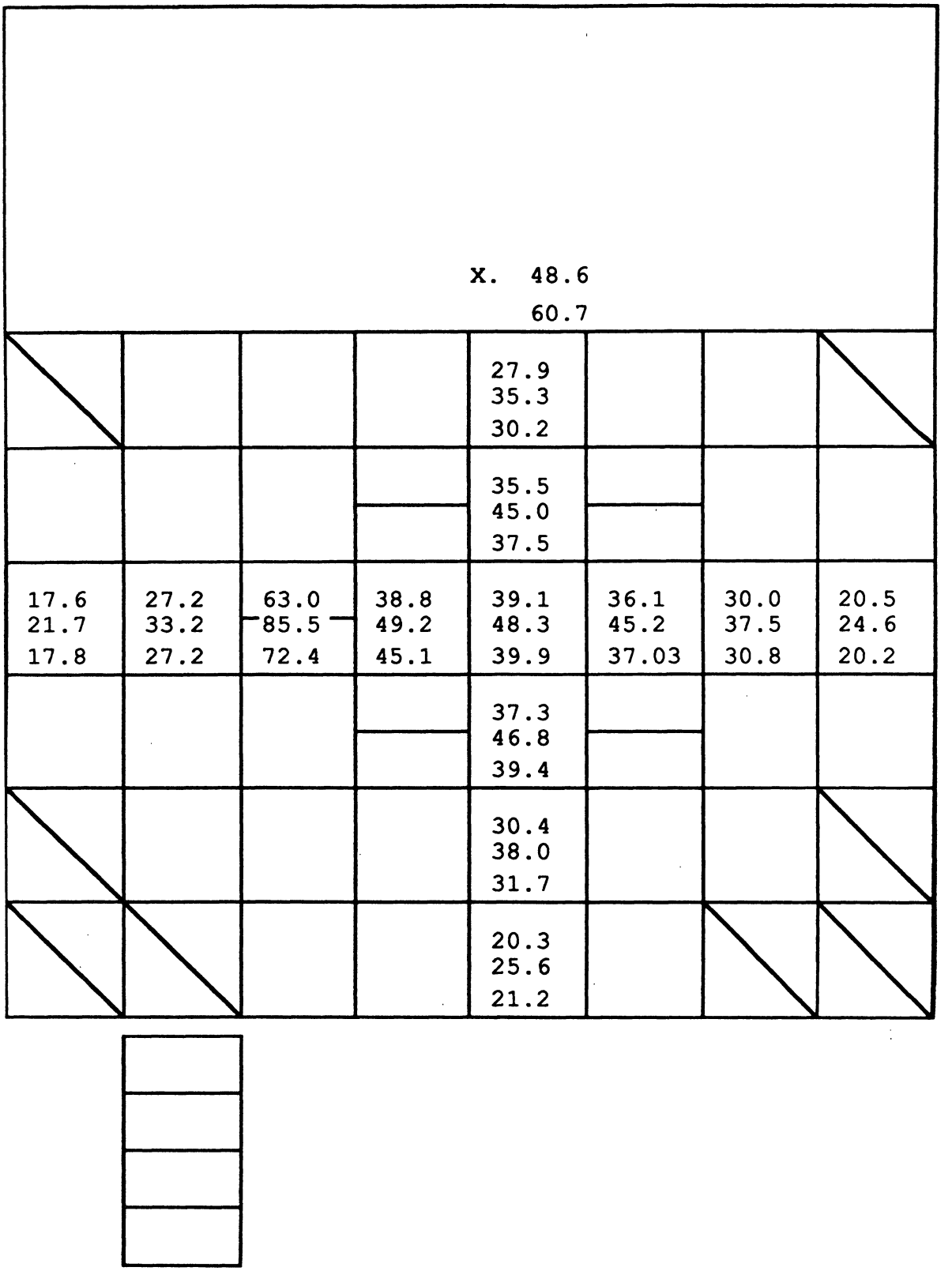

Table III-27. SPND Net Current Measurements for LEU Core of 12/20/84.

ϕ_{sc}x 10^{-13} LEU 12/20/84

				X. 1.85 2.31			
				1.19 1.50 1.28			
				1.44 1.82 1.52			
0.76 0.93 0.76	1.10 1.34 1.10	2.34 3.17 2.69	1.57 1.99 1.83	1.58 1.96 1.62	1.46 1.83 1.50	1.21 1.52 1.25	0.88 1.06 0.87
				1.51 1.90 1.60			
				1.23 1.54 1.28			
				0.87 1.10 0.91			

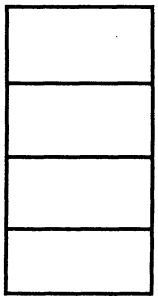

Table III-28. SPND Subcadmium Flux Map for Equilibrium LEU Core of 12/20/84.

descending order in each lattice position. Figure III-17 gives the grid plate lattice designations. Additional measured subcadmium maps are given in Section V.A. Table III-29 lists the values of f_{sc} used for each lattice or reflector position, interpolated from the measurements in Table III-17 in Section III.B.2. The format of Table III-29 gives a single value of f_{sc} for each lattice position; the upper number applies to HEU cores, the lower to LEU cores. No axial variation is assumed. All flux values are in units of 10^{13}. In the D_2O tank, data are presented with the 1/4-height flux above that for the core midplane. The positions of the typed data on the figure approximate the actual D_2O positions measured.

Figure III-18 is a plot of the north-south scan through position L-37 at the 12" height for large HEU and LEU cores. The most pronounced features of Figure III-18 are the D_2O-X/L-37 ratios, which is approximately 0.81 for the HEU cores but is 1.17 for the LEU core. A second feature is the ratio of average ϕ_{sc} for HEU vs. LEU, approximated by the average of midplane values shown in Tables III-24 and III-28. This gives a $\phi_{sc}(HEU)/\phi_{sc}(LEU)$ ratio of 1.28. This is higher than the 1.19 value predicted by the fuel loadings, and may be due to the fact that the LEU core has not reached equilibrium.

Table III-30 presents a comparison of the subcadmium fluxes measured on several cores. The 38-element LEU core is identical in shape to the HEU core of May 29, 1982, although this LEU core is still not a true equilibrium core. We infer from the data summary

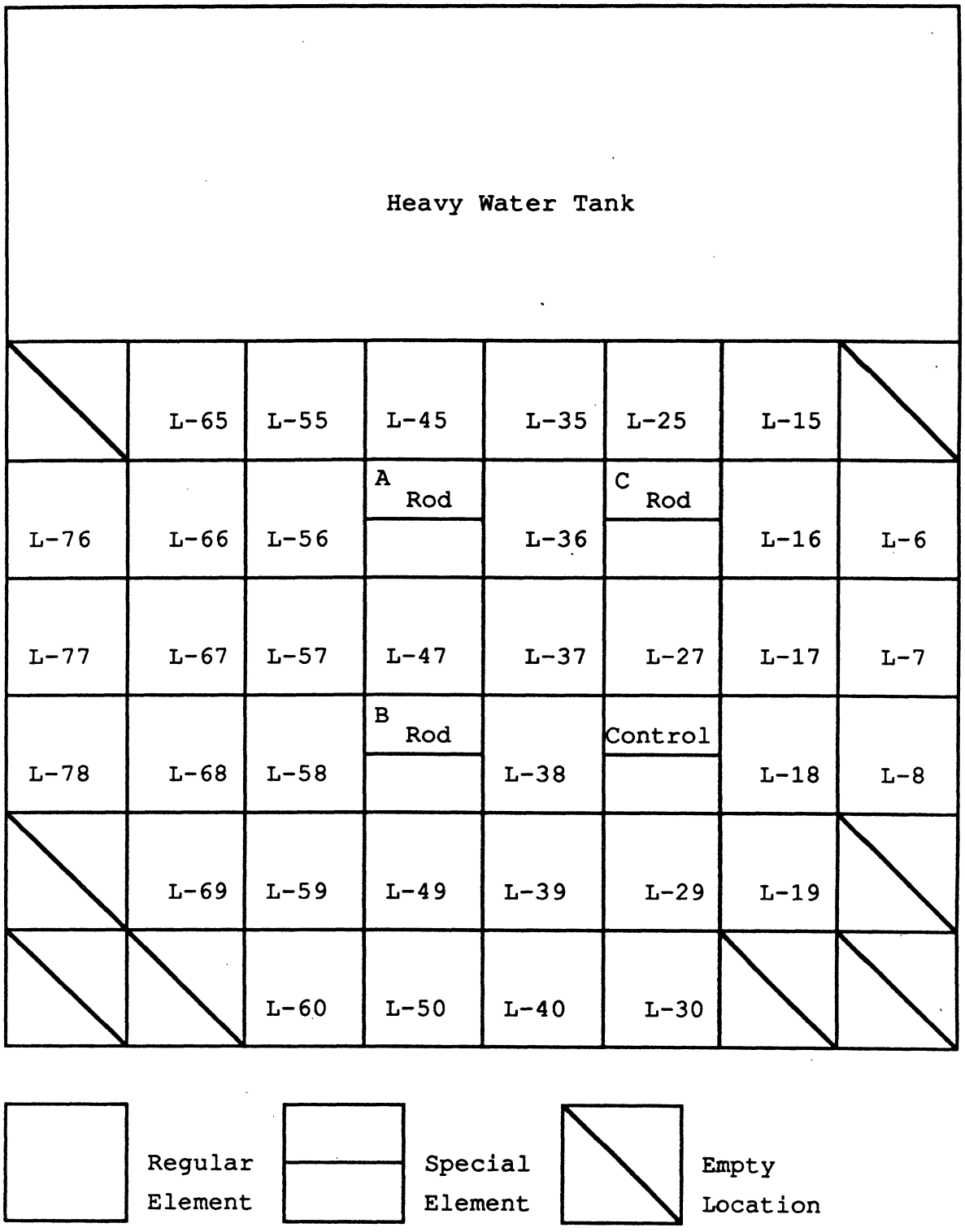

Figure III-17. Key to Lattice Positions.

D_2O

				o .895		n .895	
			t .895	s .895 .892		r .895	
				x .895 .892		w .895 .892	
	.820 L-65 .786	.820 L-55 .786	.820 L-45 .786	.800 L-35 .786	.820 L-25 .786	.820 L-15 .786	
L-76	L-66 .750	L-56 .750	A * .800	L-36 .750	C * .800	L-16 .750	L-6
.830 L-77 .795	.830 L-67 .749	* L-57 *	.800 L-47 .749	.791 L-37 .749	.800 L-27 .749	.800 L-17 .749	.830 L-7 .795
L-78	L-68 .750	L-58 .750	B * .800	L-38 .750	CR * .800	L-18 .750	L-8
		.830 L-59 .795	.800 L-49 .795	.800 L-39 .750	.800 L-29 .795	.830 L-19 .795	
			L-50	.830 L-40 .795	.830 L-30		

* special HEU = .913
LEU = .860

Values are presented as:

HEU
L-#
LEU

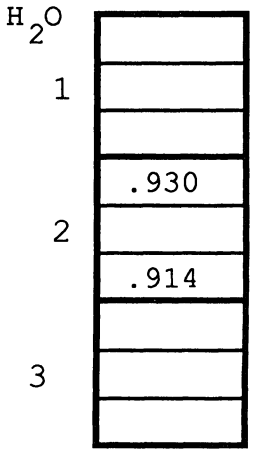

Table III-29. Values of f_{sc} used in calculation of ϕ_{sc}.

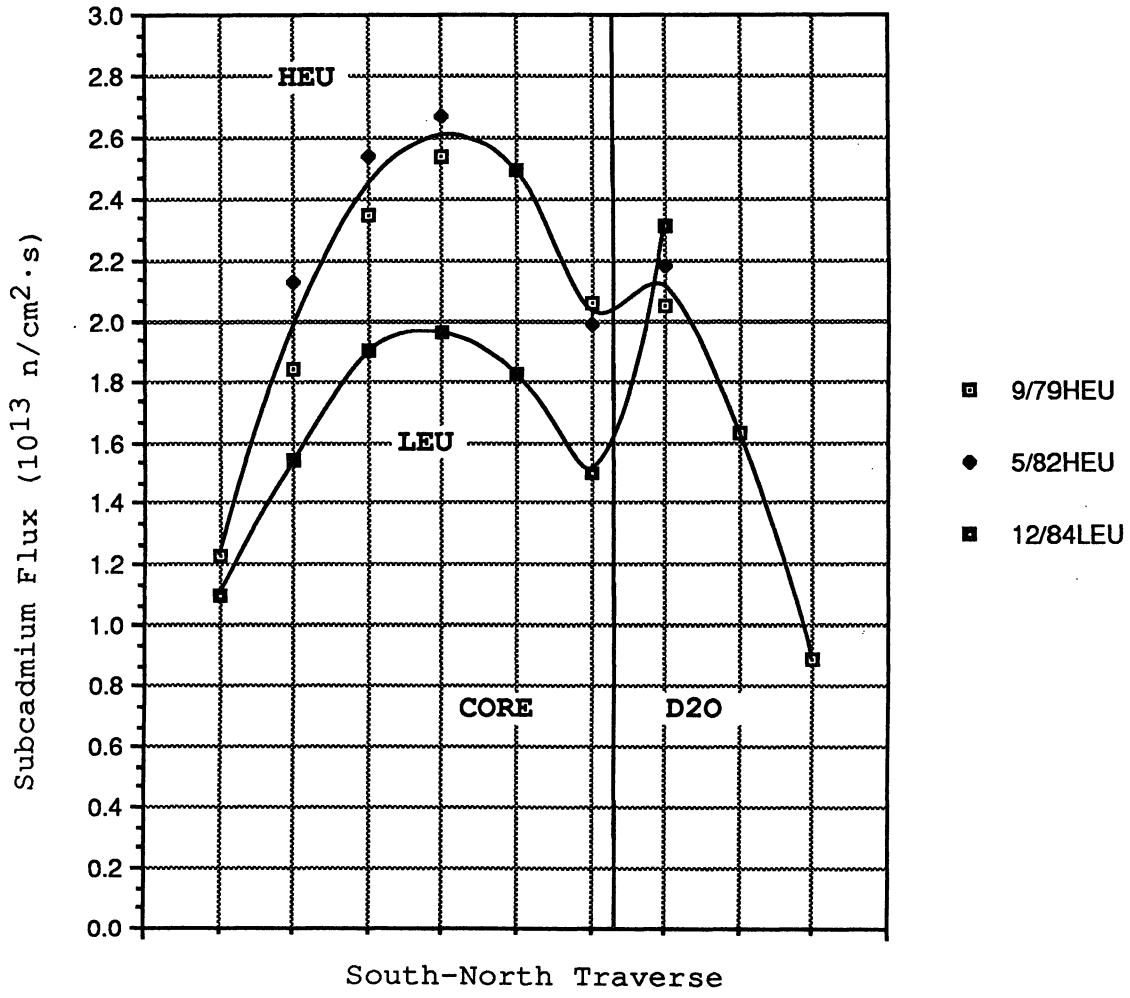

FIGURE III-18. HEU-LEU Subcadmium Flux Comparison

Table III-30. SPND Comparison of HEU and LEU ϕ_{sc} at Core Center (L-37,18" height) and at D_2O-X (18" height)

Date	Core Type and Position	$I_{SPND}^{(NET)}$	f_{sc}	f_p	S	ϕ_{sc}
9-27-79	HEU - L-37	44.3×10^{-9}A	.81	1.07	1.87	2.05×10^{13}
	D_2O-X	48.9	.90	1.07	2.92	1.60
5-29-82	HEU - L-37	46.5	.81	1.07	1.87	2.10
	D_2O-X	52.0	.90	1.07	2.92	1.71
1-18-82	Small LEU - L-37	45.2	.75	1.07	1.98	1.83
	D_2O-X	59.5	.89	1.07	2.51	2.26
4-19-82	Small LEU - L-37	43.2	.75	1.07	1.98	1.75
	D_2O-X	58.5	.89	1.07	2.51	2.22
6-28-84	LEU - L-37	37.7	.75	1.07	1.98	1.53
	D_2O-X	49.4	.89	1.07	2.51	1.88
7-19-84	LEU - L-37	37.9	.75	1.07	1.98	1.53
	D_2O-X	48.7	.89	1.07	2.51	1.85
12-13-84	LEU - L-37	38.0	.75	1.07	1.98	1.54
	D_2O-X	47.9	.89	1.07	2.51	1.82
12-21-84	LEU - L-37	39.1	.75	1.07	1.98	1.58

Note: A value of 0.81, representing a core average value, is used for f_{sc} for HEU in this table and in Section V.A.

that the ratios for core center and peak D_2O reflector subcadmium fluxes are, for the average HEU equilibrium core versus the near-equilibrium LEU core (using f_{sc}=.79 for HEU location L-37):

Core, L-37, 18": $\phi_{sc}(LEU)/\phi_{sc}(HEU) = 0.77\pm0.03$

D_2O-X, 18" $\phi_{sc}(LEU)/\phi_{sc}(HEU) = 1.10\pm0.05$

(The magnitudes of ϕ_{sc} at core midplane within the D_2O tank are found by multiplying by 1.25±0.02.)

The D_2O reflector (D_2O-X) flux has decreased substantially from the earliest (small) LEU cores to the present LEU configuration, although it is still somewhat greater than that for the HEU equilibrium cores with the identical geometry.

D. Beam Port Measurements

1. Beam Port Leakage Currents

Accurate count rates were observed at the exit positions for G-, I-, and J-ports throughout the experimental period, for A-port from 8-10-81 through 1-15-82, and for F-port from 4-14-82 through 5-19-82 (see Figure III-19). Care was taken to wait for equilibrium xenon, and data were invariably used only when shim rods were within 2"-4" of full withdrawal. All of these ports have source planes either at the outer north face of the D_2O tank (F,G,I) or are tangentially oriented 105° from north and look through reentrant voids to the central volume of the D_2O tank (A,J). That is, the effective source planes for the latter are within 8" of the north-south tank center line, and within J

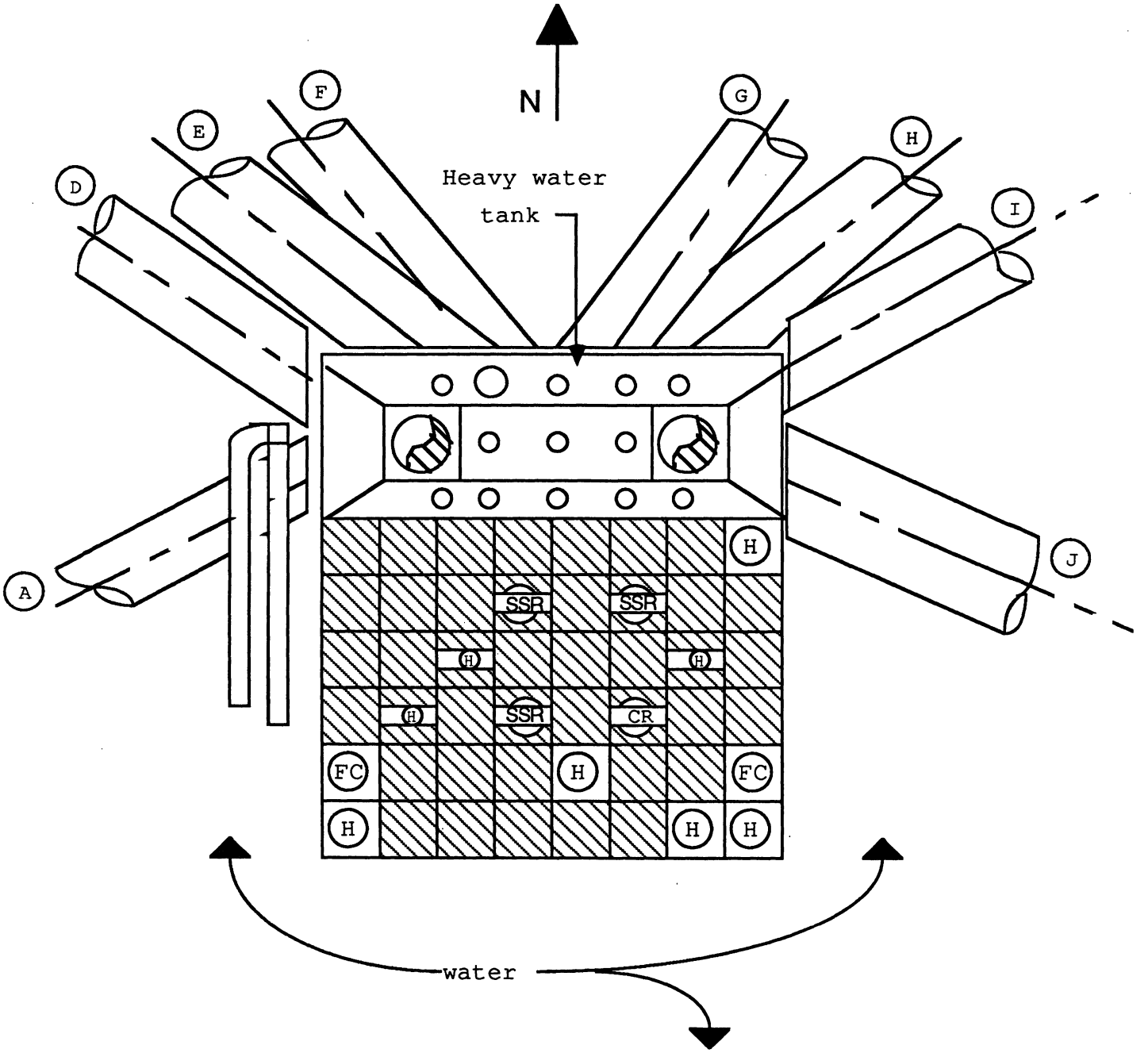

Figure III-19. FNR core Geometry, Showing Fuel Support Matrix, Heavy Water Tank and Beamports.

approximately 4" of the D_2O south face. Port axes for A, F, and are at core midplane, port axes for G, and I are 6" above midplane. The current monitored at A and G are seen only after Bragg reflection at nominal specific neutron energies of 0.06 and 0.072 eV respectively, while those from J and F correspond to the full leakage spectrum. I-port currents were also monochromatic, but the intensities of all energies within the thermal leakage Maxwellian were probed. There was no indication that the effect of monochromatization influenced any of the intensity results.

•Comparison of Fresh LEU to Equilibrium HEU

The comparison of leakage currents are recorded in Tables III-31 and III-32 for three core loading changes. The first two are given in Table III-31 and compare the effects of transforming from a representative HEU geometry to an initial small LEU geometry, and then back again in reverse order. In reading Table III-31, it is not meaningful to compare the two HEU cores or the two LEU cores because the G-port detector was recalibrated. Care was taken, however, to leave all detector stations untouched between the HEU to LEU conversion in both comparisons. The April to May 1982 LEU to HEU change should be most reliable since the data sets are separated by only one month in time. The first change compares data for the HEU loading taken in August, October and November, 1981, with that for the initial two loadings of LEU (Figure III-12), taken in January, 1982. The reverse change compares data from the LEU core of April, 1982 (Figure III-13) and

Table III-31. Comparison of HEU and LEU Leakage Flux Intensities

Port	HEU Fall 1981				LEU Jan 1982			Ratio $\frac{\text{Avg LEU}}{\text{Avg HEU}}$	Overall Ratio
	Aug	Oct	Nov	Avg c/s	Jan 8	Jan 21	Avg c/s		
A			51.6±1.5	51.6±1.5	48.5±1.5		48.5±1.5	0.94±0.04	
F									
G	310.5±6	298±4	289±6	299±10	296±4	298±4	297±4	0.99±0.04	0.98±.02
I									
J	1260±10	1210±10	1242±10	1242±10	1223±10	1250±10	1237±10	1.00±0.01	

Port	HEU May 1982					LEU April 1982				Ratio $\frac{\text{Avg LEU}}{\text{Avg HEU}}$	
	May 14	May 15,16	May 19	May 28	Avg c/s	April 14	April 20	April 21	Avg c/s		
F	8.1	8.0	7.95		8.01±0.10			9.59±0.2	9.59±0.2	1.20±.03	
G	275.3	275.5	276.6	277.5	276.2±4	324.0	326.3	322.0	324.1±5	1.17±.03	1.11±.04
I	77.4	77.5	77.0		77.3±2			87.5	87.5±2	1.13±.04	
J	1249	1269	1263	1258	1260±10	1181	1196	1206	1194±10	0.95±.01	

Table III-32. Comparison of HEU and LEU Leakage Flux Intensities

	HEU May 1982					"High Leakage" HEU July 1982		Ratio $\frac{\text{Avg H.L.HEU}}{\text{Avg HEU}}$	Overall Avg
Port	5/14	5/16	5/19	5/28	Avg^{C}/s	6/26	Avg^{C}/s		
G	275.3	275.5	276.6	277.5	276.2±4	290.2	290.2±4	1.050±0.021	1.062±.024
J	1249	1269	1263	1258	1260±10	1353	1353±10	1.074±0.012	

the reinstalled HEU core of May, 1982 (Table III-25). The two HEU cores are closely equivalent to each other and to earlier HEU data reported from September, 1979; they differ only in the substitution of a "special" element in place of a regular element on the south face. The LEU cores were somewhat different as needed to meet reactivity requirements. As may be seen by comparing Figure III-12 and III-13, there was a gradual shift toward the west face between January and April, 1982 and an increase in total number of fuel elements.

The data of Table III-31 for the January 1982 LEU cores show that within counting statistics and reproducibility in time, there was no change in leakage intensities from all three monitor stations, the average ratios of LEU to HEU levels being 0.94±0.04, 0.99±0.04, and 1.00±0.01, giving an overall ratio of 0.98±0.02.

By contrast, the reverse transformation of LEU to HEU which occurred between April and May, 1982 shows a significant increase in leakage for the LEU over the HEU loadings, for three of the four beam ports. These show LEU/HEU ratios of 1.20±.03, 1.17±.03, and 1.13±.04 for F-, G- , and I-ports. At the same time J-port shows a loss in leakage ratio of 0.95±.01. A crude estimate of the change in thermal flux per unit volume of the D_2O tank can be obtained from the average of these four stations. This gives 1.11±.04. While there has been a possible question about the pulse channel electronics at J-port in April 1982, we are inclined to believe all the data are reliable. We observe two effects; (a) a possible

shift in leakage from east to west, consistent with the LEU loading pattern of April, 1982, and (b) an average increase in leakage flux from the LEU core of at least 11%. The loss of A-port data to verify the shift is particularly unfortunate.

To estimate the effect of the higher north-south buckling for the LEU cores, a 5 row "high leakage" HEU, Figure III-14, was compared with the HEU loading of Figure III-11. In addition to extensive wire activation and SPND data taken in this core, beam port leakage currents are shown in Table III-32. As expected an increase of was about 6% was observed.

The data of Table III-31 and III-32 are not simple to interpret, and the correlation with in-core data, to be discussed below, is only partially satisfactory. We draw the following conclusions:

a) Installation of a full, unburned LEU core in place of an equilibrium HEU core will change beam port leakage by a factor between 0.95 and 1.15.

b) A significant fraction of this gain, perhaps the major fraction, occurs because of the enhanced north-south leakage associated with the clean LEU geometry. This gain would be expected to be reduced as the larger LEU equilibrium core is reached.

c) Interpretation of leakage currents from a D_2O reflector with reentrant beam port voids is dependent both on the position and angle of beam departure from the heavy water reflector. There is

evidence, for example, that J-port leakage currents closely follow in-core changes as measured in the outermost lattice position L-35 by SPND. (L-35 is the element adjacent to the D_2O tank and midway, east to west, between control rod special elements). If both sets of data from the January, 1982 LEU core are normalized to unity, the changes in J-port current and L-35 SPND response for successive LEU and HEU cores, as shown in Table III-33, are remarkably close. At the same time, the G-port current appears to compare not with in-core results, but with SPND data taken in the outer (northern) volume of the D_2O tank (position D_2O-S). This "correlation", though less impressive is also shown in Table III-33. It is evident, finally, that changes in the inner D_2O position, D_2O-X, do not correlate well with either J- or G-port data.

•Comparison of Equilibrium HEU and Near-Equilibrium LEU

Considerable effort has been made to compare thermal beam intensities for the near-equilibrium LEU core with those from the equilibrium HEU core. Both pulse and fission ion chamber data at G, I, and J ports, as well as gold foil activation at J port, were repeated several times during 11-84 through 1-85. We experienced much difficulty in providing a close comparison for the pulsed ion chamber data between 5-16-82 (equilibrium HEU) and 1-25-85 (nearly equilibrium LEU) because possible small changes occurred in electronics, pulsed source standards, crystal and beam port geometry. Unfortunately, the difficulty also extended to the J port gold activations; we found the results were sensitive to the

Table III-33. Beam Port and SPND Correlations

Core Condition	J-Port	SPND L-35	G-Port	SPND D_2O-S	SPND D_2O-X
LEU January 1982	1.0	1.0*	1.0	1.0	1.0
LEU April 1982	0.965	0.970	1.091	1.097	0.987
HEU May 1982	1.019	1.004	0.93	-	0.876
"High Leakage" HEU July 1982	1.094	1.108	0.98	-	0.934

*LEU January 1982 Current for SPND in L-35 taken as the average of values measured for LEU-1-8-82 and LEU-1-21-82

activation collimation used in 1982 (and 1979) and the precise reproducibility of position even between runs two days apart. Nevertheless, the data is presented in Tables III-34 and III-35, and will have to stand as the best LEU/HEU comparison to date. In this table we present the corrected average pulse ion chamber data taken 5-16 through 5-28-82 for the reconstructed HEU core of that date. We also present gold foil data taken 5-81 and 11-81 on earlier HEU equilibrium cores. The latest LEU data are compared by taking ratios of counts with these HEU cores. The last loading shown (6-14-85) may more nearly reflect expected equilibrium conditions.

Some comments should be made about these results. First, there is a "continuous" decline in LEU counts at G port over the period 8-3-84 to 6-14-85 which, according to pulse calibration, is not due to electronics, and is not believed due to port water vapor; it apparently reflects changes in the core loading and pattern. The same trend, to a much smaller degree, is evident at I and J. The inference may be made that we are still approaching equilibrium. Second, despite the apparent abnormal <u>increase</u> at J port, there is some correlation between pulse counting and gold activation. Third, the best ratios of LEU leakage rates to date relative to equilibrium HEU cores are:

G Port	0.73
I Port	0.94
J Port (including gold)	1.11

Table III-34. Comparison of Beam Port Leakage Data

Core Type & Date	G-Port Pulse Count/s	I-Port Pulse Count/s	J-Port Pulse Count/s Direct Beam	J-Port Sat. Au-Bare Activ. Direct Beam	Ratio $\frac{LEU}{HEU}$ (Equil)			
					G	I	J	J
HEU (5-81) HEU (11-81) HEU (5-16-82)	275.5±2.0	79.01±2.0 (E=0.0266 eV)	1269±30	17.0(No. Coll) 13.3				
LEU (8-3-84)	259.3				0.94			
LEU (8-3-84)			1608				1.27	
LEU (9-14-84)	252.0				0.91			
LEU (9-1-84)			1583				1.25	
LEU (11-30-84)	251.7				0.91			
LEU (12-19 12-21-84)	241.4±4	106.9 E=0.050eV)	1560±30		0.88	1.05*	1.23	
LEU (1-9-85)				13.7 20.7(no coll)				1.03 1.22
LEU (1-17 1-25-85)	234.6±3	77.4±2.0 E=0.0266eV)			0.85	0.98		
LEU (6-14-85)	202.0	74.0	1468		0.73	0.94	1.16	

*Original HEU data at this energy from spectral profile taken 5-15-82.

Table III-35. Comparative Beam Port Count Rates

Date of Measurement	Core Loading	G-Port Pulse c/s	I-Port Pulse c/s	J-Port Pulse c/s
HEU (5/16/82)	38 elements 2 1/2 south face (1 special at 57)	275.5±2	79.1±2	1,269±30
LEU (1/17-25/85)	38 elements 2 1/2 south face (1 special at 57	234.6±3	77.4±2	------
LEU (2/28/85)	38 elements 3 south face (1 special at 57)	231.0	------	1,542
LEU (4/19/85)	38 elements 3 south face (1 special at 57	230.9	77.0	------
LEU 6/14/85	39 elements 4 south face (1 special at 57)	202.2	74.0	1,468

Thus, it appears as though the intensity changes which are observed are strongly dependent on the core and beam port geometries.

2. Beam Port Thermal Neutron Spectrum Changes

The leakage spectrum at beamport I was measured for both the equilibrium HEU core (November, 1981) and the LEU core of April, 1982. This was undertaken to determine whether any significant thermal neutron spectrum hardening of the leakage current could be detected for the low enrichment design. Measurements were made at I-port by use of a single silicon crystal diffractometer. Flux intensity as a function of energy, from E = 0.02 eV to 0.140 eV, was obtained by a conventional θ-2θ Bragg scattering survey. A very narrow mosaic silicon crystal was used in a transmission mode; the {111} planes were used to remove second order contamination.

Data points were obtained throughout the energy interval noted above and the neutron temperature obtained by a fit to the Maxwellian function

$$\phi(E) = A \cdot E \cdot e^{-E/kT}$$

where A is a constant and k is the Boltzmann constant. The data is plotted as ln (ϕ/E) vs. E, from which kT is determined, through a least square fitting procedure, as the inverse of the slope of the plot.

Figures III-20 and III-21 show the resulting plots for the HEU and LEU respectively. The data are extremely well fit by straight lines between 0.02 eV and 0.13 eV. The temperatures obtained are 373.0±2.4°K and 370.8±1.9°K respectively The difference is well within error limits, so that we are led to conclude that no apparent spectrum change is evident at I-port. The temperatures measured are not to be considered accurate on an absolute basis, but the relative values should be reliable.

It is evident that the temperature observed will depend on the effective source volume in the D_2O tank seen by the port collimation. I-port views the D_2O tank from the NE corner face. The I-port axial line extends almost diagonally from NE to SW across the tank, making an angle of 63° with the north axis. I-port does not have a reentrant void.

It is expected that the spectrum will soften as the port axis moves away from the normal (north). In July, 1982 the diffractometer was moved to J-port where the angle of attack is 105°. A scan was repeated using the same geometry and systematics. The temperature observed was indeed lower and was found to be 330±5°K. Unfortunately, this measurement was not repeated for the standard HEU and LEU cores so that a comparison with LEU has not yet been possible at J-port.

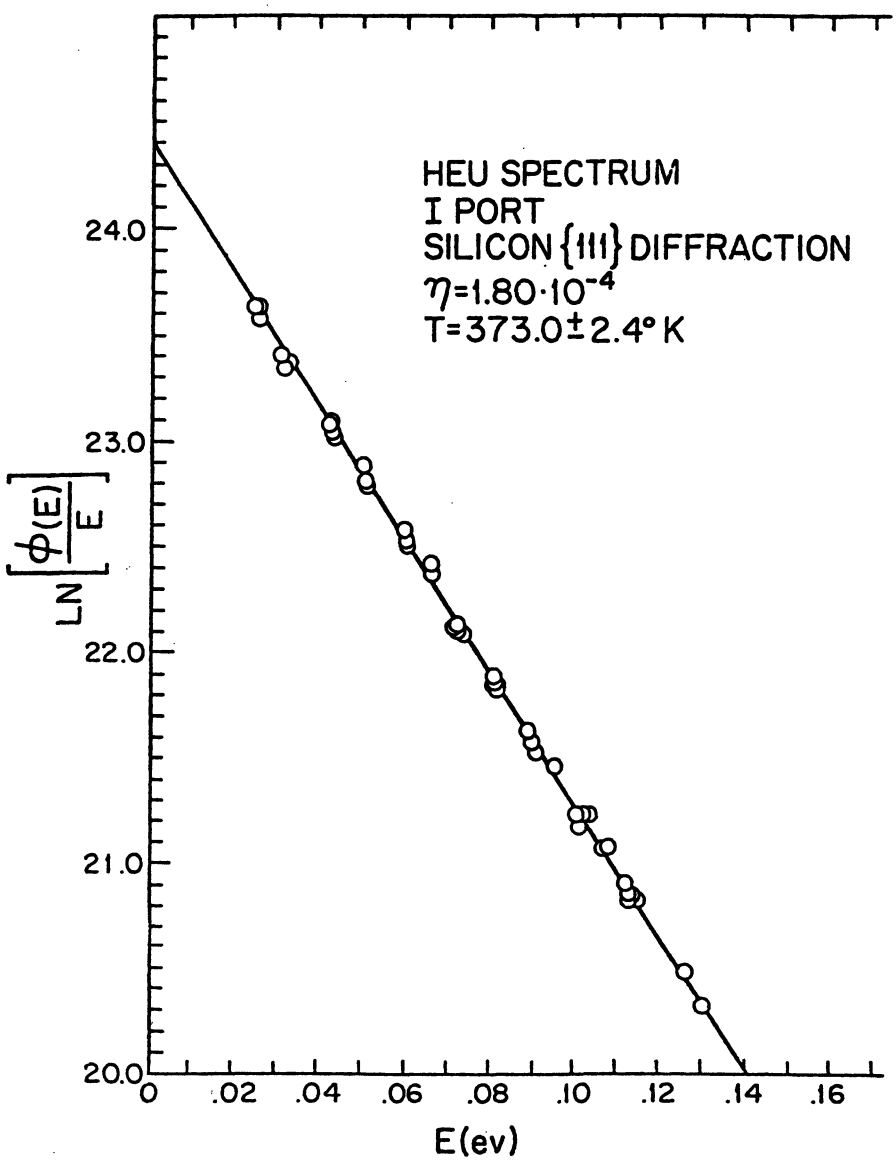

Figure III-20. HEU Thermal Neutron Leakage Spectrum

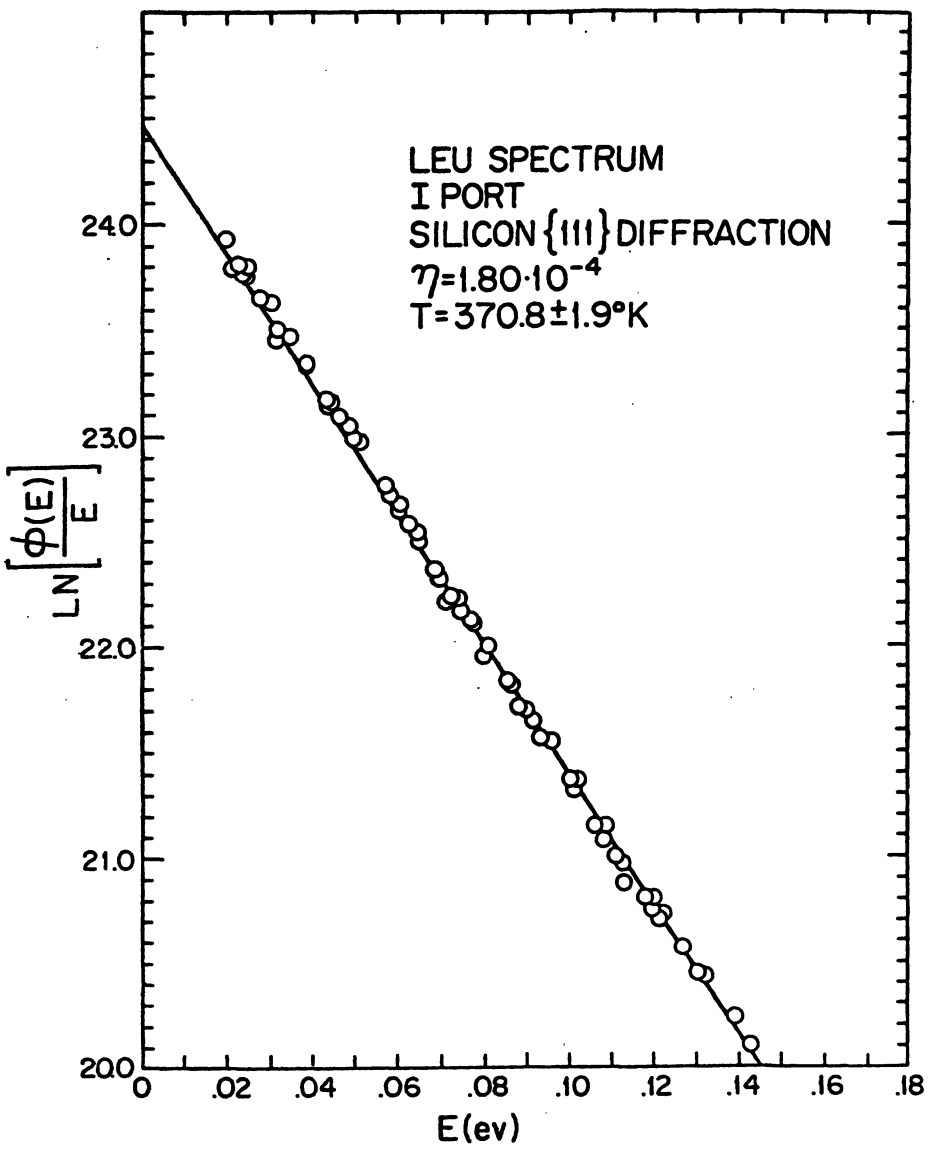

Figure III-21. LEU Thermal Neutron Leakage Spectrum

3. Beam Port Measurement Conclusions

Although the results are not as decisive as we would like, we note:

(1) no spectral change was observed at I-port between HEU and LEU fuel

(2) the observed shifts in beam port intensities depend **strongly** on port geometry and core geometry. The best estimate of an **average** ratio of equilibrium LEU to HEU intensities is .93±.19.

On the average, one can expect relatively minor leakage flux changes associated with the core conversion. The changes are least favorable for those ports which view the core more directly.

E. Summary of Demonstration Experiments Results

In summary, we have found:

•in-core spectral comparison: the LEU in-core spectrum is measurably harder than the HEU spectrum (see Figure III-7) probably due to the increased U-238 resonance absorption in the LEU fuel. For example, the in-core iron cadmium ratio decreases from 9.5 (HEU) to 8.4 (LEU).

•in-core subcadmium flux intensity comparison: while the LEU cores never reached true equilibrium during these experiments, the LEU cores grew to a size (December 1984) equivalent to the equilibrium HEU cores. This LEU in-core subcadmium flux was measured to be 74% of the equivalent size HEU core, while the

ex-core subcadmium flux in the heavy water tank was approximately 10% larger than that in the HEU cores.

•beam port intensity comparison: the results of these experiments were not as definitive as other comparisons because the intensity changes appear to be strongly dependent upon the core and beam port geometries. The best estimate of the LEU and HEU intensity ratio was found to be:

G-port (monochromatic flux):	0.73
I-port (monochromatic flux):	0.94
J-port (integrated flux):	1.11

where the angle of the beam port relative to the normal to the core increases from G- to J-port.

•beam port spectrum comparison: the Maxwellian temperature (and hence thermal spectrum) of the leakage flux at I-port was unchanged in switching from equilibrium HEU to clean LEU fuel.

•reactivity measurements: the measurements of the reactivity worths is extremely sensitive to core loading, and therefore a direct comparison is difficult. Measured power defects for HEU varied between -0.21 to -0.31% $\Delta k/k$ for HEU, and -0.23 to -0.25% $\Delta k/k$ for LEU. Thus, we are unable to quantify, within experimental error, any major shift in the power defect although we expect the magnitude of the value to be larger for LEU if we could compare identical cores. Comparison of the rod worths (in % $\Delta k/k$) between the cores of 9/79 (HEU) and 10/84 (LEU) (different from the HEU core by one less element on the south face) yielded the following

data:

	A	B	C
HEU	2.14	2.22	2.40
LEU	2.32	2.00	2.25

which lead us to conclude that the LEU rod worths may be slightly lower.

IV. NEUTRONIC ANALYSES FOR HEU AND LEU CORES

In connection with the FNR License Amendment for utilization of the LEU fuel, analysis of key FNR neutronic parameterS was performed in 1979 and 1980 for several HEU and LEU core configurations.

The important neutronic parameters analyzed include the temperature coefficient of reactivity, xenon reactivity, control rod worth, discharge burnup, and shutdown margin. Comparisons of these neutronic parameters for the batch core and equilibrium core configurations have provided a basis for assessing the impact of LEU fuel on FNR performance and utilization. The actual HEU and LEU fuel configurations selected for the FNR LEU demonstration experiments are discussed in this section together with comparison of these neutronic parameters. The neutronic analysis was updated subsequently as our neutronic codes were modified and updated, and the latest results are summarized here.

A. LEU and HEU Fuel Description

The selection of the LEU fuel design was based on extensive generic studies and survey calculations carried out by Argonne National Laboratory [Kom79a, Mat79 and Kon79b], The University of Michigan, and others. In addition, constraints were imposed on the final design as

a result of the specific FNR system configuration, FNR operational considerations, and the need to obtain approval from the U.S. Nuclear Regulatory Commission of an amendment to the HEU operating license. These constraints, which are unique to the FNR, had to be factored into the final LEU design.

Based on the above considerations, the LEU fuel design selected for the FNR was identical in all external dimensions to the HEU fuel as shown in Table IV-1. The conversion to LEU fuel results in an increase in ^{238}U loading by a factor of nearly 5 and an increase in ^{235}U loading to overcome the increased capture in ^{238}U. To accommodate the additional uranium loading, the fuel meat thickness was increased by 50% with a corresponding reduction in the cladding thickness, hence keeping a constant fuel plate thickness. The FNR licensing considerations dictated the use of fuel with at most 42 w/o uranium loading, which is considered to be an acceptable fuel design based on experience and testing to date. With 19.5% enriched uranium, the above LEU design has 167.3 g of ^{235}U per fuel element, and results in the same excess reactivity for the batch core as the HEU fuel design, as desired.

Table IV-1. HEU and LEU Fuel Designs

	HEU	LEU
Fissile enrichment (%)	93	19.5
Regular element fissile loading (gm)	140.0	167.3
Uranium density in fuel meat (w/o)	14.1	42
Fuel plates per element	18	18
Fuel meat thickness (in)	.020	.030
Clad thickness (in)	.020	.015
Fuel plate thickness (in)	.060	.060
Water channel thickness (in)	.117	.117

B. Flux and Power Distributions

Calculated power distributions for HEU and LEU cores are compared in Figures IV-1 and IV-2 for batch cores and equilibrium cores, respectively. Examination of these figures reveals only minor changes between LEU and HEU cores. The largest change in assembly power, a 2% relative increase, occurs for special element locations. Additionally, there is a small shift in the power distribution toward the heavy water tank. There is no evidence of changes which would require detailed thermal-hydraulic analysis; in fact, the ratio of peak-to-average assembly power is slightly reduced.

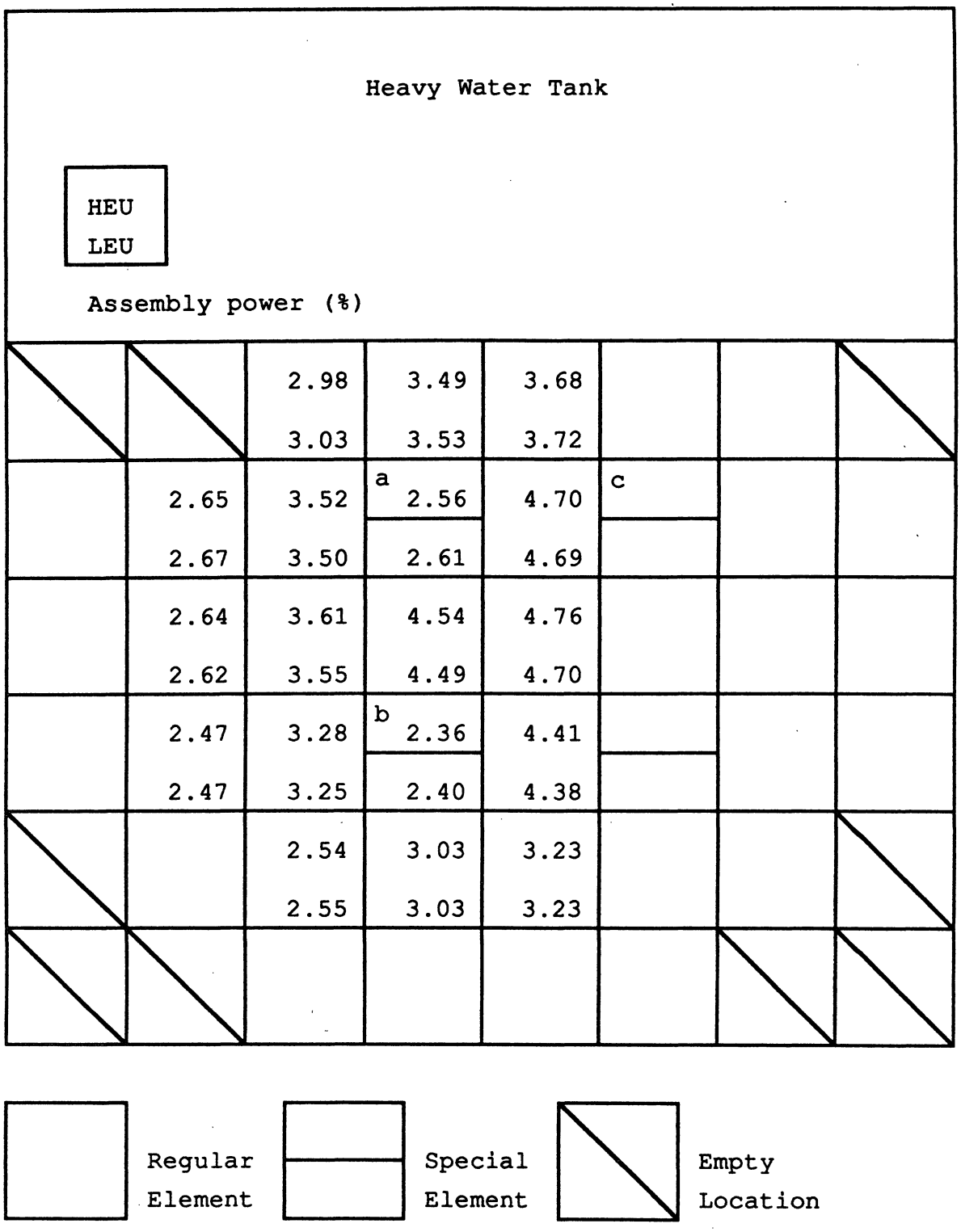

Figure IV-1. Assembly Power Distribution for HEU and LEU Batch Cores.

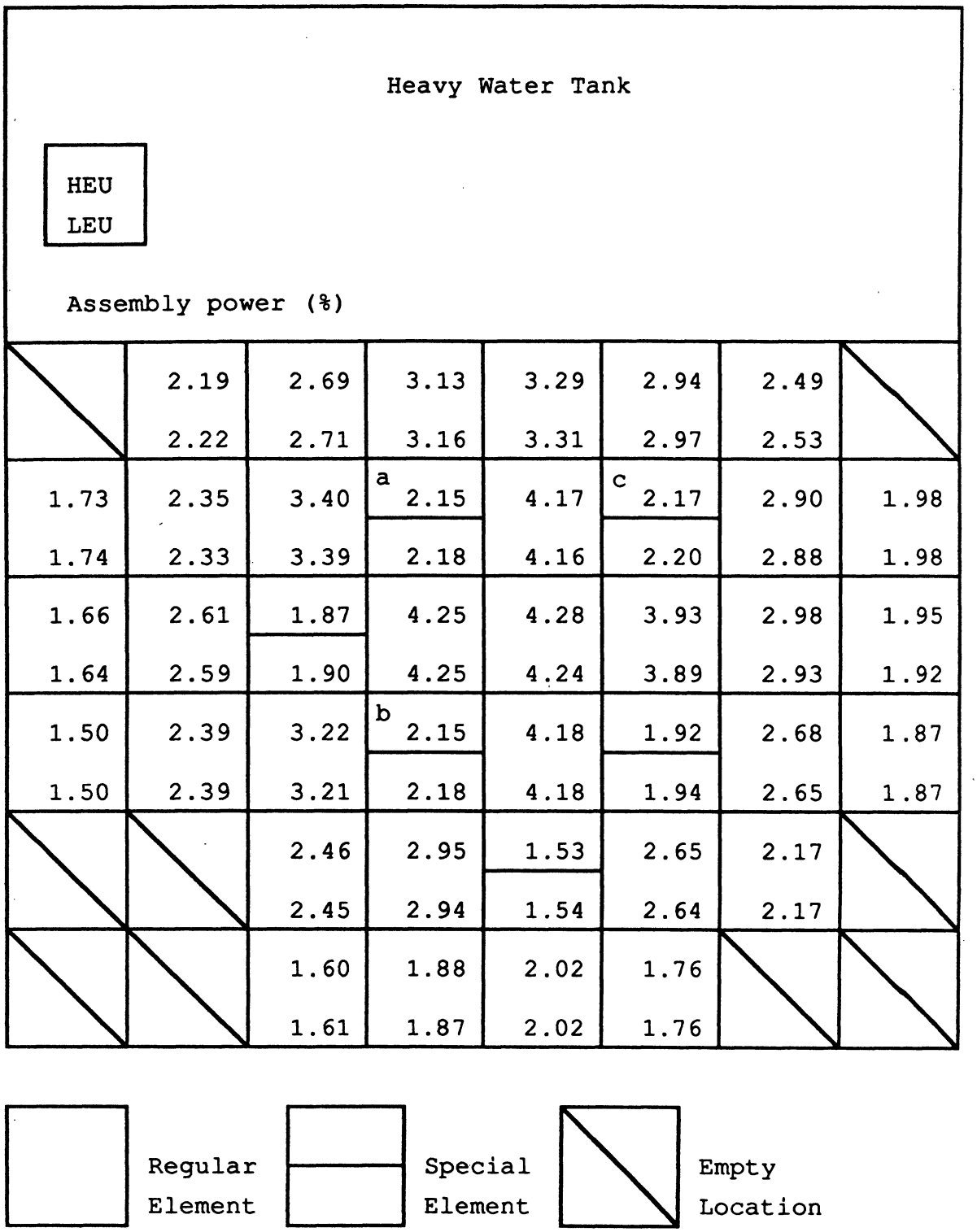

Figure IV-2. Assembly Power Distribution for HEU and LEU Equilibrium Cores.

The fast flux distribution is perturbed very little with LEU fuel. This is to be expected because the fast neutron production and removal rates are nearly equal for the two cores. The fast neutron production is approximately constant because the core power is held constant at 2 MW, while the fast neutron removal rate is nearly constant due to the similar moderating properties of the two cores. That is, the water channel dimensions are the same.

However, one expects to see significant changes in the in-core thermal flux distributions between the HEU and LEU fuels. The calculated thermal flux distributions are compared in Figures IV-3 and IV-4 for the batch and equilibrium cores, respectively. For a well-moderated thermal reactor at constant power, the thermal flux is nearly inversely proportional to the fissile loading, hence one expects a reduction in thermal flux for the LEU core. This effect is readily apparent in Figures IV-3 and IV-4, where the thermal flux in regular fuel elements is seen to decrease by about 16%. For special fuel elements, the reduction in thermal flux is only about 12%. This mitigation in the thermal flux decrease results from the effect of the thermal flux peaking in the large waterhole.

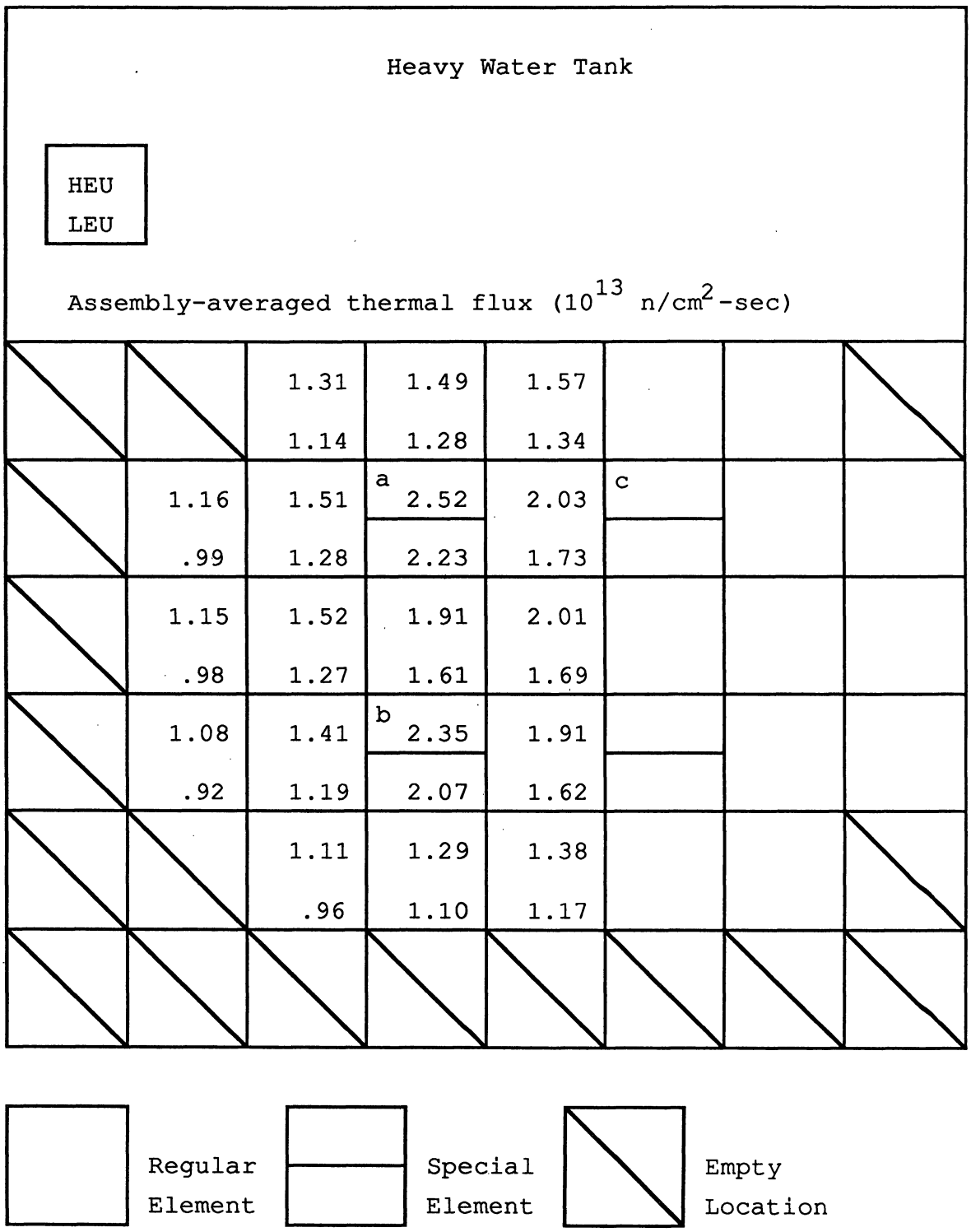

Figure IV-3. Thermal Flux Distribution for HEU and LEU Batch Cores.

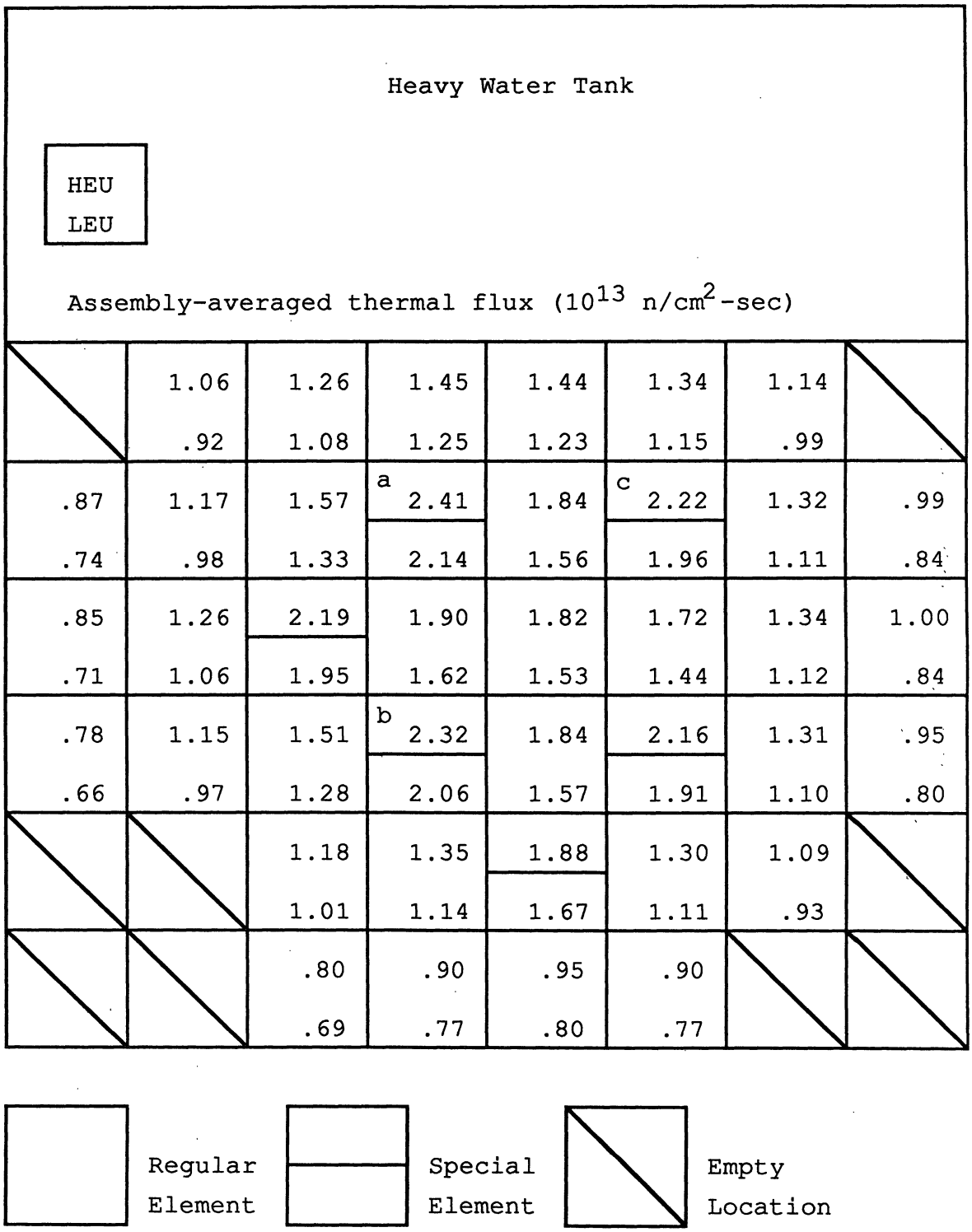

Figure IV-4. Thermal Flux Distribution for HEU and LEU Equilibrium Cores.

This peak is primarily dependent on the fast flux, which is not significantly different between the LEU and HEU fuels. As noted for the power distribution, there is also a slight shift in thermal flux toward the heavy water tank.

Ex-core thermal flux levels are important in the FNR because samples are generally irradiated in the reflector regions. In particular the heavy water reflector is of greatest interest because thermal neutron beam tubes extend from the tank to the laboratory areas. Comparison of the thermal flux levels in the light water reflector shows a flux depression varying from zero to 4%. At distances well into the light water reflector, there is essentially no change because the primary source for thermal neutrons is the slowing down of fast neutrons leaking from the core. At locations closer to the core the contribution to the thermal flux due to thermal leakage from the core is larger and, since the thermal leakage is decreased by the increased fuel loading, there is a correspondingly greater decrease in the thermal flux. Consistent with this explanation, the relative thermal flux in the heavy water tank is depressed somewhat more (4-6%) than in the light water reflector due to the increase in the relative contribution of thermal leakage to the heavy water tank thermal flux.

C. Temperature Coefficient of Reactivity and Power Defect

The isothermal temperature coefficient of reactivity was computed for the batch core model to be -8.4 pcm/°F for the HEU fuel and -12.6 pcm/°F for the LEU fuel. The large increase in the magnitude of the temperature coefficient is due almost exclusively to the fuel Doppler effects. For the HEU fuel, fuel Doppler effects are negligible due to the small amount of ^{238}U present. For the LEU fuel, the large amount of ^{238}U increases resonance absorptions in ^{238}U, resulting in much higher sensitivity to fuel temperature. The principal contribution to the temperature coefficient of reactivity for both the HEU and LEU configurations is, however, the effect of the reduction in moderator density on leakage and moderation.

In consideration of the limited capability in calculating the power defect of reactivity, a preliminary estimate has been made based on the observation that the increase in the fuel Doppler effect is the principal difference in the temperature effects between the HEU and the LEU designs. The change in power defect of reactivity is estimated in the present analysis on the basis of calculated temperature coefficients. Based on an average core temperature rise of 8°F, the power defect for the LEU fuel is estimated to be about 0.03% $\Delta k/k$ larger in magnitude than for the HEU fuel. For a typical FNR

configuration, the excess reactivity required to overcome the power defect would thus change from a measured value of 0.21% $\Delta k/k$ for HEU to 0.24% $\Delta k/k$ for LEU.

D. Xenon Reactivity Worth

The xenon reactivity worths of the HEU and LEU fuels are compared in Tables IV-2 and IV-3, for the batch and equilibrium core configurations, respectively, together with other neutronic parameters. For these cores the xenon worth is about 4% lower for the LEU than the HEU fuel. There are two competing effects responsible for this decrease: First, the larger ^{235}U loading for the LEU core results in lower in-core thermal flux levels, with a greater (10-12%) xenon concentration. Second, the increased fuel loading gives the LEU core a larger neutron absorption cross section. As total core absorption is increased, the fractional absorption in xenon, and thus the xenon reactivity worth, is decreased. Although these two effects tend to cancel one another, the latter effect dominates and xenon reactivity worth is lowered by about 0.1% $\Delta k/k$.

E. Control Rod Worth

Shim rod reactivity worth comparisons for the A, B, and C rods are given in Tables IV-2 and IV-3. The LEU batch core comparison shows a 3-4% relative decrease in shim rod

Table IV-2. Core Physics Parameters for Batch Core

	HEU	LEU	% Change
Cycle length (days)	10.0	10.0	--
Burnup reactivity change rate (% Δk/k/day)	-.027	-0.19	-30
Shim rod worth(% Δ k/k)			
A Rod	2.35	2.29	--
B Rod	2.08	2.01	--
C Rod	2.34	2.28	--
TOTAL	6.77	6.58	-2.8
Excess reactivity required (% Δ k/k)			
Xenon poisoning	2.39	2.30	-3.8
Burnup effect	.27	.19	--
Power defect	.21	.24	--
TOTAL	2.87	2.73	-4.9
Shutdown margin (%Δ k/k)	3.90	3.85	-1.3

Table IV-3. Core Physics Parameters for Equilibrium Core

	HEU	LEU	% Change
Cycle length (days)	11.0	16.5	50
Burnup reactivity change rate (% Δk/k/day)	-.028	-.020	-29
Shim rod worth (% Δk/k)			
A Rod	2.22	2.16	--
B Rod	2.13	2.06	--
C Rod	1.99	1.93	--
TOTAL	6.34	6.15	-3.0
Excess reactivity required (% Δ k/k)			
Xenon poisoning	2.23	2.13	-4.5
Burnup effect	.31	.33	--
Power defect	.21	.24	--
TOTAL	2.75	2.70	-1.8
Shutdown margin (% Δk/k)	3.59	3.45	-3.9

worth. This decrease in rod worth may be explained qualitatively by noting that, to a good approximation, the FNR rods are black and, for a black poison rod, reactivity worth is nearly proportional to the product of the poison surface area and the thermal diffusion length in the surrounding fueled region [Dud79]. The LEU thermal

diffusion length is approximately 6% lower than the corresponding HEU value, which tends to explain the calculated decrease in rod worths.

F. Comparison of Shutdown Margin

The most significant safety parameter related to core physics analysis is the shutdown margin. This parameter is obtained by subtracting the positive core excess reactivity required to overcome xenon poisoning, fuel depletion, and power defect from the total control rod reactivity worth. The present technical specifications require that the shutdown margin be at least 2.5% $\Delta k/k$. Any difference between the estimated shutdown margin and the limiting value represents excess reactivity available for experiments.

For the LEU batch core, it is seen from Tables IV-2 and IV-3 that the lower excess reactivity requirement is overshadowed by the decrease in control rod reactivity worth. The calculated shutdown margin for either LEU core is lower than for the corresponding HEU core, but is still well above the 2.5% $\Delta k/k$ requirement. Additionally, with the most reactive rod fully withdrawn, the shutdown margin is well in excess of the 0.45% $\Delta k/k$ required.

V. SIMULATION AND ANALYSIS OF THE EXPERIMENTAL DATA

Throughout the RERTR project at The University of Michigan, a heavy emphasis has been placed on simulation and analysis of the FNR experimental data obtained both for the HEU and LEU core configurations. These efforts have led to various improvements and optimizations in our neutronic analysis methodology discussed fully in Section II. They have also been valuable in comparing reactor physics parameters for the HEU and LEU configurations, and for confirmation of the initial design analysis performed. Since the potential degradation in thermal or sub-cadmium flux is one of the most important concerns that needs to be addressed regarding the conversion from the HEU to LEU fuel, a considerable effort has been spent on measurement and simulation of the thermal flux distributions in various FNR configurations. This includes analysis and representation of the iron wire and SPND geometry, which has helped us in arriving at the SPND sensitivity factor discussed in Section III. Some effort has been also spent to improve our ability to predict the criticality of the FNR core, including the initial LEU critical configuration of December 1981. Our latest neutronic calculations are based on the ENDF/B-IV cross section library, improved lumped fission-product treatment, and other improvements discussed in Section II.

Results of our recent calculations of the FNR thermal flux distributions and core eigenvalues are summarized in this section. In addition, some representative calculations for reactivity-related parameters are presented. This includes the integral and differential shim-rod worths, and power defect and void coefficient of reactivity. Presented also in this section are results of our calculations to date for neutron flux spectra at the FNR beam ports, and a discussion on uncertainties and limitations of our calculational methods.

A. Subcadmium Flux Distribution

Much of the experimental work performed during the LEU project involved the determination of subcadmium flux distributions by means of iron wire activations and rhodium SPND measurements. The determination of the subcadmium flux from the SPND and iron wire measurements is the subject of this section of the report.

1. Iron Wire Activation Analysis

We begin by presenting the methods for determining the subcadmium flux from iron wire measurements, which involve the determination of effective subcadmium cross sections for ^{58}Fe, in spectra corresponding to the core center and ex-core regions. Then, the determination of subcadmium flux distributions from rhodium SPND measurements is discussed. This includes effective sub-cadmium cadmium cross sections for rhodium in spectra

corresponding to the core and ex-core regions and the flux depression caused by the rhodium wire.

The subcadmium flux can be determined from bare and cadmium covered iron wires as follows:

$$\phi_{sc} = \frac{A_b - A_c}{\sigma_{58}} \qquad (1)$$

where A_b and A_c are the measured saturated activities per ^{58}Fe nucleus for bare and cadmium covered iron wires, respectively. Here, σ_{58} is the effective subcadmium cross section for ^{58}Fe defined as follows:

$$\sigma_{58} = \frac{\int_0^{E_c} \sigma_{58}(E)\ \phi(E)\ dE}{\int_0^{E_c} \phi(E)\ dE} \qquad (2)$$

where $\sigma_{58}(E)$ is the activation cross section for ^{58}Fe, $\phi(E)$ is the flux spectrum, and E_c is the cadmium cutoff energy. Since ^{58}Fe is a weak absorber, there is no need to consider flux depression in the wire, so all that is needed is to determine the unperturbed flux spectrum in the region where the measurement is made.

The subcadmium cross section for ^{58}Fe has been determined by utilizing several codes in the SCALE package [Wes80]. The CSAS code is used to set up the input for the NITAWL and XSDRN codes [Gre69]. The iron wire is modelled in cylindrical geometry with a surrounding environment to

simulate insertion into an LEU core, an HEU core, and penetration X of the heavy water tank. To simulate the core environments, fuel, moderator, clad, and non-lattice regions are volume averaged and homogenized. A 0.05 cm diameter iron wire is surrounded by a light water region of 0.2 cm outside diameter followed by a core region of 16 cm outside diameter.

The NITAWL code is run to perform resonance calculations for the uranium isotopes with the Nordheim Integral Treatment. NITAWL also sets up a cross section library in a format accessible by the XSDRN code. The XSDRN code is then run in a 123-group, cylindrical geometry calculation, with 4 meshes in the iron wire and 20 meshes in the surrounding region, for a total of 24 meshes. The quadrature order is S-8 and the order of scattering is P-3, with a white outer boundary condition. The XSDRN code is used to generate a 30-group library from the 123-group SCALE library. The 30-group library generated by the XSDRN code contains one set of microscopic cross sections for each isotope in each zone of the problem.

The ICE code [Wes80] is then used to generate a macroscopic cross section library for use in the ANISN code [Eug66]. Most of the analysis for both the iron wire activations and for the SPND measurements are performed with the ANISN code utilizing the 30-group library generated by the XSDRN and ICE codes.

In order to determine the subcadmium cross section for ^{58}Fe in the core region with the 30 group library, a 0.05 cm diameter iron wire is surrounded by a 0.2 cm diameter region of light water and a 40 cm diameter region of a homogenized mixture of fuel, clad, moderator and non-lattice regions. An S-8, P-1 calculation is then performed with the ANISN code to determine the flux weighted, subcadmium cross section for iron. These values are given in Table V-1. Since iron is nearly a 1/v absorber in the thermal range, the cross section for ^{58}Fe can be determined by multiplying the total iron activation cross section by the ratio of the ^{58}Fe 2200 m/s cross section to the total iron 2200 m/s cross section, and this is also given in Table V-1. In this analysis, the iron

Table V-1. Subcadmium Cross Sections for Iron Wire

Region	σ_{Fe} (b)	σ_{58} (b)
2200m/s	2.58	1.18
LEU lattice	1.86	0.850
HEU lattice	1.87	0.854
D_2O-X	2.00	0.913

number density is taken to be 0.08491/b-cm, and the cadmium cutoff energy is 0.625 eV, with the cross sections for 0.625 eV obtained by interpolating between the

corresponding values at 0.5488 eV and at 0.6552 eV available in the 30-group library.

Similar calculations were performed for an iron wire inserted into position X in the heavy water tank. A 0.05 cm diameter iron wire is surrounded by a 2.54 cm diameter region of light water followed by a 12.54 cm region of heavy water. A shell source is input on the boundary of the heavy water region to simulate the incoming current of neutrons from the core. The spectrum for the shell source was obtained from a one-dimensional, global core, slab geometry calculation. The spectrum at the core-heavy water tank interface was used as a shell source input for the iron wire activation calculation. The subcadmium cross section, thus calculated for an iron wire inserted into heavy water tank penetration X, is also given in Table V-1.

2. Analysis of SPND Measurements

The SPND measurements have been analyzed in a similar manner as the iron wire activations. Analysis of the rhodium SPND measurements is, however, complicated by two factors. First, since rhodium has a large absorption cross section, the flux is significantly perturbed by the insertion of the SPND into the core. The flux depression caused by the insertion of the rhodium SPND must be determined in order to relate SPND current measurements to subcadmium flux. Another complicating factor in the

analysis of the SPND measurements is that the detector is mounted on an Inconel paddle, which also causes a significant perturbation in the flux when the detector is inserted.

Several attempts were made to model the Inconel paddle with the one-dimensional transport theory codes, ANISN and XSDRN, by cylindricizing the paddle and preserving the volume of Inconel. It was decided that it was infeasible to adequately model the complicated geometry of the Inconel paddle in this manner since the flux depression caused by the paddle depends sensitively upon the thickness of water between the SPND and the Inconel, and also upon the thickness of the Inconel paddle. It was decided to model the SPND itself, which can be handled reasonably well in one-dimensional cyclindrical geometry, and to rely upon measurements to estimate the flux depression caused by the Inconel paddle.

From Section III.B, given a net SPND current I_{net} the subcadmium flux can be determined as follows:

$$\phi_{sc} = \frac{1.07\ I_{net}\ f_{sc}}{S_{sc}}, \qquad (3)$$

where the subcadmium activation fraction f_{sc}

$$f_{sc} = \frac{\int_V d\underline{r} \int_0^{E_c} dE\ \sigma(E)\ \phi_p(\underline{r},E)}{\int_V d\underline{r} \int_0^{\infty} dE\ \sigma(E)\ \phi_p(\underline{r},E)} \qquad (4)$$

approximates the subcadmium current fraction, and S_{sc} is the detector sensitivity. The factor 1.07 is the correction factor, experimentally determined, for the flux depression due to the Inconel paddle. In Equation (4) $\sigma(E)$ is the ^{103}Rh activation cross section, $\phi_p(E)$ is the flux seen by the detector, V is the emitter volume, and E_c is the cadmium cutoff energy. The detector sensitivity S_{sc} is determined through the beta escape probability β_{sc}, flux perturbation factor f_p and effective subcadmium cross section σ for Rh-103 as:

$$S_{sc} = NVe\beta_{sc}\sigma f_p, \qquad (5)$$

where N is the ^{103}Rh number density in the emitter and e is the electron charge. The factors σ, f_{sc} and f_p have been calculated by utilizing the codes in the SCALE package. The CSAS code is used to set up the input files for the NITAWL and XSDRN codes. The SPND is modeled in cylindrical geometry with the 0.05 cm diameter rhodium emitter wire surrounded by the aluminum oxide insulator of

0.1 cm outer diameter and the Inconel collector of 0.16 cm outer diameter. The SPND has been modeled in surrounding environments simulating HEU fuel, LEU fuel, and heavy water tank penetration X.

The XSDRN code is used to collapse the 123-group SCALE package library to 30 groups, with the group structure in the collapsed library set up to preserve most of the detail in the vicinity of the rhodium resonance around 1.3 eV. The XSDRN code produces a set of microscopic cross sections for each isotope in each region. The ICE code is then used to perform the cross section mixing and to generate a macroscopic cross section library for use in the ANISN code. Most of the transport theory analysis of the SPND detector was performed with the ANISN code in 30 group, P-1, S-8 calculations.

The core and heavy water tank surrounding environments have been simulated in exactly the same manner as described in the previous section for the analysis of the iron wire activations. The subcadmium cross sections σ for ^{103}Rh calculated by the ANISN code are given in Table V-2. The subcadmium activation fractions f_{sc} for the SPND, calculated with the ANISN code, are compared with the experimental values also in Table V-2.

The flux perturbation factors f_p for the insertion of the SPND have been determined by comparing the flux in the rhodium emitter wire with the flux in the same volume with

Table V-2. Calculated SPND Sensitivities

Location	σ (barns)		f_p		f_{sc}			S_{sc} (10^{-21} amp/ϕ_{sc})		
	ANISN	VIM	ANISN	VIM	ANISN	VIM	Meas	ANISN	VIM	Meas
HEU Regular Fuel	114.0	---	0.73	---	0.82	---	0.81	1.86	---	1.87
LEU Regular Fuel	114.0	114.1	0.75	0.730	0.80	0.83	0.75	1.90	1.86	1.98
LEU Special Fuel	---	119.0	---	0.708	---	0.92	0.86	---	1.88	2.48
LEU D_2O Reflector	120.0	115.8	0.72	0.768	0.89	0.93	0.89	1.92	1.98	2.51
H_2O Reflector	---	120.6	---	0.733	---	0.95	0.93	---	1.97	2.53

the detector removed. The flux spectra have been normalized to be the same far away from the location of the detector insertion. The flux perturbation factors are also given in Table V-2. The parameters, σ, f_{sc}, f_p and S_{sc} calculated with the ANISN code compare favorably with those obtained with the VIM Monte Carlo code [Pra76] as shown also in Table V-2. The comparison of the calculated S_{sc} with experimental data is, however, rather poor for regions where the flux spectrum is soft. Explanation of this discrepancy requires further investigation.

3. Simulation of Flux Maps

Figures V-1 through V-3 compare the absolute subcadmium fluxes determined from SPND measurements with those determined from UM2DB calculations for an equilibrium HEU core, a nearly fresh LEU core, and a mixed HEU-LEU core. SPND current measurements were converted to subcadmium fluxes through Eq. (3) with the measured values of S_{sc} and f_{sc} given in Tables V-2 and III-30. These f_{sc} values represent core average values in contrast to the position dependent values of Table III-29. The SPND currents were either measured or converted to the corresponding values at a quarter core height.

The UM2DB calculations were performed with a discrete (6x6) mesh per assembly for a total of (72x70) meshes, and HAMMER-based cross sections for the special elements, as discussed in Section II. Assembly-average

burnup distributions for these calculations were obtained through a UM2DB simulation of four years of FNR operation, totaling 141 cycles over the period September 1979 through September 1983. This fuel cycle simulation was performed with a homogeneous (2x2) mesh per assembly, for a total of (38x34) meshes, and covers both HEU and LEU core configurations. Revisions to the FNR burnup data processing code (SORT) permit correct burnup computations for any combination of in-core or ex-core residence times for any type of fuel element. As discussed in Section II, the (2x2) mesh description is believed to be adequate for fuel burnup calculations. The two-group cross sections for the light- and heavy-water reflectors were obtained from the one-dimensional XSDRN run discussed in Section II, where the material heterogeneities in the heavy water tank are homogenized by volume over three separate regions.

Absolute subcadmium fluxes have been determined from UM2DB calculations as follows. The UM2DB code computes absolute subcadmium fluxes corresponding to an input linear power generation rate. The total power of the FNR is 2MW and the core-height is 23.5 inches, which corresponds to an average linear power generation rate of 0.0335 MW/cm. In order to convert the average flux to quarter core-height flux, the ratio of the quarter core-height flux to the average axial flux was determined

from iron wire activation measurements reported in Section III. This resulted in a 5% increase applied to the UM2DB flux. The UM2DB calculations assumed a cadmium cutoff energy of 0.625 eV and a fission energy of 195 MeV/fission. Another correction factor was included to account for the subcadmium flux peaking in the light water tube penetration into the heavy water tank, which was calculated by the ANISN code to be about 10%. With these corrections, the measured and calculated fluxes are compared in Figures V-1 through V-3.

The calculated ϕ_{sc} distribution for the HEU core in Figure V-1 appears to be uniformly lower everywhere in the core, while for the other two configurations the discrepancy between the calculation and measurement is not monotonic. The measured and calculated ϕ_{sc} for the LEU fuel elements in Figures V-2 and V-3 also are rather similar to one another, and indicate in general lower values compared with the HEU values in Figure V-1. This trend correctly reflects the reduction in ϕ_{sc} in the LEU fuel associated with the decrease in enrichment and increase in thermal-group absorption cross section. The HEU-to-LEU flux ratios are, however, considerably larger in the experimental data. The UM2DB ϕ_{sc} also is considerably larger than the SPND value in the D_2O-X position, and smaller in the fuel elements facing the heavy water tank, in Figure V-3.

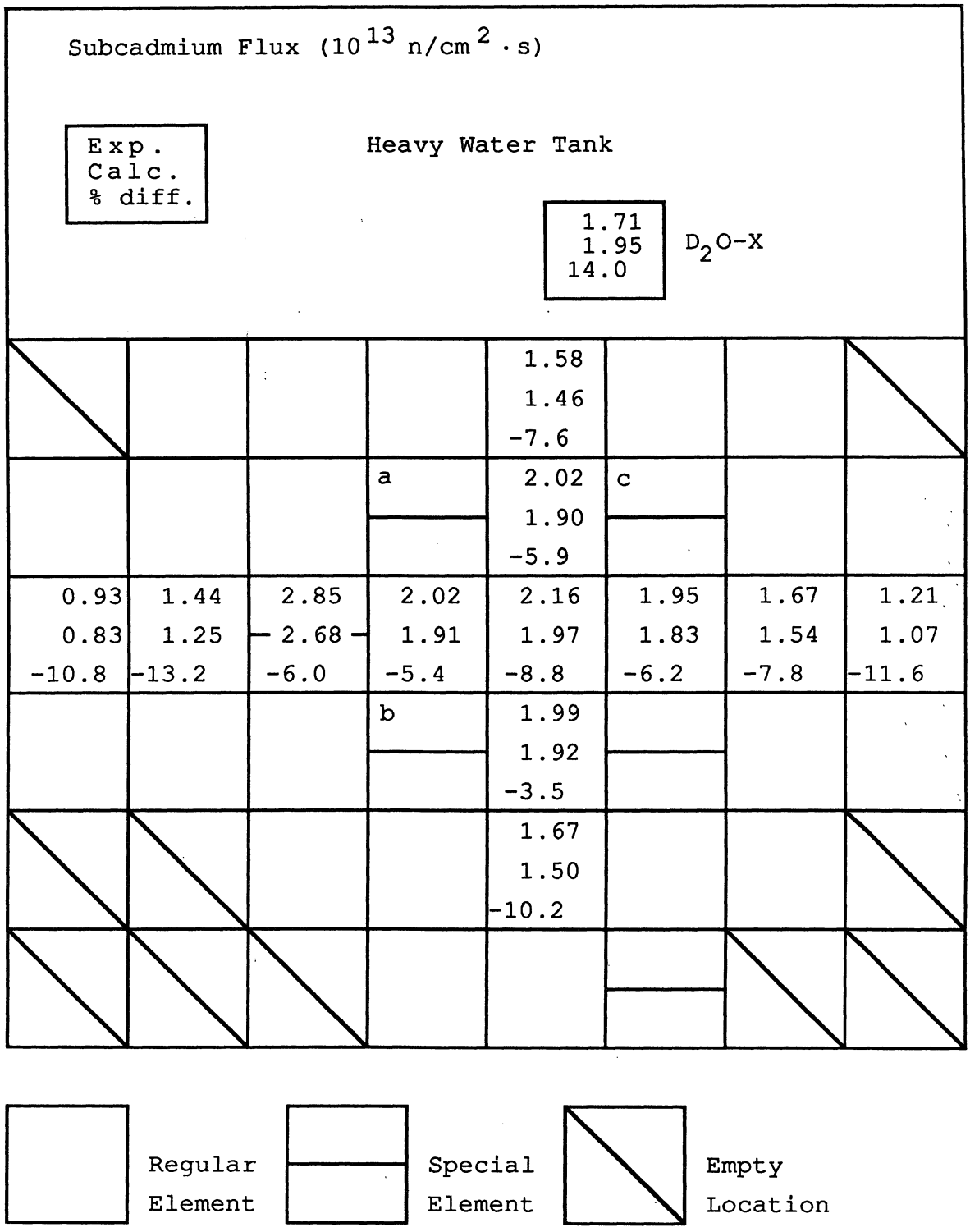

Figure V-1. Subcadmium Flux Map for May 29, 1982, HEU Core

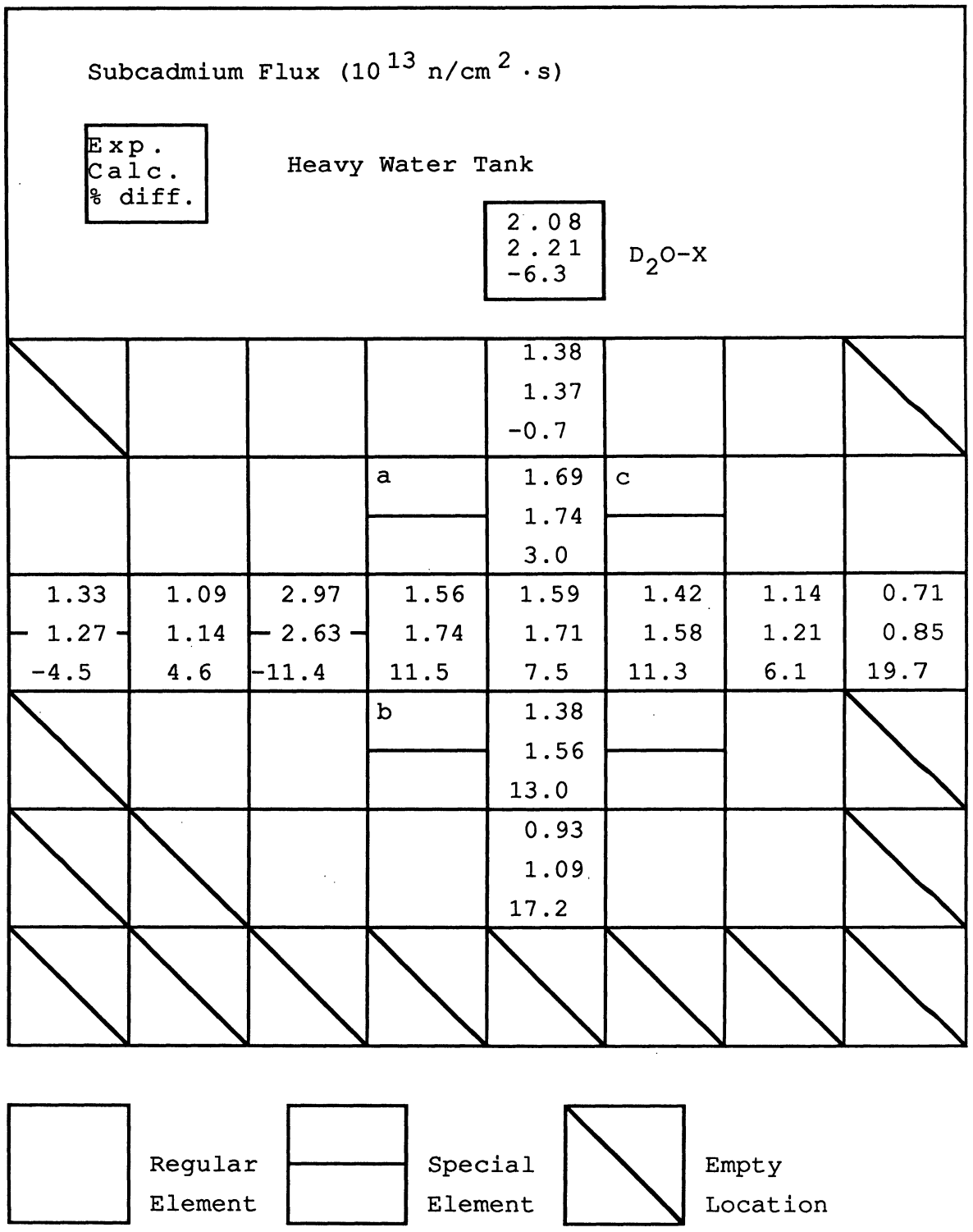

Figure V-2. Subcadmium Flux Map for September 18, 1983, LEU Core

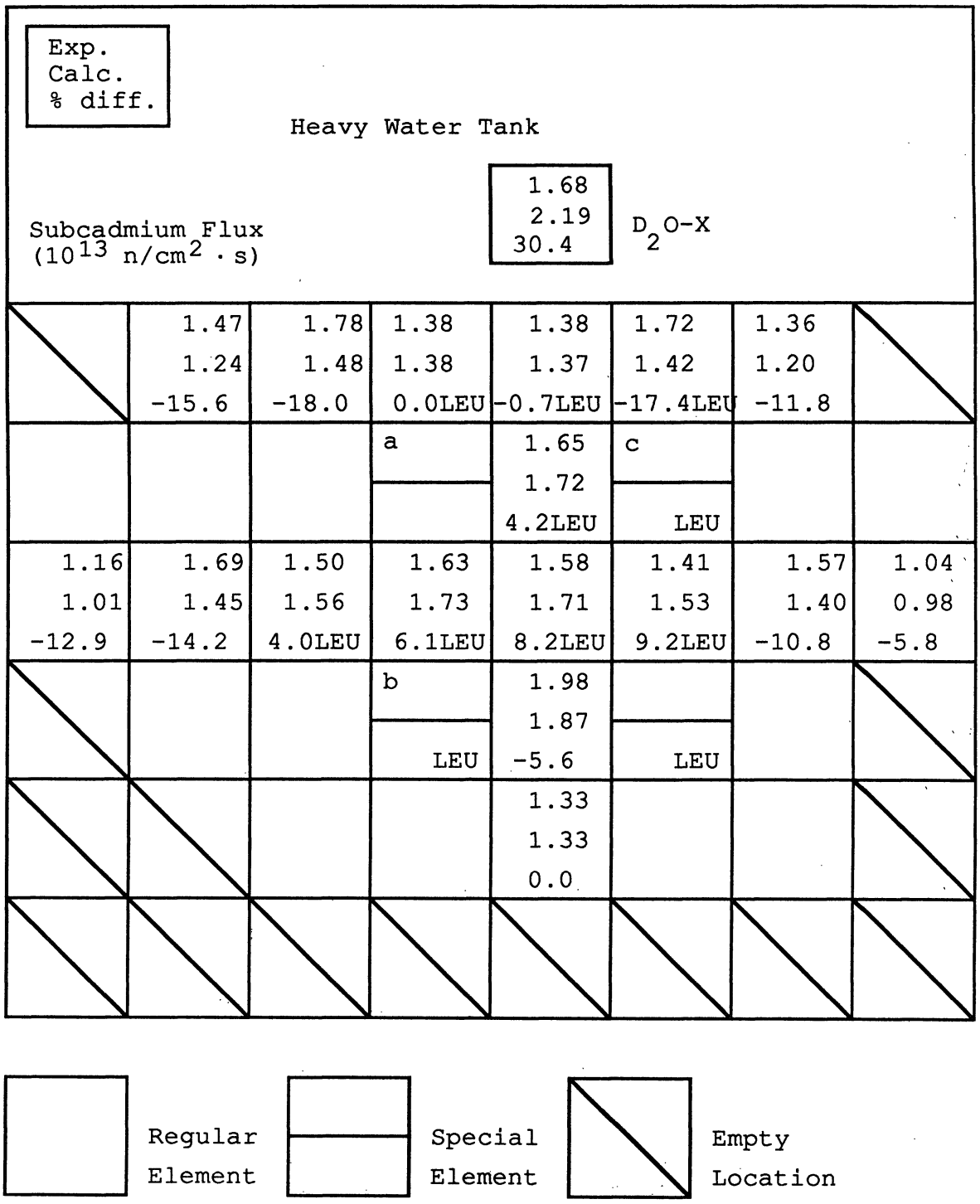

Figure V-3. Subcadmium Flux Map for October 5, 1983, Mixed Core

These discrepancies reflect uncertainties and errors both in measurements and calculations. In order to get a better perspective on the discrepancy between the calculated and SPND thermal flux maps, we compare the flux at D_2O-X and L-37 in Table V-3 for several core configurations including those of Figures V-1 through V-3. In general, the agreement between the measurement and calculation appears to be better for the LEU configurations than the HEU configurations, and the L-37

Table V-3. Subcadmium Flux at L-37 and D_2O-X

Core	Measured (SPND)			Calculated		
	L-37	D_2O-X	D_2O-X/L-37	L-37	D_2O-X	L-37/D_2O-X
05/29/82 HEU	2.16	1.71	0.792	1.97	1.95	0.990
10/01/82 HEU	2.16	1.74	0.784	2.08	2.14	1.03
06/27/83 LEU	2.16	2.16	1.23	1.75	2.24	1.28
09/18/83 LEU	2.16	2.08	1.31	1.71	2.21	1.29
10/05/83 Mixed	2.16	1.68	1.06	1.71	2.19	1.28

flux is underpredicted for the HEU configurations in our UM2DB calculations. It also appears that the agreement between the calculated and measured D_2O-X flux is rather poor for the HEU and mixed core configurations. In an effort to verify the adequacy of the 5% correction factor applied for converting the UM2DB thermal flux maps to the equivalent quarter-height maps in Figures V-1 and V-3,

three-dimensional diffusion theory calculations were performed with the UM3DB code discussed in Section II. These two-group coarse-mesh calculations used a homogeneous (2x2) mesh per assembly, with a total of (38x34) meshes, in the x-y plane and 31 axial meshes, including 14 meshes for the active fuel region. The UM3DB thermal flux maps at half-height and quarter-height are compared with core-average maps in Figures V-4 and V-5 for the May 29, 1982, HEU core and June 1983 LEU core, respectively. The comparisons between the quarter-height and core-average maps indicate that the 5% correction factor, obtained from an HEU iron-wire activation, is generally applicable both for HEU and LEU configurations. For the configurations analyzed, the applicable correction factor is in the range of 4 to 7% for Figure V-4 (HEU) and 3 to 6% for Figure V-5 (LEU).

B. Eigenvalue Calculations

1. Core Eigenvalue Bias

Core eigenvalues were calculated for several FNR core configurations with the same (6x6) UM2DB setup used in Section V.A for calculation of the subcadmium flux distributions. Table V-4 gives a comparison between the measured core eigenvalues and UM2DB eigenvalues. For depleted cores, assembly-average fuel burnup distributions were obtained with the coarse-mesh UM2DB calculations

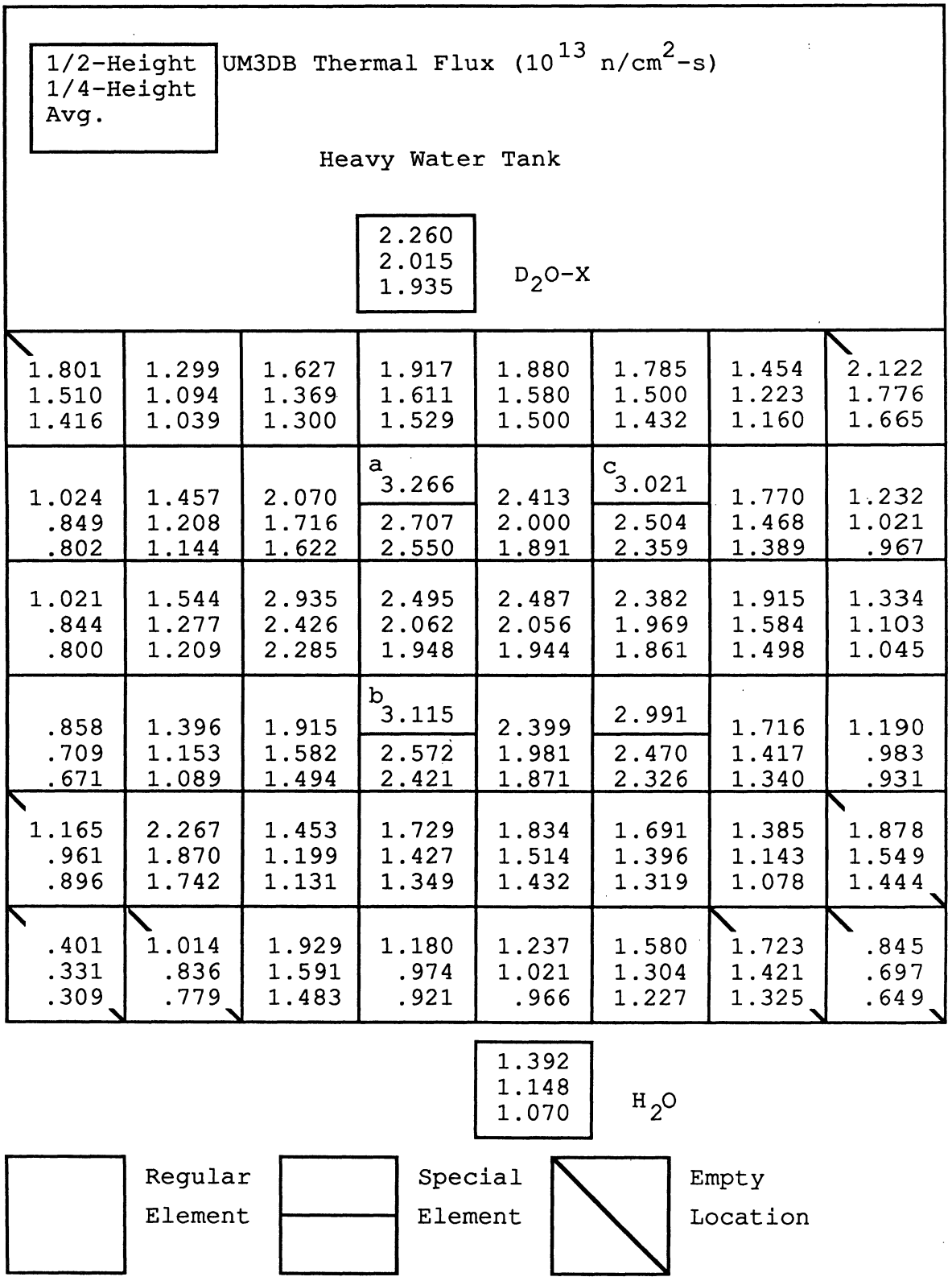

Figure V-4. UM3DB Calculated Thermal Fluxes for May 29, 1982, HEU Core

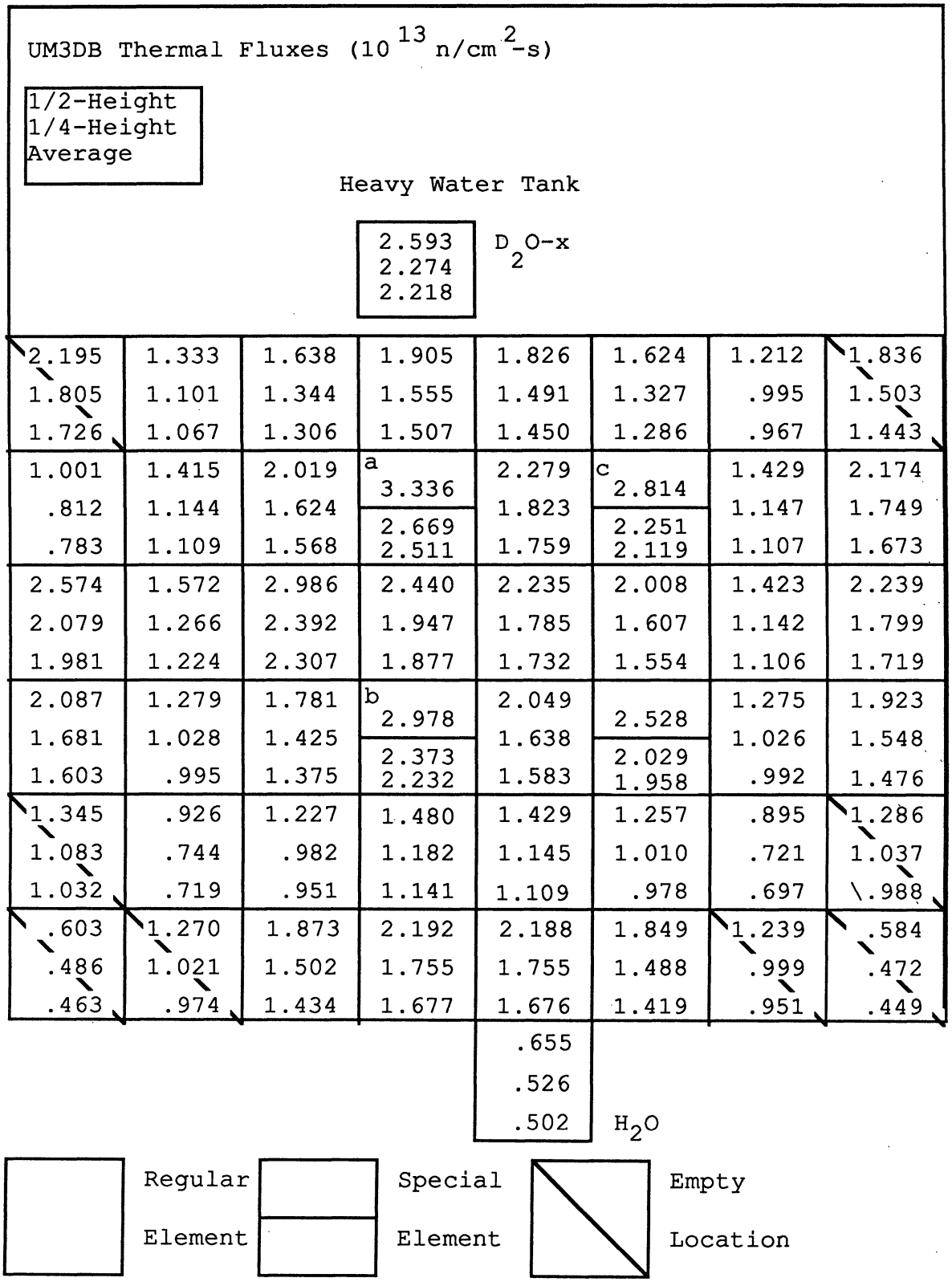

Figure V-5. UM3DB Calculated Thermal Fluxes for June, 1983, LEU Core

Table V-4. UM2DB FNR Eigenvalue Calculations

Core	Average Burnup[1] (%)	Measured ρ_{ex} (% Δk/k)	UM2DB		Absolute Bias (% Δk/k)
			Eigenvalue	(% Δk/k)	
May 11, 1982 Full power HEU	14.36	3.29	1.0462	4.42	1.00[3]
September 26, 1982 Full power HEU	14.01	3.14	1.390[4]	3.75	0.48[3]
December, 1981 Critical LEU	0.00	0.45	1.0012	0.12	-0.10[2]
June 8, 1983 Critical LEU	2.96	0.00	1.0017	0.27	0.27[2,3]
June 8, 1983 Full power LEU	3.42	3.29	1.0335	3.24	-0.18[3]
July 8, 1983 Full power LEU	4.26	3.21	1.0359[4]	3.47	0.13[3]
March, 1983 Critical Mixed	13.14	0.10	1.0106	1.05	1.18[2]
October 5, 1983 Full power Mixed	13.31	3.02	1.0368[4]	3.55	0.40[3]

[1] UM2DB calculated fuel burnup
[2] Corrected for power defect of .23% Δk/k
[3] Corrected for samarium reactivity worth of .13% Δk/k
[4] Estimated based on an earlier UM2DB run and the preceding case

discussed in Section V.A. A more detailed analysis of the initial LEU critical configuration of December 1981, is given in Section V.B.3.

Before determining the absolute bias between the calculated and measured eigenvalues, two corrections must be made to the calculations. First, UM2DB performs the calculation assuming the core is at full power. In the case of a critical loading, the eigenvalue is measured at zero power. Therefore, a power defect correction of -0.23% $\Delta k/k$ (as measured for the August 1983 LEU core) has been applied to these cases. Second, post-shutdown samarium build-up is not handled in UM2DB calculations. The effect of this limitation on the calculated core eigenvalue was examined by simulating the actual history of LEU fuel elements with the UMLEO code. For the June 1983 LEU configuration of the FNR core, it is estimated that the samarium reactivity at the beginning of the cycle is 0.13% $\Delta k/k$. This correction factor has also been applied to the calculated eigenvalues for the May 1982 HEU core and the October 1983 mixed core.

The UM2DB calculations indicate a substantially higher eigenvalue bias for the configurations containing highly depleted HEU fuel elements than LEU configurations with fresh or slightly depleted fuel elements. Overall, the UM2DB core eigenvalues indicate a bias in the range -0.2 to 1.2% $\Delta k/k$.

2. HEU/LEU Fuel Element Exchange

In order to examine some of the performance differences of the LEU and HEU elements as well as to provide additional opportunity for analytical methods verification, an experiment was performed on September 15, 1981. The experiment consisted of the substitution of a fresh LEU fuel element for a fresh HEU element in an equilibrium HEU FNR core. The substitution was first made at the center of the core. Then, after returning the core to its original configuration, the exchange was repeated at the edge of the core. After each substitution the relative reactivity worth of the LEU element was measured.

The reactivity for the exchange at the center of the core was determined from the resulting positive period. At the edge, the effect of the change was so small, however, that the period was too long to accurately measure. Thus, in this case, the reactivity effect was deduced from the change in the critical position of the regulating rod. The configuration of the HEU core is shown in Figure V-6. The center position is marked 37; the edge position is 40. The results of the experiment are summarized in Table V-5.

The HEU core and its two variations (LEU in the center, and LEU on the edge) were simulated by the UM2DB code. In the calculations each fuel element was approximated by an 8x8 mesh per assembly, with an earlier set of reflector

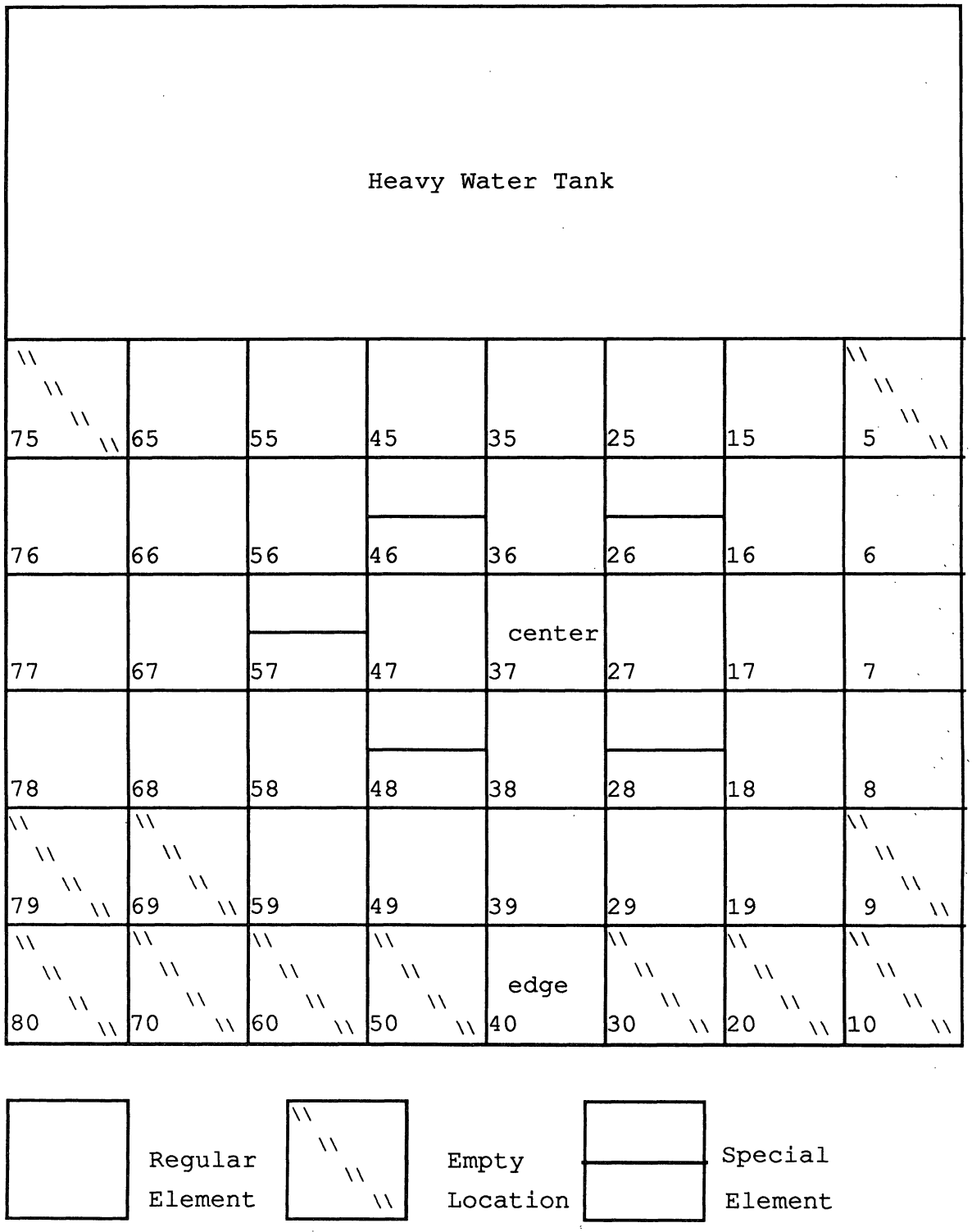

Figure V-6. Core Configuration for Single-Element Exchange Experiments

cross sections. From the calculated eigenvalues, reactivity effects of the two exchanges were determined. These values are presented in Table V-5 as are those calculated by the PERTV code which uses forward and

Table V-5. Reactivity Effect of HEU/LEU Exchange

Location of Exchange	Δk/k (%)		
	Experiment	Analytic	
		UM2DB	PERTV
Center (37)	-0.1176	-0.1301	-0.1105
Edge (40)	+0.011	+0.0036	+0.010

adjoint fluxes from the UM2DB code to calculate changes in eigenvalue. For the center exchange, where the reactivity effect is large, both analytical methods provide satisfactory results. However, the perturbation technique simulated the edge exchange much better than did the UM2DB code. This is because the small reactivity effect strains the eigenvalue convergence criteria in the UM2DB code. Although the results in Table V-5 were obtained with a mesh structure and reflector cross sections that are slightly different from those used in UM2DB calculations of Sections V.A and V.B.1, the results are still representative of our neutronic methodology.

The differences between the two elements are less apparent on the edge of the core than at the center simply because of the lower flux in that region. The reason why the LEU element is less reactive than the HEU at the center of the core but more reactive at the edge is more subtle. Infinite medium calculations shed some light on this phenomenon. In particular, the LEU element is less reactive in an infinite medium [k_∞(LEU) < k_∞(HEU)] but for a finite core, the LEU fuel is more reactive [k_{eff}(LEU) > k_{eff}(HEU)], as predicted by the UM2DB code. This is also seen by comparing the migration area, M^2, for the two fuels from the LEOPARD code; here M^2 (LEU) < M^2 (HEU), indicating the LEU fuel is less "leaky". Therefore, inserting the LEU fuel in the center of the core, where the leakage is low, is similar to an infinite medium and hence results in a lower reactivity. On the other hand, inserting it on the edge of the core, where leakage dominates, the smaller M^2 for the LEU fuel causes a slight reactivity increase.

In preparation for the October 3, 1983, loading of a mixed HEU-LEU core, fuel loading calculations were also performed with the UM2DB code to investigate the effect of replacing HEU special elements with LEU special elements at the control rod locations. The calculations indicate that a HEU special/LEU special exchange has a minimal effect on the flux distribution in the core.

3. LEU Critical Loading

The December 1981 loading of the first LEU core provided another opportunity to verify the ability of our computational methods to simulate an LEU experiment. The initial critical loading took two days and was completed at about noon on December 8 after the placement of the 23rd LEU element. Figure V-7 shows the critical configuration, the positions of the three fission chambers, and, in the upper right corner of each element location, the order of loading. Upon withdrawal of all control rods except the regulating rod, the reactor experienced a period of 113 seconds, which corresponds to an excess reactivity of 0.067%. If the worth of the regulating rod (measured to be 0.383%) is considered, the cold, clean LEU core had an excess reactivity of 0.45%.

The critical loading sequence was simulated before the test with (6x6) mesh UM2DB calculations. Table V-6 presents the eigenvalues obtained from the pre-test calculations. The nominal masses of ^{235}U were those considered in the pretest calculations. The masses labeled "actual" were calculated by summing up the mass of each loaded element as reported by the manufacturer.

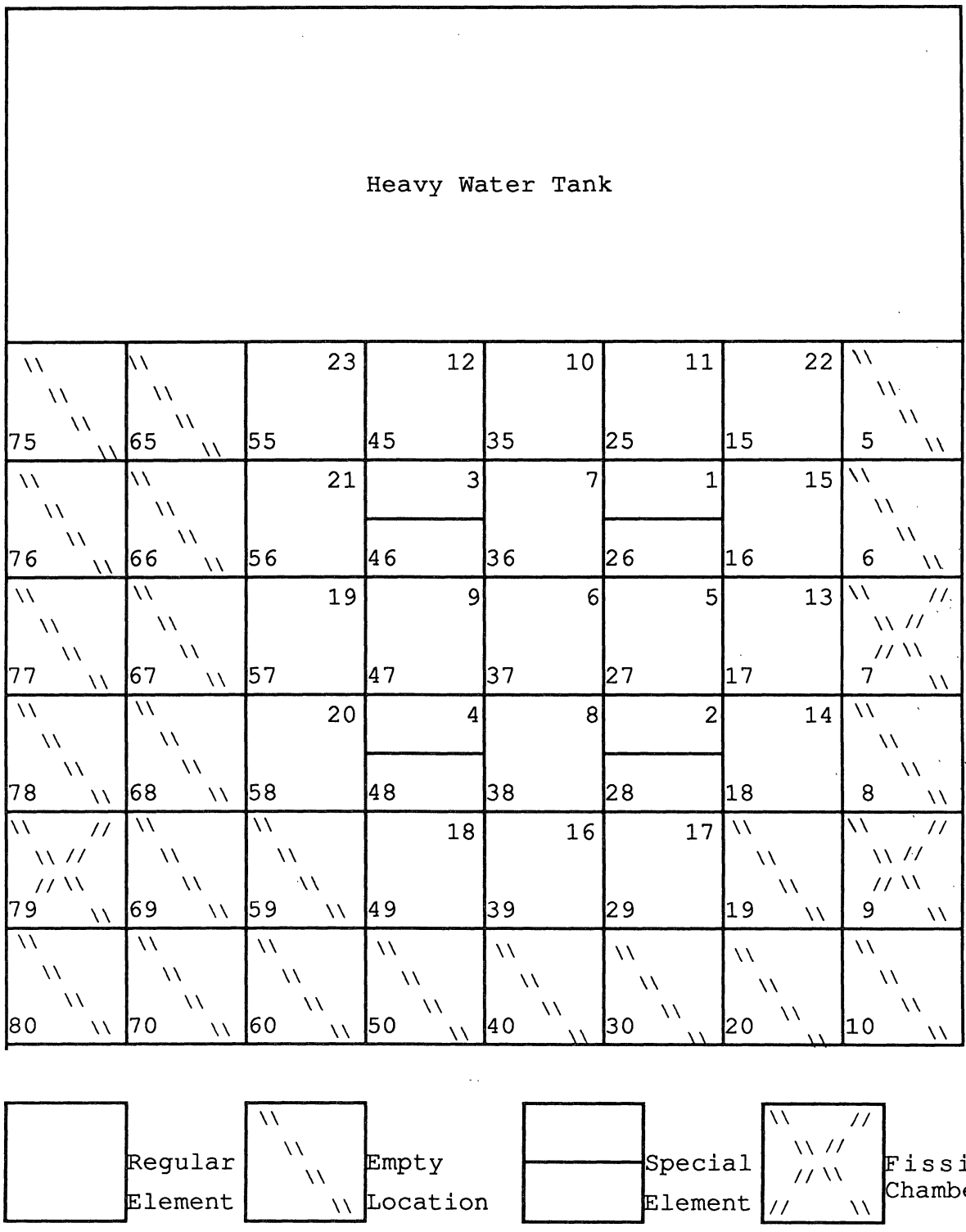

Figure V-7. LEU Critical Loading Configuration at the FNR, December 8, 1981

Table V-6. LEU Critical Loading

Number of LEU Elements	^{235}U Mass (g)		UM2DB calculated k	
	actual	nominal*	updated calculation	pretest calculation
21	3171.20	3178.7	--	0.9835
22	3344.85	3346.0	--	0.9926
23	3512.82	3513.3	1.0056	1.0025

*nominal elemental ^{235}U masses
regular: 167.3 g
special: 83.65 g

The core simulated by the UM2DB code is one with all rods withdrawn. The measured critical mass was for the 23-element LEU core with the regulating rod fully inserted. The analytical and experimental results can be compared by examining (1) the multiplication constant and (2) the estimated critical mass. The multiplication constant of 1.0045 for the LEU core with all rods withdrawn compares with the pre-test prediction of 1.0025 and the latest estimate of 1.0056. From the mass of 3512.82 g for the super-critical core and the excess reactivity, a critical mass of 3436 g ^{235}U was estimated. The value estimated from the pre-test UM2DB calculations was 3471 g.

C. Simulation of Reactivity Worth Measurements

In addition to calculation of the core eigenvalues for several FNR configurations as reported in Section V.B, efforts have been made to simulate and analyze the reactivity-related parameters measured during the LEU project. They include the integral and differential worths of shim safety rods, void coefficients of reactivity, and power defect of reactivity. The integral reactivity worths of shim rods for several FNR configurations and void coefficients of reactivity for the February 12, 1979, HEU configuration were simulated with the UM2DB code. In addition, the three-dimensional diffusion theory code, UM3DB, was used for simulation of the power defect and the differential rod worth for the June 8, 1983, LEU core configuration.

The effective absorption cross sections and the reactivity worths for the shim rods were obtained through a sequence of calculations involving the EPRI-HAMMER, TWOTRAN, and UM2DB codes, as described in Section II.E. The void coefficient simulation was performed with the UM2DB code in conjunction with a first-order perturbation theory code, PERTV. The power defect measurement was simulated with a special version of the UM3DB code, coupled with a point-wise thermal-hydraulic feedback model. For the rest of our neutronic analysis, no

point-wise thermal-hydraulic feedback has been accounted for; cross sections generated for core-average fuel and moderator temperatures are used whenever necessary.

1. Integral Reactivity Worth of Shim Rods

The integral worths of the FNR shim rods are calculated by computing the reactivity difference between a rod-in and a rod-out UM2DB run. The UM2DB calculations were done with the standard (6x6) mesh/assembly structure used for the cases presented in Sections V.A and V.B. The rod worths are determined by measuring the worth of one-half of a rod, and multiplying the result by a factor of 2. Several full-length rod worth measurements indicate the ratio of the full-length rod worth to the half-length rod worth to be between 1.88 and 1.99. Since full-length rod worth measurements involve considerable perturbation in the flux distribution due to swapping of shim rods, measured full-length worths are not directly used in our comparison. The extrapolated full-length rod worth data are compared with UM2DB calculations for three cores in Table V-7.

2. Differential Reactivity Worth of Shim Rods

Simulation of the differential reactivity worth measurement taken for shim rod A in the June 7, 1983, LEU loading was performed with the UM3DB code. This simulation is based on the same (2x2) mesh/assembly structure used in the three-dimensional diffusion theory

Table V-7. Shim Rod Worths

Core	Rod	Measurement*	Calculation	% differrence
Sept. 26, 1982 HEU	A	2.50	2.42	-3.2
	B	2.12	2.02	-4.7
	C	2.36	2.16	-8.5
July 8, 1983 LEU	A	2.84	2.72	-4.2
	B	2.32	2.24	-3.4
	C	1.91	1.75	-8.4
Oct. 5, 1983 Mixed	A	2.72	2.66	-2.2
	B	2.14	2.13	-0.5
	C	2.16	1.96	-9.3

*Estimated to be 2 x measured half rod worths

calculations of Section V.A. The experimental data for the shim rod calibration show only the position of the shim rod being calibrated. For the UM3DB simulation of the rod A worth curve, rods B and C were assumed to move in a bank, with its position calculated through experimental rod-worth curves. For example, the three shim rods were initially at A=14.7", B=14.9", and C=14.84", respectively, above the fuel plate when the reactor was critical. Rod A was then lowered to a 12" position, with rods B and C withdrawn to a 17" position to restore criticality. The UM3DB code was run for five different sets of shim rod positions, including the configuration with all shim rods withdrawn, to get a differential rod-worth curve for rod A. The results of

the UM3DB calculation are compared with the experimental data in Figure V-8. With the maximum error of -8.4%, the UM3DB reactivity worth calculation is in reasonable agreement with the experimental data.

3. Void Coefficient of Reactivity

In the void coefficient experiments performed as part of the Nuclear Engineering Department reactor laboratory course, the void is simulated by inserting an aluminum blade into the core. Because the cross sections for aluminum are finite the experiment does not truly measure the void coefficient of reactivity, but for our purposes the experiment and calculation can provide a valid basis for comparing the HEU and LEU fuels.

The void coefficient measurements taken for the February 19, 1979, LEU configuration were simulated in our effort to verify the adequacy of our calculational method. The core configuration and blade positions during the experiment are shown in Figure V-9. The comparison of calculated and measured void coefficients of reactivity in Figure V-10 indicates reasonable agreement when uncertainties in measurements are considered. The uncertainties in the measured void coefficients of reactivity in Figure V-10 represent the variation in the three separate measurements taken by students during this reactor laboratory experiment.

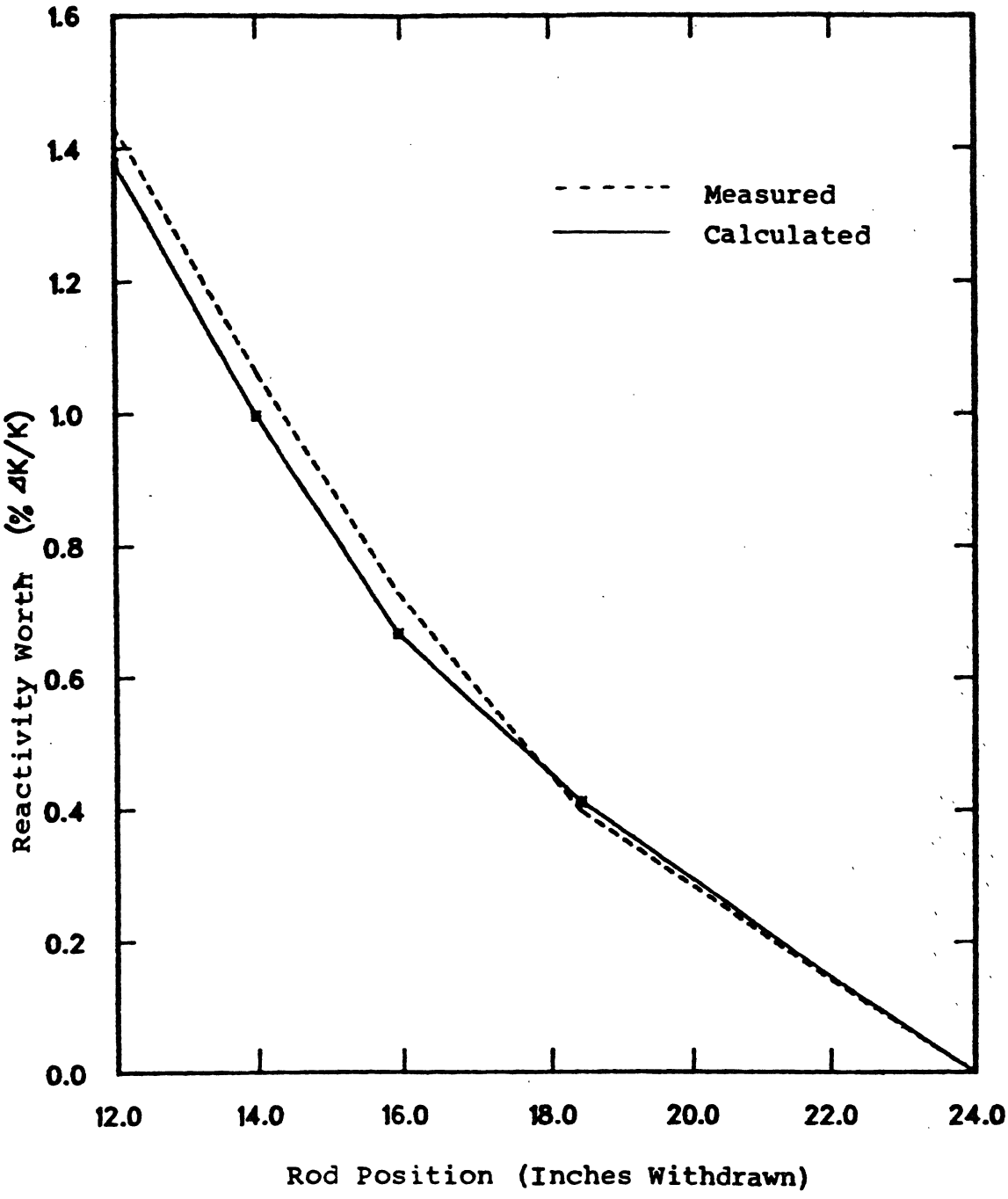

Figure V-8. Integral Rod Worth for Shim Rod A

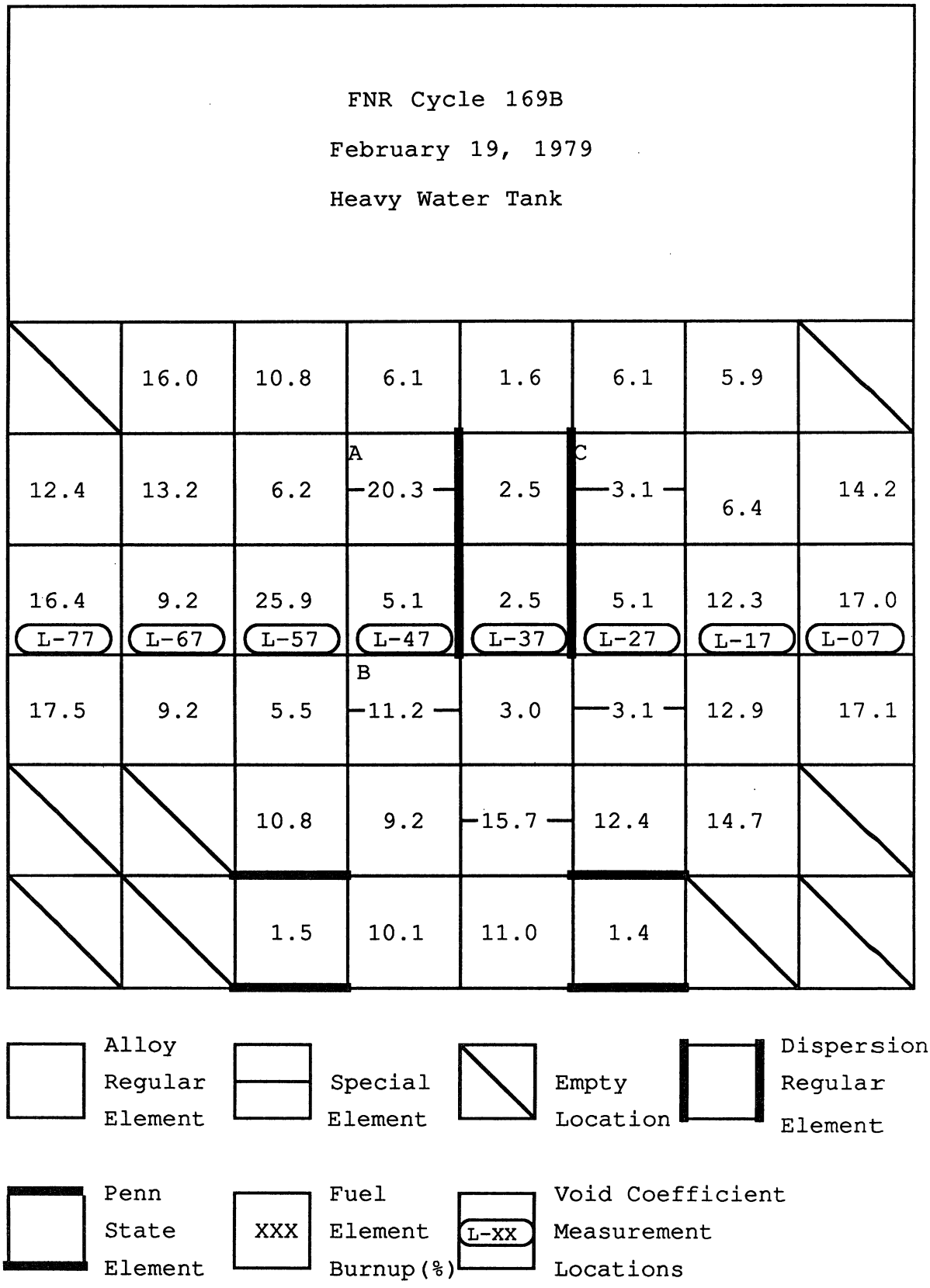

Figure V-9. Core Configuration for Void Coefficient of Reactivity Experiment

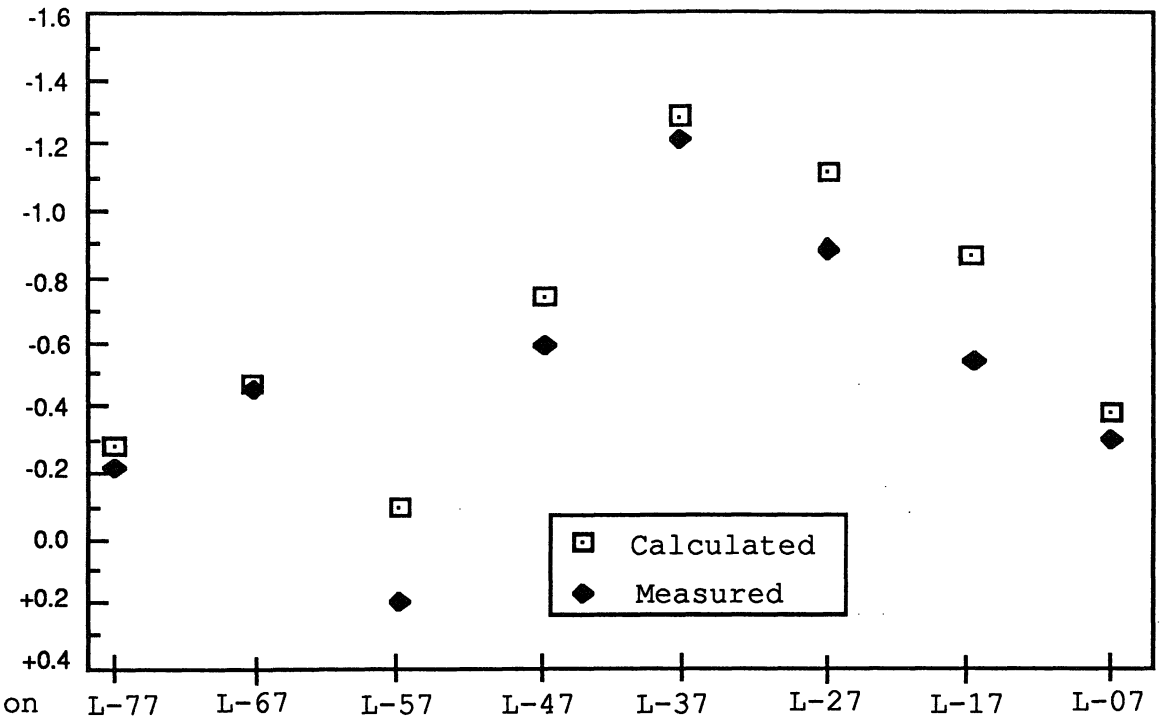

Core position	L-77	L-67	L-57	L-47	L-37	L-27	L-17	L-07
Element type	Alloy	Alloy	Special	Alloy	Dispersion	Alloy	Alloy	Alloy
Void Coefficient (%Δk/k/%ΔV/V)								
Calculated	-0.28	-0.48	-0.12	-0.75	-1.30	-1.13	-0.86	-0.37
Measured	-0.21	-0.46	+0.20	-0.58	-1.23	-0.88	-0.55	-0.28
Measurement Uncertainty	±0.07	±0.13	±0.23	±0.32	±0.02	±0.01	±0.04	±0.01

Figure V-10. Void Coefficient of Reactivity for the Cycle 169B Core

4. Power Defect of Reactivity

For the purpose of simulating power defect measurements at the FNR, a June 1982 full-power configuration was studied with the UM3DB code with point-wise fuel temperature and moderator temperature feedback incorporated. In this two-group, three-dimensional calculation, a (2x2) mesh per assembly in the x-y plane is used with 31 axial meshes including 14 meshes for the core. The thermal-hydraulic parameters used in the simulation include:

Core inlet temperature of water -- 90°F at zero power
-- 104°F at full power

Total coolant flow rate -- 985 gallons/minute

To account for uncertainty in the fraction of coolant flow bypassing the core, two cases were run with 10% and 20% bypass fraction, respectively, in addition to a zero-power case and a full-power case with uniform thermal-hydraulic feedback. The calculated power defect of reactivity is tabulated below:

Case	Power Defect (% $\Delta k/k$)
1. Uniform feedback with 10% bypass	-0.159
2. Point-wise feedback with 10% bypass	-0.202
3. Point-wise feedback with 20% bypass	-0.214

The effect of the point-wise thermal-hydraulic feedback on reactivity is significant, and the power defects for Cases 2 and 3 compare favorably with the measured values of -0.23~-0.25% $\Delta k/k$ for LEU configurations. The measured power defects range between -0.21~-0.31% $\Delta k/k$ for HEU configurations. The average coolant temperature rise of 17.1°F, calculated in Case 2, compares favorably also with typical measured values of 16°F. In contrast, the calculated core-average temperature of 19.3°F in Case 3 suggests that our parametric selection of 20% bypass fraction was perhaps too large.

D. Ex-Core Spectrum Calculations

As part of our effort in developing models to represent the complex geometry in the FNR heavy water tank, one-dimensional ANISN calculations were performed. Both scalar and angular fluxes were obtained in the ANISN calculations to compare with the flux spectra measured at the beam ports. Monte Carlo calculations of the scalar flux have been performed also with the ANDY code [Har70c], but, due to poor statistics, the result is of limited value and is not presented here.

The crystal diffractometer measurements yield the thermal neutron spectra at selected beam ports in the D_2O tank. An insignificant change in the neutron temperature [i.e., the temperature corresponding to the log $(\phi(E)/E)$ fit] at a specific port were observed between the HEU and

LEU fuel; however, a large difference in neutron temperature was observed when the diffractometer was moved to a different beam port. Although this was only one set of measurements and the core configuration was a "high-leakage" HEU core, the difference is large enough (40 K) to warrant additional investigation. Since this temperature difference was observed for I and J ports which "view" the core at angles of 63° and 105° from the north-south line, respectively (hence J-port is actually looking away from the core), the thermal neutron spectrum may depend on direction, as well as distance into the D_2O tank.

As a preliminary attempt to simulate this geometry, a one-dimensional ANISN calculation was performed utilizing a 20-group (6 fast, 14 thermal) library collapsed from the 218-group ENDF/B-IV SCALE library [Wes80]. An S8-P3 calculation was performed for a full-core north-south traverse, including the H_2O reflector, core, and D_2O tank. The resulting thermal spectra were fit to Maxwellians and a spatially-dependent neutron temperature was then obtained. Neutron temperatures were calculated for the angular flux as well as the scalar flux, to ascertain whether the neutron temperature was a function of the neutron direction, as would appear to be the case for the measured spectra. The ANISN results, which must be considered preliminary, predict a temperature decrease of

approximately 20 K for the angular flux at an angle of 130° from the north-south axis (hence similar to J-port) versus the angular flux at an angle of 50° from the north-south axis, which is more like I-port.

The obvious drawbacks of a one-dimensional calculation for this complicated geometry force us to conclude that although there may be a directional temperature effect which appears to be consistent with experiment (and physical intuition), we would prefer to defer further quantitative conclusions to more detailed calculations (e.g., Monte Carlo or 2-D discrete ordinates). As an aside, it may be worthy of mention that the ANISN-predicted neutron temperatures within the core agreed (within 10 K or so) with independent THERMOS calculations of the fuel temperature, which were performed to determine the effect of the in-core sample holder on the fuel thermal spectrum.

E. Discussion of Simulation Results and Neutronic Methods

During the course of the LEU project, a considerable amount of effort has been spent on improving our analysis of the experimental results. This has included parametric studies with unit-cell codes, multi-dimensional diffusion theory codes and transport theory codes as well as investigations into alternative methods of analysis. In spite of these efforts, there is need for further study in

many areas of our neutronic analysis. In determination of the subcadmium flux distribution, for example, we need to improve our understanding of the SPND behavior especially in the reflector environments and our simulation of the SPND geometry in general. The bias in our UM2DB core eigenvalues ranges between -0.2% and 1.2% $\Delta k/k$, which also requires further investigation.

Among the many approximations inherent in our neutronic analysis methods, we have investigated the following aspects:

i) Neutron flux spectrum is a fairly sensitive function of position in a small leaky core like the FNR core. A parametric study has been performed with the UMLEO code to represent approximately the fast neutron leakage in peripheral assemblies. The estimate for the fast neutron leakage was obtained through a two-group UM2DB run where the macroscopic cross sections were generated from a standard UMLEO unit-cell calculation. With the fast neutron leakage more realistically represented in UMLEO, two-group cross sections were regenerated and a UM2DB run performed again. This parametric case indicates that the fast-to-thermal slowing-down cross section Σ_r can decrease by 10% due to the increased leakage and hardened spectrum in peripheral assemblies, which in turn can decrease the subcadmium flux distribution by 2~4% in those assemblies.

ii) The accuracy of the discrete (6x6) mesh/assembly used in the bulk of our UM2DB runs was investigated by comparing a (6x6) run with a corresponding (12x12) mesh/assembly UM2DB run. The latter case was constructed by halving the mesh size in each mesh of the (6x6) setup. The parametric case for the June 8, 1983, LEU core shows that the assembly-center fluxes, which may be compared with SPND data, could change between -5% and +3% from the (6x6) case. The large decreases of up to 5% in the assembly-center fluxes are noticeable mostly in special elements.

iii) Simulation of partially inserted shim rods in typical full-power FNR configurations suggests that our standard (6x6) mesh/assembly UM2DB runs, without such simulation, could incur errors in subcadmium flux distribution of up to 5%, primarily near the rod locations. This maximum error of 5% would apply if the shim rods are inserted into the core by not more than 3.6", which brackets the rod configurations for 12 typical HEU and LEU configurations between 1979 and 1984.

iv) Effects of the axial geometry not represented explicitly in our UM2DB runs have been investigated through three-dimensional UM3DB runs. Representation of the pointwise axial thermal-hydraulic feedback and

equilibrium xenon distribution each would decrease the UM2DB core eigenvalues by 0.05% $\Delta k/k$. The effect of the pointwise fuel burnup distribution can be considerably larger for depleted cores, perhaps up to a decrease of 0.2% to 0.3% $\Delta k/k$ from the UM2DB eigenvalues.

v) Parametric UMLEO runs for the as-built NUKEM and CERCA fuel configurations indicate that the current UM2DB eigenvalues may have to be increased by 0.3 to 0.4% $\Delta k/k$ when the as-built parameters are properly accounted for. The corresponding effects in the flux or power distributions are expected to be minimal.

vi) A considerable amount of uncertainty exists in our present representation of material heterogeneities and flux spectrum in the heavy water tank. A more realistic representation of the heavy water tank may be necessary for eventual improvement in our understanding of the SPND behavior in the heavy water tank, as well as for improvement in our calculation of shim rod worths and thermal flux distribution.

VI. SUMMARY AND CONCLUSIONS

The whole-core LEU fuel demonstration project at the University of Michigan was begun in 1979 with the development of experimental and analytical techniques for characterizing HEU and LEU core configurations at the Ford Nuclear Reactor. Through collaborative efforts with Argonne National Laboratory, an LEU fuel design was selected in 1979 so that minimum perturbations are introduced to the neutronic, operations, and safety characteristics of the FNR. Based on the safety analysis report submitted for the LEU fuel design, approval from the U.S. Nuclear Regulatory Commission was obtained in 1981 for utilization of the LEU fuel in the FNR. Initial criticality was attained in December 8, 1981, with a whole-core LEU configuration. This was followed by low- and full-power testing of the LEU core in 1982, and transitional operation with mixed HEU-LEU configurations in 1983 through 1984. The FNR has been operating entirely with the LEU fuel since October 11, 1984, with current cycles in early 1988 essentially representing an equilibrium core configuration.

The transition from the HEU to LEU configuration has been successfully achieved with minimal effect on the operation of the reactor. Small decreases in thermal flux level and shim rod reactivity worths in the LEU core were observed relative to the HEU core, in essential agreement with the design predictions. These changes have had negligible impact on experimental utilization and safe operation of the reactor. The similarity between the LEU and HEU fuel designs required only minor administrative and procedural

changes to accommodate the LEU fuel in routine operation of the FNR.

Experimental efforts in the whole-core FNR demonstration project centered around measurement of spatial and spectral neutron flux distributions. Emphasis was placed on accurate measurements of thermal neutron flux within and outside the core, through the use of iron wire irradiations and rhodium SPNDs. These thermal flux measurements confirmed the decrease in thermal flux level predicted in the LEU design calculations. Throughout the project, SPND measurements were extensively utilized to determine thermal flux, with iron wire irradiations providing the benchmark data. To convert the SPND current measurements to thermal flux values, the detector sensitivity was determined through iron and rhodium wire irradiations.

Multiple foil activations were performed in both the HEU and LEU cores to determine detailed neutron flux spectra. New unfolding techniques were developed and comparison among different unfolding methods was made. The set of foils was selected to cover the entire thermal, epithermal and fast energy spectrum. The sensitivity of the unfolded flux to the flux spectrum input to the unfolding codes was analyzed, and inconsistencies or deficiencies in activation cross section data for the foil materials were also studied.

Other reactor parameters measured during the demonstration experiments include shim rod reactivity worth, temperature and void coefficients of reactivity, and power defect of reactivity.

Efforts were also made to measure the leakage neutron flux at various FNR beam ports to monitor the progress of the transition from the equilibrium HEU configuration to the batch LEU and then eventually to the equilibrium LEU configuration. These measurements provided an important basis for validation and development of the reactor physics methodology currently in use for analysis of the MTR-type fuel.

During the course of the project, various neutronic analysis codes were adapted, modified, or developed to perform the necessary reactor physics calculations. Major modifications were made to the UMLEO unit-cell package to implement a slab-geometry capability and an ENDF/B-IV cross section library. Macroscopic fuel depletion capability and a fuel shuffling algorithm were added to the UM2DB diffusion theory code. A three-dimensional multi-group capability was also incorporated as the UM3DB code, a version of which can handle point-wise thermal-hydraulic feedback calculations. A coupled transport-diffusion theory algorithm was developed to calculate reactivity worths for the FNR shim rods. In addition to the comparison of the calculated reactor physics parameters with the available FNR data, simulation of the HEU and LEU IAEA benchmark problems was made to provide further validation of the neutronic code package in use for the FNR analysis.

In spite of a considerable effort spent on analysis of the relevant FNR measurements, and comparison between measurements and calculations, we believe further efforts, both analytic and experimental, are desirable in several areas. They include (1) a

better understanding of the SPND characteristics especially in the heavy water tank, with complex material heterogeneities and neutron leakage effect properly represented, (2) resolution of the considerable bias in the FNR core eigenvalue currently calculated by our neutronic code package, and (3) improvement in the accuracy of the calculated flux distributions and shim rod worths.

APPENDIX A. NEW ENDF/B-IV UMLEO LIBRARY

Differences (for analysis of MTR-type fuels) between the results of the UMLEO code and those of more sophisticated codes, such as the EPRI-HAMMER code, are primarily due to differences in the libraries used [Bro79]. The UMLEO code uses an early industrial data set while the other codes employ the ENDF/B-IV data. In order to remedy this inherent difference, a new library for UMLEO was assembled from the ENDF/B-IV data.

THE new code SPITS, a heavily rewritten version of the SPOTS code, processed data supplied by W.B. Henderson [Hen80] of Westinghouse Electric Corporation into a form compatible with the UMLEO code. The Westinghouse data were created from the original ENDF/B-IV files by the ETOT-5 [Bea71] and ETOG-5 [Kus69] codes. The SPITS code copied data for three of the 25 UMLEO nuclides from the original UMLEO library. Data for the remaining 22 nuclides were read from the Westinghouse tape. Cross sections for deuterium and lumped fission products were taken from the old library because they were not included in the Westinghouse data; the new Westinghouse hydrogen data were not used because the scattering cross sections are based on free rather than the desired bound hydrogen. Plots for the various cross sections versus energy for the

23 standard nuclides were made, both for the 54-group fast library and the 172-group thermal library. Figures A-1 through A-4 illustrate the differences between the two libraries for some important nuclides.

The original UMLEO library includes bias factors which allow results of UMLEO analyses of critical and experimental lattices to agree with the experimentally obtained parameters. The bias was implemented in the SPOTS code by increasing the number of neutrons released per fission by 0.36% and by decreasing the number of neutrons released by ^{235}U undergoing fast fission by 1.22%. Although the latter effect is minor, the former effectively biases the calculated multiplication factor by 0.36%. Comparison of the UMLEO results obtained using a new library without the biases with the corresponding results of more sophisticated codes indicate that the biases are not needed in the new UMLEO library because both the library and the codes used for comparison consistently use the ENDF/B-IV data.

In order to determine the usefulness of the new library and its differences from the old library, extensive comparisons and studies were made. The two UMLEO libraries were compared with benchmark codes, the important differences between the two libraries were deduced using a sensitivity method. In addition, an

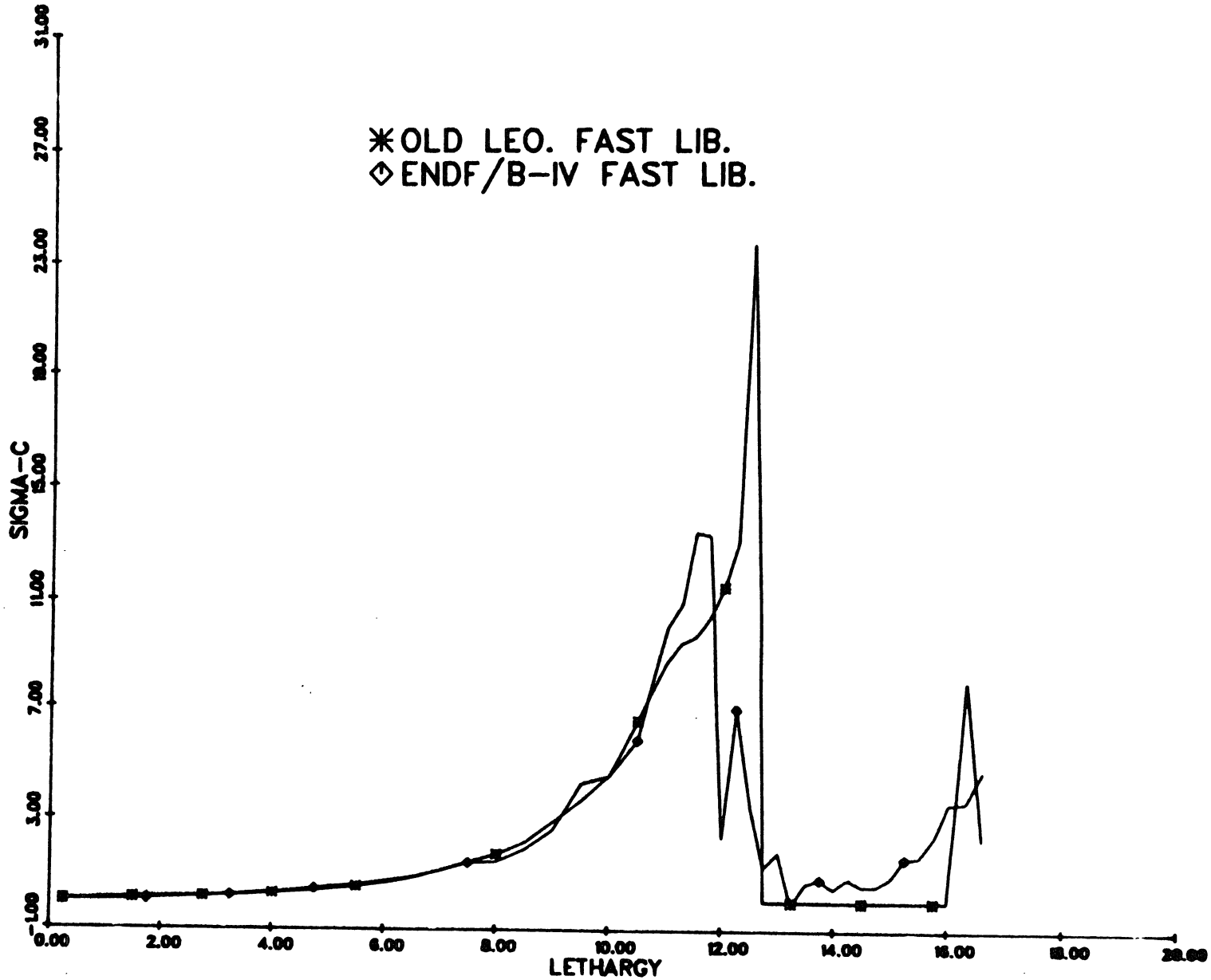

Figure A-1. LEOPARD Library Comparison: ^{235}U Capture Cross-Section vs. Lethargy

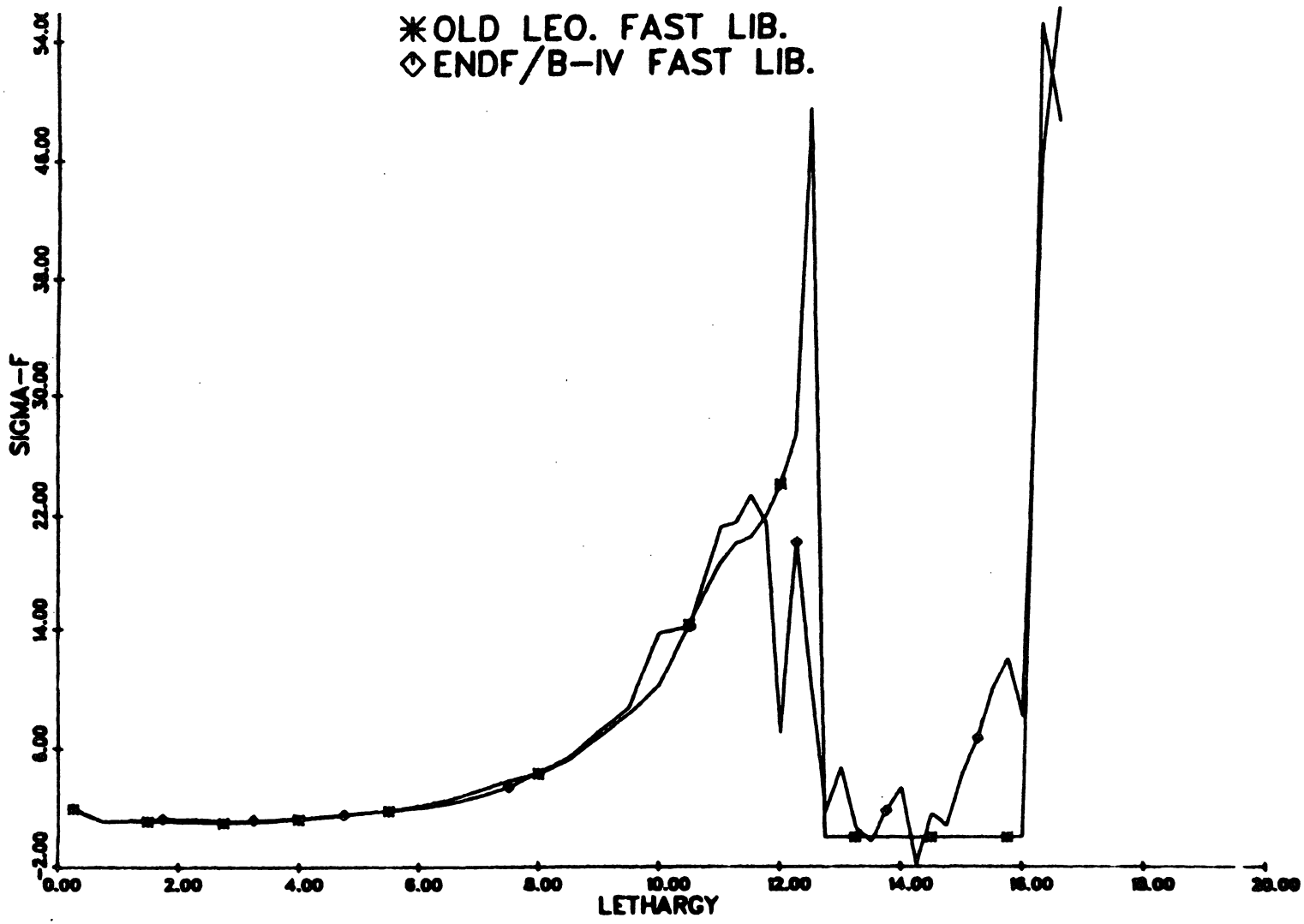

Figure A-2. LEOPARD Library Comparison: ^{235}U Fission Cross-Section vs. Lethargy

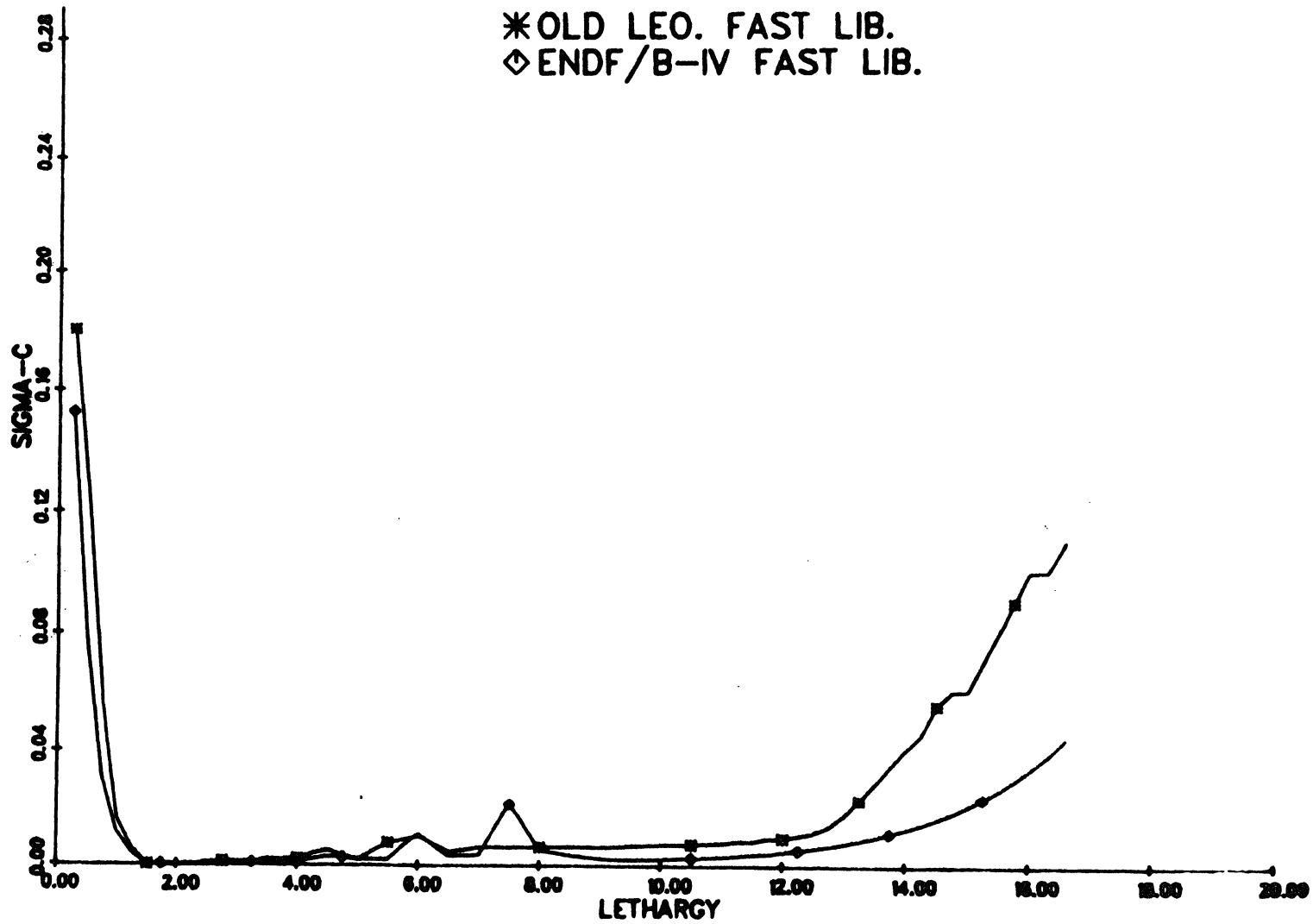

Figure A-3. LEOPARD Library Comparison: ^{27}Al Capture Cross-Section vs. Lethargy

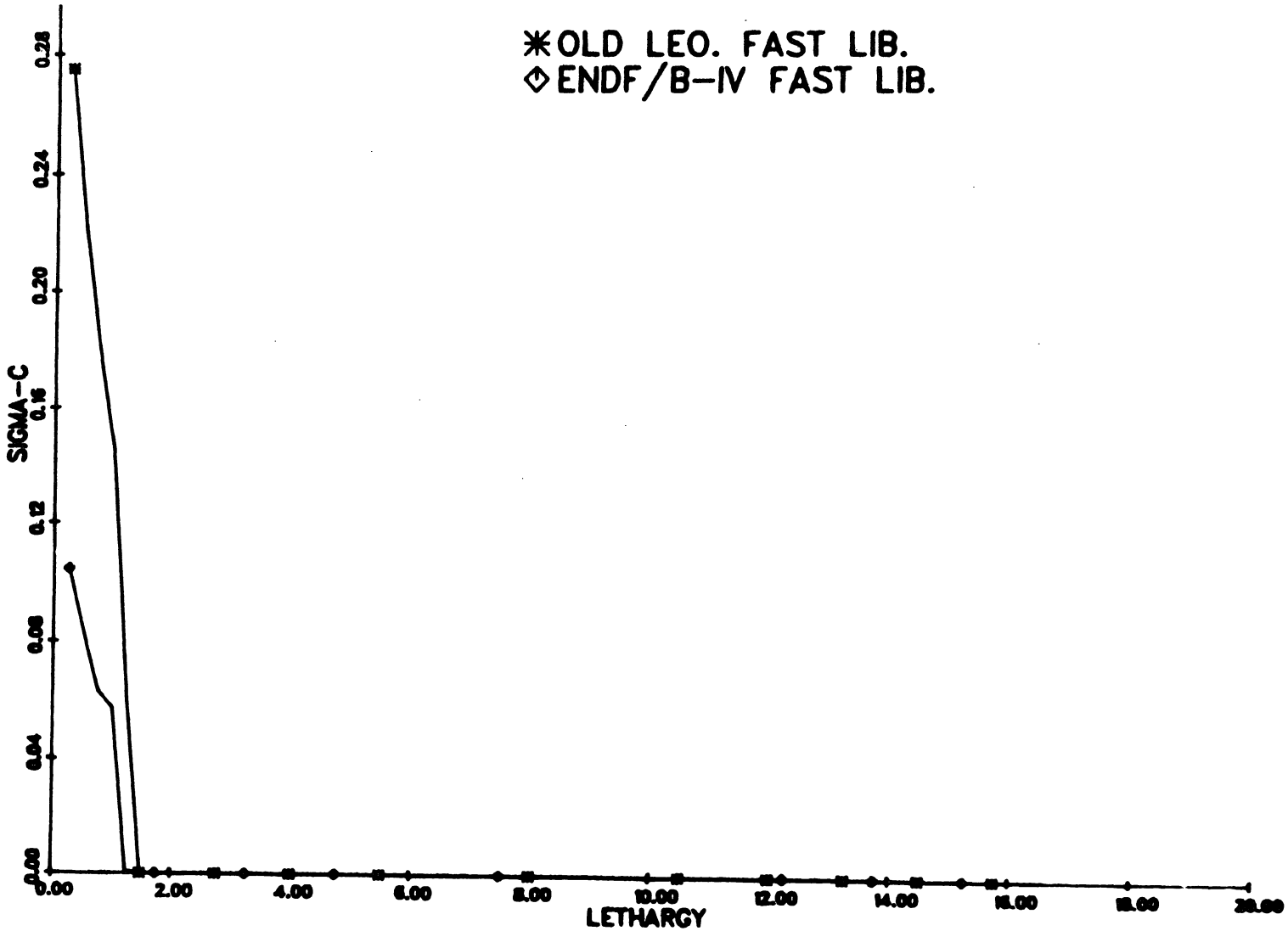

Figure A-4. LEOPARD Library Comparison: ^{16}O Capture Cross-Section vs. Lethargy

experimental critical lattice was analysed, and both HEU and LEU FNR fuel depletion studies were performed with the UM2DB code.

The benchmark codes used for comparison between the UMLEO results using the old and new libraries were the EPRI-HAMMER, VIM [Pra76] and EPRI-CELL [Cob75] codes. The sample case analyzed were typical HEU and LEU plate-type MTR fuels [Woo79]. Comparison of the microscopic cross sections generated by these codes indicate that for the fast energy range those generated using the new library generally agree more closely with those of the benchmark codes than do those generated using the old library. In the thermal energy range, however, the microscopic cross sections of the old library compare more favorably with the benchmark cross sections.

Before any conclusions can be made, however, the importance of the various cross sections must be evaluated. To do this, a code incorporating a sensitivity technique was used to determine the contributions of differences in cross sections of the two UMLEO libraries to the infinite multiplication factor. The contribution of a particular difference was calculated by multiplying the difference in the macroscopic cross section by the importance of that cross section to k_∞. Values of the most important cross sections in the new library are

generally in better agreement with the corresponding values generated by the benchmark codes than are those of the old library as seen in Table A-1 for the HEU case.

The materials for which the differences between cross sections of the two libraries have the largest influence on k_∞ are ^{16}O, ^{27}Al and ^{235}U. The differences between the values of these cross sections of the two libraries can be seen in Figures A-1 through A-4. Although, individually the contributions may be as much as 0.6%$\Delta k/k$, they tend to cancel one another resulting in a much smaller net difference. The net difference calculated directly by UMLEO was 0.12%$\Delta k/k$. The sensitivity method code calculated a slightly different value, 0.14%, as a consequence of the approximate nature of the technique; however, this difference is acceptable and verifies the basic approach of the method.

In an effort to determine how well the new library simulates experimental data, the TRX rodded UO_2 lattice [Har70b] with water/metal ratio of 2.35 was analyzed using both the old and new cross section data sets. Both libraries predict the experimental results quite well, but in most cases the old library provides slightly better accuracy, as can be observed in Table A-2. It is difficult to draw a conclusion from this result because one cannot be sure if the errors are introduced by the

Table A-1. HEU Microscopic Cross-Sections Important to the Infinite Multiplication Factor

Nuclide	Cross Section	Contribution to k (% Δ k/k) [a]	Value				
			Old UMLEO	New UMLEO	Hammer	VIM [b]	E-Cell [b]
^{235}U	σ_{a3}	-0.602	37.5	40.2	39.7	40.2	39.9
^{16}O	σ_{a1}	+0.552	3.70-2 [c]	1.13-2	1.16-2	1.11-2	9.10-3
^{235}U	$\nu\sigma_{f3}$	+0.541	59.9	64.3	63.9	64.4	64.0
^{235}U	σ_{a4}	-0.523	442	445	424	417	421
^{27}Al	σ_{a3}	+0.396	2.91-2	1.03-2	1.08-2	1.07-2	1.03-2
^{235}U	$\nu\sigma_{f4}$	-0.228	921	918	873	859	869
^{27}Al	σ_{a1}	+0.073	9.60-3	6.27-3	6.80-3	6.43-3	6.15-3
^{235}U	$\nu\sigma_{f1}$	+0.038	3.11	3.69	3.43	3.50	3.40
^{27}Al	σ_{a4}	-0.027	0.163	0.164	0.152	0.151	0.151
^{235}U	σ_{a1}	-0.013	1.25	1.30	1.30	1.34	1.31
^{27}Al	σ_{a2}	+0.011	3.50-3	3.02-3	3.06-3	2.57-3	2.71-3
^{1}H	σ_{a4}	+0.009	0.24367	0.24393	0.233	0.230	0.232
	Remaining Cross Sections	-0.020	----	----	----	----	----
	All Cross Sections	+0.146	----	----	----	----	----

[a] Contribution to $k = \frac{\Delta \Sigma}{k_\infty} \frac{\partial k_\infty}{\partial \Sigma'}$ Σ = macroscopic cross-section

[b] [Woo79]

[c] -2

Table A-2. TRX Rodded UO_2 Critical Lattice Results (W/F = 2.35)

Parameter[a]	Experiment[b]	Old UMLEO		New UMLEO	
		Value	% diff.	Value	% diff.
ρ_{28}	1.311	1.2698	- 3.1	1.2843	- 2.0
δ_{25}	0.0981	0.0994	+ 1.3	0.1061	+ 8.2
δ_{28}	0.0914	0.0890	- 2.6	0.0887	- 3.0
CR*	0.792	0.7668	- 3.2	0.7607	- 4.0
B^2	0.0057	0.00564	- 1.1	0.00562	- 1.4
k^c	1.0	0.9984	- 0.16	0.9977	- 0.23

(a) $\rho_{28} = \dfrac{^{238}\text{U epithermal capture}}{^{238}\text{U thermal capture}}$

$\delta_{25} = \dfrac{^{235}\text{U epithermal fission}}{^{235}\text{U thermal fission}}$

$\delta_{28} = \dfrac{^{238}\text{U fissions}}{^{235}\text{U fissions}}$

$\text{CR*} = \dfrac{^{238}\text{U captures}}{^{235}\text{U fissions}}$

B^2 = critical buckling

(b) [Har70b]

(c) Measured value assumed to be 1.0; calculated value is based on a UMLEO run with measured critical buckling input

calculational scheme or by the cross section data base. In addition, the error in the experimental data, which may be as much as 2% must be considered.

Two-group macroscopic constants for the 93% enriched FNR fuel generated by the UMLEO and EPRI-HAMMER codes are compared in Table A-3. In most cases, the parameters calculated incorporating the new library agree more closely with the EPRI-HAMMER parameters. The thermal diffusion closely with the EPRI-HAMMER parameters. The thermal diffusion coefficient and thermal absorption cross section calculated using the old library are exceptions because, as indicated earlier, microscopic thermal constants in the old library are generally in better agreement with those of the HAMMER code.

Complete burnup cross section table sets of both the HEU and LEU fuel have been reproduced by the UMLEO code using the new library for comparison with the sets previously generated using the old library. Using each set, batch core depletion studies have been made with the UM2DB code. In addition, a HEU critical experiment of the FNR core was simulated by the UM2DB code using the old and new cross section data sets.

The infinite multiplication factor of the fresh fuel calculated by the UMLEO code incorporating the new library is higher than that obtained with the old library -- as

Table A-3. Two-Group Constants of 93% Enriched FNR Fuel

Parameter	HAMMER Value	Old UMLEO		New UMLEO	
		Value	% diff.	Value	% diff.
k_∞	1.5556	1.5415	- 0.91	1.5455	- 0.65
ϕ_1/ϕ_2	2.460	2.439	- 0.84	2.457	- 0.13
Age	50.79	52.01	+ 2.46	51.26	+ 0.99
D_1	1.3956	1.4455	+ 3.58	1.4126	- 1.22
Σ_{a1}	1.8578-3	2.0697-3	+11.41	1.8359-3	- 1.18
Σ_{r1}	2.5621-2	2.5722-2	+ 0.39	2.5719-2	+ 0.38
$\nu\Sigma_{f1}$	2.2663-3	2.0874-3	- 7.39	2.2241-3	- 1.86
D_2	2.7607-1	2.8677-1	+ 3.88	2.8960-1	+ 4.90
Σ_{a2}	5.9558-2	6.0115-2	+ 3.01	6.0469-2	+ 3.62
$\nu\Sigma_{f2}$	9.3737-2	9.5112-2	+ 1.47	9.4850-2	+ 1.19

much as 0.26% for the HEU case and 0.22% for the LEU fuel. As the fuel is depleted the two values become closer to one another as noted in Table A-4. This is a consequence of the higher absorption cross section of ^{235}U in the new library resulting in an increased burnup rate for that nuclide. The value of the effective multiplication factor, which was calculated with a constant buckling 0.00914 cm^{-2}, shows a larger difference. The discrepancy in k_{eff} can be attributed to the large difference in the fast non-leakage probability P_{FNL}. At the beginning-of-life the difference in k_{eff} is 0.89% decreasing to 0.75% for the HEU case after 500 days of depletion. For the LEU case, the difference is initially 0.82% and decreases to 0.59% after 700 days. The new library yields higher values of k_{eff} and k_{∞} throughout the depletion steps.

To further assess the impact of the new UMLEO library on fuel depletion calculations, the HEU and LEU batch core configurations were analyzed for the FNR core. In the UM2DB depletion calculations covering the fuel depletion from beginning-of-life through 200 days of full power operation, differences in k_{eff} for the HEU and LEU cores obtained with the two UMLEO cross section libraries stay nearly constant with depletion. Again, the new library predicted the higher value, as seen in Figures A-5 and

Table A-4. HEU FNR Burnup Effect on LEOPARD Results

Time Days	Burnup MWD/T	^{235}U % Burnup		k_∞			k_{eff}*			P_{FNL}*		
		Old UMLEO	New UMLEO	Old UMLEO	New UMLEO	% diff	Old UMLEO	New UMLEO	% diff	Old UMLEO	New UMLEO	% diff
0	0	0	0	1.5417	1.5447	+0.26	1.0011	1.0100	+0.89	0.6785	0.6809	+0.35
30	10814	1.49	1.49	1.4886	1.4934	+0.32	0.9680	0.9771	+0.94	0.6789	0.6821	+0.47
100	36046	4.93	4.95	1.4674	1.4712	+0.26	0.9534	0.9619	+0.89	0.6793	0.6826	+0.49
200	72092	9.84	9.86	1.4388	1.4421	+0.23	0.9338	0.9417	+0.85	0.6799	0.6833	+0.50
300	108137	14.73	14.76	1.4089	1.4119	+0.21	0.9132	0.9207	+0.82	0.6806	0.6841	+0.51
400	144182	19.61	19.66	1.3777	1.3802	+0.18	0.8917	0.8987	+0.79	0.6812	0.6848	+0.53
500	180229	24.22	24.54	1.3447	1.3466	+0.14	0.8691	0.8756	+0.75	0.6819	0.6856	+0.54

*calculated with $B^2 = 0.00914\ cm^{-2}$

A-6. For the fresh HEU core the difference is 0.83%. After about fifteen days of fuel burnup, it peaks to about 0.90%. With time the difference gradually decreases to 0.80% at 200 days. The LEU core behaves in a similar manner. Initially, the difference in eigenvalue is 0.74%. After a peak difference of 0.80% at about 20 days, the difference slowly decreases to 0.69% at 200 days. The decrease, as before, can be attributed to the faster depletion of ^{235}U with the new library.

The eigenvalues calculated in the UM2DB simulation of the HEU critical experiment performed on June 13, 1977, during FNR cycle 147B are 1.0024 and 1.0102 for the old and new libraries, respectively. The difference of 0.78% is consistent with that found in the cases mentioned above. This case is not a completely independent evaluation of the differences between the two libraries because the data input to establish the middle-of-life core (i.e., fuel burnup distribution) were calculated for both cases using the old UMLEO library.

In summary, the new ENDF/B-IV library shows better agreement with the results of more sophisticated codes on both the macro- and microscopic levels. Cores analyzed with the new library are predicted to deplete slightly faster but with higher initial multiplication factor than are cores studied using the old library.

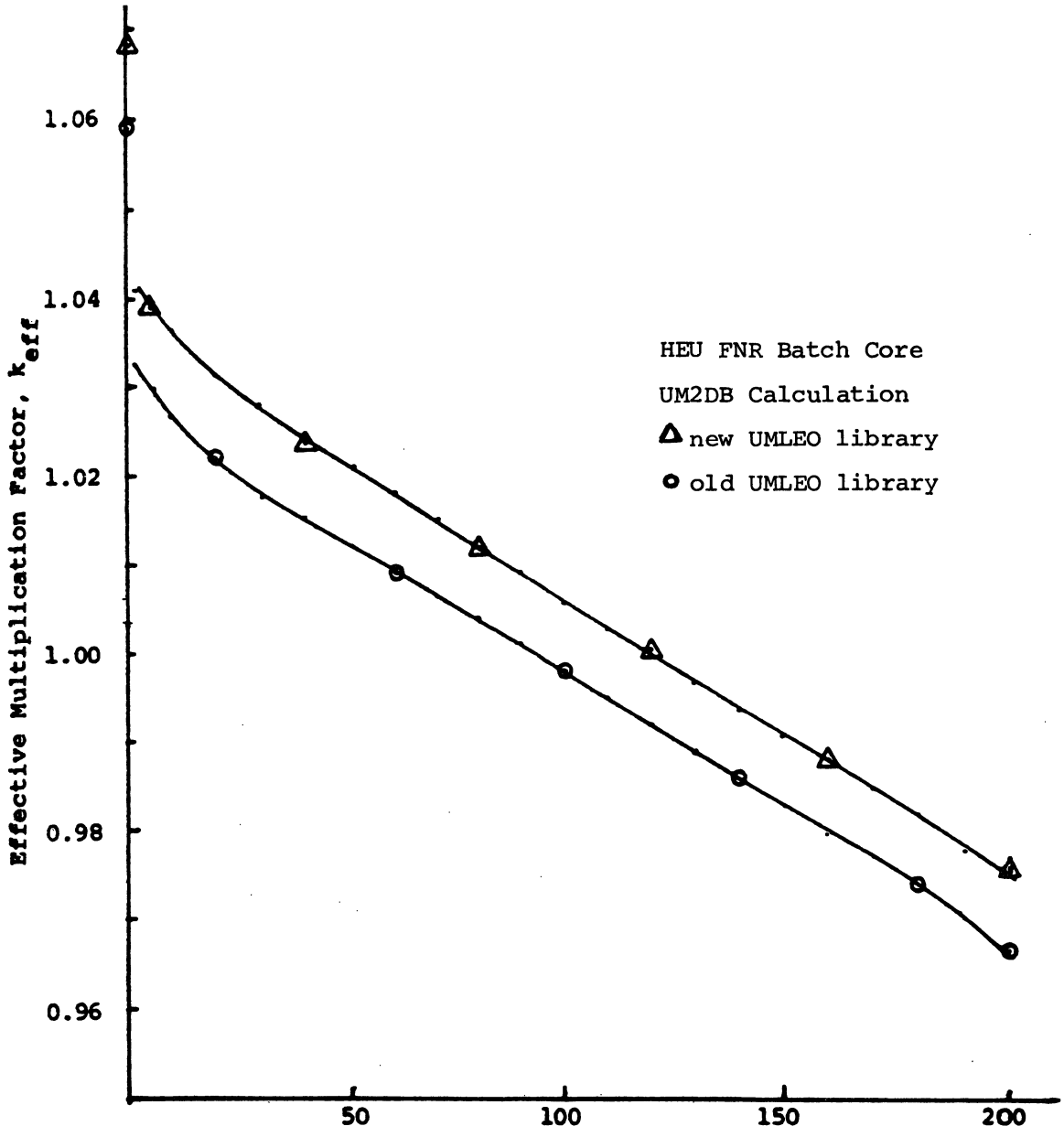

Figure A-5. Effective Multiplication Factor vs. Fuel Depletion

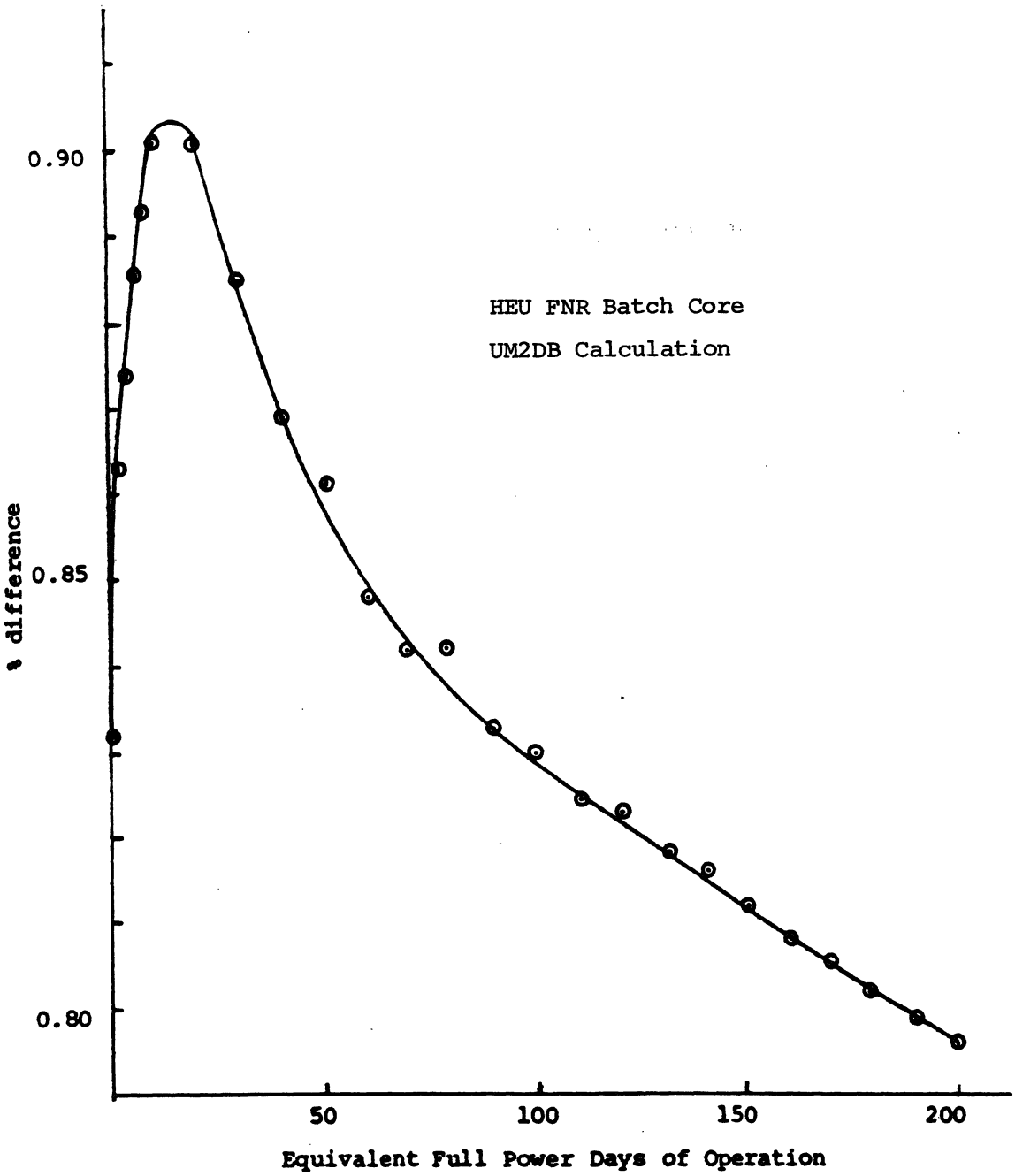

Figure A-6. Difference in the Effective Multiplication Factor Due to Different Libraries vs. Fuel Depletion

APPENDIX B. SELECTED DATA BASE FOR THE FORD NUCLEAR REACTOR

Table B-1. FNR Shim Safety Rod Composition and Geometry

Nuclide	Number density* (atoms/b-cm)
^{10}B	.001108
^{11}B	.005184
Fe	.05644
Ni	.0113
Cr	.0164

*based on composition and density of boron stainless steel, 15 w/o natural boron, from [AND62]

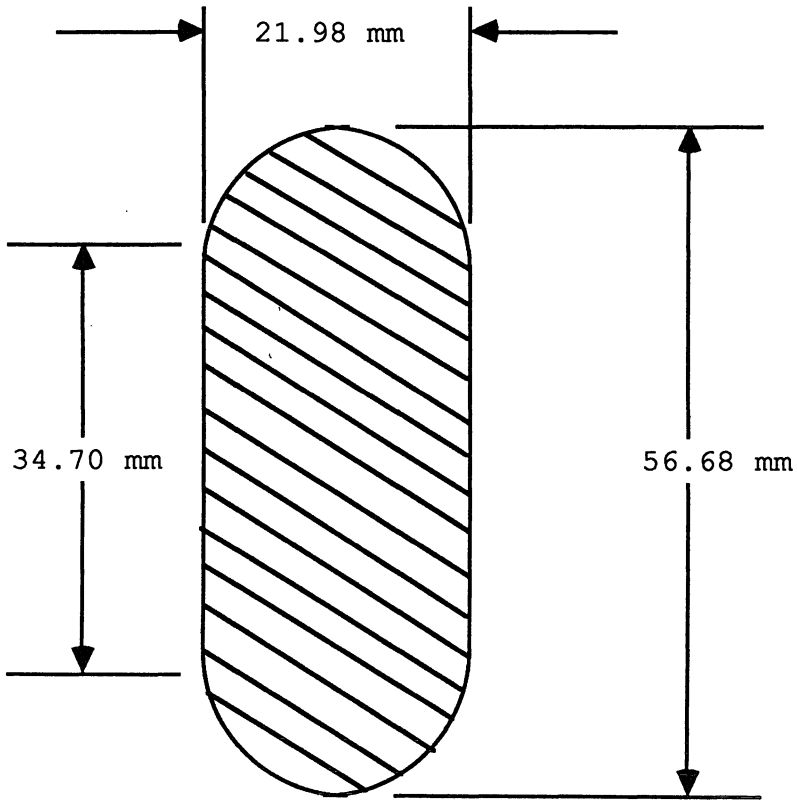

Table B-2. FNR Fuel Element Dimensions and Composition

	HEU Alloy Regular[1]	HEU Alloy Special	HEU Dispersion Regular[1]	LEU Regular	LEU Special
Fuel Meat Length (in)	23.5	23.5	23.0	23.5[2]	23.5[2]
Fuel Meat Width[3]	2.4	2.4	2.26	2.4[2]	2.4[2]
Fuel Meat Thickness[4]	0.022	0.022	0.025	0.032	0.032
Water Gap	0.115	0.115	0.122	0.115[2]	0.115[2]
Clad Thickness	0.020	0.020	0.015	0.015	0.015
Unit Cell Thickness	0.177	0.177	0.177	0.177	0.177
Number of Fuel Plates	18	9	18	18	9
Side Plate Width	3.17	3.17	3.15	3.15	3.15
Side Plate Thickness	0.189	0.189	0.189	0.189	0.189
Side Plate to Place Spacing	2.562	2.562	2.564	2.564	2.564
Fuel Curvature Radii	5.5	5.5	5.5	5.5	5.5
Special Guide Plate Width	----	2.562	----	----	2.564
Special Guide Plate Thickness	----	0.125	----	----	0.125
Fuel Meat Composition (gm)					
^{235}U	140.61	69.86	139.89	167.3	83.65
^{234}U	1.51	0.75	0.92	0.00	0.00
^{236}U	0.75	0.38	0.63	0.00	0.00
^{238}U	8.04	4.0	8.68	691.0	345.0
Aluminum	908.0	451.0	878.0	1180.0	590.0
Iron	3.7	1.8	3.5	8.2	4.1
Weight % Uranium in Fuel Meat	14.2	14.2	14.55	42.0	42.0
Cross Sectional Areas (in^2)					
Total Element	9.666	9.666	9.666	9.666	9.666
Lattice	7.654	3.827	7.207	7.654	3.827
Non-lattice	2.012	5.840	2.459	2.012	5.84
Metal in Non-lattice[5]	1.381	1.930	1.510	1.374	1.924
Water in Non-lattice	0.631	3.910	0.949	0.638	3.916

[1] New regular fuel elements added to the FNR core after December 4, 1978 were dispersion fuel elements. The last alloy regular fuel elements were discharged from the core during the summer of 1981.

[2] Dimensions chosen to be consistent with HEU alloy fuel element data.

[3] Fuel meat width is for a flat fuel plate.

[4] Fuel meat thickness calculated as: unit cell thickness - 2 x clad thickness - water gap; e.g. HEU alloy, .177" - 2 x .020" - .115" = .022"

[5] Modeling trace elements in the aluminum alloy is important.

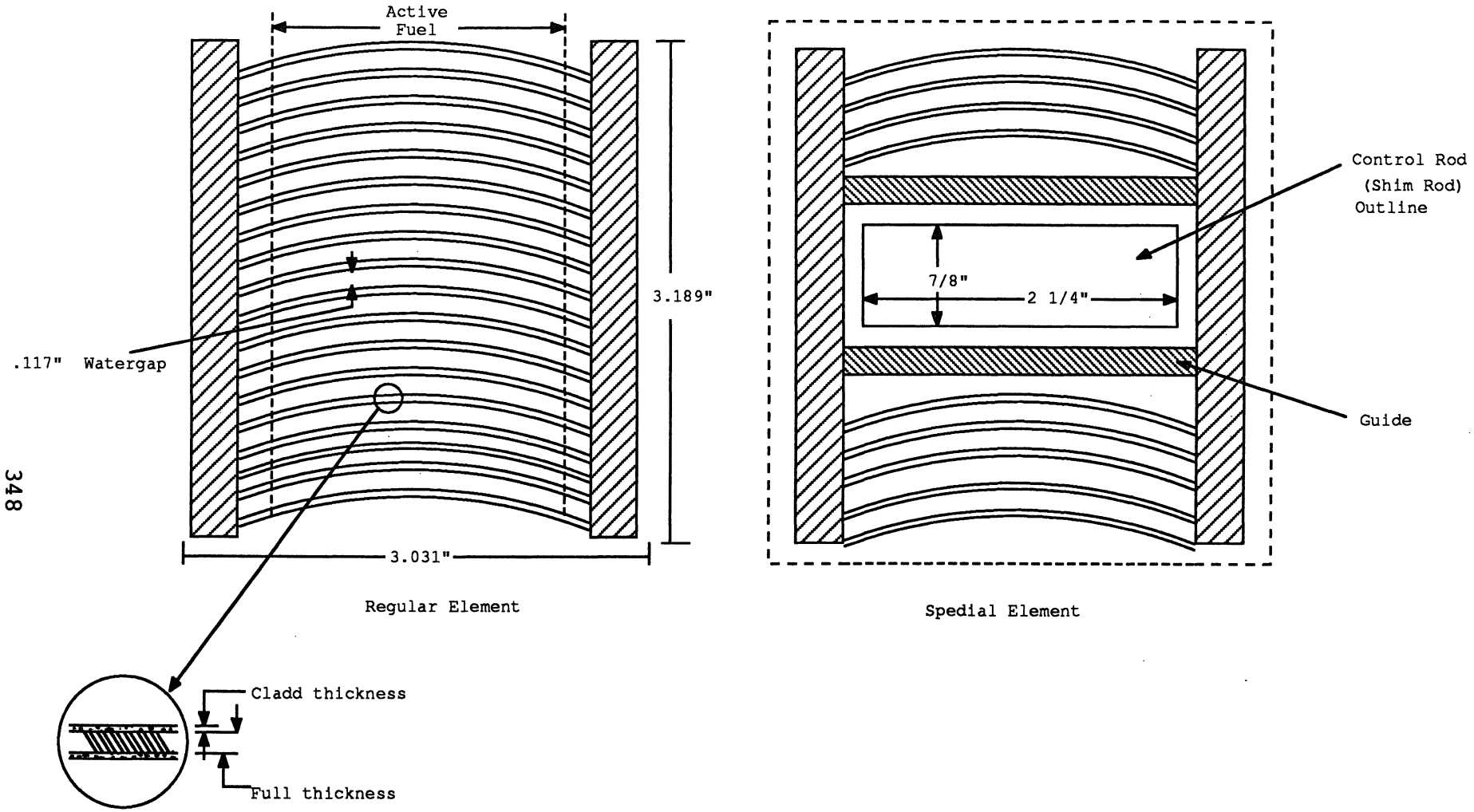

Figure B-1. FNR Fuel Element Schematics

Heavy Water (0.2~0.3m)			1.64 1.67				
Heavy Water (0.1~0.2m)			1.64 1.67				
Heavy Water (0~0.1m)			1.66 1.16	Aluminum (6mm)		1.66 1.07	
1.68 1.59	1.66 1.56	1.67 1.58	1.68 1.60	1.69 1.61	1.69 1.61	1.68 1.59	1.69 1.61
1.71 1.70	1.72 1.70	1.73 1.72	a 1.75 1.74	1.75 1.74	c 1.75 1.74	1.73 1.71	1.72 1.70
1.73 1.71	1.74 1.72	1.77 1.76	1.79 1.78	1.77 1.76	1.76 1.75	1.74 1.72	1.72 1.71
1.73 1.72	1.75 1.74	1.79 1.79	b 1.81 1.84	1.78 1.78	1.76 1.74	1.73 1.72	1.72 1.71
1.74 1.73	1.76 1.75	1.78 1.77	1.79 1.78	1.77 1.76	1.74 1.73	1.73 1.72	1.73 1.72
1.72 1.70	1.75 1.74	1.77 1.76	1.76 1.75	1.75 1.73	1.73 1.72	1.73 1.72	1.72 1.71

Water Reflector 1.71 / 1.67

Regular Element

Special Element

xx / xx

Fast group ($10\ m^{-2}$)

Thermal group ($10\ m^{-2}$)

Figure B-2. Axial Buckling Map for the FNR Core

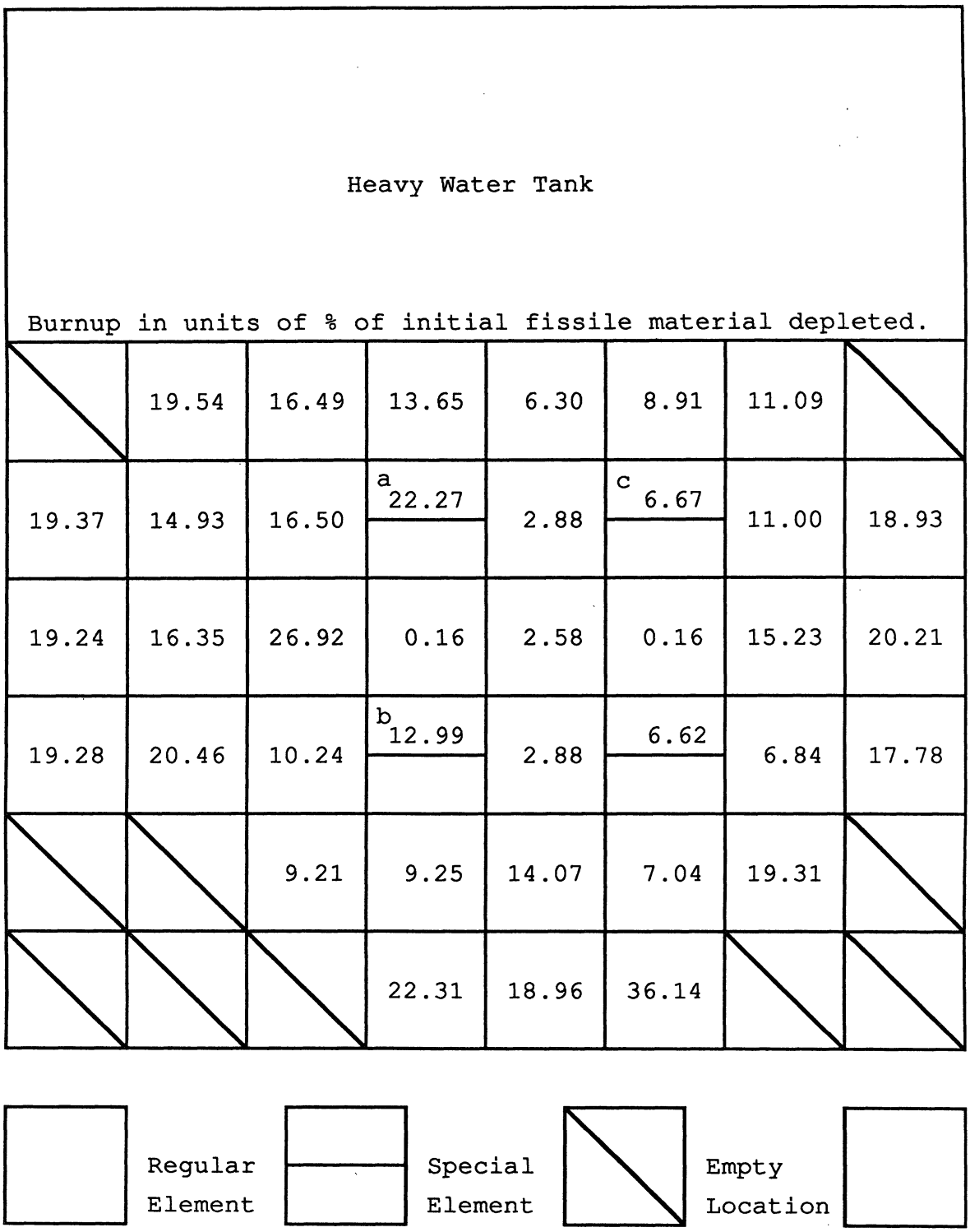

Figure B-3. Assembly Average Burnup for May 11, 1982, HEU Core

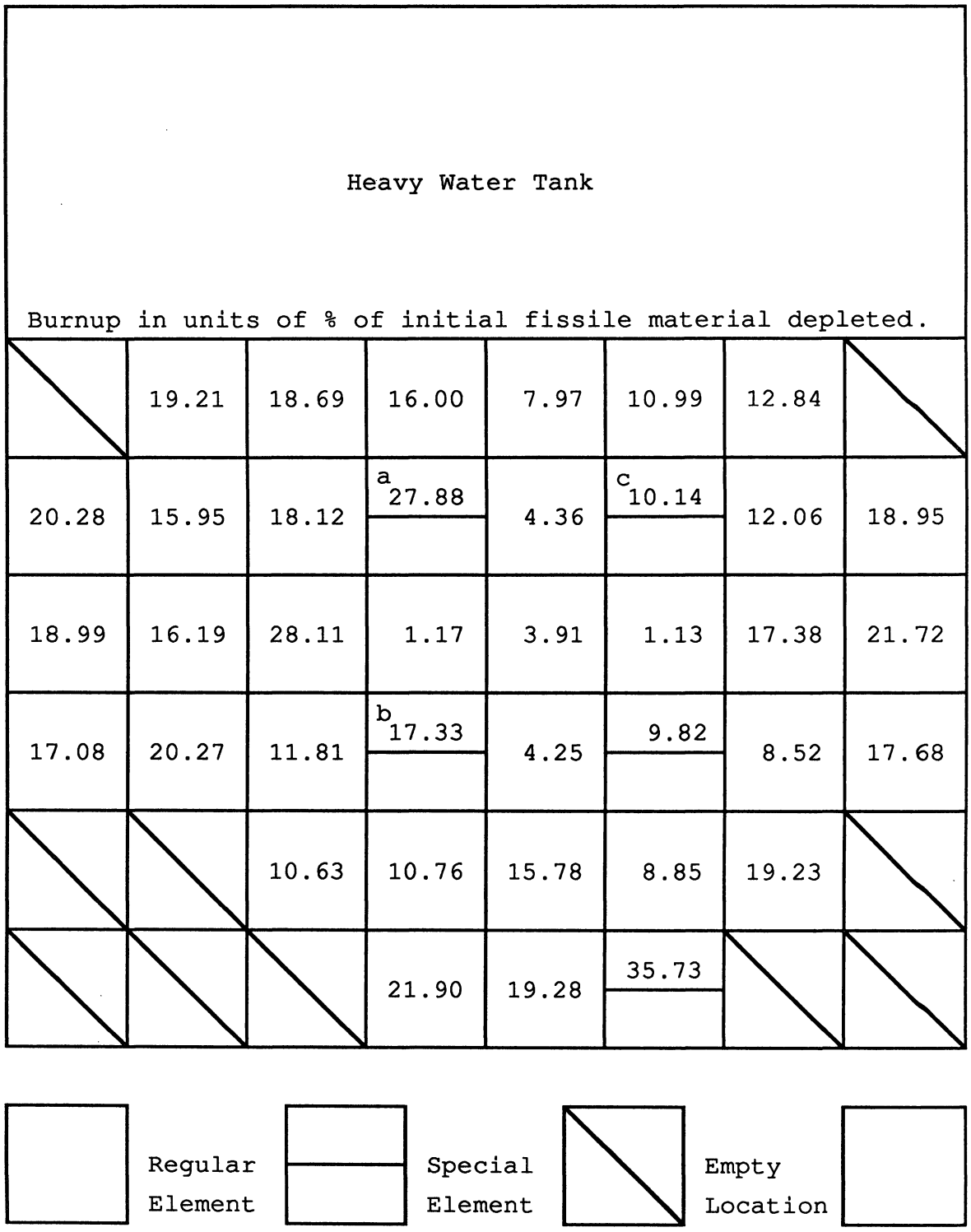

Figure B-4. Assembly Average Burnup for May 29, 1982, HEU Core

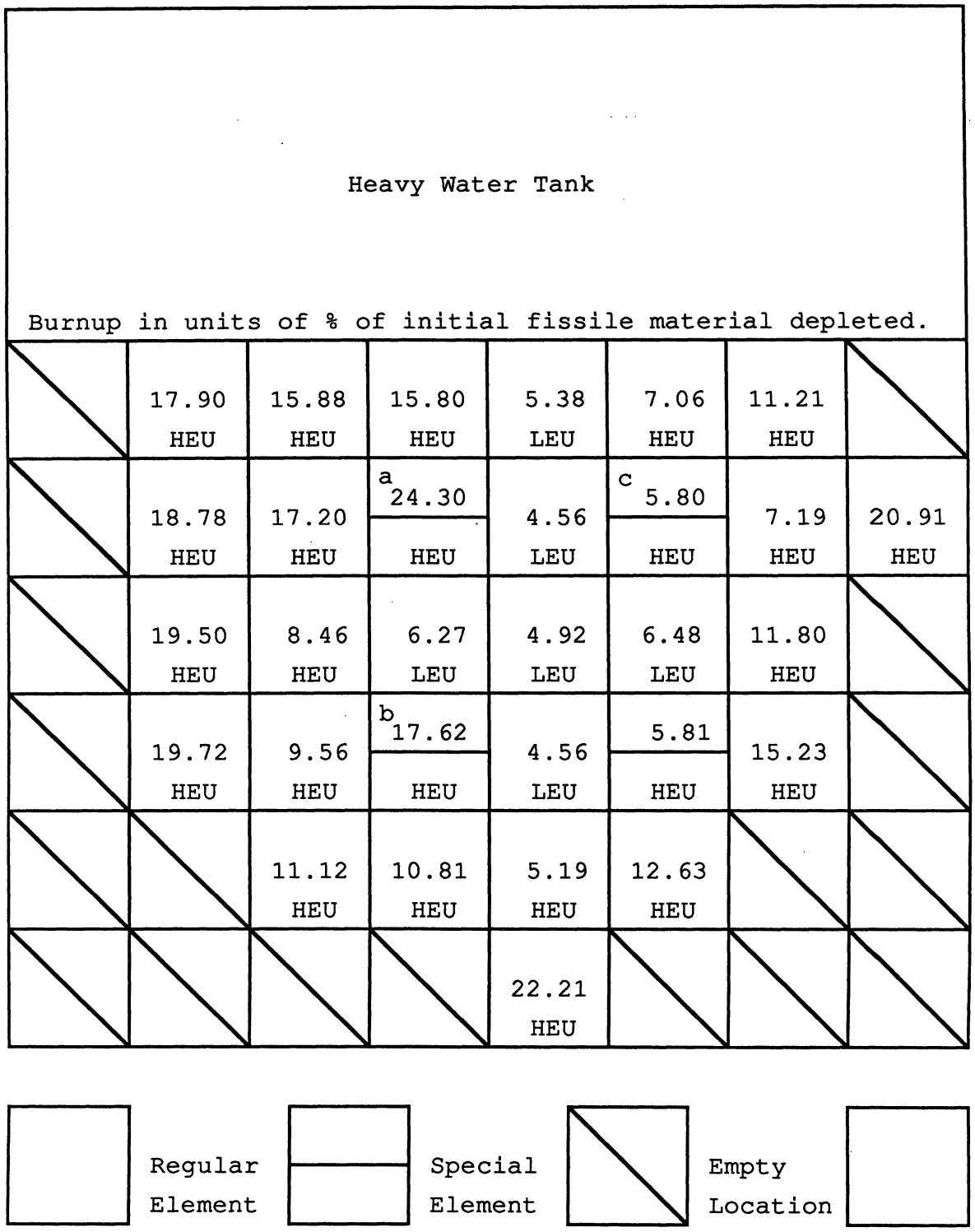

Figure B-5. Assembly Average Burnup for March 1983 Mixed Core

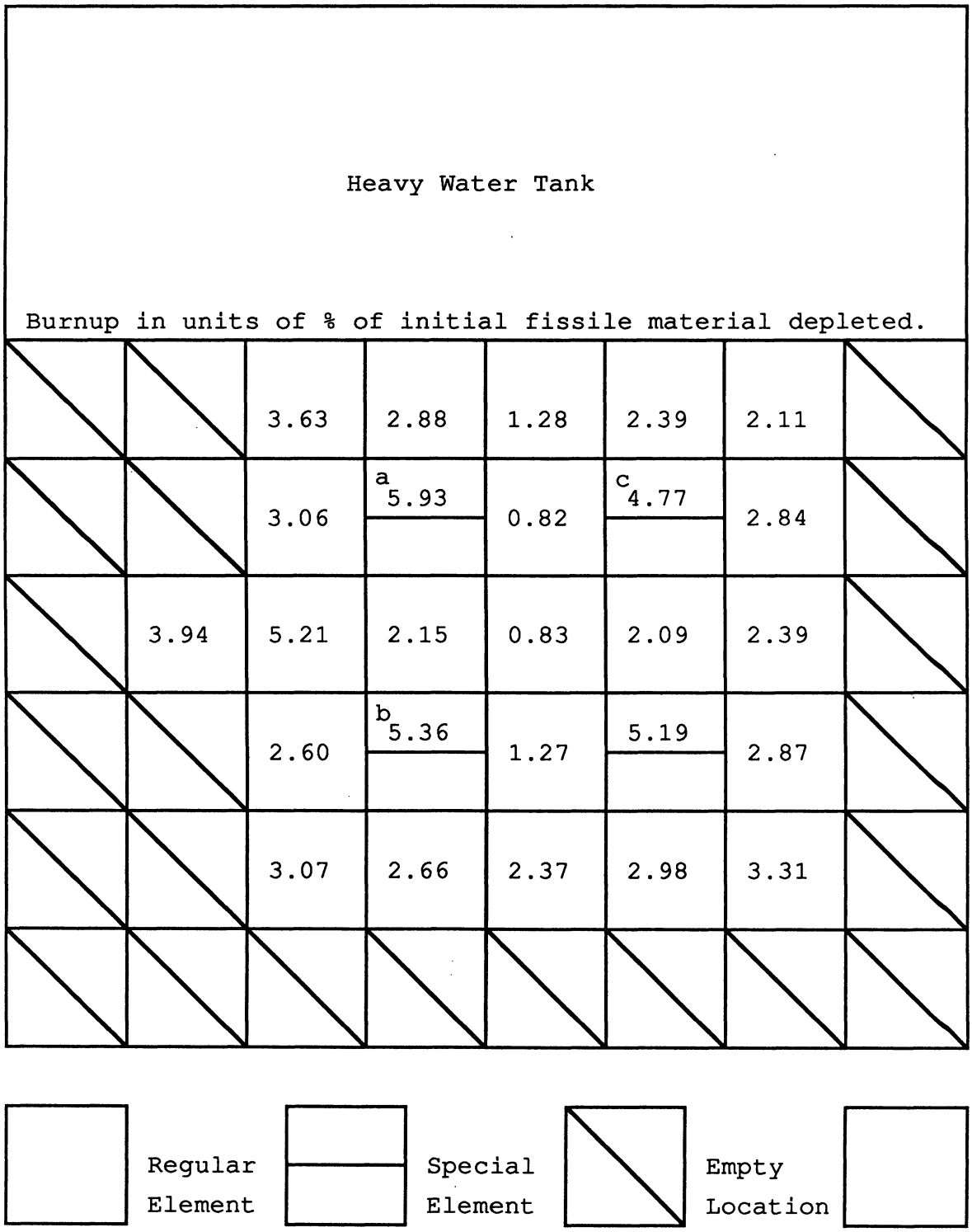

Figure B-6. Assembly Average Burnup for June 8, 1983, LEU Core

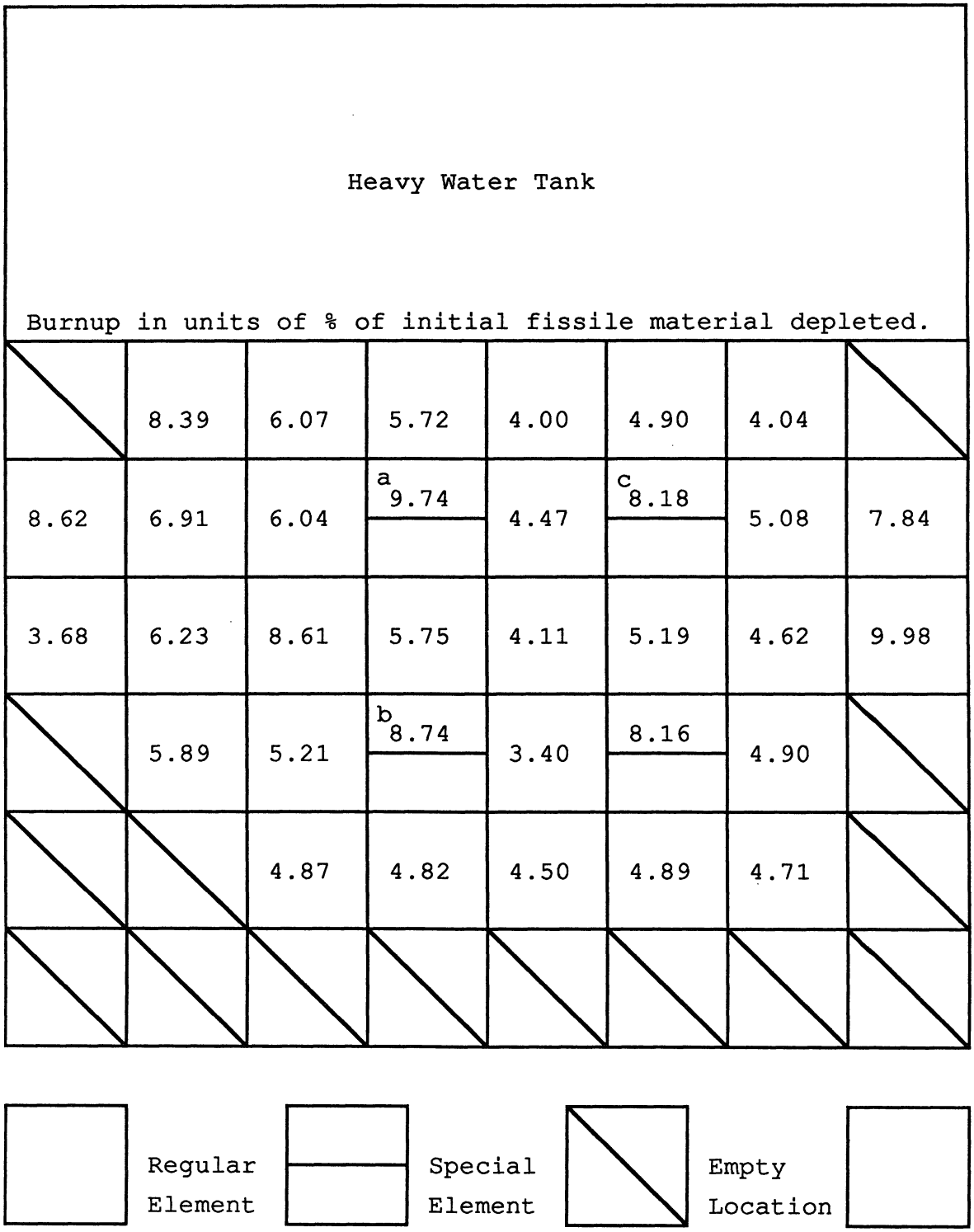

Figure B-7. Assembly Average Burnup for September 18, 1983, LEU Core

Heavy Water Tank

Burnup in units of % of initial fissile material depleted.

	19.72 HEU	12.97 HEU	4.12 LEU	4.67 LEU	7.28 HEU	12.92 HEU	
20.76 HEU	19.63 HEU	17.87 HEU	a 7.75 / LEU	4.23 LEU	c 6.98 / LEU	10.40 HEU	19.07 HEU
20.97 HEU	11.99 HEU	5.52 LEU	5.18 LEU	4.24 LEU	5.23 LEU	9.17 HEU	20.43 HEU
	19.64 HEU	14.61 HEU	b 7.75 / LEU	9.33 HEU	7.00 / LEU	17.21 HEU	
	19.74 HEU	19.62 HEU	13.96 HEU	13.09 HEU	17.96 HEU	19.04 HEU	

Regular Element

Special Element

Empty Location

Figure B-8. Assembly Average Burnup for October 5, 1983, Mixed Core

References

[Abr64] Abramowitz, M. and I. A. Stegun, Eds., **Handbook of Mathematical Functions**, National Bureau of Standards (1964).

[Adv77] "Advanced Recycle Methodology Program System Documentation, EPRI-CELL Code Description, Part II, Chapter 5," Electric Power Research Institute (1977).

[Amo57] Amouyal, A., P. Benoist, and J. Horowitz, **J. Nucl. Energy, 6**, 79 (1957).

[Ams57] Amster, H. and R. Suarez, "The Calculation of Thermal Constants Averaged over a Wigner-Wilkins Flux Spectrum: Description of the SOFOCATE Code," WAPD-TM-39, Bettis Atomic Power Laboratory (1957).

[And62] Anderson, W. K., R. L. Eichinger, R. A. Harlow, and G. J. Gosgrove,, "Boron-Stainless Steels," **Neutron Absorber Materials for Reactor Control**, W. K. Anderson and J. S. Theilacker, Eds., 235-269, U.S. Government Printing Office (1962).

[Anl77] "Argonne Code Center: Benchmark Problem Book," ANL-7416, Supplement 2, Argonne National Laboratory (June, 1977).

[Bal69a] Baldwin, M. N., R. H. Clark, and J. E. Rogers, "Physics Verification Program Part II, Final Report," BAW-3647-7, Babcock and Wilcox Company (1969); see also BAW-3647-13.

[Bal69b] Baldwin, M. N., and J. E. Rogers, **IEEE Trans. Nucl. Sci., NS-16**, 1781 (1969).

[Bar78] Barhen, J., W. Rothenstein and E. Taviv, "The HAMMER Code System," EPRI NP-565, Electric Power Research Institute (1978).

[Bar63] Barry, R. F., "LEOPARD - A Spectrum Dependent Non-Spatial Depletion Code," WCAP-3269-26, Westinghouse Electric Corporation (1963).

[Bea71] Beard, C. L., R. S. Dannels, "ETOT - A FORTRAN IV Program to Process Data from the ENDF/B File to Thermal Library Format," WCAP-7363, ENDF-146, Westinghouse Electric Corporation (1971).

[Bic35] Bickley, W. C. and J. Nayler, Jr., **Phil. Mag., 20,** 343 (1935).

[Boh57] Bohl, H., E. M. Gelbard and G. H. Ryan, "MUFT-4 -- Fast Neutron Spectrum Code for the IBM-704," WAPD-TM-72, Bettis Atomic Power Laboratory (1957).

[Bre65] Breen, R. J., O. J. Marlowe and C. J. Pfieffer, "HARMONY: System for Nuclear Reactor Depletion Computations," WAPD-TM-478, Bettis Atomic Power Laboratory (1965).

[Bro79] Brown, F. B., D. C. Losey, D. K. Wehe, J. C. Lee, and W. R. Martin, **Trans. Am. Nucl. Soc., 33,** 746 (1979).

[Cal67] Caldwell, W. R., "PDQ-7 Reference Manual," WAPD-TM-678, Westinghouse Electric Corporation (1967).

[Car65] Carlvik, I., Proc. Third International Conf. on Peaceful Uses of Atomic Energy, Vol. II, 225, International Atomic Energy Agency, Geneva (1965).

[Cob75] Cobb, W. R., W. J. Eich and D. E. Tivel, "EPRI-CELL Code Description," Advanced Cycle Methodology Program System Documentation, Nuclear Associates International Corporation (1975).

[Coo62] Cooper, P.N., K. Kirth, M. Kerridge, R. F. Mathams, A. J. Salmon and K. G. Stephens, "Some Measurements of Reactivity in Light-Water Highly Moderated Highly Enriched Uranium Assembly," **Reactor Sci. Tech., 16,** 65 (1962).

[Deb72] Debair, R. P., M. Grin and O. Simoni, EVR 4775e, Joint Nuclear Research Center, Ispra Establishment, Italy (1972).

[Dud79] Duderstadt, J. J. and W. R. Martin, **Transport Theory,** Wiley-Interscience, NY (1979).

[Eng62] England, T. R., "CINDER -- A One-Point Depletion and Fission Product Program," WAPD-TM-334, Bettis Atomic Power Laboratory (1962).

[Eng67] Engle, W. W., Jr., "A Users Manual for ANISN, A One Dimensional Discrete Ordinates Transport Code with Anisotropic Scattering," K-1693, Oak Ridge National Laboratory (1967).

[Eng76] England, T. R., W. B. Wilson and M. G. Stamtelatos, "Fission Product Data for Thermal Reactor, Part 2 --

User Manual for EPRI-CINDER Code and Data," EPRI-NP-356, Electric Power Research Institute (1976).

[Fab68] Fabry, A. and M. DeCoster, "Integral Test of Capture Cross Sections in the Energy Range 0.1-2.0 MeV", Proceedings of the Second Conference on Neutron Cross Sections and Technology, Spec. Publ. 299, Vol. 2, p 1263, National Bureau of Standards (1968).

[Fer77] Ferguson, D. R. and K. L. Derstine, **Nucl. Sci. Eng., 64,** 593 (1977).

[Fil72] Filmore, F. L., ANL ZPR-TM-121, Argonne National Laboratory (1972).

[Fri74] Frigerio, N. A., **Nucl. Instr. Meth., 114,** 175 (1974).

[Gol73] Goldstein, N. P., **IEEE Trans. Nucl. Sci., NS-20,** 549 (1973).

[Gre69] Greene, N. M. and C. W. Crave, Jr., "XSDRN: A Discrete Ordinates Spectral Averaging Code," ORNL-TM-2500, Oak Ridge National Laboratory (1969).

[Gre79] Greenwood, L. R., personal communication, 1979.

[Gru68] Grundl, J. A., "A Study of Fission-Neutron Spectral with High-Energy Activation Detectors", **Nucl. Sci. Eng., 31,** 191 (1968).

[Gun75] Gunst, J. C. Connor and D. E. Conway, "Measured and Calculated Fission-Product Poisoning in Neutron Irradiated Uranium-233," **Nucl. Sci. Eng., 58,** 387 (1975).

[Har67] Harris, L., Jr., **Measurement of Fast Neutron Spectra in Water and Graphite,** Ph.D. Thesis, Department of Nuclear Engineering, University of Michigan, Ann Arbor, MI, 68 (1967).

[Har68] Hardie, R. W. and W. W. Little, Jr., "1DX: A One-Dimensional Diffusion Code for Generating Nuclear Cross Sections," BNWL-954, Battelle Pacific Northwest Laboratory (1968).

[Har70a] Hardie, R. W. and W. W. Little, Jr., "3DB: A Three-Dimensional Diffusion Code For Generating Nuclear Cross Sections," BNWL-1264, Battelle Pacific Northwest Laboratory (1970).

[Har70b] Hardy, J., D. Klein and J. J. Volpe, "A Study of Physics Parameters in Several Water-Moderated Lattices of Slightly Enriched and Natural Uranium," WAPD-TM-931, Westinghouse Electric Corporation (1970).

[Har70c] Harris, D. R., "ANDYMG3: The Basic Program of a Series of Monte Carlo Programs for Time-Dependent Transport of Particle and Photons," LA-4539, Los Alamos Scientific Laboratory (1970).

[Hen80] Henderson, W. D., Private Communication, Westinghouse Electric Corporation, to J. C. Lee, University of Michigan (August 1, 1980).

[Hil64] Hilborn, J. W., **Nucleonics, 22,** 2, 69 (1964).

[Hon60] Honeck, H. C., **Nucl. Sci. Eng., 8,** 193 (1960).

[Hon62] Honeck, H. C., "A Thermalization Transport Code for Reactor Lattice Calculations," BNL-5826, Brookhaven National laboratory (1962).

[Iae80] "Research Reactor Core Conversion from the Use of Highly Enriched Uranium to the Use of low Enriched Uranium Fuels Guidebook," IAEA-TEC DOC-233, International Atomic Energy Agency (1980).

[Jab73] Jabbawy, S., J. Karni, W. Rothenstein and S. Velner, **Nuclear Data in Science and Technology,** Vol. II, p. 147, International Atomic Energy Agency, Vienna (1973).

[Joh57} Johnson, E. B., "Power Calibration for BSR Loading 33," CF-57-11-30, Oak Ridge National Laboratory (1957).

[Kap60] Kaplan, S. and A. F. Henry, "An Experiment to Measure Effective Delayed Neutron Fraction," WAPD-TM-209, Westinghouse Electric Corporation (1960).

[Ker80] Kerr, W., et al., "Low Enrichment Fuel Evaluation and Analysis Program, Summary Report for the Period of January, 1979-December, 1979," Department of Nuclear Engineering and Michigan-Memorial Phoenix Project Report, The University of Michigan (1980).

[Ker81] Kerr, W., et al., "Low Enrichment Fuel Evaluation and Analysis Program, Summary Report for the Period of January, 1980- December 1980," Department of Nuclear Engineering and Michigan-Memorial Phoenix Project Report, The University of Michigan (1981).

[Ker83] Kerr, W., et al., "Low Enrichment Fuel Evaluation and Analysis Program, Summary Report for the Period of January, 1981-December, 1982," Department of Nuclear Engineering and Michigan-Memorial Phoenix Project Report, The University of Michigan (1983).

[Ker84] Kerr, W., et al., "Low Enrichment Fuel Evaluation and Analysis Program, Summary Report for the Period of January, 1983-June, 1984," Department of Nuclear Engineering and Michigan-Memorial Phoenix Project Report, The University of Michigan (1984).

[Kir81] Kirk, M. A., R. C. Birtcher, T. H. Blewitt, L. R. Greenwood, R. J. Popek, and R. R. Heinrich, "Measurements of Neutron Spectra and Fluxes at Spallation-Neutron Sources and Their Application to Radiation Effects Research", **Journal of Nuclear Materials, 96,** 37 (1981).

[Kom79a] Komoriya, H. to J. L. Snelgrove, "Reduced Enrichment Fuel Element Loading Calculations for the Ford Nuclear Reactor," Argonne National Laboratory Internal Memorandum (February 14, 1979).

[Kom79b] Komoriya, H., **Trans. Am. Nucl. Soc., 33,** 745 (1979).

[Kro75] Kroon, J., AECL-5124, 135, Atomic Energy of Canada Limited (1975).

[Kus69] Kusner, D. E. and R. S. Dannels, "ETOG-1, A FORTRAN IV Program to Process Data from the ENDF/B File to the MUFT, GAM, and ANISN Format," WCAP 3845-1, Westinghouse Electric Corporation (1969).

[Laa75] Laaksonen, T., and J. Sasstamoinen, AECL-5124, 111, Atomic Energy of Canada Limited (1975).

[Lat73] Lathrop, K. D. and F. W. Brinkley, "TWOTRAN-II: An Interfaced Exportable Version of the TWOTRAN Code for Two-Dimensional Transport," LA-4848-MS, Los Alamos Scientific Laboratory (1973).

[Lit69] Little, W. W., Jr. and R. W. Hardie, "2DB User's Manual -- Revision I," BNWL-831, REVI, Battelle Pacific Northwest Laboratory (1969).

[Mat79] Matos, J. E. and K. E. Freese, **Trans. Am. Nucl. Soc., 33,** 739 (1979).

[Mce67] McElroy, W. N., et al., "SAND-II and Associated Codes," AFWL-TR-67-41, Vol. II, Air Force Weapons Laboratory,

Kirtland Air Force Base, NM (1967).

[Mce69] McElroy, W. N., "Implications of Recent Fission-Averaged Cross-Section Measurements", **Nucl. Sci. Eng., 36,** 109 (1969).

[Mor81] Moreira, J., "The Effective Delayed Neutron Fraction for the FNR," M.S. Project Report, Department of Nuclear Engineering, The University of Michigan (1981).

[Per77] Perey, F. G., "Least Squares Dosimetry Unfolding: The Program STASYL," ORNL/TM-6062 (ENDF-254), Oak Ridge National Laboratory (1977).

[Pra76] Prael, R. W. and L. J. Milton, "A User's Manual for the Monte Carlo Code VIM," FRA-TM-84, Argonne National Laboratory (1976).

[Rat81] Rathkopf, J., "Development of ENDF/B-IV Cross Section Library for the LEOPARD Code," Master's Project Report, Department of Nuclear Engineering, The University of Michigan (1981).

[Rot75] Rothenstein, W., "ENDF/B-IV Thermal Reactor Lattice Benchmark Analysis with Monte Carlo Resonance Treatment," BNL-NCS-50451, p. 222, Brookhaven National Laboratory (1975).

[Rut67] Rutherford, C. H., "MO807 -- A Diffusion Theory Fitting Program Using Fortran-IV," WAPD-TM-671, Bettis Atomic Power Laboratory (1967).

[Sch79] Schmittroth, F., "FERRET Data Analysis Code," HEDL-TME-79-40, Hanford Engineering Development Laboratory (1979).

[Str65] Strawbridge, L.E. and R. F. Barry, "Criticality Calculations for Uniform Water-Moderated Lattices," **Nucl. Sci. Eng., 23,** 58 (1965).

[Sui67] Suich, J. E. and H. C. Honeck, "The HAMMER System," DP-1064, Savannah River laboratory (1967).

[Von75] Vondy, D. R., T. B. Fowler, and G. W. Cunningham, "VENTURE: A Code Block for Solving Multigroup Neutronics Problems Applying the Finite-Difference Diffusion Theory Approximation to Neutron Transport," ORNL-5062, Oak Ridge National Laboratory (1975).

[War72] Warren, H. D., **Nucl. Sci. Eng., 48,** 331 (1972).

[Weh84] Wehe, D. K., "Measurements of Neutron Spectra in HEU and LEU Fuels," Ph.D. Thesis, Department of Nuclear Engineering, The University of Michigan (1984).

[Weh83a] Wehe, D. K. and J. S. King, "FNR Demonstration Experiments Part II: Subcadmium Neutron Flux Measurements", Proc. of the Int. Meeting on Development, Fabrication, and Application of Reduced Enrichment Fuels for Research and Test Reactors, ANL/RERTR/TM-4, Argonne National Laboratory (1983).

[Weh83b] Wehe, D. K. and J. S. King, "FNR Demonstration Experiments - Part I: Beam Port Leakage Currents and Spectra", Proc. of the Int. Meeting on Development, Fabrication, and Application of Reduced Enrichment Fuels for Research and Test Reactors, ANL/RERTR/TM-4, Argonne National Laboratory (1983).

[Wes80] Westfall, R. M. et al., "SCALE: A Modular Code System for Performing Standardized Computer Analysis for Licensing Evaluation," NUREG/CR-0200, Radiation Shielding Information Center, Oak Ridge National Laboratory (1980).

[Wig44] Wigner, E. P. and J. E. Wilkins, Jr., "Effect of the Temperature of the Moderator on the Velocity Distribution of Neutrons with Numerical Calculations for H as Moderator," AECD-2275, Oak Ridge National Laboratory (1944).

[Woo79] Woodruff, W. L., "Comparison of EPRI-CELL and VIM (Monte Carlo) Generated Microscopic Cross Section Data for a Slab Cell Representative of MTR-Type Research and Test Reactors using Highly-Enriched and Reduced-Enrichment Uranium Fuels," Argonne National Laboratory Internal Memorandum (January 3, 1979).

DISTRIBUTION FOR ANL/RERTR/TM-17

Internal:

A. Schriesheim
C. E. Till
Y. I. Chang
L. G. LeSage
M. J. Lineberry
J. F. Marchaterre
J. I. Sackett
M. J. Steindler
D. C. Wade
L. C. Walters
R. W. Weeks
P. I. Amundson
M. H. Derbidge
D. W. Green
C. E. Klotz
A. Travelli (50)
M. M. Bretscher
R. J. Cornella
J. R. Deen
J. E. Matos
S.-C. Mo
E. M. Pennington
R. B. Pond
J. L. Snelgrove (2)
W. L. Woodruff
ANL Contract File
ANL Patent Department
TIS Files (3)

External:

DOE-OSTI, for distribution per UC-520 (78)

ANL Libraries

Manager, Chicago Operations Office, DOE

Manager, Argonne Area Office, DOE-CH

D. E. Bailey, DOE-NE
R. H. Williamson, DOE-IA
S. Ceja, DOE-IA

University of Michigan:

R. R. Burn
W. Kerr
J. S. King
J. C. Lee
W. R. Martin (25)
D. K. Wehe

Engineering Physics Division Review Committee

Robert J. Budnitz, Future Resources Associates, Inc.
Michael J. Driscoll, Massachusetts Institute of Technology
George H. Gillespie, G. H. Gillespie Associates
W. Reed Johnson, University of Virginia
James E. Leiss, Broadway, Virginia
Gerold Yonas, Sandia National Laboratories